Design of Protected Superconducting Qubits

Clarke Smith

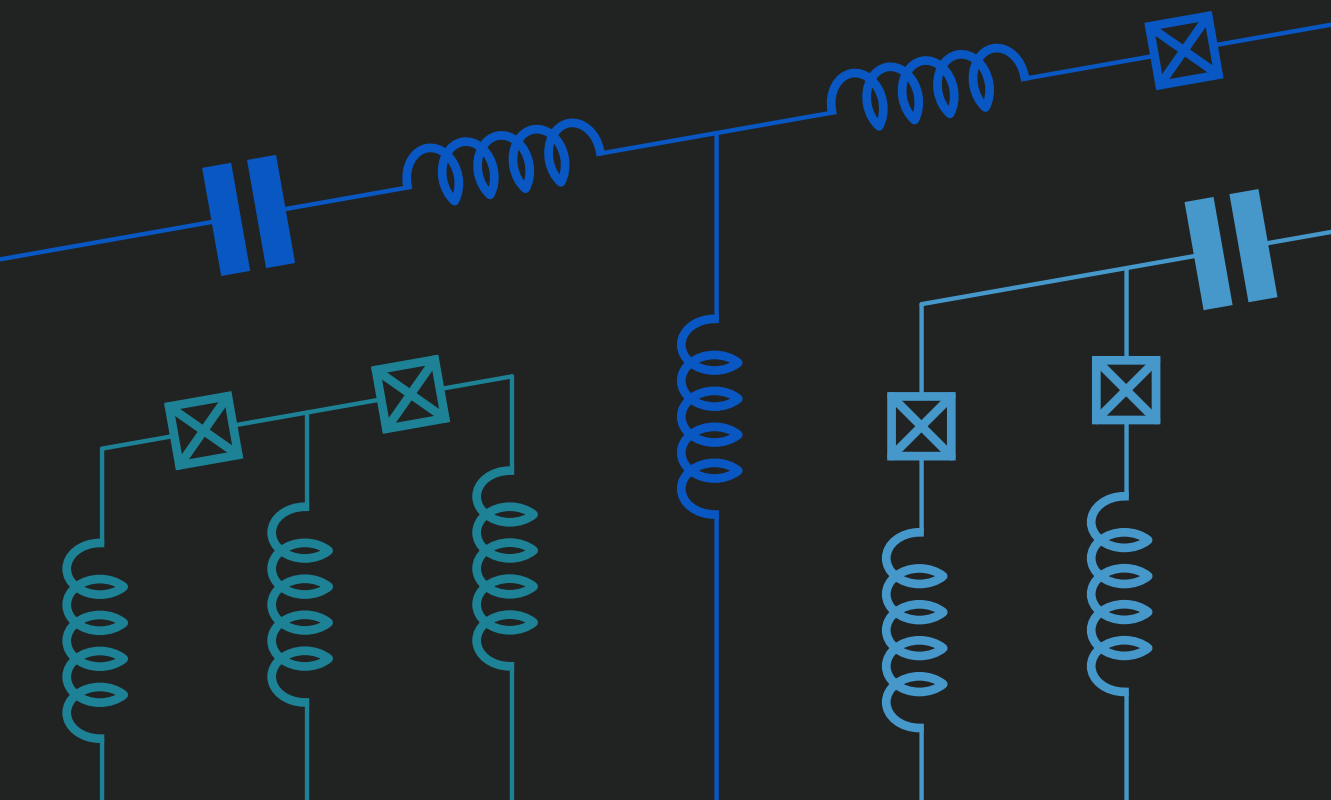

Abstract

Design of Protected Superconducting Qubits

William Clarke Smith
2019

Controllable quantum systems that are shielded *at the Hamiltonian level* from the random fluctuations of their environments could provide a valuable resource for quantum information science. While these "protected qubits" promise unprecedentedly low error rates, this might come at the expense of ease of physical implementation. This thesis focuses on overcoming this apparent design problem in protected qubits within the context of superconducting circuits and their quantized electromagnetic fields. We describe the essential design tools: quantization of nonlinear lumped element circuits, approximation by an effective Hamiltonian, numerical diagonalization to compute energy levels and matrix elements, Hamiltonian verification via spectroscopy, and noise characterization using time-domain measurements. At each stage, examples are given from the following systems: the fluxonium artificial atom, the double fluxonium artificial molecule, and our candidate protected qubit—the $\cos 2\varphi$ qubit. We validate the principle of designed protection, with numerical predictions of the insensitivity of the $\cos 2\varphi$ qubit to all expected decoherence mechanisms, and describe the current experimental status.

Design of Protected Superconducting Qubits

A Dissertation
Presented to the Faculty of the Graduate School
of
Yale University
in Candidacy for the Degree of
Doctor of Philosophy

by
William Clarke Smith

Dissertation Director: Michel Devoret

December 2019

CONTENTS

LIST OF FIGURES

LIST OF TABLES

LIST OF SYMBOLS

Symbol	Definition/Result
	Physical constants
h, $\hbar$	Planck constant and reduced version $\hbar = h/2\pi$
e	Elementary charge *Note*: Euler's constant is denoted e
Φ_0, ϕ_0	Magnetic flux quantum $\Phi_0 = h/2e$ and reduced version $\phi_0 = \Phi_0/2\pi$ *Shorthand*: $\mu\Phi_0 = \Phi_0 \times 10^{-6}$
k_B	Boltzmann constant
ϵ_0	Vacuum permittivity
μ_0	Vacuum permeability
Δ	Superconducting gap (the spectroscopic gap is 2Δ)
ξ_0	Coherence length
$\mathcal{R}_Q$	Reduced superconducting resistance quantum *Note*: regular/reduced and normal/superconducting versions are $R_K = h/e^2$, $R_Q = h/(2e)^2$, $\mathcal{R}_K = \hbar/e^2$, and $\mathcal{R}_Q = \hbar/(2e)^2$
	Generic variables
t	Time
ω, f	Angular frequency (the Fourier partner to time t) and frequency $f = \omega/2\pi$
Γ	Rate
T	Temperature
E	Energy *Note*: $E = k_B T$ by the equipartition theorem *Note*: $E = \hbar\omega$ by Planck's law
λ	Generic Hamiltonian parameter
ε	Classical control field
$\mathbf{E}$	Electric field
$\mathbf{B}$	Magnetic field
$\mathbf{J}$	Electric current density
$\mathbf{x}$	Position
$\hat{\mathbf{x}}$, $\hat{\mathbf{n}}$	Unit position and normal vectors
$\mathcal{A}$	Area
$\mathcal{C}$	Closed curve
$\mathcal{S}$	Closed surface

Symbol	Definition/Result
	States
$\|n\rangle$, $\|m\rangle$	Harmonic oscillator eigenstates with excitation indices $n, m = 0, 1, 2, \ldots$
$\|\alpha\rangle$	Coherent state with amplitude α
$\|\mu\rangle$, $\|\nu\rangle$	Generic eigenstates of an artificial atom with excitation indices μ and ν *Convention*: $\mu, \nu = g, e, f, h, \ell, d, \ldots$ in order of ascending energy
$\|\varphi\rangle$	Superconducting phase eigenstate
$\|N\rangle$	Cooper pair number eigenstate
$\|\circlearrowright\rangle$, $\|\circlearrowleft\rangle$	Persistent current eigenstates
$\|\pm\rangle$	Symmetric and antisymmetric superpositions of persistent currents $\|\pm\rangle = \frac{1}{\sqrt{2}}(\|\circlearrowright\rangle \pm \|\circlearrowleft\rangle)$
$\|\psi\rangle$	Generic eigenstate
$\|r\rangle$, $\|\bar{r}\rangle$	Generic bath eigenstates
E_μ	Eigenenergy corresponding to $\|\mu\rangle$
$E_{\mu\nu}$, $\omega_{\mu\nu}$, $f_{\mu\nu}$	Transition energy, angular frequency, and frequency for $\mu \to \nu$ $E_{\mu\nu} = E_\nu - E_\mu$ and $\omega_{\mu\nu} = E_{\mu\nu}/\hbar = 2\pi f_{\mu\nu}$
ΔE, $\Delta\omega$	Qubit energy splitting and angular frequency $\Delta\omega = \Delta E/\hbar$ *Note*: usually coincide with E_{ge} and ω_{ge}, respectively
ϵ_μ	Charge dispersion of the energy level E_μ
ϵ	Charge dispersion of the qubit splitting ΔE
p_μ	Population of $\|\mu\rangle$
	Operators
N, M, P	Number of Cooper pairs
φ, θ, ϕ	Superconducting phase
Q	Generalized electric charge $Q = -\int_{-\infty}^{t} \mathrm{d}t'\, I(t') = 2eN$[1] *Also*: out-of-phase quadrature of electric field
Φ	Generalized magnetic flux $\Phi = \int_{-\infty}^{t} \mathrm{d}t'\, V(t') = \phi_0\varphi$[1]
V	Voltage $V = \dot{\Phi}$[1]
I	Current $I = -\dot{Q}$[1] *Also*: in-phase quadrature of electric field
H	Hamiltonian
$\mathcal{L}$	Lagrangian
U	Potential
$\mathcal{O}$, $\mathcal{O}_0$	Generic system operator and expectation value in the qubit manifold $\mathcal{O}_0 = \frac{1}{2}(\langle g\|\mathcal{O}\|g\rangle + \langle e\|\mathcal{O}\|e\rangle)$
$\mathcal{M}$	Generic system operator that couples qubit states: $\langle g\|\mathcal{M}\|e\rangle \sim 1$
$\mathcal{E}$	Generic bath operator
a, $a^\dagger$	Bosonic annihilation and creation operators
n	Photon number operator $n = a^\dagger a$
ρ	Density matrix
σ_x, σ_y, σ_z	Pauli operators
$\mathcal{U}$	Unitary transformation
Λ	Change-of-basis matrix

1 Note that the sign choice is for Φ as the position-like coordinate and Q as the momentum-like coordinate.

Symbol	Definition/Result
	Parameters
E_C	"Coulomb" energy $E_\mathrm{C} = e^2/2C$ for a capacitance C (energy stored by a capacitor with plates charged $\pm e$)
E_L	"Lorentz" energy $E_\mathrm{L} = \phi_0^2/L$ for an inductance L (twice the energy stored by an inductor with magnetic flux ϕ_0)
E_J	Josephson energy $E_\mathrm{J} = \phi_0 I_0 = \phi_0^2/L_\mathrm{J}$ for a Josephson junction with critical current I_0, or equivalently, linear inductance L_J (energy required for one Cooper pair to tunnel across the junction)
E_S	Phase-slip energy [for a single Josephson junction, $E_\mathrm{S} \sim (E_\mathrm{J}^3 E_\mathrm{C})^{1/4} \mathrm{e}^{-\sqrt{8E_\mathrm{J}/E_\mathrm{C}}}$]
I_0	Josephson critical current
C	Capacitance
L	Inductance
ω_0	Angular frequency of an LC oscillator $\omega_0 = (LC)^{-1/2}$
Z_0	Characteristic impedance of an LC oscillator $Z_0 = (L/C)^{1/2}$
χ	Dispersive shift of a qubit on its readout resonator (an angular frequency)
κ	Readout resonator linewidth (an angular frequency)
Q	Quality factor $Q = \omega_0/\kappa$
Φ_zpf, φ_zpf	Amplitude of zero-point flux and phase fluctuations *Note*: for an LC oscillator Hamiltonian $H = 4E_\mathrm{C}N^2 + \frac{1}{2}E_\mathrm{L}\varphi^2$, $\Phi_\mathrm{zpf} = \phi_0\varphi_\mathrm{zpf}$ and $\varphi_\mathrm{zpf} = (2E_\mathrm{C}/E_\mathrm{L})^{1/4}$
Q_zpf, N_zpf	Amplitude of zero-point charge and Cooper pair number fluctuations *Note*: for an LC oscillator, $Q_\mathrm{zpf} = 2eN_\mathrm{zpf}$ and $N_\mathrm{zpf} = \frac{1}{2}(E_\mathrm{L}/2E_\mathrm{C})^{1/4}$
Q_g	Offset charge
N_g	Offset charge in number of Cooper pairs $N_\mathrm{g} = Q_\mathrm{g}/2e$
Φ_ext	External magnetic flux
φ_ext	Normalized external magnetic flux $\varphi_\mathrm{ext} = \Phi_\mathrm{ext}/\phi_0$
ϕ_ext	Periodic normalized external magnetic flux $\phi_\mathrm{ext} = \left\lvert\varphi_\mathrm{ext} - 4\pi \,\mathrm{round}\, \frac{\varphi_\mathrm{ext}}{4\pi}\right\rvert$
n_th	Number of thermal photons in a readout resonator
$\bar{n}$	Number of coherent photons in a readout resonator
α	Coherent state amplitude $\lvert\alpha\rvert^2 = \bar{n}$
n_0, N_0	Truncated Hamiltonian dimension in Fock and charge bases
δ	Dimensionless asymmetry parameter e.g. two Josephson junctions with tunneling energies $(1 \pm \delta_\mathrm{J})E_\mathrm{J}$
T_1, Γ_1	Relaxation time and its corresponding rate $\Gamma_1 = 1/T_1$
T_ϕ, Γ_ϕ	Pure-dephasing time and rate $\Gamma_\phi = 1/T_\phi$
T_2, Γ_2	Decoherence time and rate $\Gamma_2 = 1/T_2 = 1/(2T_1) + 1/T_\phi$ $T_{2\mathrm{R}} = 1/\Gamma_{\phi\mathrm{R}}$: value from a Ramsey-type measurement $T_{2\mathrm{E}} = 1/\Gamma_{\phi\mathrm{E}}$: value from a spin-echo-type measurement
$\Gamma_{\mu\to\nu}$	Transition rate from $\lvert\mu\rangle$ to $\lvert\nu\rangle$
t_gate, τ_gate	Gate time
ω_ir	Infrared cutoff angular frequency
x_qp	Quasiparticle density relative to Cooper pair density

Symbol	Definition/Result
	Miscellaneous
$Z(\omega)$	Impedance
$Y(\omega)$	Admittance
$S_{XY}[\omega]$	Spectral correlation density $S_{XY}[\omega] = \int_{-\infty}^{\infty} \mathrm{d}t\, \mathrm{e}^{i\omega t}\langle X(t)Y(0)\rangle$ (see App. A for Fourier transform conventions)
A_λ	$1/f$ noise spectral density amplitude for parameter λ i.e. $S_{\lambda\lambda}[\omega] \approx 2\pi A_\lambda/\lvert\omega\rvert^p$ such that $0.5 \lesssim p \lesssim 1.5$
$f_\phi(t)$	Phase decay envelope $f_{\phi\mathrm{R}}(t)$: as measured in a Ramsey-type experiment $f_{\phi\mathrm{E}}(t)$: as measured in a spin-echo-type experiment
m	Order of a generalized Josephson element $m = 1, 2, 3, \ldots$ *Note*: potential energy appears as $(-1)^m E_\mathrm{J} \cos m\varphi$
ℓ	Phase-space separation between qubit states
τ	Time spent in arbitrary qubit state before a quantum jump
Σ	Normalized covariance between times spent between quantum jumps
$\mathcal{O}_\psi$	Normalized matrix element of $\mathcal{O}$ to the ground state $\lvert\mathcal{O}_\psi\rvert^2 = \lvert\langle\psi\rvert\mathcal{O}\lvert g\rangle\rvert^2/\langle g\rvert\mathcal{O}^\dagger\mathcal{O}\lvert g\rangle$
$\mathcal{H}$	Hilbert space
$H_n(x)$	Physicists' Hermite polynomial of order n
$\mathscr{L}_a^b(x)$	Associated Laguerre polynomial of order a and index b
	Notation
$\overline{\bullet}$	Temporal average
$\langle \bullet \rangle$	Expectation value/ensemble average
$[\bullet]$	Units of the physical quantity $\bullet$
$[\bullet, \circ]$	Commutator
$\lvert \bullet\ \circ\rangle$	Composite eigenket $\lvert \bullet\ \circ\rangle = \lvert\bullet\rangle \otimes \lvert\circ\rangle$
$\bullet \to \circ$	Transition from $\lvert\bullet\rangle$ to $\lvert\circ\rangle$
$\bullet \oplus \circ$	Direct sum
$O(\bullet)$	Big O notation for order
round$(\bullet)$	Nearest-integer rounding function

Acronyms

SNAIL	Superconducting Nonlinear Asymmetric Inductive eLement
SQUID	Superconducting QUantum Interference Device
WKB	Wentzel-Kramers-Brillouin
GKP	Gottesman-Kitaev-Preskill
cQED	circuit Quantum ElectroDynamics
FWHM	Full Width at Half Maximum
HEMT	High Electron-Mobility Transistor
JPC	Josephson Parametric Converter
STIRAP	STImulated Raman Adiabatic Passage
OFHC	Oxygen-Free High-Conductivity

Special terms

Fluxonium qubit A small Josephson junction ($E_C \lesssim E_J$) shunted by a large linear superinductance ($E_L \ll E_J$).

Fluxonium artifical atom A fluxonium qubit sharing a fraction of its superinductance with an electric dipole antenna used as a readout resonator.

Double fluxonium artificial molecule Two fluxonium qubits strongly coupled via sharing half of their individual superinductances.

$\cos 2\varphi$ *qubit* A Josephson-junction-like circuit element, which only permits the tunneling of pairs of Cooper pairs, shunted by a large capacitance.

ACKNOWLEDGEMENTS

This dissertation is the product of countless discussions involving many people, and it would be a husk of its present form without their vital contributions. I owe them all a great deal of gratitude.

The most important role was played by my advisor, Michel Devoret, who above all showed me that there is no limit to the depth to which something can be understood. I would also like to thank the other members of my committee—Rob Schoelkopf, Steve Girvin, and Leonid Glazman—for their insight and support. Additionally, I thank Vlad Manucharyan both for pioneering the fluxonium circuit, on which most of the results in this thesis are built, and for serving as my external reader.

A substantial amount of credit is due to Angela Kou, for her sustained effort in training me as a scientist and for being my closest colleague during my Ph.D. The remaining members of the fluxonium project—Uri Vool and Ioan Pop—also played significant roles. Finally, I am indebted (in alphabetical order) to Philippe Campagne-Ibarcq, Luigi Frunzio, Alex Grimm, Gijs de Lange, Mazyar Mirrahimi, Kyle Serniak, Shyam Shankar, Steven Touzard, Jaya Venkatraman, and Xu Xiao, each in their own individual way.

This thesis is dedicated to my dog, Echo.

1

INTRODUCTION

1.1 Historical context

Quantum mechanics was first developed by physicists seeking a fundamental understanding of matter and its interaction with light at atomic scales. It has progressively evolved into a domain of science bordering both macroscopic signal processing and information/computation theory, with the early work of Feynman [Feynman 1982] on quantum computation and simulation often being cited as a visionary call to arms. Extending the initial goals of quantum mechanics beyond purely microscopic entities is also closely linked with the development of mesoscopic physics, a particular hallmark of which is the prediction of coherent tunneling across superconducting weak links [Josephson 1962]. Finally, the study of quantum dynamics in the presence of friction has progressed to the investigation of open quantum systems (see the Caldeira-Leggett model of quantum dissipation [Caldeira and Leggett 1983], for example). At the intersection of these subfields lie superconducting circuits: arrangements of superconducting electrodes connected by Josephson junctions. In a variety of circumstances, the first two energy eigenstates of a superconducting circuit can be manipulated much faster than they dissipate, and we call them a superconducting quantum bit (qubit) [Bouchiat et al. 1998].

Alongside superconducting circuits, there are a handful of promising approaches to building hardware for an eventual quantum computer. Any list of near-term implementations should also include trapped ions [Cirac and Zoller 1995], nitrogen-vacancy centers (and other natural atoms embedded in crystals) [Jelezko et al. 2004], and spin qubits in quantum dots [Petta et al. 2005], at the absolute minimum. On the horizon, there are also approaches based on nonabelian anyons [Freedman et al. 2003] as well as hybrid quantum systems (e.g. using magnons [Tabuchi et al. 2015] or phonons [Chu et al. 2017]). Moreover, there are various potential applications for superconducting circuits peripheral to quantum information: quantum sensing, quantum simulation, quantum annealing, and so on. Hereafter, we focus on superconducting circuits in the context of quantum computation.

The dimensions of superconducting circuits typically range from 10 nm to 1 mm, meaning they comprise 10^9 to 10^{12} atoms and are reasonably mesoscopic [Devoret and Schoelkopf 2013]. Their utility hinges on their relatively low dissipation—owing to superconductivity—and large electric dipole moments—owing to their large size relative to atoms and the strength of Coulomb repulsion. For these reasons, in addition to the commercial availability of nanofabrication equipment, microwave electronics, and dilution refrigerators, the field has seen rapid progress and a considerable rise in popularity over the past decade. In particular, state-of-the-art coherence times ($T_2 \sim 100\,\mu$s [Z. Wang et al.

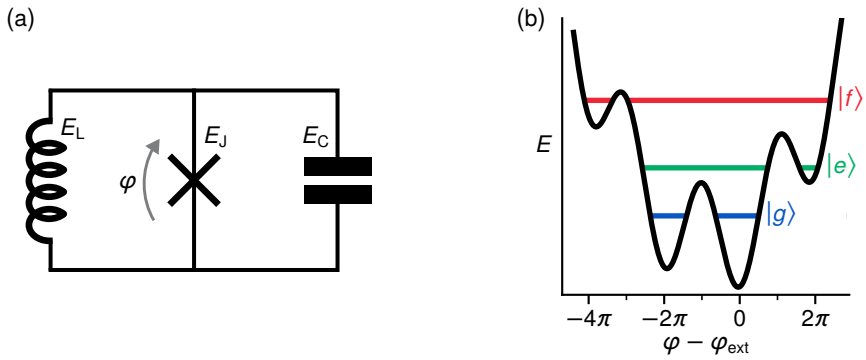

Figure 1.1 Generic single degree-of-freedom superconducting circuit. (a) Electrical circuit diagram. (b) Example potential energy and the lowest three energy levels, in the situation where multiple wells exist, showing that the ground state is generally localized in some subset of the wells.

2019]) are almost 5 orders of magnitude longer than those originally measured ($T_2 \sim 2\,\text{ns}$ [Nakamura et al. 1999]).

1.2 Programmability of circuit Hamiltonians

A less obvious reason, perhaps, for these improvements is the programmability of the entire Hamiltonian of a circuit. The combination of superconductivity and the Coulomb interaction also renders circuit Hamiltonians very well described in terms of macroscopic degrees of freedom, often superconducting phase differences and excess numbers of Cooper pairs between electrodes. It turns out that the functional form (nontrivial for circuits with multiple degrees of freedom, i.e. with capacitance matrices of rank greater than one) and the energy scales of the Hamiltonian may both be designed. Over the last two decades, this has allowed physicists to engineer different varieties of qubits to combat particular detrimental effects. Two excellent examples are given by the quantronium [Vion et al. 2002] and transmon [J. Koch et al. 2007] qubits, and they can be viewed as basic demonstrations of protected superconducting qubits.

To illustrate this programmability and the variety of superconducting circuits that it has spawned, we consider the generic circuit for a single degree-of-freedom qubit (see Fig. 1.1a). A linear inductance with inductive energy E_L, a Josephson junction with tunneling energy E_J, and a capacitance with capacitive energy E_C are placed in a parallel configuration. Since we will discuss circuits in depth in Ch. 2, at this point it suffices to say that this circuit has one degree of freedom (up to a choice of electromagnetic gauge): the superconducting phase φ across the junction, which is conjugate to the number of tunneled Cooper pairs N. The Hamiltonian is

$$H = 4E_C(N - N_g)^2 + \tfrac{1}{2}E_L(\varphi - \varphi_{ext})^2 - E_J \cos\varphi, \tag{1.1}$$

	E_J/E_C	E_L/E_J	$\overline{N_g}$	$\overline{\varphi_{ext}}$	Symbol (Region)	Representative reference
Cooper pair box	0.3–1	0	1/2		(M)	Nakamura et al. (1999)
Quantronium	1–10	0	1/2		(M)	Vion et al. (2002)
Transmon	10–10^3	0	any		(M)	Schreier et al. (2008)
rf-SQUID	$\gtrsim 10^3$	0.3–10		π	(II)	Friedman et al. (2000)
Flux qubit	10–100	0.3–1		π	(II)	van der Wal et al. (2000)
C-shunt flux qubit	20–200	1–5		π	(I)	Yan et al. (2016)
L-shunt transmon	20–10^3	0.5–5		0	(I)	
Fluxonium	1–10	10^{-3}–0.1		π	(II)	Manucharyan et al. (2009)
Heavy fluxonium	10–100	10^{-3}–0.1		$\pi - \delta$ $0<\lvert\delta\rvert\ll\pi$	(II)	Earnest et al. (2018)
Phase qubit	$\gtrsim 10^4$	0.1–1		0	(II)	Steffen et al. (2006)

Table 1.1 Varieties of superconducting qubits. The groups of rows correspond to qubit types with similar character. The first two columns indicate the effective mass E_J/E_C and the (inverse) number of potential minima E_L/E_J. The second two columns indicate the operating value of the offset charge $\overline{N_g}$ and that for the external flux $\overline{\varphi_{ext}}$. The final two columns list the correspondence to Fig. 1.2 and an example literature reference.

where we have introduced the offset charge N_g (in number of Cooper pairs) as well as the external flux φ_{ext} (in number of reduced magnetic flux quanta ϕ_0) [J. Koch et al. 2009]. Note that $\phi_0 = \hbar/2e$, with $\hbar$ being the reduced Planck constant and e the elementary charge. The phase φ is readily thought of as the position of a particle, in which case N plays the role of momentum. The Hamiltonian then describes the particle moving over a one-dimensional curve $U = \frac{1}{2}E_L(\varphi - \varphi_{ext})^2 - E_J \cos\varphi$ (plotted in black in Fig. 1.1b) with inverse mass E_C. The compactness of Eq. 1.1 should not be mistaken for simplicity: even the static properties of the lowest eigenstates can prove challenging to model.

Indeed, the general result is quite complicated. Depending on the ratio E_L/E_J (and the value of φ_{ext}), there may be any number of potential minima that the particle could get stuck in, or that quantum fluctuations could cause tunneling between. The number of available potential wells (say, at $\varphi_{ext} = \pi$), and the number of wells in which the ground state resides, form a foundation for classifying this behavior. Within the parameter space $0.1 < E_J/E_C < 10^5$ and $0.02 < E_L/E_J < 2$, a host of options exist (see Fig. 1.2). It is precisely this rich landscape that has led to the variety of qubits in use today. Ten examples are listed in Tab. 1.1 and plotted in Fig. 1.2.

1.3 Role of protected qubits

Possibly even more impressive than the improvement in raw coherence by a factor of $\sim 10^5$ are the associated advances toward quantum error correction, i.e. the idea that qubits encoded in a Hilbert space $\mathcal{H}$ (such that $\dim \mathcal{H} \gg 2$) can perform much better than their

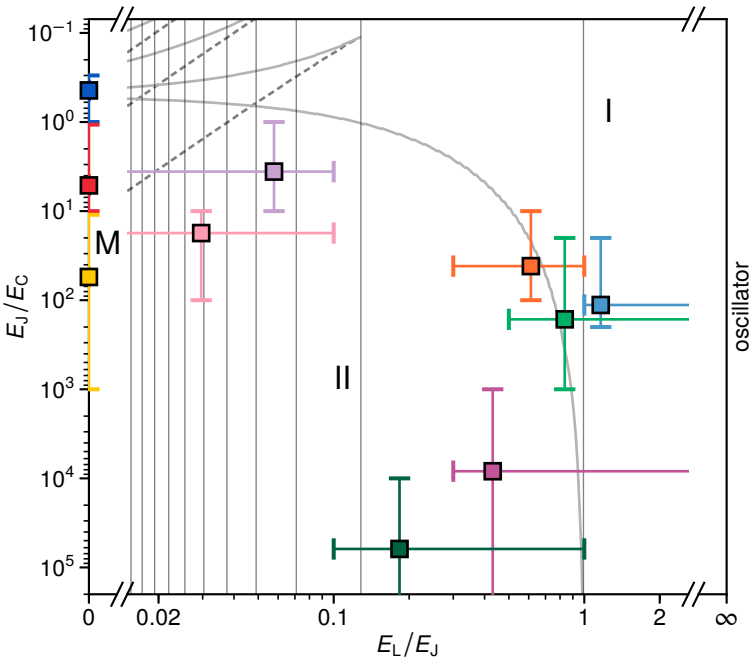

Figure 1.2 Locations of different superconducting qubit varieties in parameter space, forming a Mendeleev-like table. The types listed in Tab. 1.1 are plotted as color-coded points with error bars representing the respective parameter region. Thin black vertical lines mark the appearance of additional potential wells (from right to left). Thick grey lines delineate regions where the ground state is localized in a different number of potential wells. Specifically, the solid/dashed grey lines mark the intersection of the ground state energy with a potential maxima/minima. All curves are calculated at $\varphi_{\text{ext}} = \pi$.

dim $\mathcal{H} = 2$ counterparts [Gottesman 1997]. Here, performance is roughly characterized by the number of gates that can be done before a qubit decoheres, T_2/t_{gate} (where $t_{\text{gate}} \sim 10\,\text{ns}$ is the gate time [Chow et al. 2010] and $T_2/t_{\text{gate}} \sim 10^4$ for current devices [Z. Wang et al. 2019]). On the software side, progress has been made in developing new error correction codes [e.g. Mirrahimi et al. 2014] and executing gates on both logically-encoded qubits [Gao et al. 2019] and error-corrected qubits [Hu et al. 2019]. On the other hand, hardware advances include (i) improved gate/readout fidelities [Kelly et al. 2015, Ristè et al. 2015, Ofek et al. 2016], (ii) autonomous stabilization [Murch et al. 2012, Shankar et al. 2013, Leghtas et al. 2015, Puri et al. 2017], (iii) protected qubits [Douçot and Ioffe 2012, and references therein], and (iv) reduced noise spectral densities [Martinis et al. 2005, Houck et al. 2008, Paik et al. 2011, Rigetti et al. 2012, Barends et al. 2013, Kumar et al. 2016]. This thesis addresses strategy (iii).

At this point, we should clarify our meaning of the term "protection." We define a protected qubit to be the lowest two energy eigenstates $|g\rangle$ and $|e\rangle$ of a Hamiltonian H,

endowed with the property

$$\langle \mu|(\mathcal{O}-\mathcal{O}_0)|\nu\rangle \sim \mathrm{e}^{-\ell} \qquad \forall \mu,\nu \in \{g,e\} \tag{1.2}$$

for any operator $\mathcal{O}$ (with mean $\mathcal{O}_0$[1]) that couples to the fluctuations of the environment [Ioffe and Feigel'man 2002]. The above equation, where $\ell \gg 1$ is a dimensionless parameter characterizing the phase-space distance between $|g\rangle$ and $|e\rangle$—i.e. the nonlocality of the encoding, means that each $\mathcal{O}$ is exponentially close to the identity in the qubit subspace. The condition is satisfied when the qubit is made exponentially insensitive to variations in the operators $\mathcal{O}$ that couple to the noise of the environment, which often possess some degree of locality in phase space. Hence, protected qubits require a nonlocal encoding in a subset of the system Hilbert space which is invariant with respect to the local $\mathcal{O}$.

Note that this type of protected manifold does not encompass steady-states of driven-dissipative systems (as they are not eigenstates) or spectral density suppression via solid-state engineering. Subtleties aside, Eq. 1.2 has the simple interpretation that every operator $\mathcal{O}$ should not be able to map $|g\rangle \to |e\rangle$ or $\frac{1}{\sqrt{2}}(|g\rangle + |e\rangle) \to \frac{1}{\sqrt{2}}(|g\rangle - |e\rangle)$, and vice versa. According to Fermi's Golden Rule, the first condition corresponds to protection from relaxation and the second to protection from pure dephasing.

1.4 Protection in the $\cos 2\varphi$ qubit

To make our arguments in the preceding section more concrete, we now consider the idealized prototype of a protected qubit shown in Fig. 1.3a. This $\cos 2\varphi$ *qubit* is composed of a circuit element with degenerate phase states (the cross-hatched box)—which has been developed in recent years as a building block for topologically protected qubits [Douçot and Vidal 2002, Gladchenko et al. 2009]—shunted by a large capacitance [Smith et al. 2019]. At this stage, we simply describe the circuit using the Hamiltonian

$$H = 4E_{\mathrm{C}}(N-N_{\mathrm{g}})^2 - E_{\mathrm{J}}\cos 2\varphi, \tag{1.3}$$

which resembles that in Eq. 1.1 with $E_{\mathrm{L}} \to 0$ and an additional factor of 2 in the argument of the cosine. As we see in Fig. 1.3b, this factor depicts an engineered π-periodicity of the Hamiltonian in φ. Due to the physical 2π-periodicity of the superconducting phase, this Hamiltonian has two nearly degenerate ground states.

Indeed, these two ground states are expected to host a protected qubit, in the sense that Eq. 1.3 satisfies Eq. 1.2. To see this, first note that pairs of Cooper pairs are the only charge excitations permitted to tunnel through this element [Douçot and Vidal 2002]. We will see in Ch. 2 that this follows the conjugacy relation $[\varphi, N] = i$, which gives

$$-E_{\mathrm{J}}\cos 2\varphi = -\tfrac{1}{2}E_{\mathrm{J}}\sum_{N=-\infty}^{\infty}\left(|N\rangle\langle N+2| + |N+2\rangle\langle N|\right) \tag{1.4}$$

1 In general, we can say $\langle\mu|\mathcal{O}|\mu\rangle = \mathcal{O}_0 \pm \delta$ and $|\langle g|\mathcal{O}|e\rangle| = \epsilon$. From this, the meaning of $\mathcal{O}_0$ is clear and protection demands that both $\delta \sim \mathrm{e}^{-\ell}$ and $\epsilon \sim \mathrm{e}^{-\ell}$. We are using the notation where the number $\mathcal{O}_0$ stands for the matrix $\mathcal{O}_0 I$ in Eq. 1.2, with I the identity.

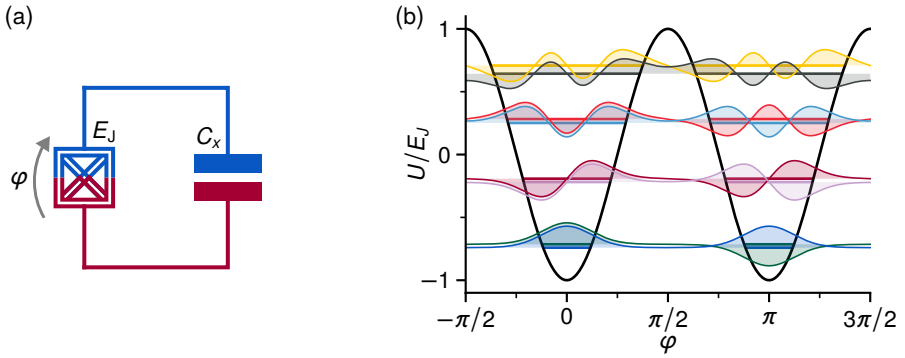

Figure 1.3 The principle of the $\cos 2\varphi$ qubit. (a) Electrical circuit for the idealized protected qubit. The cross-hatched circuit element comprises a self-capacitance in parallel with an inductive element that exclusively permits the tunneling of pairs of Cooper pairs. The superconducting island is indicated by color. (b) Potential energy of the ideal charge-protected qubit with the lowest energy levels and wavefunctions.

in terms of the Cooper pair number states $|N\rangle$. Since the circuit element only allows pairs of Cooper pairs to tunnel, the parity of the number of Cooper pairs that have tunneled is preserved under the action of the Hamiltonian. This leads to two nearly degenerate ground states $|+\rangle$ and $|-\rangle$, which are symmetric superpositions of even and odd Cooper pair number states, respectively [Gladchenko et al. 2009]. Since these states have no overlap in charge space (equivalently, they have opposite periodicity in phase space—see Fig. 1.3b), we have $\langle -|\mathcal{O}|+\rangle = 0$ for any sufficiently local $\mathcal{O}$. In the persistent current basis, we have $|\pm\rangle = \frac{1}{\sqrt{2}}(|\circlearrowright\rangle \pm |\circlearrowleft\rangle)$, where $|\circlearrowright\rangle$ and $|\circlearrowleft\rangle$ are respectively localized near $\varphi = 0$ and $\varphi = \pi$. Because these persistent current states have suppressed overlap in phase space for large E_J/E_C (i.e. they are roughly inversely periodic in charge space), we have $\langle \circlearrowleft|\mathcal{O}|\circlearrowright\rangle \to 0$ for similarly local $\mathcal{O}$. These are precisely the conditions captured by Eq. 1.2 [Ioffe and Feigel'man 2002, Douçot et al. 2004, 2005], resembling a Gottesman-Kitaev-Preskill (GKP) encoding on a circle [Gottesman et al. 2001].

Additionally, the large shunt capacitance has been introduced to combat the remaining source of noise that the qubit is not protected against. The ground state splitting obeys

$$\Delta E \approx 16 E_C \sqrt{\frac{2}{\pi}} \left(\frac{2E_J}{E_C}\right)^{3/4} e^{-\sqrt{2E_J/E_C}} \cos(\pi N_g),$$

for large E_J/E_C, following from the asymptotic form of the Mathieu characteristic values [Meixner et al. 1980]. The two ground state energies oscillate out of phase with one another in N_g. Moreover, this shows that the splitting, as well as the charge dispersion, is exponentially suppressed in E_J/E_C. The role of the shunt capacitance is to decrease the charging energy E_C and hence mitigate offset charge noise, much like in the transmon qubit [J. Koch et al. 2007].

1.5 Questions addressed by this thesis

This dissertation is based on the following question: having defined the protection of quantum information by Eq. 1.2, how do we design a superconducting circuit that is protected with respect to a given set of operators that couple to the fluctuations of the environment? It is clear that, as a general inverse problem, this question is too formidable. We have thus set a more modest goal for ourselves, which is to provide a pragmatic answer involving the process of trial and error. Imagining a candidate circuit, we develop the tools to theoretically and experimentally verify whether the candidate offers the certain degree of protection defined by maximal coherence times.

1.6 Thesis outline

Our discussion is roughly divided into analysis of the static and dynamic properties of superconducting qubits, each of which involves both theoretical and experimental considerations. For the static component, we begin with a review of superconducting circuit quantization in Ch. 2, specifically with respect to flux-tunable qubits. We conclude with a pedagogical construction of the candidate $\cos 2\varphi$ qubit. Then, in Ch. 3, we comment on the necessity to make approximations and discard the less-important degrees of freedom, again paying particular attention to the $\cos 2\varphi$ qubit. Ch. 4–5 concentrate on the mapping between the theoretical circuit Hamiltonian and experimental observations. This is done by comparing the energy levels obtained by numerical diagonalization (Ch. 4) to transition frequencies measured in spectroscopy experiments (Ch. 5). Examples are given using the fluxonium artificial atom and the double fluxonium molecule.

We then turn our attention to the dynamic component in Ch. 6, which addresses the experimental characterization of noise and describes some results, ranging from quantum jump measurements in the fluxonium to time-domain coherence measurements in the double fluxonium. Using these results and others, we predict theoretically the degree of protection of the $\cos 2\varphi$ qubit in Ch. 7. Our main finding is that the $\cos 2\varphi$ qubit is expected to exhibit coherence times in the millisecond range, demonstrating protection from all known decoherence mechanisms common to superconducting qubits. Finally, we present an overview of the progress made toward experimental implementation of the $\cos 2\varphi$ qubit in Ch. 8, before summarizing and concluding in Ch. 9.

2

LUMPED ELEMENT CIRCUIT QUANTIZATION

2.1 Regime of applicability of the lumped element model

The electromagnetic fields associated with distributed structures are conveniently described by Maxwell's equations. However, when one cares more about the structure of the first few modes in the frequency domain, and their interactions with outside sources, than the exact spatial distribution of fields, a description in terms of lumped circuit elements is more convenient. Convergence of lumped element models and Maxwell's equations reassuringly occurs when the number of elements tends to infinity. In many cases, though, aggressive truncation still permits high degrees of accuracy.

To be more precise, we consider a given distributed arrangement of conducting material, which in principle always hosts an infinite number of electromagnetic resonant modes. For example, a narrow wire with finite length d supports standing waves, like a vibrating string, whose electric current distributions obey a harmonic series. To model a given mode by its lumped element equivalent (an LC oscillator), we require that $\lambda \gg d$, where λ is the wavelength of the mode. For a straight and uniform wire, this is not possible because the lowest frequency/highest wavelength mode has $\lambda = 2d$. However, if this wire is properly deformed, so that its endpoints are large or its path meanders, this frequency is pushed much lower while keeping d constant, and the lumped element approximation becomes reasonable. As such, we summarize the condition for the validity of the lumped element model as

$$\text{mode frequency} \ll \frac{\text{speed of light}}{\text{maximum spatial extent}}. \tag{2.1}$$

This condition is met in a variety of circumstances, including superconducting circuits and their microwave environments. In these systems, the mode frequencies fall in the gigahertz range and the spatial extents are on the order of centimeters, so Eq. 2.1 is satisfied by a factor of approximately 30.

On the other hand, lumped element models of distributed structures are inherently linear, in the sense that Maxwell's equations are linear. When weak links between superconductors are incorporated, we must account for the fact that the superconducting ground state wavefunctions have nonzero spatial extent ξ_0. This coherence length can exceed the dimension of the link, leading to Josephson tunneling between the superconductors. These Josephson junctions are characterized by a nonlinear relationship between the superconducting phase (from one superconductor to the other) and the tunneling current.

Although outside the realm of Maxwell's equations, this effect can still be captured by a lumped element circuit—provided it is extended to include nonlinear circuit elements.

This chapter reviews the features of lumped circuits that are relevant to designing a protected qubit. The three essential types of circuit elements—capacitances, inductances, and Josephson junctions—are described in Sec. 2.2 and their possible arrangements are discussed in Sec. 2.3. We then outline a procedure for quantizing a given lumped element circuit in Sec. 2.4 and illustrate the method in the case of the $\cos 2\varphi$ qubit in Sec. 2.5.

2.2 Basic ingredients

All lumped circuits consist of a set of nodes connected by branches corresponding to circuit elements [Yurke and Denker 1984]. These elements could connect more than two nodes [e.g. Riwar et al. 2016], but we restrict our attention to the dipolar case.[1] These dipole circuit elements bridge distinct electrodes corresponding roughly to isolated pieces of metal in the physical device. This correspondence is very precise in the case of two superconductors separated by a Josephson junction, but fairly hazy in the case of a rectangular microwave cavity, for instance. Although variably complex structures can be cast in terms of lumped circuits [e.g. Hays et al. 2018], here we only consider the two linear elements—capacitances and inductances—and the nonlinear Josephson junction.

2.2.1 Linear circuit elements

A capacitance models the Coulomb forces exerted between collections of electric charges. The simplest picture is that of a parallel-plate capacitor, with one plate charged $+Q$ and the other $-Q$, relative to equilibrium. The constitutive relation assumes the form $Q = CV$, where V is the voltage drop and C is the capacitance, which may also be viewed as the linear response of the charge to a voltage. The instantaneous energy stored in a capacitor is given by $E = \int_0^Q \mathrm{d}Q'\, V(Q') = \frac{1}{2C}Q^2$. In the proceeding discussion, it is convenient to introduce a generalized instantaneous charge $Q(t) = -\int_{-\infty}^{t} \mathrm{d}t'\, I(t')$ such that $\dot{Q} = -I$, referenced with respect to $t \to -\infty$.

Linear inductances model the force required to push an electric current through a conductor. Solenoids provide a simple picture, where the magnetic field created by a flowing current exerts a Lorentz force on the moving charges constituting the current. In this case, a magnetic flux Φ threads the solenoid coil. The constitutive relation is $\Phi = LI$, where I is the current and L is the inductance (or the linear response of the flux to a current). The instantaneous energy of the inductor is $E = \int_0^\Phi \mathrm{d}\Phi'\, I(\Phi') = \frac{1}{2L}\Phi^2$. This discussion takes care of the case where the energy of the inductance is exclusively stored in a magnetic field—a so-called *geometric inductance*—but there is also the kinetic energy of the charges carrying the current itself, which corresponds to a so-called *kinetic inductance*. For large structures, like the solenoid, the geometric inductance usually dominates. Conversely, in smaller structures such as Josephson junctions, the kinetic inductance often does. Naturally, the flux Φ has a different meaning in kinetic inductances. It should be replaced by the generalized instantaneous flux $\Phi(t) = \int_{-\infty}^{t} \mathrm{d}t'\, V(t')$ such that $\dot{\Phi} = V$, similarly to the generalized charge. Note that this definition is equivalent to Faraday's law of induction.

1 In graph theory, this is a "connected multigraph with no loops." The edges and vertices of the graph are the branches and nodes of the circuit, respectively. Note that what we refer to as a loop in circuit theory is called a cycle in graph theory.

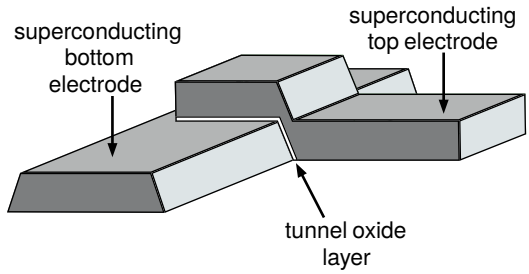

Figure 2.1 Schematic of a typical Josephson junction fabricated using electron-beam lithography [Devoret and Martinis 2004]. Cooper pairs tunnel across the oxide layer from one superconducting electrode to the other. In our devices, the aluminum superconducting films are 20–30 nm thick and the oxide layer is approximately 1 nm thick.

This flux no longer requires association with a magnetic field, just as the voltage drop corresponds to a difference in electrochemical potential and is not necessarily associated with an electric field.

2.2.2 Josephson junctions

The Josephson effect describes the coherent tunneling of Cooper pairs between two superconductors separated by a weakly transmissive barrier [Josephson 1962], called a Josephson junction (see Figs. 2.1–2).[2] Here, the bottom superconducting electrode has superconducting phase φ_2 and the top has phase φ_1, so that the difference is $\varphi = \varphi_1 - \varphi_2$. The complete Josephson effect comprises a pair of relationships: one between the generalized flux Φ across the junction and the phase drop φ, and one between the current I flowing through the junction and φ.

The first relationship reads $\Phi = \phi_0 \varphi$, where $\phi_0 = \hbar/2e$ is the reduced magnetic flux quantum—the regular magnetic flux quantum is $\Phi_0 = h/2e$. Here, the phase is defined as that of the top electrode relative to the bottom (the arrow points upward in Fig. 2.2b) and it has the same direction as the generalized flux. From this equation and our definition of the generalized flux, the voltage across the junction obeys $V = \phi_0 \dot{\varphi}$.

The second relationship gives the current passing through the junction $I = I_0 \sin\varphi$ as a nonlinear function of the phase drop. In this equation, I_0 is the critical current of the junction, i.e. the maximum value it can support before tunneling becomes incoherent, and it can be recast in terms of a tunneling energy $E_\mathrm{J} = I_0 \phi_0$. This enables us to write the inductive energy of a Josephson junction as $E = \int_0^\Phi \mathrm{d}\Phi' \, I(\Phi') = E_\mathrm{J} \int_0^\varphi \mathrm{d}\varphi' \, \sin\varphi' = E_\mathrm{J}(1 - \cos\varphi)$. In this expression, the constant term is typically neglected and we write $E = -E_\mathrm{J} \cos\varphi$.

There is an obvious resemblance between Fig. 2.1 and a parallel-plate capacitor; indeed, the instantaneous energy of a Josephson junction should also include a capacitive term. To represent a junction in a circuit, we use the symbol in Fig. 2.2a, which has the meaning of a nonlinear inductance in parallel with a capacitance (see Fig. 2.2b). Nondimensionalizing

2 See App. D for a more rigorous and microscopic discussion.

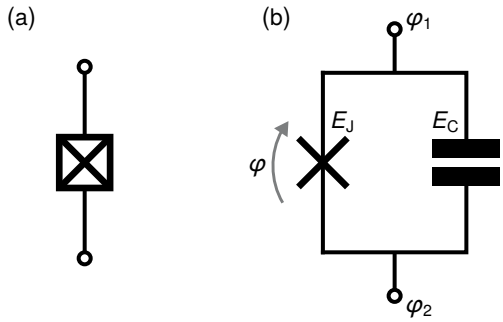

Figure 2.2 Circuit representations of a Josephson junction. (a) Electrical circuit symbol, where the dipolar nature of the junction is represented by the two leads connected to nodes (small circles). (b) Equivalent electrical circuit showing the parallel decomposition into inductive and capacitive components, with characteristic energy scales E_J and E_C. The upper and lower nodes correspond to superconductors with phases φ_1 and φ_2, and the energy of the junction only depends on the dynamics of $\varphi = \varphi_1 - \varphi_2$.

the charge across the capacitance using $Q = 2eN$, where N is charge in number of Cooper pairs, we find the Hamiltonian of a Josephson junction to be

$$H_J = 4E_C(N - N_g)^2 - E_J \cos\varphi, \tag{2.2}$$

with $E_C = e^2/2C_J$ and C_J being the junction capacitance. The constant N_g has been introduced to represent the equilibrium number of Cooper pairs across the junction, which in general depends on surface properties and need not be integer-valued.

Up to Eq. 2.2, our discussion has been essentially classical; however, H_J should be read as a quantum Hamiltonian due to the appearance of N_g.[3] In situations where the quantum fluctuations of φ about its mean value $\langle\varphi\rangle$ are small, i.e. $\langle\varphi^2\rangle - \langle\varphi\rangle^2 \ll 1$, Eq. 2.2 may be Taylor expanded to yield

$$H_J \approx 4E_C(N - N_g)^2 + \tfrac{1}{2}E_J(\varphi - \langle\varphi\rangle)^2,$$

where constant terms are neglected. As we will discuss further in Sec. 2.3, the variables φ and N are conjugate in the quantum sense:

$$[\varphi, N] = i. \tag{2.3}$$

We have arrived at the Hamiltonian of a harmonic oscillator, and the displacements N_g and $\langle\varphi\rangle$ can be dispensed with by means of the gauge transformation

$$\mathcal{U} = e^{i\langle\varphi\rangle N} e^{iN_g\varphi}. \tag{2.4}$$

3 We avoid the notation where quantum operators $\mathcal{O}$ are written with hats as $\hat{\mathcal{O}}$. In this dissertation, the particular meanings are intended to be clear from context.

Bringing the energy of a linear inductance $\frac{1}{2L}\Phi^2$ into agreement with the second term in the above Hamiltonian, we see that we can identify a Josephson inductance L_J so that $E_\mathrm{J} = \phi_0^2/L_\mathrm{J}$. Conversely, we can define an inductive energy $E_\mathrm{L} = \phi_0^2/L$ for a linear inductance.

Eq. 2.3 cannot be interpreted as the same type of conjugacy that position and momentum share. Due to the 2π-periodicity of Eq. 2.2, we have to take care to maintain the circle topology of the domain of φ (and the corollary: the integer-valued domain of N). Note that the periodicity is broken in the earlier truncation of the Taylor expansion. In the language of Fourier transforms, position and momentum are continuous-variable Fourier pairs while phase and number are cyclic-discrete Fourier pairs. To be more precise [Devoret 1997], the phase eigenstates $|\varphi\rangle$ and number eigenstates $|N\rangle$ obey

$$|\varphi\rangle = \sum_{N=-\infty}^{\infty} \mathrm{e}^{iN\varphi}|N\rangle \qquad\qquad |N\rangle = \int_0^{2\pi} \frac{\mathrm{d}\varphi}{2\pi}\mathrm{e}^{-iN\varphi}|\varphi\rangle. \tag{2.5}$$

We note that completeness demands $\sum_N |N\rangle\langle N| = 1$ and $\int_0^{2\pi} \frac{\mathrm{d}\varphi}{2\pi}|\varphi\rangle\langle\varphi| = 1$. Most importantly, we can insert the completeness relation for φ to evaluate

$$\mathrm{e}^{i\varphi} = \int_0^{2\pi} \frac{\mathrm{d}\varphi}{2\pi}\mathrm{e}^{i\varphi}|\varphi\rangle\langle\varphi| = \sum_{N=-\infty}^{\infty} |N\rangle\langle N+1|$$

using the integral representation of the Kronecker delta, $\int_0^{2\pi} \frac{\mathrm{d}x}{2\pi}\mathrm{e}^{i(p-q)x} = \delta_{p,q}$. This gives a physical intuition for the Josephson current-phase relation: the unusual term in the Hamiltonian, which we took for granted, corresponds to single Cooper pair tunneling across the junction, since $\cos\varphi = \frac{1}{2}\sum_N(|N\rangle\langle N+1| + |N+1\rangle\langle N|)$.

2.3 Structure of a circuit

In the preceding section, we described three types of circuit elements, but not how they interact with one another. This interaction is captured by the structure of the underlying graph, i.e. the set of nodes and their connections. Here we show how Kirchhoff's laws take into account both this structure and the specific circuit elements involved, imposing constraints that ultimately couple the degrees of freedom. We also discuss the relationship between Kirchhoff's laws and the possibility of circuit topology through interference effects.

2.3.1 Electromagnetic degrees of freedom

The contribution of each circuit element to the full Hamiltonian depends on one degree of freedom, e.g. Q or V for a capacitance, which corresponds to the change in that variable across the element. These are branch variables, like φ in Fig. 2.2b. Node variables, on the other hand, correspond to the values of those degrees of freedom on the nodes of the circuit, like φ_1 and φ_2 in Fig. 2.2b. Generally, branch variables are differences in node variables.[4] Node variables often provide a shortcut for imposing Kirchhoff's laws on account of there typically being fewer nodes than branches.

4 Though each branch variable can be expressed in terms of two node variables, the inverse is not true—an arbitrary node variable is a sum of all the branch variables connecting it to some reference node.

As mentioned briefly in Sec. 2.2, the two essential variables are the generalized flux and charge, which we repeat here for clarity along with their conjugacy relation,

$$\Phi(t) = \int_{-\infty}^{t} \mathrm{d}t'\, V(t') \qquad Q(t) = -\int_{-\infty}^{t} \mathrm{d}t'\, I(t') \qquad [\Phi, Q] = i\hbar. \tag{2.6}$$

We have considered flux as the position-like degree of freedom, so that voltage $V = \dot{\Phi}$ is velocity-like, but the alternative choice of charge as the position-like coordinate is equally valid.[5] This analogy can be continued, with charge $Q = CV$ or flux $\Phi = LI$ being the conjugate momentum and the capacitance C or the inductance L playing the role of mass. Note that the final equation in Eq. 2.6 is written as Eq. 2.3 in dimensionless form.

2.3.2 Kirchhoff's laws as constraints

We start with a sketch of the derivation of Kirchhoff's current law and suppose that the electric and magnetic fields in the region containing the entire circuit are $\mathbf{E}$ and $\mathbf{B}$, while the current density in the conductive region is $\mathbf{J}$. For a given node, locally enclosed by a surface S and with total charge Q, Ampère's law gives us

$$0 = \oint_S \mathrm{d}^2x \left(-\frac{1}{\mu_0}\nabla\times\mathbf{B} + \mathbf{J} + \epsilon_0\frac{\partial\mathbf{E}}{\partial t}\right)\cdot\hat{\mathbf{n}} = \oint_S \mathrm{d}^2x\, \mathbf{J}\cdot\hat{\mathbf{n}} + \dot{Q} = \sum_{i\in\text{node}} I_i. \tag{2.7}$$

In the second equality, we used the fact that $\oint_S \mathrm{d}^2x\,(\nabla\times\mathbf{B})\cdot\hat{\mathbf{n}} = 0$ by Stokes' theorem and $Q = \epsilon_0 \oint_S \mathrm{d}^2x\,\mathbf{E}\cdot\hat{\mathbf{n}}$ by Gauss's law. In the final equality, we assumed that the total charge Q is conserved and we call I_i the current flowing out of the node through branch i. This assumption amounts to treating the charge carriers as an incompressible fluid.

For Kirchhoff's voltage law, we use the same definitions but consider a given loop of area $\mathcal{A}$ enclosing a total magnetic flux Φ. The integral form of Faraday's law gives us

$$0 = \int_{\mathcal{A}} \mathrm{d}^2x \left(\nabla\times\mathbf{E} + \frac{\partial\mathbf{B}}{\partial t}\right)\cdot\hat{\mathbf{n}} = \oint_C \mathrm{d}x\,\mathbf{E}\cdot\hat{\mathbf{x}} + \dot{\Phi} = \sum_{i\in\text{loop}} V_i. \tag{2.8}$$

In the second equality, we used the fact that $\int_{\mathcal{A}} \mathrm{d}^2x\,(\nabla\times\mathbf{E})\cdot\hat{\mathbf{n}} = \oint_C \mathrm{d}x\,\mathbf{E}\cdot\hat{\mathbf{x}}$, again by Stokes' theorem with C being the curve enclosing $\mathcal{A}$, and $\Phi = \int_{\mathcal{A}} \mathrm{d}^2x\,\mathbf{B}\cdot\hat{\mathbf{n}}$ by definition. In the last equality, we assumed that the total flux Φ is conserved and we call V_i the voltage drop (counterclockwise) across the i-th circuit element on the loop. This time, we are treating the magnetic flux vortices as an incompressible fluid. In this sense, the Kirchhoff laws are semiclassical constraints.

Using $I_i = -\dot{Q}_i$ and $V_i = \dot{\Phi}_i$, wan can integrate these laws to find the equivalent constraints for charge and flux

$$\sum_{i\in\text{node}} Q_i = Q_\text{g} \qquad \sum_{i\in\text{loop}} \Phi_i = \Phi_\text{ext}, \tag{2.9}$$

5 This requires a sign change for every formula in Eq. 2.6, and so the current $I = \dot{Q}$ becomes the velocity-like variable [Girvin 2014].

Constraint	n_J	n_L	n_C	Characterization
$\sum_{i\in\mathrm{node}} \frac{\Phi_i}{L_i} = 0$	0	$\neq 0$	0	Inductive node
$\sum_{i\in\mathrm{node}} Q_i = Q_\mathrm{g}$	any	0	any	Capacitive node
$\sum_{i\in\mathrm{node}} Q_i = \mathrm{const.}$	any	$\neq 0$	any	Mixed node
$\sum_{i\in\mathrm{loop}} \frac{Q_i}{C_i} = 0$	0	0	$\neq 0$	Capacitive loop
$\sum_{i\in\mathrm{loop}} \Phi_i = \Phi_\mathrm{ext}$	any	any	0	Inductive loop
$\sum_{i\in\mathrm{loop}} \Phi_i = \mathrm{const.}$	any	any	$\neq 0$	Mixed loop

Table 2.1 Assorted varieties of Kirchhoff's conservation laws. The nonnegative integers n_J, n_L, and n_C define the number of the corresponding bounding elements. For mixed nodes and loops, the conservation law is only defined up to an inconsequential constant, which acquires physical significance once the corresponding offset becomes pinned.

where the integration constants have been made explicit. They correspond physically to offset charge $Q_\mathrm{g} = 2eN_\mathrm{g}$ and external flux $\Phi_\mathrm{ext} = \phi_0\varphi_\mathrm{ext}$. In certain situations, these constants can be removed from the Hamiltonian using gauge transformations like the one used in Sec. 2.2, because they have no physical effect. For instance, the offset charge on a node that connects to ground through linear inductances will not matter, and neither will the external flux through a loop that connects to the exterior[6] through capacitances. The various forms of these laws are summarized in Tab. 2.1.

2.3.3 Interference effects and the question of *circuit topology*

To begin, since the circuits we consider contain more than one variety of element, we cannot easily introduce a rigorous definition of *circuit topology* because there is no clear concept of continuous space at finite frequencies $\omega > 0$.[7] Nonetheless, there are three basic numbers that efficiently describe the structure of a given circuit, much like topological parameters. One of these arises from first quantization and the other two stem from the two types of quantum electromagnetic interference effects.

The first type of interference is the Aharonov-Bohm effect, where point-like electric charges accumulate a geometric phase when traveling around a pole-like magnetic field. From Eq. 2.9 and Tab. 2.1, we notice that this will occur in loops bounded by inductances and Josephson junctions. These inductive loops permit a Cooper pair to travel completely

6 We take "exterior" to mean ground with respect to flux (usually the area encompassing the circuit).

7 The task is simple at $\omega = 0$ and $\omega \to \infty$, but these limits cannot adequately capture the case $0 < \omega < \infty$. For circuits with repeated patterns, on the other hand, topology is naturally defined [e.g. Albert et al. 2015, Pino et al. 2015].

around the perimeter, encircling the pinned external magnetic flux φ_{ext} and hence acquiring an Aharonov-Bohm phase of φ_{ext}.

The second type of interference is the Aharonov-Casher effect, where a pole-like magnetic field accumulates a geometric phase when traveling around a point-like electric charge. This time, Eq. 2.9 and Tab. 2.1 show that this will occur in nodes bounded by capacitances and Josephson junctions. Such capacitive nodes permit a fluxon (a magnetic flux quantum) to travel around the node, traversing the capacitances and junctions, encircling the pinned offset charge N_{g} and acquiring an Aharonov-Casher phase of $2\pi N_{\text{g}}$.

From the discussion in this section, we have seen how various circuit structures are possible, but that only inductive loops and capacitive nodes give rise to interference effects due to the accumulation of geometric phases. These effects form the basis for a possible classification of circuits based on: (i) the number of degrees of freedom, (ii) the number of inductive loops, and (iii) the number of capacitive nodes.[8] Note that quantity (i) corresponds to the number of first-quantized electromagnetic modes of the circuit. These three numbers can be *loosely* thought of as topological parameters that specify the circuit topology.

2.4 Recipe for quantizing a lumped element circuit

This section presents general features of circuit quantization, i.e. the process of constructing a quantum Hamiltonian for a lumped element circuit, with a particular focus on the algorithmic treatment of circuits with multiple strong nonlinearities. The cases of weak and/or single nonlinearities have been treated elsewhere [Nigg et al. 2012, Solgun et al. 2014]. We are chiefly concerned with the former situation because it applies to the three circuits discussed in detail in this thesis: the fluxonium artificial atom, the double fluxonium, and the $\cos 2\varphi$ qubit. This procedure is neither unique nor completely original [Burkard et al. 2004], but we describe it because of its extensive use in designing and analyzing these three systems.

2.4.1 Reduce circuit

A useful first step, to simplify the analysis, is to combine all parallel and series combinations of inductances and capacitances in the circuit according to

$$L_{\text{series}} = \sum_i L_i \qquad \frac{1}{L_{\text{parallel}}} = \sum_i \frac{1}{L_i} \qquad \frac{1}{C_{\text{series}}} = \sum_i \frac{1}{C_i} \qquad C_{\text{parallel}} = \sum_i C_i.$$

This simplification reduces the number of circuit elements and often exposes important features of the circuit.

2.4.2 Sketch Lagrangian

After this simplification, we write down the Lagrangian using branch flux variables Φ_i (where i runs over all circuit elements in the reduced circuit) as the position-like degrees

8 This bears resemblance to the classification of graphs based on the number of vertices, edges, and faces (and the associated Euler characteristic).

of freedom, noting that capacitive energies correspond to kinetic energies of the form $\frac{1}{2C}Q^2 \to \frac{1}{2}C\dot{\Phi}^2$. This Lagrangian reads

$$\mathcal{L} = \tfrac{1}{2}\dot{\boldsymbol{\Phi}}^{\mathrm{T}}\boldsymbol{C}\,\dot{\boldsymbol{\Phi}} - \tfrac{1}{2}\boldsymbol{\Phi}^{\mathrm{T}}\boldsymbol{L}^{-1}\boldsymbol{\Phi} + \sum_{i=1}^{J} E_{\mathrm{J},i}\cos\varphi_i \tag{2.10}$$

in matrix form, where the entries of $\boldsymbol{\Phi}$ are Φ_i and the phases φ_i are defined by $\Phi_i = \phi_0\varphi_i$. The Josephson junctions have tunneling energies $E_{\mathrm{J},i}$ for $i = 1, 2, \ldots, J$. We have chosen an indexing convention so that the fluxes Φ_i are first assigned to the junctions (which also have capacitances), then the capacitances, then the inductances. Therefore, the capacitance matrix $\boldsymbol{C}$ and the inductance matrix $\boldsymbol{L}$ are defined through

$$\boldsymbol{C} = \boldsymbol{C}_{\mathrm{sub}} \oplus 0 \qquad \boldsymbol{C}^{-1} = \boldsymbol{C}_{\mathrm{sub}}^{-1} \oplus 0 \qquad \boldsymbol{L} = 0 \oplus \boldsymbol{L}_{\mathrm{sub}} \qquad \boldsymbol{L}^{-1} = 0 \oplus \boldsymbol{L}_{\mathrm{sub}}^{-1}$$

in order to pick out the capacitive and inductive subgraphs corresponding to $\boldsymbol{C}_{\mathrm{sub}}$ and $\boldsymbol{L}_{\mathrm{sub}}$. In the above, the zero matrix is denoted by 0 (with it having the dimension of $\boldsymbol{L}_{\mathrm{sub}}$ in the first two equations and $\boldsymbol{C}_{\mathrm{sub}}$ in the second two). Note that only $\boldsymbol{C}_{\mathrm{sub}}$ and $\boldsymbol{L}_{\mathrm{sub}}$ are invertible, but they are guaranteed to be, and hence the second and fourth equations should be read as definitions and not consequences of the first and third equations.

2.4.3 Impose Kirchhoff's laws

At this point, there is in principle a separate Kirchoff law corresponding to every independent loop and node of the circuit. However, many of these equations describe the dynamics of the modes and are not strictly constraints. Since we are using flux coordinates, we know that the Kirchoff laws that we may ignore correspond to capacitive nodes with $n_{\mathrm{J}} \neq 0$ or mixed nodes (see Tab. 2.1). The remaining constraints; which correspond to loops, inductive nodes, and capacitive nodes with $n_{\mathrm{J}} = 0$; will be written in terms of the voltages $\dot{\Phi}_i$, if capacitances are involved, or otherwise the fluxes Φ_i.

First we deal with the voltage constraints. They can be captured[9] by a matrix $\boldsymbol{V}$ and imposed as follows:

$$\boldsymbol{V}\dot{\boldsymbol{\Phi}} = 0 \quad \Rightarrow \quad \boldsymbol{V}_{\mathrm{sd}}\dot{\boldsymbol{\Phi}}_{\mathrm{sd}} = -\boldsymbol{V}_{\mathrm{sc}}\dot{\boldsymbol{\Phi}}_{\mathrm{sc}} \quad \Rightarrow \quad \dot{\boldsymbol{\Phi}}_{\mathrm{sd}} = -\boldsymbol{V}_{\mathrm{sd}}^{-1}\boldsymbol{V}_{\mathrm{sc}}\dot{\boldsymbol{\Phi}}_{\mathrm{sc}},$$

where we have made the partition/rearrangement $\boldsymbol{V} = \begin{pmatrix}\boldsymbol{V}_{\mathrm{sd}} & \boldsymbol{V}_{\mathrm{sc}}\end{pmatrix}$ and $\boldsymbol{\Phi}^{\mathrm{T}} = \begin{pmatrix}\boldsymbol{\Phi}_{\mathrm{sd}}^{\mathrm{T}} & \boldsymbol{\Phi}_{\mathrm{sc}}^{\mathrm{T}}\end{pmatrix}$. The subscripts "sd" and "sc" refer to the chosen semi-dependent and semi-constrained coordinates. Note that $\boldsymbol{V}_{\mathrm{sd}}$ is square and it is invertible for at least one particular partition, because the rows of $\boldsymbol{V}$ are linearly independent. The transformation equations are given by

$$\boldsymbol{\Phi} = \boldsymbol{\Lambda}_V\boldsymbol{\Phi}_{\mathrm{sc}} \qquad \begin{cases}\boldsymbol{C} \to \boldsymbol{C}_{\mathrm{sc}} = \boldsymbol{\Lambda}_V^{\mathrm{T}}\boldsymbol{C}\boldsymbol{\Lambda}_V \\ \boldsymbol{L}^{-1} \to \boldsymbol{L}_{\mathrm{sc}}^{-1} = \boldsymbol{L}^{-1}\end{cases} \qquad \boldsymbol{\Lambda}_V = \begin{pmatrix}-\boldsymbol{V}_{\mathrm{sd}}^{-1}\boldsymbol{V}_{\mathrm{sc}} \\ I\end{pmatrix}, \tag{2.11}$$

where the identity matrix I has the dimension of $\boldsymbol{\Phi}_{\mathrm{sc}}$. We have eliminated $\boldsymbol{\Phi}_{\mathrm{sd}}$—all of which belong to capacitances or junctions—and are left with fewer coordinates $\boldsymbol{\Phi}_{\mathrm{sc}}$.

9 The constraints from capacitive nodes also introduce offset charges, but in this case, such nodes are not bounded by Josephson junctions and these offsets can be removed by the gauge transformation in Sec. 2.2.

We proceed similarly for the flux constraints. The equations corresponding to inductive loops introduce external flux offsets, which we combine[10] with $\boldsymbol{\Phi}$ into $\tilde{\boldsymbol{\Phi}}$, and similarly for $\boldsymbol{\Phi}_{\mathrm{sc}}$ and $\tilde{\boldsymbol{\Phi}}_{\mathrm{sc}}$. The constraints are then captured by a matrix $\boldsymbol{F}$ and imposed as follows:

$$\boldsymbol{F}\tilde{\boldsymbol{\Phi}} = \boldsymbol{F}\boldsymbol{\Lambda}_V\tilde{\boldsymbol{\Phi}}_{\mathrm{sc}} = 0 \quad \Rightarrow \quad \boldsymbol{F}_{\mathrm{d}}\tilde{\boldsymbol{\Phi}}_{\mathrm{d}} = -\boldsymbol{F}_{\mathrm{c}}\tilde{\boldsymbol{\Phi}}_{\mathrm{c}} \quad \Rightarrow \quad \tilde{\boldsymbol{\Phi}}_{\mathrm{d}} = -\boldsymbol{F}_{\mathrm{d}}^{-1}\boldsymbol{F}_{\mathrm{c}}\tilde{\boldsymbol{\Phi}}_{\mathrm{c}},$$

where this time we have made the partition/rearrangement $\boldsymbol{F}\boldsymbol{\Lambda}_V = \begin{pmatrix}\boldsymbol{F}_{\mathrm{d}} & \boldsymbol{F}_{\mathrm{c}}\end{pmatrix}$ in addition to $\tilde{\boldsymbol{\Phi}}_{\mathrm{sc}}^{\mathrm{T}} = \begin{pmatrix}\tilde{\boldsymbol{\Phi}}_{\mathrm{d}}^{\mathrm{T}} & \tilde{\boldsymbol{\Phi}}_{\mathrm{c}}^{\mathrm{T}}\end{pmatrix}$. The subscripts "d" and "c" refer to the chosen dependent and constrained coordinates. Similarly to the case of the voltage constraints, the matrix $\boldsymbol{F}_{\mathrm{d}}$ is square and invertible for some partition, justifying the final equation above. The transformation equations read

$$\tilde{\boldsymbol{\Phi}}_{\mathrm{sc}} = \boldsymbol{\Lambda}_F\tilde{\boldsymbol{\Phi}}_{\mathrm{c}} \qquad \begin{cases}\boldsymbol{C}_{\mathrm{sc}} \to \boldsymbol{C}_{\mathrm{c}} = \boldsymbol{\Lambda}_F^{\mathrm{T}}\boldsymbol{C}_{\mathrm{sc}}\boldsymbol{\Lambda}_F \\ \boldsymbol{L}_{\mathrm{sc}}^{-1} \to \boldsymbol{L}_{\mathrm{c}}^{-1} = \boldsymbol{\Lambda}_F^{\mathrm{T}}\boldsymbol{L}_{\mathrm{sc}}^{-1}\boldsymbol{\Lambda}_F\end{cases} \qquad \boldsymbol{\Lambda}_F = \begin{pmatrix}-\boldsymbol{F}_{\mathrm{d}}^{-1}\boldsymbol{F}_{\mathrm{c}} \\ I\end{pmatrix}, \tag{2.12}$$

where the identity matrix I has the dimension of $\tilde{\boldsymbol{\Phi}}_{\mathrm{c}}$. We have now eliminated $\tilde{\boldsymbol{\Phi}}_{\mathrm{d}}$ and are left with $\tilde{\boldsymbol{\Phi}}_{\mathrm{c}}$. This procedure has eliminated as many degrees of freedom as possible using Kirchhoff's laws.[11]

2.4.4 Formulate Hamiltonian

We now return to Eq. 2.10 projected into the fully constrained subspace,

$$\mathcal{L} = \tfrac{1}{2}\dot{\boldsymbol{\Phi}}_{\mathrm{c}}^{\mathrm{T}}\boldsymbol{C}_{\mathrm{c}}\dot{\boldsymbol{\Phi}}_{\mathrm{c}} - \tfrac{1}{2}\tilde{\boldsymbol{\Phi}}_{\mathrm{c}}^{\mathrm{T}}\boldsymbol{L}_{\mathrm{c}}^{-1}\tilde{\boldsymbol{\Phi}}_{\mathrm{c}} + \sum_{i=1}^{J} E_{\mathrm{J},i}\cos\varphi_i.$$

In this Lagrangian, each degree of freedom $\Phi_{\mathrm{c},i}$ will appear in both the kinetic and potential energy. Note that the phases in the Josephson potentials are written in terms of the constrained variables using $\boldsymbol{\varphi} = \boldsymbol{\Lambda}_V\boldsymbol{\Lambda}_F\tilde{\boldsymbol{\varphi}}_{\mathrm{c}}$ with $\tilde{\boldsymbol{\varphi}}_{\mathrm{c}} = \tilde{\boldsymbol{\Phi}}_{\mathrm{c}}/\phi_0$. The gauge transformation in Sec. 2.2 will remove all external fluxes that are not enclosed by at least one junction, so we can move the external fluxes into the third term. We hence write

$$\mathcal{L} = \tfrac{1}{2}\dot{\boldsymbol{\Phi}}_{\mathrm{c}}^{\mathrm{T}}\boldsymbol{C}_{\mathrm{c}}\dot{\boldsymbol{\Phi}}_{\mathrm{c}} + \mathbf{Q}_{\mathrm{g}}^{\mathrm{T}}\dot{\boldsymbol{\Phi}}_{\mathrm{c}} - \tfrac{1}{2}\boldsymbol{\Phi}_{\mathrm{c}}^{\mathrm{T}}\boldsymbol{L}_{\mathrm{c}}^{-1}\boldsymbol{\Phi}_{\mathrm{c}} + \sum_{i=1}^{J} E_{\mathrm{J},i}\cos\Big(\textstyle\sum_j \boldsymbol{\Lambda}_{ij}\,\varphi_{\mathrm{c},j} - \varphi_{\mathrm{ext},i}\Big),$$

where $\varphi_{\mathrm{ext},i}$ is the effective external flux for the i-th Josephson junction, j indexes the constrained degrees of freedom, and $\boldsymbol{\Lambda} = \boldsymbol{\Lambda}_V\boldsymbol{\Lambda}_F$. We have also added the second term to account for offset charges $\mathbf{Q}_{\mathrm{g}}$, which had not been introduced by the constraints due to our choice of flux variables. The Hamiltonian is obtained by invoking the equations

$$\mathbf{Q}_{\mathrm{c}} = \frac{\partial\mathcal{L}}{\partial\dot{\boldsymbol{\Phi}}_{\mathrm{c}}} = \boldsymbol{C}_{\mathrm{c}}\dot{\boldsymbol{\Phi}}_{\mathrm{c}} + \mathbf{Q}_{\mathrm{g}}$$

10 Since the external fluxes are assumed to be static, we are permitted to introduce them at this point; we could have written the first equation in Eq. 2.11 as $\tilde{\boldsymbol{\Phi}} = \boldsymbol{\Lambda}_V\tilde{\boldsymbol{\Phi}}_{\mathrm{sc}}$.

11 Interestingly, one way to avoid imposing these various constraints is to analyze the Euler-Lagrange equations of motion for the *unconstrained* Lagrangian in Eq. 2.10. The constraints then emerge as the equations of motion that oscillate at zero- or infinite-frequency.

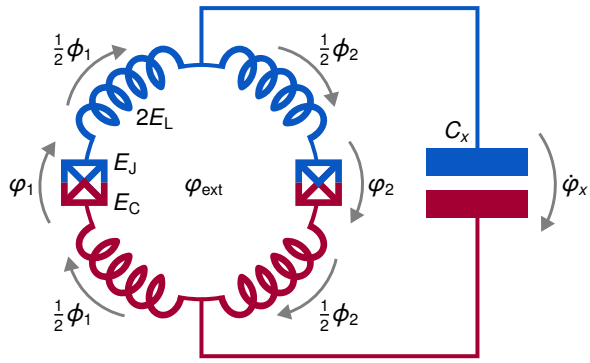

Figure 2.3 Electrical circuit diagram for the $\cos 2\varphi$ qubit. All four linear inductances have inductive energy $2E_L$, both Josephson junctions have charging energy E_C and tunneling energy E_J, and the shunt capacitance is C_x. When the magnetic flux threading the inductive loop is tuned to $\varphi_{ext} = \pi$, the loop collectively behaves as a Josephson junction with respect to pairs of Cooper pairs. The Cooper pair parity between the two colored islands is preserved, rendering two ground states roughly degenerate.

to find the conjugate charges $\mathbf{Q}_c$. We then arrive at the Hamiltonian

$$H = \tfrac{1}{2}(\mathbf{Q}_c - \mathbf{Q}_g)^T \boldsymbol{C}_c^{-1}(\mathbf{Q}_c - \mathbf{Q}_g) + \tfrac{1}{2}\boldsymbol{\Phi}_c^T \boldsymbol{L}_c^{-1}\boldsymbol{\Phi}_c - \sum_{i=1}^{J} E_{J,i}\cos\Big(\textstyle\sum_j \boldsymbol{\Lambda}_{ij}\,\varphi_{c,j} - \varphi_{ext,i}\Big). \quad (2.13)$$

2.4.5 Promote variables to operators

The final step is to promote the fluxes and charges in Eq. 2.13 to operators. Since we have imposed the constraints properly, we have the conjugacy relations $[\Phi_{c,i}, Q_{c,i}] = i\hbar$ for all remaining variables indexed by i, as in Eq. 2.6.

2.5 Example: Hamiltonian of the $\cos 2\varphi$ qubit

To make the manipulations described in Sec. 2.4 more concrete, in this section we quantize the circuit shown in Fig. 2.3, which is designed to realize the $\cos 2\varphi$ qubit introduced in Sec. 1.4. In the following chapter, we will show how an effective $\cos 2\varphi$ term emerges in the Hamiltonian. This circuit is composed of two identical arms, each containing a Josephson junction in series with superinductances[12], arranged in parallel [Kitaev 2006, Brooks et al. 2013] and shunted by a large capacitance. These superinductances are split in half and placed on either side of the respective Josephson junctions to avoid large capacitances shunting the junctions.

12 Superinductances are effective circuit elements possessing large characteristic impedances $Z_0 = \sqrt{L/C}$ relative to the reduced superconducting resistance quantum $R_Q = \hbar/(2e)^2$. They have been implemented using mainly Josephson junction arrays, which can provide large kinetic inductances [Manucharyan et al. 2009, 2012, Masluk et al. 2012].

We follow Step 1 from the preceding chapter and combine the trivial combinations of inductances and capacitances. In Fig. 2.3, there are two such combinations: the pairs of linear inductances on either arm. Since these inductances are in series, they share the same phase drops $\phi_1/2$ or $\phi_2/2$ and collectively act like one element with twice the inductance, i.e. an inductive energy E_L and phase ϕ_1 or ϕ_2.

At this point, we can write the Lagrangian for the reduced circuit, which has five elements: two inductances, two Josephson junctions, and one capacitance. Using the phase degrees of freedom in the diagram, we write the Lagrangian

$$\mathcal{L} = \frac{\hbar^2}{16E_\mathrm{C}}\left(\dot\varphi_1^2 + \dot\varphi_2^2 + \tfrac{1}{x}\dot\varphi_x^2\right) - \tfrac{1}{2}E_\mathrm{L}\left(\phi_1^2 + \phi_2^2\right) + E_\mathrm{J}\cos\varphi_1 + E_\mathrm{J}\cos\varphi_2,$$

where $x = C_\mathrm{J}/C_x$ is the ratio of the junction capacitance to the shunt capacitance, and it will eventually be a small parameter. This is a simple case of Eq. 2.10 in Step 2.

Left with five degrees of freedom, we notice that there are three loops in the circuit, one of which is a combination of the other two. These correspond to the constraint equations

$$\dot\phi_1 + \dot\varphi_1 + \dot\varphi_x = 0 \qquad -\dot\phi_2 - \dot\varphi_2 + \dot\varphi_x = 0 \qquad \phi_1 + \varphi_1 + \phi_2 + \varphi_2 = \varphi_\mathrm{ext}.$$

The first two are equivalent voltage constraints and the last is a flux constraint, as described by the matrix equations in Step 3.

At this point, it is convenient to choose a symmetric combination of coordinates. To that end, we rewrite the Lagrangian as

$$\begin{aligned}\mathcal{L} = \frac{\hbar^2}{16E_\mathrm{C}}&\left[\tfrac{1}{2}(\dot\varphi_1 + \dot\varphi_2)^2 + \tfrac{1}{2}(\dot\varphi_1 - \dot\varphi_2)^2 + \tfrac{1}{x}\dot\varphi_x^2\right]\\ &- \tfrac{1}{2}E_\mathrm{L}\left[\tfrac{1}{2}(\phi_1 + \phi_1)^2 + \tfrac{1}{2}(\phi_1 - \phi_2)^2\right] + 2E_\mathrm{J}\cos\left(\frac{\varphi_1 - \varphi_2}{2}\right)\cos\left(\frac{\varphi_1 + \varphi_2}{2}\right)\end{aligned}$$

and define the new coordinates

$$\phi = \varphi_1 + \varphi_2 \qquad \varphi = \tfrac{1}{2}(\varphi_1 - \varphi_2) \qquad \vartheta = \phi_1 + \phi_2 \qquad \theta = \tfrac{1}{2}(\phi_1 - \phi_2),$$

which allow the first constraint to be written as $\vartheta = \varphi_\mathrm{ext} - \phi$. This eliminates the dependence on ϑ. Note that the prefactor in the definition of φ is chosen to bring the coordinate into agreement with the phase drop across the inductive loop, up to an additive constant, in the limit that θ vanishes. The last two constraint equations can be combined into $\dot\varphi_x = -(\dot\varphi + \dot\theta)$, giving the Lagrangian

$$\mathcal{L} = \frac{\hbar^2}{16E_\mathrm{C}}\left[\tfrac{1}{2}\dot\phi^2 + 2\dot\varphi^2 + \tfrac{1}{x}(\dot\varphi + \dot\theta)^2\right] - E_\mathrm{L}\left[\tfrac{1}{4}(\phi - \varphi_\mathrm{ext})^2 + \theta^2\right] + 2E_\mathrm{J}\cos\varphi\cos\frac{\phi}{2}. \quad (2.14)$$

Introducing the Cooper pair numbers M, N, and P respectively conjugate to ϕ, φ, and θ, we obtain the Hamiltonian

$$\begin{aligned}H = 4E_\mathrm{C}&\left[2M^2 + \tfrac{1}{2}(N - N_\mathrm{g} - P)^2 + xP^2\right]\\ &+ E_\mathrm{L}\left[\tfrac{1}{4}(\phi - \varphi_\mathrm{ext})^2 + \theta^2\right] - 2E_\mathrm{J}\cos\varphi\cos\frac{\phi}{2},\end{aligned} \quad (2.15)$$

E_C/h (GHz)	E_L/h (GHz)	E_J/h (GHz)	x
2	1	15	0.02

Table 2.2 Circuit parameters used for numerical simulations of the $\cos 2\varphi$ qubit. In Ch. 7, the additional parameter of inductive asymmetry is added.

and complete Step 4. Note that the offset charge N_g has been introduced due to the periodicity of the Hamiltonian in φ, which also reflects the presence of a superconducting island; that is, a capacitive node with $n_J \neq 0$; as colored in Fig. 2.3.

Quantization is completed by promoting the variables to operators, as in Step 5. When the external magnetic flux threading the inductive loop reaches half of a flux quantum, i.e. when $\varphi_{ext} = \pi$, the loop contributes an effective $\cos 2\varphi$ term to the Hamiltonian instead of the conventional $\cos\varphi$ term, as we will show in the next chapter. Using Eq. 2.5, we also see that $\cos 2\varphi = \frac{1}{2}\sum_N(|N\rangle\langle N+2| + |N+2\rangle\langle N|)$, and so it corresponds to tunneling of pairs of Cooper pairs. At this particular bias point, a Cooper pair can only tunnel through one of the Josephson junctions if it is accompanied by another Cooper pair tunneling through the other junction (in either direction). Conversely, a fluxon tunneling across a single Josephson junction corresponds to a half-fluxon tunneling across the whole element.

From Eq. 2.15, we see that this circuit has three coupled modes. The ϕ mode is flux dependent and is strongly and nonlinearly coupled, via the Josephson junctions, to the φ mode. The φ mode is offset-charge dependent and strongly but linearly capacitively coupled to the θ mode. Our analysis and the effects observed in the remainder of this thesis require the parameter regime $E_L \ll E_J$, $E_C \lesssim E_J$, and $x \ll 1$.[13] In particular, the parameters chosen for numerical simulations are listed in Tab. 2.2 and are similar to those of recent fluxonium devices [Manucharyan et al. 2009, Earnest et al. 2018]. We emphasize the difference between this circuit and the dc Superconducting QUantum Interference Device (SQUID), due to the parameter regime [Clarke and Braginski 2004]. In the case of the dc-SQUID, the parameter regime $E_L \gtrsim E_J$ confines $\phi \approx \varphi_{ext}$, restoring the $\cos\varphi$ term even near half flux.

13 Specifically, the theory in Sec. 3.3.1 breaks down at $E_L \sim E_J$, at which point numerical instanton methods must be used, and the protection in Sec. 7.2.3 breaks down for $x \gtrsim 0.1$.

3

EFFECTIVE CIRCUIT HAMILTONIANS

Although the procedure presented in Sec. 2.4 provides an algorithmic method for determining the Hamiltonian of a given superconducting circuit, in many circumstances these Hamiltonians provide little physical insight or practical utility on their own. This can be the case because there are too many degrees of freedom, the Hamiltonian is written in a basis that inadequately captures the relevant physics, or the various terms are not easily identified as large and small. In these situations, one has to rely on transformations and approximations to obtain an *effective Hamiltonian*. To make this point clear, we review the transmon qubit as an example in Sec. 3.1. We then survey the various transformations and approximations at hand in Secs. 3.2 before deriving the effective Hamiltonian for the $\cos 2\varphi$ qubit in Sec. 3.3.

3.1 Transmon qubit

The transmon qubit is composed of a Josephson junction shunted by a large capacitance. This capacitance increases the effective mass of the equivalent "particle in a box," confining the eigenstates deep in their potential. The Hamiltonian was introduced peripherally as Eq. 1.1 for $E_\mathrm{L} = 0$ and $E_\mathrm{J} \gg E_\mathrm{C}$, and also as Eq. 2.2 with C_J replaced by $C_\mathrm{J} + C_x$, with $C_x \gg C_\mathrm{J}$ being the shunt capacitance. For clarity, we repeat it here:

$$H = 4E_\mathrm{C}(N - N_\mathrm{g})^2 - E_\mathrm{J}\cos\varphi. \tag{3.1}$$

The exact solutions to the time-independent Schrödinger equation are given by Mathieu functions [J. Koch et al. 2007] and are notoriously challenging to handle [Meixner et al. 1980]. In this case, one often exploits the fact that $E_\mathrm{J} \gg E_\mathrm{C}$ to Taylor expand the potential about its minimum (as in Sec. 2.2.2) and obtain the effective Hamiltonian

$$H_\mathrm{eff} = 4E_\mathrm{C}N^2 + \tfrac{1}{2}E_\mathrm{J}\varphi^2 - \tfrac{1}{4!}E_\mathrm{J}\varphi^4, \tag{3.2}$$

where the last term is considered to be perturbative. Note that the dependence on the offset charge N_g has been removed as a consequence of truncating the Taylor series.

The first two terms in Eq. 3.2 constitute the dominant part of the Hamiltonian, and they describe a harmonic oscillator. Introducing the bosonic creation and annihilation operators $a^\dagger$ and a that diagonalize this part, the Hamiltonian becomes

$$H_\mathrm{eff} = \hbar\omega_0\left(a^\dagger a + \tfrac{1}{2}\right) - \tfrac{1}{12}E_\mathrm{C}(a + a^\dagger)^4 \tag{3.3}$$

These new operators are linear combinations of φ and N, with coefficients given by the zero-point fluctuation amplitudes $\varphi_{\text{zpf}} = (2E_{\text{C}}/E_{\text{J}})^{1/4}$ and $N_{\text{zpf}} = \frac{1}{2}(E_{\text{J}}/2E_{\text{C}})^{1/4}$—from which the Heisenberg uncertainty relation is readily minimized: $\varphi_{\text{zpf}} N_{\text{zpf}} = \frac{1}{2}$. The transformation and its inverse are

$$\varphi = \varphi_{\text{zpf}}(a^\dagger + a) \qquad N = iN_{\text{zpf}}(a^\dagger - a) \qquad\qquad a = \frac{1}{2}\left(\frac{\varphi}{\varphi_{\text{zpf}}} + i\frac{N}{N_{\text{zpf}}}\right),$$

while the harmonic level splitting is $\hbar\omega_0 = \sqrt{8E_{\text{J}}E_{\text{C}}}$.

One usually goes a step further by noticing that the harmonic component tends to rotate the a and $a^\dagger$ operators at rates $-\omega_0$ and $+\omega_0$, respectively. Hence, the most important terms in Eq. 3.3 are those that preserve excitation number and so do not rotate. This is the rotating-wave approximation[1] and it yields the so-called "black-box-quantized" Hamiltonian [Nigg et al. 2012]

$$H_{\text{bbq}} = \left(\hbar\omega_0 - \tfrac{1}{2}E_{\text{C}}\right)a^\dagger a - \tfrac{1}{2}E_{\text{C}}(a^\dagger a)^2, \tag{3.4}$$

where constant terms have been discarded and we have made use of the commutation relation $[a, a^\dagger] = 1$, which follows from $[\varphi, N] = i$. Finally, we are able to see that the eigenstates are nearly harmonic oscillator eigenstates $|n\rangle$, so that $a^\dagger a|n\rangle = n|n\rangle$ and n is a nonnegative integer, with energies $(\hbar\omega_0 + \frac{1}{2}E_{\text{C}})n - \frac{1}{2}E_{\text{C}}n^2$. This has practical significance, because the $g \to e$ transition energy is $E_{ge} = \hbar\omega_0 - E_{\text{C}}$ while the $e \to f$ transition energy is $E_{ef} = \hbar\omega_0 - 2E_{\text{C}}$, and so the ground-excited state manifold can be addressed without populating higher excited states. This anharmonicity permits the transmon to be used as a qubit. Note that these manipulations have also been used to concoct a variety of interesting synthetic Hamiltonians [Leghtas et al. 2015, Puri et al. 2017].

This example serves to illustrate that, even in single degree-of-freedom circuits, a variety of transformations and approximations is required to extract useful physical properties. The situation becomes drastically more complicated when circuits have multiple degrees of freedom. In those cases, certain degrees of freedom must be eliminated, and we may not have the luxury of small parameters, like $E_{\text{C}}/E_{\text{J}}$ in the above example.

3.2 Survey of techniques

3.2.1 Transformations

The transformations available for manipulating circuit Hamiltonians are numerous and context dependent. Generally, these techniques only yield an equivalent representation of the Hamiltonian, and not an effective one. Rather than discussing the details of each option, we provide a non-exhaustive list and some comments on individual utility.

Normal modes Canonically transformed variables without bilinear coupling to each other; see Sec. 4.3 for an example. The transformation corresponds to $\varphi_1 \to \lambda_{11}\varphi_1 + \lambda_{12}\varphi_2$ and $\varphi_2 \to \lambda_{21}\varphi_1 + \lambda_{22}\varphi_2$ in the two-variable case.

1 More generally, the rotating-wave approximation neglects the terms rotating faster than a threshold, and not all rotating terms. This particular application is the most aggressive form and it corresponds to taking the time-averaged Hamiltonian.

Gauge transformations Renormalized equilibrium positions according to $\varphi \to \varphi + \langle\varphi\rangle$; see Sec. 2.2.2 for an example. For circuits, this corresponds to a choice of ac ground and hence corresponds to a choice of electromagnetic gauge.

Discrete Fourier transforms Applicable in the case of many coordinates possessing a high degree of symmetry; they are often useful in exposing collective oscillations, such as the modes of a Josephson junction array [Masluk et al. 2012].

Bogoliubov transformations Modified creation/annihilation operators $a^\dagger$ and a (see App. D) to the effect of removing certain types of coupling or nonlinearity using $a \to ua + va^\dagger$ in the single-mode case [for an application to coupling amplification, see Leroux et al. 2018]. This is analogous to the normal mode transformation.

Displaced frames Applicable to circuits with microwave drives, where a unitary of the form $\mathcal{U} = \mathrm{e}^{-\xi a^\dagger + \xi^* a}$ has the effect of $a \to a + \xi$.

Rotating frames Accessed by a unitary of the form $\mathcal{U} = \mathrm{e}^{i\int^t \mathrm{d}t' H'(t')/\hbar}$, where the integral runs from some reference time up to t. They remove certain Hamiltonian terms while introducing others, which can be helpful in separating dynamics with very different timescales. Moving between the pictures of quantum mechanics can be viewed as rotating frame transformations.

3.2.2 Approximations

The transformations above are almost universally used in conjunction with some approximations, at which point the Hamiltonians under consideration become "effective." The approximations also span a diverse range, and we provide here a brief list.

Taylor series Expansions and their subsequent truncation, as demonstrated in Sec. 2.2.2, provide a useful strategy for simplifying Hamiltonians with coordinates whose quantum fluctuations are small.

Energy minimization Retaining the leading term of the Taylor series only. This has the effect of neglecting quantum fluctuations altogether, and can be justified for high-frequency modes, such as the higher harmonics of the Josephson junction array [Masluk et al. 2012].

Fourier series Another type of expansion, which aid in simplifying periodic Hamiltonians to their dominant harmonic components without strict restrictions on the size of quantum fluctuations.

Mean-field approximations Neglect quadratic two-body quantum fluctuations, usually when there are a large number of particle; see App. D. Coupling terms then become one-body terms, which require self-consistent treatment.

Rotating-wave approximations Prioritize the retainment of the slowest rotating terms, as mentioned above when going from Eq. 3.3 to Eq. 3.4.

Perturbation theory Useful in some cases (see Apps. B and D) to eliminate terms that do not contribute at the lowest orders of the theory.

Continuum limits Ease the evaluation of certain sums [e.g. to model a transmission line as a chain of *LC* oscillators; see Pozar 2012].

Note that the first two techniques (Taylor series and energy minimization) differ qualitatively from the second four (Fourier series, mean-field approximations, rotating-wave approximations, and perturbation theory). The former rely on *large* energy scales to confine the relevant phase space of the system into a region where the Hamiltonian can be easily approximated. The latter rely on *small* energy scales for the certain terms in the Hamiltonian, which are discarded or treated crudely. In the following section, we use a selection of these techniques to simplify the Hamiltonian of the $\cos 2\varphi$ qubit.

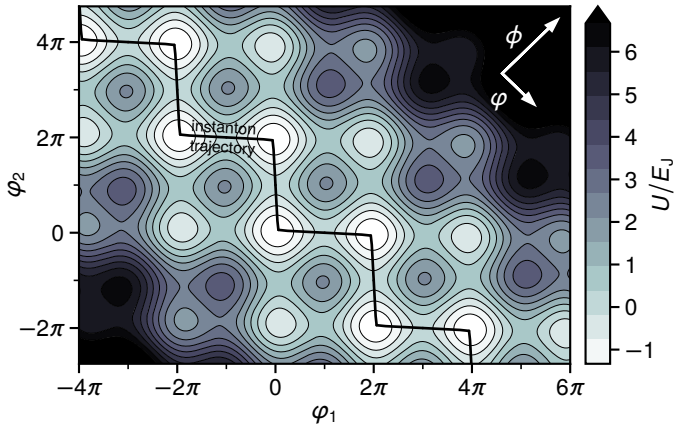

Figure 3.1 Contour map of the potential energy U of the $\cos 2\varphi$ qubit at $\varphi_{\text{ext}} = \pi$, as projected onto the $\varphi_1\varphi_2$-plane. The numerically computed instanton trajectory shown in black corresponds to the average tunneling path between the various degenerate potential minima. Constraining the Hamiltonian to this single degree of freedom minimizes the energy of the system and exposes the $\cos 2\varphi$ term.

3.3 Example: Semiclassical treatment of the $\cos 2\varphi$ qubit

3.3.1 Instanton trajectory and collective-type behavior

The example of the transmon in Sec. 3.1 illustrates the basic concept of finding an effective Hamiltonian. We now provide an involved example using the $\cos 2\varphi$ Hamiltonian written in Eq. 2.15. We start by examining the potential energy

$$U = E_{\text{L}}\left[\tfrac{1}{4}(\varphi_1 + \varphi_2 - \varphi_{\text{ext}})^2 + \theta^2\right] - 2E_{\text{J}}\cos\left(\frac{\varphi_1 - \varphi_2}{2}\right)\cos\left(\frac{\varphi_1 + \varphi_2}{2}\right) \tag{3.5}$$

in the $\varphi_1\varphi_2$-plane, i.e. roughly a 45° rotated version of the $\varphi\phi$-plane, which is plotted in Fig. 3.1. Note that we have projected out one degree of freedom by setting $\theta = 0$, that is, by minimizing the energy with respect to θ. The cosine terms in the residual potential form a two-dimensional "egg carton" of wells. The minimum of the quadratic term in the potential occurs at $\varphi_1 + \varphi_2 = \varphi_{\text{ext}}$, which generally falls between adjacent diagonal ridges of the cosine wells. At the special value of $\varphi_{\text{ext}} = \pi$, these two ridges are degenerate, as shown.

In pursuit of a one-dimensional potential, we are tempted to further minimize the energy to eliminate another coordinate. The challenge here is that we cannot draw a straight line through all the lowest-lying minima in Fig. 3.1. Near $\varphi_{\text{ext}} = \pi$, we consider the path of the system between neighboring potential minima by numerically solving for a two-dimensional instanton trajectory [for an instructive example, see Matveev et al. 2002]. The instanton trajectory corresponds to the maximally probable tunneling path[2] and is a natural choice for our final degree of freedom. We solve for this trajectory by inverting the

2 Constraining a system to move along its instanton trajectory is also known as the WKB approximation.

potential $U \to -U$ and solving the classical equation of motion for a particle moving from one maximum to its neighbor. For this to resemble quantum tunneling, the particle must begin and end with zero kinetic energy and the amount of time must tend to infinity. The Lagrangian in Eq. 2.14, projected as above and with ϕ replaced by $\phi + \varphi_{\text{ext}}$, corresponds to

$$\mathcal{L}_{\text{eff}} = \frac{\hbar^2}{16E_{\text{C}}}\left(\tfrac{1}{2}\dot{\phi}^2 + 2\dot{\varphi}^2 + \tfrac{1}{x}\dot{\varphi}^2\right) + \tfrac{1}{4}E_{\text{L}}\phi^2 - 2E_{\text{J}}\cos\varphi\cos\frac{\phi+\varphi_{\text{ext}}}{2},$$

and its Euler-Lagrange equations of motion (at $\varphi_{\text{ext}} = \pi$) are

$$\begin{aligned}\frac{\hbar^2}{16E_{\text{C}}}\ddot{\phi} &= \tfrac{1}{2}E_{\text{L}}\phi + E_{\text{J}}\cos\varphi\cos\frac{\phi}{2}\\ \frac{\hbar^2}{16E_{\text{C}}}\left(4+\tfrac{2}{x}\right)\ddot{\varphi} &= -2E_{\text{J}}\sin\varphi\sin\frac{\phi}{2}.\end{aligned}$$

These can be solved, subject to the initial and final conditions, using numerical methods such as Mathematica. The result is overlaid in Fig. 3.1; it resembles a zig-zag.

We then constrain the system to this zig-zag path, which, for the parameters listed in Tab. 2.2, is well-described by

$$\phi = \frac{1}{1+z}\left(2\left|\varphi - 2\pi\,\text{round}\,\frac{\varphi}{2\pi}\right| + z\varphi_{\text{ext}}\right), \tag{3.6}$$

where $z = E_{\text{L}}/E_{\text{J}}$ is a small parameter. We comment that this approximation neglects quantum fluctuations that are perpendicular to the path in Eq. 3.6. This is consequently a semiclassical approximation: we have minimized the energy of the system with respect to the dynamical coordinate orthogonal to the trajectory [Matveev et al. 2002]. Moreover, from Fig. 3.1, we see that the approximation we have made is that fluxons tunnel across a single Josephson junction at a time.

Plugging Eq. 3.6 into the Hamiltonian in Eq. 2.15 yields an unsightly mess equipped with absolute values and rounding functions. This is avoided using two more approximations: the potential is expanded in both its Fourier series, as it is now nearly π-periodic in φ, and its Taylor series about $z = 0$, and those series are truncated. This yields $H \approx H_{\text{eff}}$ with the effective Hamiltonian being given by

$$\begin{aligned}H_{\text{eff}} = 4E_{\text{C}}&\left\{\tfrac{1}{2}\left[1+\frac{1}{(1+z)^2}\right]^{-1}(N-N_{\text{g}}-P)^2 + xP^2\right\} + E_{\text{L}}\theta^2\\ &- E_{\text{L}}\left(\tfrac{16}{3\pi} - \tfrac{56}{9\pi}z\right)(\pi-\phi_{\text{ext}})\cos\varphi\\ &- E_{\text{J}}\left\{1 - \tfrac{5}{4}z + \tfrac{1}{48}\left[81 - 2\pi^2 - 6(\pi-\phi_{\text{ext}})^2\right]z^2\right\}\cos 2\varphi\\ &+ E_{\text{L}}\left(\tfrac{16}{45\pi} - \tfrac{88}{75\pi}z\right)(\pi-\phi_{\text{ext}})\cos 3\varphi\\ &- E_{\text{L}}\left(\tfrac{1}{12} - \tfrac{17}{72}z\right)\cos 4\varphi,\end{aligned}$$

where we have restored the θ dependence and retained terms through the fourth harmonic and $O(z^2)$. In this expression, $\phi_{\text{ext}} = \left|\varphi_{\text{ext}} - 4\pi\,\text{round}\,\frac{\varphi_{\text{ext}}}{4\pi}\right|$ is a periodic version of φ_{ext}. This treatment exposes the "$\cos 2\varphi$ nature" of the potential at $\varphi_{\text{ext}} = \pi$, where the $\cos\varphi$ and $\cos 3\varphi$ terms vanish and we see that the dominant correction term is of the form $\cos 4\varphi$.

Truncating more aggressively, i.e. discarding terms higher than the second harmonic or $O(z)$, we obtain

$$H_{\text{eff}} = 4E_{\text{C}}\left[\frac{1}{4(1-z)}(N - N_{\text{g}} - P)^2 + xP^2\right] + E_{\text{L}}\theta^2 \\ - \tfrac{16}{3\pi}E_{\text{L}}(\pi - \phi_{\text{ext}})\cos\varphi - E_{\text{J}}\left(1 - \tfrac{5}{4}z\right)\cos 2\varphi, \tag{3.7}$$

which is the central result of this chapter. This effective Hamiltonian has an advantage over the full Hamiltonian in Eq. 2.15 because it has made transparent the emergence of π-periodicity in φ, which was originally opaque. An added complication is that the φ mode is still strongly coupled to the θ mode. The resulting hybridization is a central ingredient to understanding properties of the system beyond the ground state manifold [Süsstrunk et al. 2013]. In the remainder of this chapter, we discuss the energy eigenvalues and eigenstates of the $\cos 2\varphi$ qubit.

3.3.2 Energy levels and emergent modes

From numerical diagonalization[3] of Eq. 2.15, we obtain the dependence of the energy levels on external flux as shown in Fig. 3.2. At $\varphi_{\text{ext}} = \pi$ (the dashed line in Fig. 3.2), the spectrum resembles a doubled harmonic oscillator with energy $\sqrt{16xE_{\text{L}}E_{\text{C}}}$. Once φ_{ext} deviates from π, half of the energy levels increase in energy linearly with slope $\sim\frac{32}{3}E_{\text{L}}$.[4] The other half of the energy levels form a flux-independent harmonic ladder.

We can understand this level structure as that of two emergent modes. The first mode is flux dependent and its excitations correspond to the number of fluxons enclosed by the inductive loop in Fig. 2.3. In turn, the number of enclosed fluxons identically maps onto the magnitude and chirality of the circulating persistent current in the inductive loop. The second mode is flux independent and its excitations correspond to quantized charge density oscillations, or plasmons, across the inductive loop/shunt capacitance in Fig. 2.3. Each plasmon involves the two superinductances (energy $2E_{\text{L}}$ in parallel) and the shunt capacitance (energy xE_{C}), and hence has energy $\sqrt{16xE_{\text{L}}E_{\text{C}}}$. Hereafter, we refer to these modes as the "fluxon mode" and the "plasmon mode," respectively. Additionally, we assign the labels $|m\bullet\rangle$ to the lowest-energy states, where m denotes the number of plasmons and $\bullet$ (or $\circ$) denotes the presence (or absence) of a fluxon excitation relative to the ground state.[5] Note that the fluxon placeholder indices are defined by

$$\bullet/\circ = \begin{cases} \circlearrowleft/\circlearrowright & \text{for } \varphi_{\text{ext}} \bmod 2\pi < \pi \\ -/+ & \text{for } \varphi_{\text{ext}} \bmod 2\pi = \pi \\ \circlearrowright/\circlearrowleft & \text{for } \varphi_{\text{ext}} \bmod 2\pi > \pi \end{cases},$$

where $|m\pm\rangle = |m\rangle \otimes \frac{1}{\sqrt{2}}(|\circlearrowright\rangle \pm |\circlearrowleft\rangle)$ and the index $\circlearrowleft$ represents the persistent current direction. This labeling serves the purpose of assigning quantum numbers consistently for

3 A more complete discussion of numerical diagonalization is left for Ch. 4, where it is explained in the context of a simpler circuit: the fluxonium artificial atom [Smith et al. 2016]. We only present the results for the $\cos 2\varphi$ qubit here [for more details, see Smith et al. 2019].

4 This term is simply the potential energy at $\varphi = \pi$ relative to that at $\varphi = 0$ (with $\phi_{\text{ext}} = 0$) found from Eq. 3.7.

5 Here we restrict the Hilbert space to the two fluxon states with lowest energy.

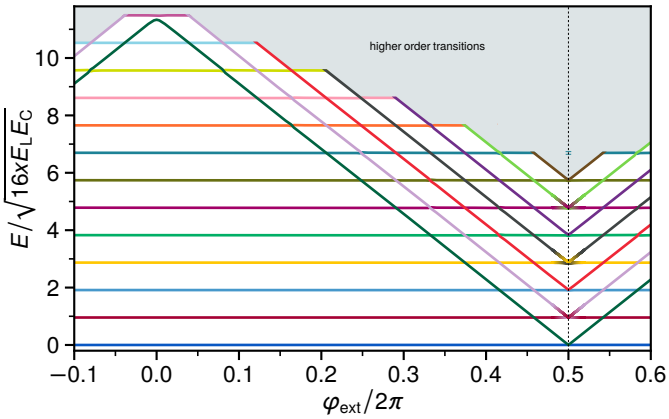

Figure 3.2 Calculated energy spectrum of the $\cos 2\varphi$ qubit as a function of the external flux at $N_g = 0$. The curves shown correspond to transition energies from the ground state, normalized by the approximate plasmon energy $\sqrt{16xE_LE_C}$. The essential feature is the presence of a flux-independent plasmon mode (maroon) and a flux-dependent fluxon mode (dark green), which is nearly degenerate with the ground state at $\varphi_{ext} = \pi$. The coloring reflects the assigned quantum numbers.

all external flux values (see the colors in Fig. 3.2[6]), except the particular case $\varphi_{ext} \bmod 2\pi = 0$, when additional fluxon states are required for classification.

To explain the energy level structure at $\varphi_{ext} = \pi$ exactly, we factor Eq. 3.7 into the form [for the factorization of electronic parity sectors, see Aasen et al. 2016]

$$H_{eff} = H_+ \oplus H_-.$$

The Cooper pair number parity sectors are governed by the Hamiltonians

$$H_\pm = 4E_C\left[\frac{1}{4(1-z)}(2\tilde{N} + k_\pm - N_g - P)^2 + xP^2\right] + E_L\theta^2 - E_J\left(1 - \tfrac{5}{4}z\right)\cos\tilde{\varphi}.$$

In the above, $k_+ = 0$ and $k_- = 1$ while $\tilde{\varphi}$ and $\tilde{N}$ should be viewed as conjugate operators corresponding to pairs of Cooper pairs. Note that this expression is an exact reformulation of Eq. 3.7. In the limit that $E_J \gg E_C$, we may Taylor expand the potential about $\tilde{\varphi} = 0$ and retain the first few terms. This step discards the effects of the offset charge, rendering H_+ and H_- identical. We then diagonalize the linear part of the Hamiltonian, yielding

$$H_\pm \approx 4E_C\left(\frac{1}{1-z}\tilde{N}_n^2 + \frac{x}{1+z}P_n^2\right) + E_L\theta_n^2 + \tfrac{1}{2}E_J\left(1 - \tfrac{3}{4}z\right)\tilde{\varphi}_n^2 - \tfrac{1}{24}E_J(\tilde{\varphi}_n + z\theta_n)^4 \qquad (3.8)$$

to leading order in z. The corresponding transformation is given by

6 Note that the coloring changes for only the odd-numbered plasmon states, due to the fact that the eigenstate with even overall parity has lower energy for each plasmon state, and that the overall parity includes both a plasmon and a fluxon component.

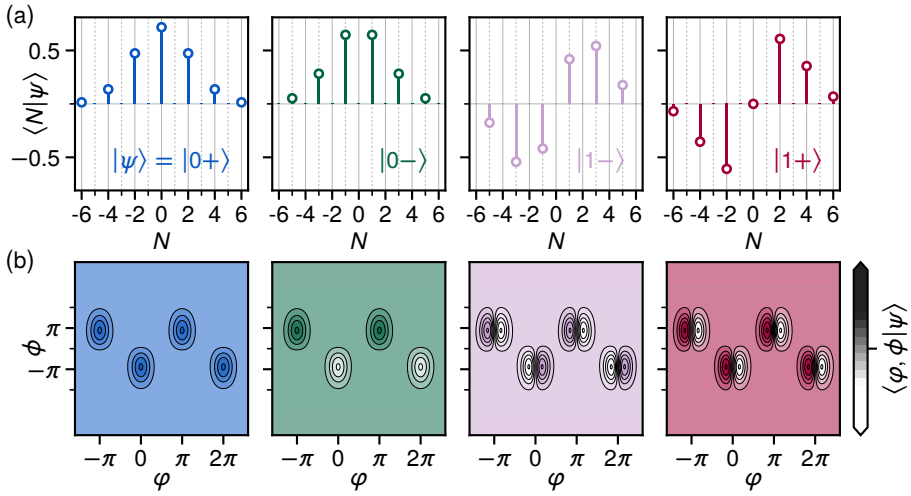

Figure 3.3 Projected wavefunctions for the lowest four eigenstates of the $\cos 2\varphi$ qubit at $\varphi_{\text{ext}} = \pi$ and $N_{\text{g}} = 0$, computed by numerical diagonalization of Eq. 2.15. (a) Charge wavefunctions $\langle N|\psi\rangle = \langle N|m\pm\rangle$ show that the plasmon excitation index $m = 0, 1, 2, \ldots$ indicates the functional form while the fluxon excitation index $\pm$ indicates Cooper pair number parity. (b) Phase wavefunctions $\langle\varphi, \phi|\psi\rangle$ show that the intrawell excitation number corresponds to the plasmon index and that the bonding/antibonding configuration corresponds to the fluxon index.

$$\begin{pmatrix}\tilde{\varphi}\\ \theta\end{pmatrix} = \begin{pmatrix}1 & z\\ -\frac{1}{2} & 1\end{pmatrix}\begin{pmatrix}\tilde{\varphi}_{\text{n}}\\ \theta_{\text{n}}\end{pmatrix}.$$

Eq. 3.8 reveals two weakly anharmonic modes: the plasmon mode at the low frequency of $\sqrt{16xE_{\text{L}}E_{\text{C}}}/h$ and a junction self-resonant mode at the high frequency of $\sqrt{8E_{\text{J}}E_{\text{C}}}/h$. These modes are coupled by a quartic nonlinearity, which has the primary effect of inducing a Kerr shift on the junction self-resonant mode. At frequencies lower than $\sqrt{8E_{\text{J}}E_{\text{C}}}/h$, the energy level structure is that of a two-fold degenerate harmonic oscillator, in agreement with the simulated energy spectrum at $\varphi_{\text{ext}} = \pi$ (see the dashed line in Fig. 3.2).

3.3.3 Wavefunctions

Calculated charge wavefunctions $\langle N|\psi\rangle$ and phase wavefunctions $\langle\varphi, \phi|m\pm\rangle$, obtained from numerical diagonalization of Eq. 2.15, are shown in Figs. 3.3a–b for the four lowest-energy states at $\varphi_{\text{ext}} = \pi$. Roughly, the phase wavefunctions are computed by projection of the θ coordinate and a Fourier transform to the $\varphi\phi$-plane, while the charge wavefunctions are computed by projection of the θ coordinate and constraint to the trajectory in Eq. 3.6 [for more details, see Smith et al. 2019].

The charge wavefunctions are essentially grid states with Fock-state envelopes [Gottesman et al. 2001, Bell et al. 2014]. For fluxon excitation index $+/-$, these grid states are

superpositions of even/odd Cooper pair number states.[7] Additionally, m corresponds to the order of the Fock state envelope. Note that a logical qubit encoded in $|0+\rangle$ and $|0-\rangle$ is protected from spurious transitions except those mediated by operators that flip Cooper pair number parity.

On the other hand, the phase wavefunctions are approximately Fock states localized within the potential energy wells (see Sec. 3.3.1) [Manucharyan et al. 2009]. The fluxon index $+/-$ denotes whether the state $|m\pm\rangle$ is a symmetric (bonding) or antisymmetric (antibonding) superposition of states localized within opposite ridges of potential wells. These ridges correspond to persistent currents of opposite chirality, and hence also to the absence/presence of a fluxon in the inductive loop of the circuit [Dempster et al. 2014]. In this picture, m refers to the Fock order of the localized states. Finally, operators that flip Cooper pair parity correspond to odd functions of ϕ or functions of φ with period an odd division of 2π, which can be seen from Fig. 3.3b to mediate the transition $m+ \rightarrow m-$.

7 The correspondence between Cooper pair number parity and the symmetry of the phase wavefunction can be seen from the π-periodicity/π-antiperiodicity of $|+/-\rangle$ and Eq. 2.5 [Devoret 1997].

4

NUMERICAL DIAGONALIZATION

You may use any degrees of freedom you like to describe a physical system, but if you use the wrong ones, you'll be sorry!

Steven Weinberg [Guth et al. 1983]

In Ch. 3, we saw two examples of how one might approximate, using analytic methods, a circuit Hamiltonian such as Eq. 2.13 by an effective version that accounts for the essential behavior. A complementary tactic is to employ numerical methods, which have several useful facets. Whereas the analytic approach exploits symmetry and/or separation of energy scales, the numerical approach tends to excel precisely when these conditions are not met. This is not without limitation, and these methods should also be viewed as approximations. Finite computational resources force a compromise to be made between Hilbert space size, numerical precision, and speed of the calculation. However, modern computers equipped with well-chosen numerical routines are capable of modeling a broad class of systems. This can be a tremendous asset in certain cases, namely:

(i) validation of the effective Hamiltonian by numerical comparison with the original Hamiltonian, which also provides error estimates;
(ii) examination of the full Hamiltonian behavior when the chain of transformations and approximations is not clear; and
(iii) design of an experiment, where the choice of parameters is crucial and even the full Hamiltonian must be verified with high degrees of accuracy (see Ch. 5).

An illustrative example, which is discussed in detail in Sec. 4.3, is the problem of simulating the coupling between a highly nonlinear mode and a harmonic oscillator. This situation is faced in understanding the fluxonium qubit inductively coupled to a readout antenna. Even when the native coupling is small compared to the other Hamiltonian terms, resonant interactions between the qubit and the antenna can quickly render perturbation theory, and other analytic techniques, invalid. Our solution is to employ numerical Hamiltonian diagonalization, which can efficiently capture nonperturbative effects in a similar way as quasi-degenerate perturbation theory. We restrict our attention in this chapter to diagonalization, but emphasize the diverse utility of numerical strategies in general.

4.1 Hamiltonian equivalence to energy levels and selection rules

For a time-independent Hamiltonian H, the Schrödinger equation reads

$$H|\mu\rangle = E_\mu|\mu\rangle, \tag{4.1}$$

where μ is an eigenstate index. This eigenvalue equation defines both a unitary change-of-basis matrix Λ, whose columns are the $|\mu\rangle$, and the nonvanishing elements E_μ of the Hamiltonian matrix in this basis, $\Lambda H \Lambda^\dagger = \mathrm{diag}(\{E_\mu\})$. The Hamiltonian is a function of a set of physical degrees of freedom, for instance $\{\varphi_i\}$ with i indexing the physical modes, and their conjugate variables $\{N_i\}$. If we suppose that the kinetic part of H is diagonal, i.e. it has the form $\sum_i 4E_{\mathrm{C},i}N_i^2$, then

$$[\varphi_i, H] = 4E_{\mathrm{C},i}\left[\varphi_i, N_i^2\right] = 8iE_{\mathrm{C},i}N_i$$

by the commutation relation. Taking the inner product with respect to $\langle\mu|$ and $|\nu\rangle$ gives

$$\langle\mu|\varphi_i|\nu\rangle = i\frac{8E_{\mathrm{C},i}}{E_{\mu\nu}}\langle\mu|N_i|\nu\rangle,$$

where the $\mu \to \nu$ transition energy is defined to be $E_{\mu\nu} = E_\nu - E_\mu$. This exercise shows that the Hamiltonian H is exactly equivalent to its energy levels E_μ and matrix elements $\langle\mu|\varphi_i|\nu\rangle$.[1] This quick calculation shows that the charge matrix elements $\langle\mu|N_i|\nu\rangle$ are proportional to those of the phase operator, with the scale given by the transition energy $E_{\mu\nu}$.

More generally, we may consider the matrix elements to be a representation of the selection rules of the system, that is, the tendency of an external probe coupled to φ_i or N_i to induce the $\mu \to \nu$ transition. In the case of closed quantum mechanics, the Hamiltonian, and hence alternatively the energy levels and selection rules, constitute a complete description of the system. Moreover, these energy levels and matrix elements can be readily translated into dynamical properties using techniques from perturbation theory, dephasing theory, and linear response theory [e.g. Kubo 1957]. The scope of the dynamical treatment in this dissertation is limited to these quasi-static methods—namely to estimate coherence times.

4.2 Hamiltonian matrix assembly

4.2.1 Choice of basis

In order to extract the energy levels and eigenstates of a Hamiltonian, a basis must be chosen in which to construct the Hamiltonian matrix. This matrix can, with varying degrees of efficiency, be fed into a specialized diagonalization routine.[2] This choice can be nontrivial, and the optimal strategy is to choose a basis that most efficiently captures the underlying relevant physics of the system. More precisely, given a fixed Hilbert space dimension and feature of interest, e.g. the $g \to e$ transition frequency or the $\langle g|\varphi|e\rangle$ matrix element, the optimal basis minimizes the error. The transmon qubit Hamiltonian is used as an example of this in Sec. 4.2.2.

A practical complication is that the Hamiltonian matrix elements can be difficult to calculate in the proper basis. For example, in the limiting case where the basis of Hamiltonian eigenstates is chosen, computing the matrix elements coincides with exact

1 The $E_{\mathrm{C},i}$ are also needed to calculate the $\langle\mu|N_i|\nu\rangle$ given the $\langle\mu|\varphi_i|\nu\rangle$ and the E_μ.

2 Results presented here use the packages `scipy.linalg` and `scipy.sparse` in Python for diagonalization. They are built upon the LAPACK and ARPACK packages, respectively. Note that `scipy.linalg` is recommended over `numpy.linalg` by the developers [Jones et al. 2001].

diagonalization. Hence, a compromise is necessary when choosing a basis in which to diagonalize a Hamiltonian.

There are three essential bases that may be used for diagonalization of a circuit Hamiltonian:[3] the phase basis spanned by the phase eigenstates $|\varphi\rangle$, the charge basis spanned by the Cooper pair number states $|N\rangle$, and the harmonic oscillator Fock basis spanned by the photonic number states $|n\rangle$. Since the $|n\rangle$ are eigenvectors of $a^\dagger a$, where a and $a^\dagger$ are linear combinations of φ and N as introduced in Sec. 3.1, the Fock basis can be viewed as a particular linear combination of the charge and phase bases.

Fock basis The bosonic Fock basis is spanned by the eigenstates $|n\rangle$ such that $n < n_0$ with n_0 being the truncation dimension of the Hamiltonian matrix, with wavefunctions given by the Hermite functions

$$\langle\varphi|n\rangle = \frac{1}{\sqrt{2^n n!}} \frac{1}{(2\pi\varphi_{\text{zpf}}^2)^{1/4}} e^{-(\varphi/2\varphi_{\text{zpf}})^2} H_n\left(\frac{\varphi}{\sqrt{2}\varphi_{\text{zpf}}}\right) \tag{4.2}$$

for the Hamiltonian $H = 4E_C N^2 + \frac{1}{2}E_J\varphi^2$ where $\varphi_{\text{zpf}} = (2E_C/E_J)^{1/4}$. This basis effectively captures the physics of confined potentials, i.e. $U(\varphi)$ such that U is lower bounded and $U \to \infty$ as $|\varphi| \to \infty$, because the wavefunctions themselves are localized. It can also be used for systems where the relevant eigenstates approximately occupy the same region, especially when the potential can be well-approximated by a parabola, e.g. in the transmon qubit. Additionally, the wavefunctions in Eq. 4.2 can make evaluating Hamiltonian matrix elements using integrals difficult (see Sec. 4.3) but this is ameliorated using algebraic computations with a and $a^\dagger$, and their associated commutation relation.

Charge basis The charge basis, equivalently the Cooper pair number basis, is spanned by the states

$$\{|N\rangle : N = -N_0, -N_0 + 1, \ldots, N_0 - 1, N_0\},$$

where $2N_0 + 1$ is the dimension of the truncated Hamiltonian matrix. From Eq. 2.5, this basis is automatically 2π-periodic in φ, making it a good match for similarly periodic Hamiltonians like the Josephson Hamiltonian H_J in Eq. 2.2. For this basis, the drawback lies in the fact that the matrix elements for unbounded potential terms in $U(\varphi)$ are more or less impossible to calculate because their Fourier series diverges. Similarly, terms that are periodic in φ with period less than 2π also pose a challenge. This issue can be avoided, however, by rescaling φ so that the potential term with largest period is 2π-periodic, at which point manipulations like Eq. 1.4 may be used to represent the terms with smaller periods further from the main diagonal in the Hamiltonian matrix.

Phase basis The Fock and charge bases have the shared property that their constituent eigenvectors are discrete, owing to the confinement of the harmonic oscillator Hamiltonian and the 2π-periodicity of the Josephson Hamiltonian in φ. At present, superconducting

3 This is only true for circuits without *quantum phase-slip elements*, which allow fluxon tunneling and are therefore characterized by nonlinear capacitive energies $-E_P \cos 2\pi N$, with E_P the tunneling energy and N the number of Cooper pairs that have crossed [Mooij and Nazarov 2006]. Such elements are the dual to Josephson junctions, and circuits containing them can have quantized phases. Note that a circuit with both quantized charge and phase would host GKP eigenstates [Gottesman et al. 2001].

circuits have not made extensive use of the third category of Hamiltonian: one that is quadratic in φ and periodic in N.[3] Diagonalization of such a Hamiltonian could proceed in the phase basis much like the Josephson Hamiltonian in the charge basis. On the other hand, artificial discretization of the phase basis may provide utility for certain circuits. The procedure requires breaking up the interval $[0, 2\pi)$ into an arbitrary number of subintervals separated by $\delta\varphi$. The Hamiltonian could then be written in the basis spanned by

$$\left\{|\varphi\rangle = |p\,\delta\varphi\rangle : p = 0, 1, 2, \ldots, \lfloor 2\pi/\delta\varphi \rfloor\right\},$$

and the process bears some similarity to finite difference methods.

Role of transformations As alluded in our discussion of the charge basis, these bases are not unique, even for a single degree of freedom. In addition to rescaling degrees of freedom, which can be important in the charge basis for simultaneous treatment of terms like $\cos\varphi$ and $\cos 2\varphi$, one may carry out a variety of approximations and transformations to aid the efficiency of numerical diagonalization. An example is provided by the linear transformation to normal coordinates in the fluxonium artificial atom—see Sec. 4.3.2. Another case is that of Eq. 1.1 when $E_\mathrm{L} \ll E_\mathrm{J}$, which corresponds the fluxonium qubit and where numerical diagonalization is improved using the linearly inductive term and the capacitive term as the Fock basis, i.e. neglecting to include the quadratic part of the Josephson term. This ensures that the basis wavefunctions have sufficient width to span the multiple potential minima in Fig. 1.1b.

4.2.2 Convergence and numerical efficiency

To expand on our the earlier comments about choosing an optimal basis depending on the desired output of the calculation for a given system, we revisit the transmon from Sec. 3.1. The full Hamiltonian is written in Eq. 3.1, and it can be approximated by Eq. 3.2. The former, which is 2π-periodic in φ, suggests that the charge basis should be used:

$$H = 4E_\mathrm{C} \sum_{N=-\infty}^{\infty} (N - N_\mathrm{g})^2 |N\rangle\langle N| - \tfrac{1}{2}E_\mathrm{J} \sum_{N=-\infty}^{\infty} \left(|N\rangle\langle N+1| + |N+1\rangle\langle N|\right).$$

On the other hand, the approximate Hamiltonian is unbounded and this prompts an expansion in the Fock basis:

$$H_\mathrm{eff} = \sqrt{8E_\mathrm{J}E_\mathrm{C}} \sum_{n=0}^{\infty} (n + \tfrac{1}{2})|n\rangle\langle n| - \tfrac{1}{12}E_\mathrm{C} \sum_{n=0}^{\infty}\sum_{m=0}^{\infty} \langle n|(a + a^\dagger)^4|m\rangle|n\rangle\langle m|.$$

The sums appearing in either of these expressions inevitably must be truncated, and the Fock basis expansion can readily be extended to include higher-order terms in the Taylor series. The optimal choice hinges on the specific calculation. If we are seeking the $g \to e$ transition frequency, then the Fock basis is superior due to the strong localization of both eigenstates, owing to the fact that $E_\mathrm{J} \gg E_\mathrm{C}$. On the other hand, if we are seeking the charge dispersion ϵ_g of the ground state $|g\rangle$, which is the oscillation amplitude of the ground state

energy in N_g, then the charge basis is superior.[4] We also note that the Hamiltonian in the charge basis is much sparser than that in the Fock basis, and it includes N_g explicitly.

4.2.3 Contrast with perturbation theory

Properly implemented numerical diagonalization routines can be extremely powerful tools, especially when considering novel circuits and designing protected qubits, but the results are not always transparent. One may need to plot wavefunctions, compute matrix elements, and diagonalize for many parameter values before developing an intuition for the system. Perturbative techniques present an alternative (see App. B). In the spirit of Ch. 3, perturbation theory can be used to justify the elimination of terms in the Hamiltonian that do not contribute to the lowest orders of the theory, For the purpose of calculations, on the other hand, perturbation theory offers an alternative protocol where the dominant component of the Hamiltonian is diagonalized and corrections to the eigenstates and energy levels are included iteratively. In some cases, e.g. if the first-order correction vanishes or the unperturbed Hamiltonian requires numerical diagonalization, perturbation theory can offer less accuracy and comparable computational complexity.

4.3 Example: Energy levels of the fluxonium artificial atom

This section presents the quantization and numerical diagonalization of the *fluxonium artificial atom*: a fluxonium qubit, a small Josephson junction shunted by a superinductance, inductively coupled to an electric dipole antenna used as a readout resonator [Smith et al. 2016]. The energy levels of the two-mode fluxonium artificial atom are then compared with experimental results as well as those obtained using a perturbative calculation.

4.3.1 Fluxonium qubit

Experimentally, the *fluxonium qubit* is realized as one small Josephson junction in parallel with a series array of ∼100 larger Josephson junctions [Manucharyan et al. 2009, J. Koch et al. 2009]. In the limit of large size difference between these two types of junctions, the capacitances and nonlinear inductances across the array junctions may be neglected, and they form a collective, linear superinductance[5]. When the external magnetic flux threading the loop is $\varphi_{ext} = \pi$, the two lowest energy quantum states are approximately the symmetric and antisymmetric superpositions of counter-circulating persistent-current states, similar to the flux qubit [Mooij et al. 1999, Orlando et al. 1999, Chiorescu et al. 2003, 2004]. The large shunt inductance serves the purpose of rendering the Cooper pair number N continuous rather than discrete, and consequently the Hamiltonian is independent of the static offset charge N_g.

The superinductances used in fluxonium qubits to date have mostly been implemented using arrays of large Josephson junctions [Manucharyan 2012]. In this structure, the large

4 Diagonalization in the Fock basis *can* also determine charge dispersions, but it requires much larger Hilbert spaces for a given accuracy. This requires modeling the quantum tunneling between neighboring potential wells by including harmonic oscillator wavefunctions with excitation index large enough for their widths to extend beyond 2π.

5 Early implementations of superinductances demonstrated inductance values up to ∼300 nH [Manucharyan et al. 2009, Masluk et al. 2012], but they have since been pushed into the microhenry range [Bell et al. 2012, Shearrow et al. 2018, Pechenezhskiy et al. 2019].

size of the junctions ensures their linearity and suppressed individual phase-slip rate, while the large number of junctions M in the chain ensures a large total inductance. Practically, the largest inductances are made by increasing M until the self-resonant modes of the array are pushed to low frequencies. To see this, we quote the result from Masluk et al. (2012),

$$\omega_k = \omega_\mathrm{J}\sqrt{\frac{1-\cos\frac{\pi k}{M}}{\frac{C_0}{2C_\mathrm{J}}+1-\cos\frac{\pi k}{M}}},$$

for the frequency of the k-th harmonic of a periodic array, obtained by invoking a discrete Fourier transform on the linear circuit. Here, $\omega_\mathrm{J} = 1/\sqrt{L_\mathrm{J}C_\mathrm{J}} \sim 20\,\mathrm{GHz}$ is the junction plasma frequency and C_0 is the ground capacitance of each island in the array. The common mode of the array corresponds to $k = 0$, for which the phase drops across all junctions are equal. For frequencies lower than that of the fundamental mode, for which $k = 1$, the array is well-approximated by a linear inductance. Evidently, we have $\omega_1 \approx \frac{\pi}{M}\omega_\mathrm{J}\sqrt{C_\mathrm{J}/C_0}$ for $M \to \infty$ and hence the maximum M will be limited by C_J/C_0.

4.3.2 Fluxonium qubit inductively-coupled to a dipole antenna

Motivated by the efficient description of the low-lying fluxonium eigenstates in terms of persistent currents, we inductively couple the fluxonium qubit and readout resonator [Pop et al. 2014, Vool et al. 2014]. This additional resonator is required for dispersive measurement (see Ch. 5 for additional details) and, in our system, consists of an LC oscillator whose capacitance and inductance are formed by an electric dipole antenna and another Josephson junction array, respectively. The inductive coupling is achieved using shared junctions between the arrays of both oscillators. The resulting fluxonium-resonator system is depicted by the schematic diagram in Fig. 4.1a.

To analyze this system, we (i) replace the distributed dipole antenna capacitor by a lumped element capacitance, and (ii) replace the large Josephson junction arrays by linear inductances. Approximation (i) is justified by the antenna length ($\sim$1–2 mm) being much smaller than the wavelength of the resonator ($\sim$3–6 cm) [Pop et al. 2014]. On the other hand, (ii) is permitted when all array junctions are much larger than the small junction of the qubit and the relevant frequencies are below the fundamental mode of the array [Masluk et al. 2012, Ferguson et al. 2013]. Fig. 4.1b shows the resulting electrical circuit.

Having obtained a circuit with five elements, we use Kirchhoff's laws as described in Sec. 2.4 to write the Lagrangian in terms of two degrees of freedom: the flux across the capacitance of the readout resonator Φ_r and that across the small junction of the qubit Φ_q. In the limit that $L_\mathrm{q} \gg L_\mathrm{r} \sim L_\mathrm{s}$, i.e. the unshared inductance of the qubit is much larger than either the unshared inductance of the readout resonator or the shared inductance, the circuit is well-described by the Lagrangian

$$\begin{aligned}\mathcal{L} = {} & \tfrac{1}{2}C_\mathrm{r}\dot{\Phi}_\mathrm{r}^2 - \frac{1}{2(L_\mathrm{r}+L_\mathrm{s})}\Phi_\mathrm{r}^2 + \frac{L_\mathrm{s}}{L_\mathrm{q}(L_\mathrm{r}+L_\mathrm{s})}\Phi_\mathrm{r}\Phi_\mathrm{q} \\ & + \tfrac{1}{2}C_\mathrm{J}\dot{\Phi}_\mathrm{q}^2 - \frac{1}{2L_\mathrm{q}}\Phi_\mathrm{q}^2 + E_\mathrm{J}\cos(\varphi_\mathrm{q}-\varphi_\mathrm{ext}),\end{aligned} \tag{4.3}$$

upon $\varphi_\mathrm{q} \to \varphi_\mathrm{q} - \varphi_\mathrm{ext}$. Here, C_J and E_J denote the capacitance and Josephson tunneling energy of the small junction, while C_r represents the dipole capacitance of the readout

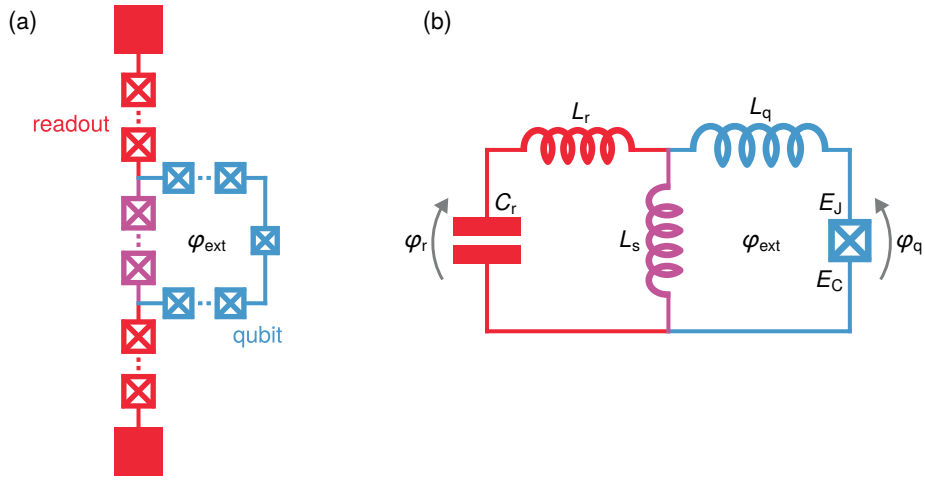

Figure 4.1 Circuit representations of the fluxonium artificial atom. (a) Schematic diagram reflecting the geometric layout of the device, making the Josephson junction arrays and the pads of the antenna readout resonator explicit. The fluxonium qubit (blue) is coupled to the antenna (red) via an array of shared junctions (purple). (b) Lumped element approximation to the schematic. The junction arrays are considered linear inductances and the distributed antenna capacitance is taken to be dipolar.

mode. Note that the first two terms in Eq. 4.3 describe the readout mode and the last three terms correspond to the qubit mode. All coupling between these modes is captured by the bilinear mutually inductive third term.

To linearize Eq. 4.3, we must temporarily dispense with components of the cosine term. For weakly anharmonic, capacitively-shunted qubits, the cosine can be replaced by the quadratic term in its Taylor expansion [Nigg et al. 2012, Solgun et al. 2014]. An example is the transmon, which have examined in Sec. 3.1. For highly anharmonic, inductively-shunted qubits, the cosine should be discarded altogether. The fluxonium belongs to this class, owing to its large inductive shunt and single Cooper pair charging effects.

We proceed by examining the classical Euler-Lagrange equations of motion

$$\begin{pmatrix} \ddot{\Phi}_r \\ \ddot{\Phi}_q \end{pmatrix} = \begin{pmatrix} -\frac{1}{C_r(L_r+L_s)} & \frac{L_s}{C_rL_q(L_r+L_s)} \\ \frac{L_s}{C_JL_q(L_r+L_s)} & -\frac{1}{C_JL_q} \end{pmatrix} \begin{pmatrix} \Phi_r \\ \Phi_q \end{pmatrix}. \tag{4.4}$$

in matrix notation for the linearized Lagrangian, obtained by taking $E_J \to 0$ in Eq. 4.3. We may decouple the equations of motion Eq. 4.4 by diagonalizing the above matrix. Defining Λ to be the change-of-basis matrix that does so, we are guaranteed that the equations of motion are decoupled in the normal coordinates

$$\begin{pmatrix} \Phi_R \\ \Phi_Q \end{pmatrix} = \Lambda^{-1} \begin{pmatrix} \Phi_r \\ \Phi_q \end{pmatrix} \qquad \Lambda = \begin{pmatrix} \lambda_{11} & \lambda_{12} \\ \lambda_{21} & \lambda_{22} \end{pmatrix}. \tag{4.5}$$

	Device A1	Device A2
C_r (fF)	20.3	20.1
L_r (nH)	15.6	19.7
L_s (nH)	4.5	2.9
C_J (fF)	5.3	5.9
L_q (nH)	386	430
E_J/h (GHz)	6.20	9.08
$1-\lambda_{11}$	1.5×10^{-3}	4.1×10^{-4}
λ_{12}	1.5×10^{-2}	8.4×10^{-3}
λ_{21}	-5.6×10^{-2}	-2.9×10^{-2}
$1-\lambda_{22}$	1.1×10^{-4}	3.5×10^{-5}

Table 4.1 Circuit parameters for devices A1 and A2 as defined in Fig. 4.1b, and used for energy level calculations and their comparison to experimentally obtained values in Figs. 4.2–3. The final four rows define the normal mode transformation in Eq. 4.5.

Transforming the Lagrangian in Eq. 4.3 into these coordinates yields

$$\mathcal{L} = \tfrac{1}{2}C_R\dot{\Phi}_R^2 - \frac{1}{2L_R}\Phi_R^2 + \tfrac{1}{2}C_Q\dot{\Phi}_Q^2 - \frac{1}{2L_Q}\Phi_Q^2 + E_J\cos(\lambda_{21}\varphi_R + \lambda_{22}\varphi_Q - \varphi_{ext}). \tag{4.6}$$

In this expression, C_i and L_i with $i = R, Q$ denote the normal mode capacitances and inductances given by

$$\begin{aligned} C_R &= \lambda_{11}^2 C_r + \lambda_{21}^2 C_J \\ C_Q &= \lambda_{12}^2 C_r + \lambda_{22}^2 C_J \\ \frac{1}{L_R} &= \frac{\lambda_{11}^2}{L_r + L_s} + \frac{\lambda_{21}^2}{L_q} - \frac{2\lambda_{11}\lambda_{21}L_s}{L_q(L_r + L_s)} \\ \frac{1}{L_Q} &= \frac{\lambda_{12}^2}{L_r + L_s} + \frac{\lambda_{22}^2}{L_q} - \frac{2\lambda_{12}\lambda_{22}L_s}{L_q(L_r + L_s)} \end{aligned}$$

We note that this normal mode basis, in which the coupling between modes is entirely captured by the cosine term in Eq. 4.6, conveniently makes obvious the inherited nonlinearity of the readout as well as the nonlinear nature of the coupling [Nigg et al. 2012]. To draw an analogy to the circuit quantum electrodynamics (cQED) literature, we observe that $|\lambda_{11}| \gg |\lambda_{12}|$ and $|\lambda_{21}| \ll |\lambda_{22}|$ in our devices (see Tab. 4.1), which means that mode R is vastly more linear than mode Q.[6] This allows us to refer to modes R and Q in Eq. 4.6 as the *readout-like* and *qubit-like* modes, respectively, which we will henceforth refer to as *readout* and *qubit*.

6 Strictly speaking, this requires $\sqrt{L_R/C_R} \lesssim \sqrt{L_Q/C_Q}$ so that the magnitudes of φ_R and φ_Q in Eq. 4.6 are at most comparable.

4.3.3 Numerical diagonalization in the normal mode Fock basis

Continuing as in Sec. 2.4, we define the conjugate charges $Q_i = \partial\mathcal{L}/\partial\dot{\Phi}_i$ for the two normal modes. These steps yield the Hamiltonian

$$H = \frac{1}{2C_\mathrm{R}}Q_\mathrm{R}^2 + \frac{1}{2L_\mathrm{R}}\Phi_\mathrm{R}^2 + \frac{1}{2C_\mathrm{Q}}Q_\mathrm{Q}^2 + \frac{1}{2L_\mathrm{Q}}\Phi_\mathrm{Q}^2 - E_\mathrm{J}\cos\left(\lambda_{21}\varphi_\mathrm{R} + \lambda_{22}\varphi_\mathrm{Q} - \varphi_\mathrm{ext}\right). \quad (4.7)$$

For diagonalization, we express this Hamiltonian in the normal mode harmonic oscillator basis $\{|nm\rangle\}$, where n and m correspond to the number of excitations in the readout and qubit modes as the (infinite-dimensional) matrix

$$H = \hbar\sum_{n,m\in\mathbb{N}}(\omega_\mathrm{R}n + \omega_\mathrm{Q}m)|nm\rangle\langle nm| - E_\mathrm{J}\sum_{n,n',m,m'\in\mathbb{N}}\Big[\cos\varphi_\mathrm{ext}\left(c^\mathrm{R}_{nn'}c^\mathrm{Q}_{mm'} + s^\mathrm{R}_{nn'}s^\mathrm{Q}_{mm'}\right) + \sin\varphi_\mathrm{ext}\left(c^\mathrm{R}_{nn'}s^\mathrm{Q}_{mm'} - s^\mathrm{R}_{nn'}c^\mathrm{Q}_{mm'}\right)\Big]|nm\rangle\langle n'm'|. \quad (4.8)$$

Here, ω_i is the dressed harmonic oscillator frequency of normal mode i. The cosine and sine matrix elements can be computed analytically as follows, where $\mathscr{L}_a^b$ are the associated Laguerre polynomials and it is understood that $\lambda_\mathrm{R} = \lambda_{21}$ and $\lambda_\mathrm{Q} = \lambda_{22}$ [Gradshteyn and Ryzhik 2007]:

$$\begin{aligned} c^i_{k\ell} &= \langle k|\cos(\lambda_i\varphi_i)|\ell\rangle \\ &= \begin{cases} (-1)^{\frac{\ell-k}{2}}\sqrt{\frac{k!}{\ell!}}(\lambda_i\varphi_{\mathrm{zpf},i})^{\ell-k}\mathrm{e}^{-(\lambda_i\varphi_{\mathrm{zpf},i})^2/2}\mathscr{L}_k^{\ell-k}\left[(\lambda_i\varphi_{\mathrm{zpf},i})^2\right] & \text{for } k+\ell \text{ even}, \\ 0 & \text{for } k+\ell \text{ odd}, \end{cases} \end{aligned} \quad (4.9)$$

$$\begin{aligned} s^i_{k\ell} &= \langle k|\sin(\lambda_i\varphi_i)|\ell\rangle \\ &= \begin{cases} 0 & \text{for } k+\ell \text{ even}, \\ (-1)^{\frac{\ell-k+1}{2}}\sqrt{\frac{k!}{\ell!}}(\lambda_i\varphi_{\mathrm{zpf},i})^{\ell-k}\mathrm{e}^{-(\lambda_i\varphi_{\mathrm{zpf},i})^2/2}\mathscr{L}_k^{\ell-k}\left[(\lambda_i\varphi_{\mathrm{zpf},i})^2\right] & \text{for } k+\ell \text{ odd}. \end{cases} \end{aligned} \quad (4.10)$$

In these equations, the amplitude of zero-point fluctuations of the phases are given by $\varphi_{\mathrm{zpf},i} = \sqrt{Z_i/2\mathcal{R}_\mathrm{Q}}$, where $Z_i = \sqrt{L_i/C_i}$ is the characteristic impedance and $\mathcal{R}_\mathrm{Q} = \hbar/(2e)^2$ is the reduced superconducting resistance quantum.

We treat the full analytic expression Eqs. 4.8–10 for the Hamiltonian matrix of the fluxonium-resonator system as in Fig. 4.1b, when $L_\mathrm{q} \gg L_\mathrm{r} \sim L_\mathrm{s}$. Computing the lowest energy levels requires truncating both readout and qubit Hilbert spaces. This is done by restricting the basis to $\{|nm\rangle : n \le n_0, m \le m_0\}$ with finite cutoff dimensions n_0 and m_0, which may be viewed as a perturbative expansion in powers of $1/n_0$ and $1/m_0$ and from which we only retain the leading order terms. We choose $n_0 \sim 5$ and $m_0 \sim 20$ in order to simultaneously minimize truncation errors and computational cost.[7] Such numerical diagonalization yields the full solution to the time-independent Schrödinger equation

$$H|n\mu\rangle = E_{n\mu}|n\mu\rangle,$$

7 The computational complexity for the perturbative calculation in App. B is $O(m_0^4)$ while that for exact diagonalization is $O(n_0^3m_0^3)$. For our system, these are of the same order.

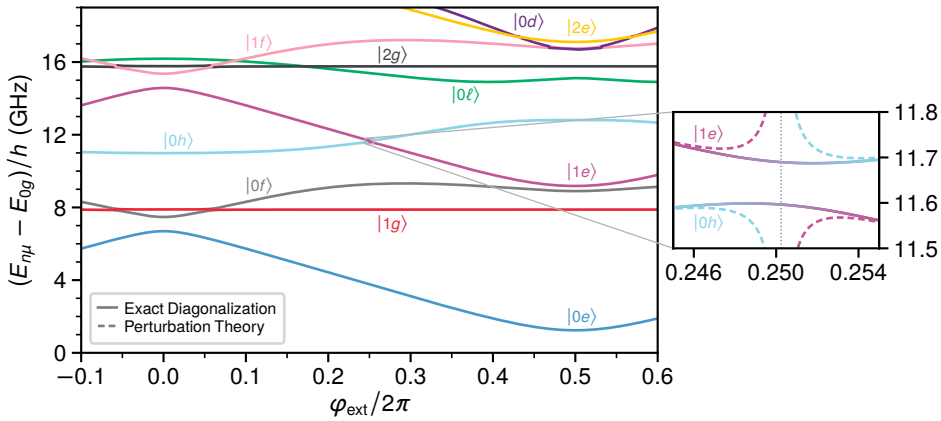

Figure 4.2 Energy spectrum of the fluxonium artificial atom as a function of the external flux. The plotted curves correspond to energy levels $E_{n\mu}$, found by numerical diagonalization, relative to the ground state energy E_{0g}. The inset magnifies the anticrossing between the $0 \to 1$ readout transition and the $e \to h$ qubit transition, showing the divergence of second-order perturbation theory.

where μ denotes the qubit excitation.[8] The computed energy spectrum for device A1 (see Tab. 4.1) as a function of the external flux φ_{ext} is plotted in Fig. 4.2 for the first nine transitions from the ground state.

In order to assign the quantum numbers n and μ to these energy levels, which undergo anticrossings as external flux is varied, we additionally diagonalize a decoupled version H_0 of the Hamiltonian Eq. 4.7. This Hamiltonian is obtained by setting $\varphi_{\text{R}} \to 0$ in the argument of the cosine in Eq. 4.7 or equivalently by setting $c^{\text{R}}_{nn'} \to 1$ and $s^{\text{R}}_{nn'} \to 0$ in Eq. 4.8. Computing the energy levels for H_0 only requires truncating the qubit Hilbert space. This time, the basis is restricted to $\{|nm\rangle : m \leq m_0\}$ with finite m_0. As before, we take $m_0 \sim 20$, and we reiterate that numerical methods are the only tractable option. This procedure results in the solution of

$$H_0|n\mu\rangle_0 = E^{(0)}_{n\mu}|n\mu\rangle_0.$$

Note that the eigenstates are easily separable: $|n\mu\rangle_0 = |n\rangle|\mu\rangle_0$ and $E^{(0)}_{n\mu} = \hbar\omega_{\text{R}}(n+\frac{1}{2}) + E_\mu$. In other words, the decoupled spectrum has built-in quantum numbers. Quantum numbers are then assigned by comparing the coupled energy spectrum $E_{n\mu}$ to the decoupled spectrum $E^{(0)}_{n\mu}$. In the limit of weak coupling, we may simply take n and μ for a given coupled level to be those of the nearest decoupled level. In this scheme, the quantum numbers labeling a chosen energy level abruptly switch at level anticrossings, as shown in Fig. 4.2.

8 Our notation $E_{n\mu}$ for an energy level with the joint quantum numbers n and μ is structurally the same as the transition energy $E_{\mu\nu} = E_\nu - E_\mu$, but the meaning should be clear in each case.

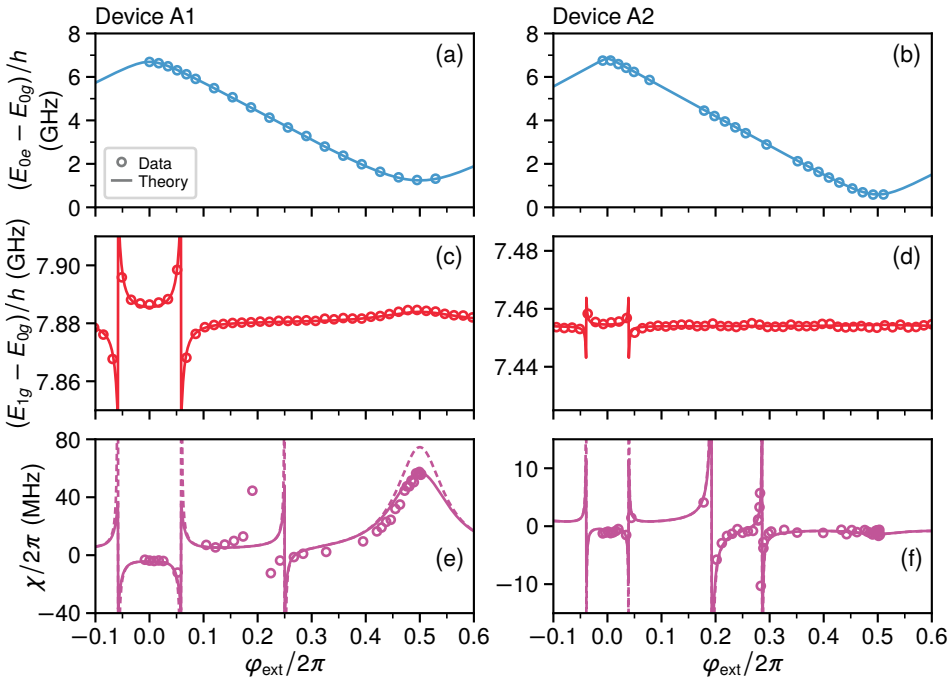

Figure 4.3 The fluxonium dispersive Hamiltonian: theory vs. experiment as a function of external flux bias. Circles indicate values measured using spectroscopy (see Ch. 5 for details on the methods). Solid/dashed lines indicate theoretical fits obtained by numerical diagonalization/second-order perturbation theory. (a–b) (Blue) Qubit $g \to e$ transition frequency. (c–d) (Red) Readout $0 \to 1$ transition frequency. (e–f) (Purple) Dispersive shift of the readout frequency by the qubit.

4.3.4 Agreement with experiment

We test the accuracy of our circuit model and analysis by comparing the simulated spectrum to experimentally obtained spectroscopy data at various values of φ_{ext} and for the two devices with different parameters in Tab. 4.1.[9] These devices were measured in a rectangular waveguide in a transmission configuration, the details of which are discussed in Ch. 5, and the data is plotted in Fig. 4.3. It is clear that the measured readout $0 \to 1$ transition frequency and the qubit $g \to e$ transition frequency should be compared to the quantities $(E_{1g} - E_{0g})/h$ and $(E_{0e} - E_{0g})/h$ from diagonalization, respectively, in the limit of zero temperature. Similarly, the dispersive shift χ may also be computed from diagonalization via

$$\chi = \frac{1}{\hbar}\Big[(E_{1e} - E_{0e}) - (E_{1g} - E_{0g})\Big]. \tag{4.11}$$

These three numerically computed quantities are also plotted in Fig. 4.3. In addition, the dispersive shift calculated from the perturbative approach in App. B is also plotted in Figs.

9 Note that experimentally, we only have control over the time average of the external flux $\overline{\varphi_{\text{ext}}}$, rather than the instantaneous flux φ_{ext}. Hereafter, we only discriminate between the two when the meaning is ambiguous.

4.3e–f [Zhu et al. 2013].

The parameters in Tab. 4.1 are found by fitting these simulated quantities to those measured experimentally. The readout capacitance C_R is predicted independently using a commercial high-frequency electromagnetic solver (Ansys HFSS), a finite-element electromagnetic modeling program. The chief discriminating factor between device A1 and device A2 was the qubit-readout coupling strength. The turns ratio between the shared inductance and the readout unshared inductance was $L_s/L_r \approx 0.29$ for device A1, while $L_s/L_r \approx 0.15$ for device A2. Moreover, the value of E_J was roughly 50% higher for device A2 than device A1, resulting in a significantly lower $g \to e$ transition frequency at $\varphi_{ext} = \pi$.

Theoretical and experimental results in Fig. 4.3 agree well, with the exception of two features. First, the location in external flux of the singularity in χ for device A1 differs between the model and measurements. We attribute this to the $e \to h$ qubit transition crossing the $0 \to 1$ readout transition, which involves the $|0h\rangle$ state, whose transition frequency is ~ 12 GHz from the ground state. Our approximation of the Josephson junction array composing the unshared superinductance of the qubit breaks down at these frequencies due to the fundamental mode of the array occurring at ~ 11 GHz [Masluk et al. 2012, Ferguson et al. 2013, G. Viola and Catelani 2015]. Second, perturbation theory consistently overestimates the dispersive shift in the vicinity of avoided crossings for both device A1 and (to a lesser extent) device A2. This is most apparent at $\varphi_{ext} = \pi$ for device A1, at which point $\chi/2\pi$ is calculated to be 75 MHz using perturbation theory and 57 MHz using numerical diagonalization. The error in the perturbative calculation stems from the $e \to f$ qubit transition becoming nearly resonant with the $0 \to 1$ readout transition.

5

HAMILTONIAN VERIFICATION BY SPECTROSCOPY

5.1 Circuit Hamiltonians: theory vs. experiment

In Chs. 2–4, our discussion of superconducting qubit design has been based entirely on theoretical analysis of *static Hamiltonians*. The sole exception was the data shown in Fig. 4.3, which served to illustrate that our theoretical predictions of energy levels are in extremely close agreement with their experimental counterparts. Of course, the task of designing a protected physical qubit requires much more than static theoretical analysis—it requires experimental measurements of both transition frequencies and coherence times, in addition to a theoretical model of these coherence times—in order to transcend the realm of science fiction. In this chapter, and later in Ch. 8, we change gears and present methods and results for the dispersive measurement of transition frequencies in a few different circuits. In Ch. 6 and Ch. 7, we address the experimental measurement and theoretical prediction of coherence times, respectively.

The primary technique for these measurements is microwave spectroscopy, either using a single tone or multiple tones and a heterodyne interferometer. See Secs. 5.2 and 5.3.2 for the single-tone multiplexed spectroscopy of antenna resonators in a waveguide and the two-tone spectroscopy of the double fluxonium circuit, respectively. For a proposal to use additional tones for the readout of the $\cos 2\varphi$ qubit, on the other hand, see Ch. 8. In this scheme, generated microwaves are attenuated and filtered before being impinged on a physical device in a dilution refrigerator, at which point they excite discrete energy levels with a high degree of frequency resolution. Measurements of the response of the system to these microwaves yield the transition frequencies, which we have seen may be compared to those computed using numerical diagonalization.

Although it is obviously true that these measurements must be made in order to provide evidence that a given circuit has been physically implemented, there are two less obvious reasons for performing them. First, they enable us to explore the physical parameter space that is experimentally accessible to circuits (e.g. see Tab. 1.1 and Fig. 1.2). Second, they can be used to probe the limitations of the lumped element model or the effective Hamiltonian. We demonstrate this second point in Sec. 5.3 using the double fluxonium spectroscopy. As we will see, this circuit depends on two external fluxes, and our initial simple model, which assumed these offsets to be equal, was shown to be invalid in light of the measurements. In any case, these two peripheral but important reasons for carrying out careful spectroscopic measurements help ground our circuit designs in reality.

Before proceeding to a discussion of the dispersive measurement scheme used for superconducting qubits, we offer a few comments. Across the various types of qubits, coherence times have been limited to $T_2 \sim 100\,\mu s$, which corresponds to a decoherence rate of $\Gamma_2 = 1/T_2 \sim 10\,\text{kHz}$ [for example, Z. Wang et al. 2019]. On the other hand, their $g \to e$ transition frequencies are typically around 5 GHz, which means that the transition linewidth is smaller than the frequency by a factor of $\sim 10^6$. This difference in scale makes it difficult to experimentally probe the coherence properties using spectroscopic techniques, and indeed time-domain measurements are more suitable (see Ch. 6). Similarly, although transition frequency measurements yield the energy levels of a given circuit, they cannot completely determine the Hamiltonian without measurements of the matrix elements, as we saw in Sec. 4.1. Therefore, we regard microwave spectroscopy as playing an important but limited role in designing a protected qubit.

5.2 Dispersive measurement scheme

5.2.1 Readout resonator

We begin by reviewing the standard dispersive readout scheme for superconducting qubits [Blais et al. 2004, Wallraff et al. 2004]. The central idea is to measure the state of the qubit indirectly using an ancillary readout mode in the system. This mode is designed to be highly harmonic in order to accommodate many photons and hence enable rapid measurement. All experimental results presented in Chs. 4–6 use electric dipole antennas, mounted in rectangular waveguides, as readout resonators. For the data in Ch. 8 on the experimental implementation of the $\cos 2\varphi$ qubit, a copper microwave cavity is used both as a sample holder and as a readout resonator.

Being almost-harmonic oscillators, readout resonators are determined by two parameters: their resonant frequency $\omega_0/2\pi$ and their full width at half maximum (FWHM) linewidth $\kappa/2\pi$.[1] This linewidth captures both internal losses in the resonator as well as its coupling to external probes. Usually, the readout is designed so that the coupling is much stronger than the internal loss to minimize the amount of measurement signal dissipated, but much weaker than the resonant frequency itself, i.e. $\kappa \ll \omega_0$.

The readout resonator also couples to the measured subsystem, which is often a superconducting qubit with eigenstates $|g\rangle$ and $|e\rangle$. In Eq. 4.11, we saw that the dispersive shift χ characterizes the frequency shift of the $0 \to 1$ transition frequency of the readout resonator due to the qubit being in $|e\rangle$ rather than $|g\rangle$. The qubit readout signal-to-noise ratio is maximized when $\chi \approx \kappa$ [Hatridge et al. 2013]. Since large values of χ correspond to strong hybridization between the qubit and readout, in which case the qubit inherits some loss of the readout due to the Purcell effect, we require small χ. Note that a favorable signal-to-noise ratio then demands small κ, in agreement with $\kappa \ll \omega_0$ above.

5.2.2 Example: Multiplexed readout in a rectangular waveguide

We now provide a basic description of the experimental setup used for three out of the four experiments presented in this thesis. These are: measurements of the fluxonium dispersive Hamiltonian (see Fig. 4.3), simultaneous monitoring of fluxonium qubits (see here and

1 The characteristic impedance Z_0 of the resonator is another parameter, which this discussion neglects. For distributed microwave resonators, these impedances are on the order of 100Ω.

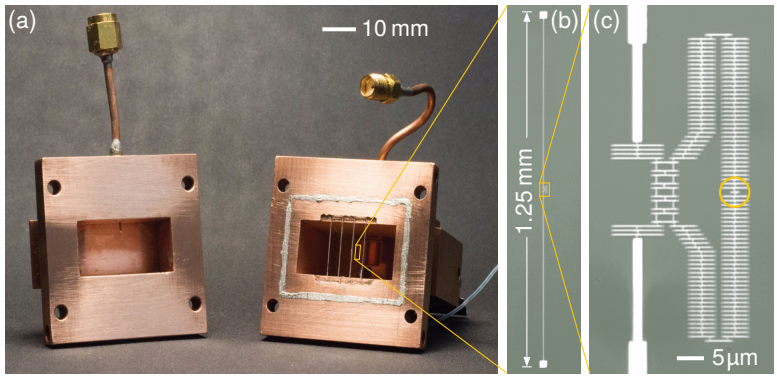

Figure 5.1 Dispersive measurement of fluxonium artificial atoms in a rectangular waveguide operated in a reflection configuration (see App. E). (a) Image of the copper rectangular waveguide, showing the reflection and impedance-matched transmission terminations on the left and right, respectively. An additional input pin on the left is used to inject sub-cutoff microwave tones. Superconducting wire wound around the waveguide permits external flux biasing. (b) Optical image of the electric dipole antenna used as a readout resonator in device S1. (c) Optical image of the fluxonium qubit in device S1, with the small Josephson junction circled.

Ch. 6) [Kou et al. 2018], and measurements of the double fluxonium circuit (see Sec. 5.3 and Ch. 6).[2] In these cases, the readout resonator was implemented as an electric dipole antenna coupled to the system via a shared inductance and was measured in a rectangular waveguide sample holder. The Josephson junctions were fabricated from $Al/AlO_x/Al$ using the bridge-free double-angle evaporation technique [Lecocq et al. 2011] on sapphire wafers.

A WR-102 waveguide, with transverse inner dimensions $1.020\,\text{in.} \times 0.510\,\text{in.}$, served as a low-loss wide-bandwidth electromagnetic environment for frequency multiplexed readout as shown in Fig. 5.1a. Note that related work has mostly focused on cross-talk between qubits on a shared substrate [McDermott et al. 2005, Chen et al. 2012, Schmitt et al. 2014] as well as quantum simulation [van Loo et al. 2013]. The waveguide had an insertion loss of $-0.3\,\text{dB}$ over a band of $6–8\,\text{GHz}$, enabling direct microwave stimulation of the electric dipole antenna readout resonators. The waveguide was operated in a reflection configuration and featured an additional coaxial pin in close proximity to the samples, which was used for microwave drives far below the passband, in addition to a superconducting magnetic field coil for biasing the external flux. See App. E for additional design details.

The waveguide sample holder was thermally anchored to the mixing chamber of a dilution refrigerator with a base temperature of $\sim 16\,\text{mK}$. Magnetic isolation from its environment was achieved using an aluminum shield coated with infrared-absorbing material to protect against high-frequency radiation. A high-permeability cryoperm shield enclosing the aluminum shield further screened stray magnetic fields [Geerlings 2013]. Input microwave signals were channeled into the waveguide through 63 dB of total attenuation as well as infrared-frequency filters [Geerlings 2013, Rigetti et al. 2012]. Output signals were

2 The fourth experiment, involving the $\cos 2\varphi$ qubit, uses a slightly different setup as explained in Ch. 8.

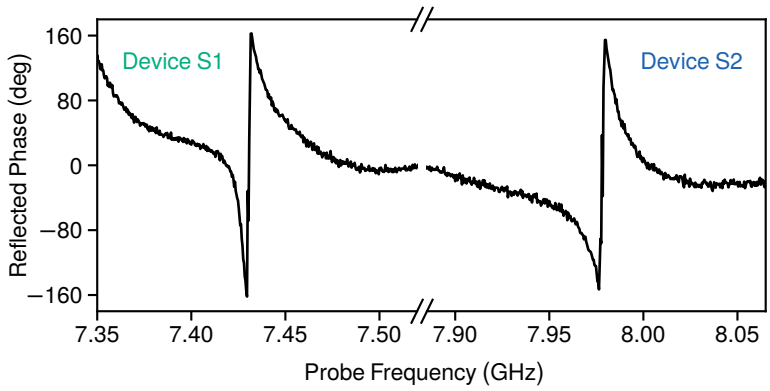

Figure 5.2 Reflection single-tone spectroscopy trace within the 6–8 GHz passband of the waveguide. The probe tone is injected into the waveguide through the impedance-matched coupler, reflected off the waveguide termination, and output through the same coupler. Two resonances are shown as nearly-360° phase rolls, corresponding to devices S1 and S2.

	Device S1	Device S2
$\omega_R/2\pi$ (GHz)	7.430	7.979
L_r (nH)	22	20
L_s (nH)	8.35	8.35
E_C/h (GHz)	3.31	3.14
E_L/h (GHz)	0.38	0.39
E_J/h (GHz)	9.08	8.76

Table 5.1 Circuit parameters for the two fluxonium devices S1 and S2 measured simultaneously in a rectangular waveguide—see Figs. 5.1 and 5.2 for measurements, and Sec. 4.3 for variable definitions.

passed through two isolators and then amplified using a high electron mobility transistor and a commercial microwave amplifier at 300 K.

For the simultaneous measurement of quantum jumps of fluxonium qubits, multiple samples were mounted in the same waveguide, as can be seen in Fig. 5.1a. The antennas were *LC* oscillators with inductances provided by Josephson junctions and capacitances by the long metal electrodes, as modeled in Sec. 4.3 and shown in Fig. 5.1b. Additionally, dc-SQUIDs served as tunable shared inductances to adjust the coupling of the antennas to the fluxonium qubits, which were composed of an array of large junctions in series with a single small junction—see Fig. 5.1c.[3] The fit parameters for the two devices studied in depth are listed in Tab. 5.1.[4] Although the two devices had difference antenna frequencies, the inductances shared with the qubits were nominally equal. The phase of the signal

3 These experiments were conducted at $\varphi_{ext} \lesssim \pi$ in both fluxonium devices, which corresponds to $\varphi_{ext} \lesssim 0.02\pi$ through the coupling SQUIDs, which we observed to be too small to change the frequencies of the antennas.

4 These are different samples than those referenced in Ch. 4, but the experimental setup is identical.

reflected from the waveguide is shown in Fig. 5.2 for the two antennas. We observed resonances associated with the readout antennas for device S1 and device S2, which correpond to linewidths of $\kappa/2\pi = 10\,\text{MHz}$ and 14 MHz, respectively.

We used two-tone spectroscopy to measure the qubit $g \to e$ transition frequency. This involved sending a $\sim 100\,\mu\text{s}$ saturation pulse at a variable qubit frequency followed by a $\sim 30\,\mu\text{s}$ readout pulse at the fixed $0 \to 1$ transition frequency. Our room temperature heterodyne interferometry setup independently mixed the outgoing readout pulse as well as a reference readout pulse with local oscillator signals (at a frequency detuned from the readout by 50 MHz) and then digitized and analyzed the 50 MHz components. Finally, the dispersive shift χ was measured by applying a π-rotation pulse at the qubit $g \to e$ transition frequency and then performing pulsed single-tone spectroscopy of the $0 \to 1$ readout transition with the interferometer. This was compared to the result from the same procedure with an off-resonant π-pulse to determine χ.

5.3 Example: Double fluxonium artificial molecule spectroscopy

In this section, we report an experiment in which we built an artificial molecule whose magnetic moment could be tuned via an applied external flux [Kou et al. 2017]. This was motivated by the question of whether coupled superconducting circuits can be engineered so that their low-energy degrees of freedom are delocalized. Previous work on coupled superconducting circuits [Izmalkov et al. 2004, Majer et al. 2005, 2007, Yoshihara et al. 2010, Chen et al. 2014] had focused on the regime where the ground state configuration of the coupled system remains essentially localized within individual artificial atoms. Artificial molecules, on the other hand, have degrees of freedom that are delocalized between constituent artificial atoms, in analogy with the electronic motion that is delocalized between several nuclei in natural molecules. Here, the experimentalist is able to tailor the type and strength of coupling between individual artificial atoms. In particular, by cleverly choosing the coupling between constituent atoms, the experimentalist can make the states of an artificial molecule sensitive to different components of external fields. As an example, we can consider molecules with magnetic dipole moments versus molecules with only magnetic quadrupole moments. Magnetic dipoles are sensitive to uniform magnetic fields while magnetic quadrupoles are only sensitive to magnetic field gradients. In natural molecules, however, the order of the magnetic moment cannot easily be changed.

The *double fluxonium artificial molecule* is composed of two fluxonium qubits strongly coupled via a shared inductance. At low applied external flux, the ground state $|g\rangle$ is a separable state comprising persistent currents flowing in the same direction while the excited state $|e\rangle$ is an odd superposition of persistent currents flowing in opposite directions. The $\{|g\rangle, |e\rangle\}$ manifold is predominantly sensitive to common-mode flux noise that affects both atoms simultaneously. As the applied external flux is increased, $|g\rangle$ changes character and becomes the even superposition of persistent currents flowing in opposite directions while $|e\rangle$ essentially retains its symmetry. An energy gap of ~ 10 times larger than the ground-excited state transition energy in a single fluxonium qubit at its external flux sweet spot, determined by the substantial shared superinductance, decouples external-flux-dependent states from the external-flux-independent states in the $\{|g\rangle, |e\rangle\}$ manifold. While this $\{|g\rangle, |e\rangle\}$ manifold has become insensitive to common-mode flux noise, it remains sensitive to differential-mode flux noise. Previous experiments have addressed the common-mode/differential-mode flux noise dichotomy but only near the flux noise

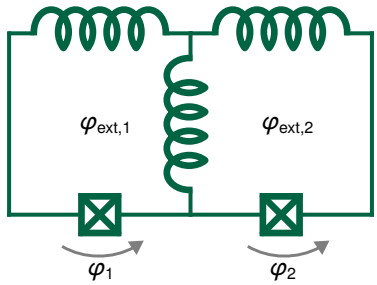

Figure 5.3 Lumped element circuit of the double fluxonium molecule. Two conventional fluxonium qubits, threaded by external fluxes $\varphi_{\text{ext},1}$ and $\varphi_{\text{ext},2}$, are coupled by a shared inductance equal in magnitude to their unshared inductances. All three superinductances represent Josephson junction arrays and each have inductive energy E_{L}, while the two small Josephson junctions have tunneling energy E_{J} and charging energy E_{C}.

sweet spot [Yoshihara et al. 2010, Gustavsson et al. 2011, Bell et al. 2014]. Here, we perform spectroscopy on the fluxonium-based molecule and observe transitions between the ground state and excited states over multiple quanta of applied external flux. We investigate decoherence mechanisms in the device and conclude that the coherence of the $g \rightarrow e$ transition is limited by local flux noise.

5.3.1 Double fluxonium circuit

Our system is composed of two fluxonium atoms coupled via a shared inductance as shown in Fig. 5.3. The artificial molecule obeys the Hamiltonian:

$$\begin{aligned} H = {} & 4E_{\text{C}}(N_1^2 + N_2^2) + \tfrac{1}{3}E_{\text{L}}(\varphi_1^2 + \varphi_2^2 + \varphi_1\varphi_2) \\ & - E_{\text{J}}\cos(\varphi_1 - \varphi_{\text{ext},1}) - E_{\text{J}}\cos(\varphi_2 - \varphi_{\text{ext},2}), \end{aligned} \tag{5.1}$$

where E_{C} and E_{J} correspond to the Josephson junctions, whose parameters are taken to be identical. The phase drops and conjugate Cooper pair numbers are φ_i and N_i, respectively, with i indexing the junctions. The three superinductances in the circuit are nominally equal, with energy E_{L}. Finally, the external magnetic fluxes are $\varphi_{\text{ext},1}$ and $\varphi_{\text{ext},2}$. The $\varphi_1 \cdot \varphi_2$ term in Eq. 5.1 reflects the inductive coupling in the circuit and corresponds to its "molecular" aspect. This coupling term has a positive sign and favors opposite phase differences across the two Josephson junctions. The two fluxonium atoms are strongly coupled; the strength of the coupling term in the artificial molecule is equal to the inductive energy $E_{\text{L}}/h \sim 1\,\text{GHz}$ of each individual fluxonium atom.

With the help of a gauge transformation (in this case, a shift of the phases φ_i to $\varphi_i + \varphi_{\text{ext},i}$), we can rewrite Eq. 5.1 as:

$$H = 4E_C(N_1^2 + N_2^2) + \tfrac{1}{4}E_L\left[(\varphi_1 + \varphi_2 + \varphi_{cm})^2 + \tfrac{1}{3}(\varphi_1 - \varphi_2 + \varphi_{dm})^2\right] - 2E_J \cos\left(\frac{\varphi_1 + \varphi_2}{2}\right)\cos\left(\frac{\varphi_1 - \varphi_2}{2}\right), \tag{5.2}$$

where we have introduced the common-mode and differential-mode reduced external fluxes, $\varphi_{cm} = \varphi_{ext,1} + \varphi_{ext,2}$ and $\varphi_{dm} = \varphi_{ext,1} - \varphi_{ext,2}$. This form of the Hamiltonian illustrates the sensitivity of the molecule to both modes of magnetic field fluctuations. If the spatial field variation is small on the scale of the device then φ_{cm} and φ_{dm} are proportional to the value of the magnetic field and its gradient at the position of the device, respectively. Therefore, we define the artificial molecule to be "dipolar" when it is sensitive to both φ_{cm} and φ_{dm} and "quadrupolar" when it is only sensitive to the differential flux φ_{dm}.

The artificial molecule is operated in the two regimes by changing an applied external magnetic flux φ_{ext}, which sets the temporal average of the common-mode flux $\frac{1}{2}\overline{\varphi_{cm}} = \varphi_{ext}$. To a much weaker extent, it also sets the temporal average of the differential-mode flux $\frac{1}{2}\overline{\varphi_{dm}} = \delta_A\varphi_{ext}$, where $\delta_A \ll 1$. In the first regime, $0 \leq \varphi_{ext} \lesssim 0.7\pi$, the molecule essentially behaves like a magnetic dipole: equal phases drop across both junctions in the molecule. As shown in Fig. 5.4, the potential has one deep well centered near $(\varphi_1, \varphi_2) = (0, 0)$ and the ground state is localized in this well. This ground state is simply the product of the single fluxonium-atom ground states and corresponds to currents flowing in the same direction in both loops. The direction of current flow is determined by the direction of the applied external flux. It helps to think of the persistent current chirality as the spin of the fluxonium atom. The excited state, then, corresponds to the singlet spin state while the ground state corresponds to the $m_s = 1$ triplet spin state. To transition from $|g\rangle$ to $|e\rangle$, the persistent current in one of the loops needs to change direction, which is analogous to flipping a spin. The transition frequency here is then determined by the applied external flux and is, hence, sensitive to noise in the common-mode flux.

As the external flux is increased, the two fluxonium atoms start to behave like a molecule with a quadrupole moment but no dipole moment. In this regime, the potential landscape of the molecule has two degenerate potential wells as shown in Fig. 5.4. The degeneracy of the wells comes from the symmetry between φ_1 and φ_2 in the Hamiltonian in Eq. 5.1. These two wells correspond to the two possible configurations of persistent currents flowing in opposite directions in each loop. The energy splitting between $|g\rangle$ and $|e\rangle$ is determined by the tunneling between the two lowest degenerate potential wells.

The ground-excited state manifold of the molecule near $\varphi_{ext} = \pi$ is formed from superpositions of the currents flowing in opposite directions in the two fluxonium atoms as shown in Fig. 5.4. The $|g\rangle$ state thus corresponds to the $m_s = 0$ triplet spin state and the $|e\rangle$ state corresponds to the singlet spin state. This ground-excited state manifold is gradiometric; the transition is insensitive to fluctuations in external flux that are uniform across both loops. We note that in the limit of perfect symmetry between the two fluxonium atoms, this ground-excited state manifold is also insensitive to first order to fluctuations in external flux that occur only in individual loops.

As a consequence of this insensitivity, f_{ge} is nearly constant over a large range in φ_{ext}, which should protect this transition from common-mode flux noise. Another way to see this is to consider that both junctions must undergo a quantum phase slip in order to tunnel between the two lowest potential wells. The persistent currents in both fluxonium atoms must flip direction together. A double phase slip is a second-order process where the

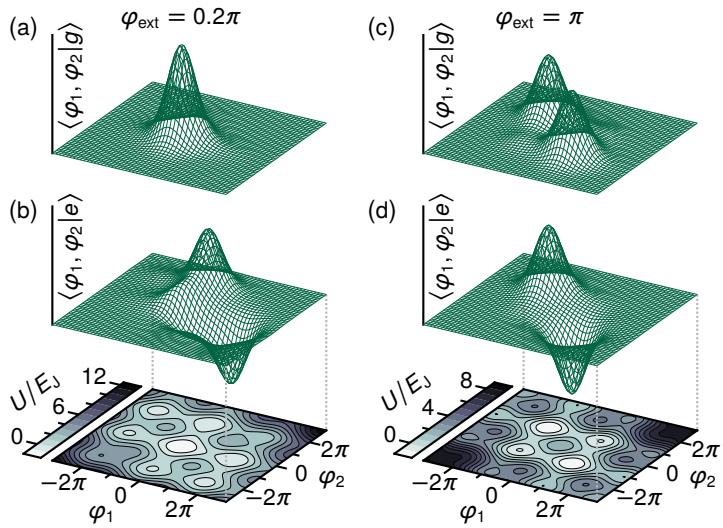

Figure 5.4 Phase wavefunctions of the ground and first excited states of the fluxonium artificial molecule. Contour maps of the potential energy landscape are shown on the bottom-most layer. (a–b) Wavefunctions at $\varphi_{\text{ext}} = 0.2\pi$, i.e. in the rough vicinity of zero external flux. (c–d) Wavefunctions at $\varphi_{\text{ext}} = \pi$, i.e. at half flux. From left to right, the ground state wavefunction undergoes a transition from being single-peaked to doubly-peaked.

molecule has to make a virtual transition through a higher-energy state with the currents circulating in the same direction in the two fluxonium loops. The energy splitting is then on the order of E_S^2/E_Δ, where $E_S \sim (E_J^3 E_C)^{1/4} e^{-\sqrt{8E_J/E_C}}$ is the energy of a single phase slip in an individual fluxonium atom [Matveev et al. 2002, Meier et al. 2015] and $E_\Delta \sim \frac{2}{3}\pi^2 E_L$ is the energy difference between the states with counter-circulating currents in the two loops and the states with currents flowing in the same direction in the two loops. We note here that the decoherence rate associated with an unwanted phase slip will be suppressed by a factor of E_S/E_Δ when compared with the single fluxonium atom.

5.3.2 Two-tone spectroscopy

The artificial molecule device (device M1) is shown in Fig. 5.5a. Each fluxonium atom consisted of a small Josephson junction, which provided nonlinearity, in series with an array of 40 larger junctions. The array of 40 junctions had an inductance of 140 nH and served as the superinductance for each atom.[5] The fluxonium atoms were connected in parallel with an additional array of 40 junctions, which provided inductive coupling between the atoms. The artificial molecule was inductively coupled to a readout antenna via shared Josephson junctions, which had an inductance of 3.0 nH.

The inductively-loaded readout antenna was an *LC* oscillator where the inductance was provided by 14 Josephson junctions and the capacitance was provided by the long

5 We expect the resonant frequency of the array mode to be ∼12.5 GHz, which is above the transition frequencies of interest for the molecule. We can then treat the array of junctions simply as a large inductance.

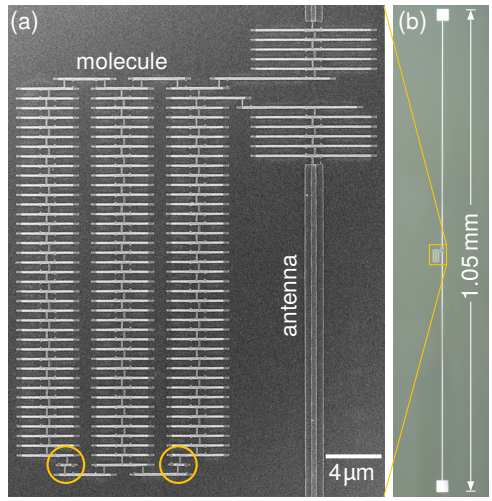

Figure 5.5 Physical device for the double fluxonium molecule. (a) Scanning electron micrograph of device M1, showing its coupling via shared Josephson junctions to an antenna readout resonator on the right, as well as the two small Josephson junctions in yellow circles. (b) Optical image of the full antenna.

					$\varphi_{\text{ext}} = \pi$			
Device	E_C/h (GHz)	E_L/h (GHz)	E_J/h (GHz)	δ_A	f_{ge} (MHz)	T_1 (μs)	T_{2R} (μs)	T_{2E} (μs)
M1	3.41	1.15	9.39	0.0028	105	60	0.45	1.6
M2	3.38	1.07	9.46	0.0035	110	50	1.25	5.4
M3	3.25	1.18	9.83	0.014	197	300	0.31	1.2

Table 5.2 Parameters for three different artificial molecule devices: M1, M2, and M3. The energy scales E_C, E_L, and E_J characterize the circuit elements in Fig. 5.3, while δ_A is the external flux asymmetry parameter. The parameters measured at $\varphi_{\text{ext}} = \pi$ corresponding to the $g \to e$ transition include the transition frequency f_{ge}, the relaxation time T_1, the Ramsey coherence time T_{2R}, and the spin-echo decoherence time T_{2E}.

metal electrodes as shown in Fig. 5.5b. The antenna had a resonant frequency of $\omega_R/2\pi = 7.875$ GHz and a FWHM linewidth of $\kappa/2\pi = 6$ MHz. We observed transitions between $|g\rangle$ and the first three excited states using the dispersive readout scheme outlined in the preceding section. The resulting data is shown in open circles in Fig. 5.6 and the results from numerical diagonalization are shown in solid lines.

At the critical point (indicated by the start of the hatched area in Fig. 5.6) at $\varphi_{\text{ext}} \approx 0.7\pi$, we observed the transition frequency from $|g\rangle$ to $|f\rangle$ start to increase as a function of flux. For $\varphi_{\text{ext}} > 0.7\pi$, the $g \to e$ transition frequency f_{ge} became very small. At its lowest point, f_{ge} reached 105 MHz at $\varphi_{\text{ext}} = \pi$. In contrast with other flux-based qubits such as the flux

qubit [van der Wal et al. 2000] and the fluxonium [Manucharyan et al. 2009], f_{ge} was also remarkably flat as a function of φ_{ext} near $\varphi_{\text{ext}} = \pi$, as shown in Fig. 5.6. At $\varphi_{\text{ext}} \approx 0.7\pi$, the potential landscape of the system transitions from having a single lowest potential well to having two degenerate potential wells. The former ground state of the molecule—currents circulating in the same direction in both loops—becomes the $|f\rangle$ state. For $\varphi_{\text{ext}} > 0.7\pi$, the $|g\rangle$ and $|e\rangle$ states are superpositions of currents flowing in opposite directions in the two loops as shown in Fig. 5.4. The energy splitting between $|g\rangle$ and $|e\rangle$ in this regime is $\sim E_{\text{S}}^2/E_{\Delta}$, which results in the very small f_{ge} value.

We also note that the artificial molecule had different $g \to e$ transition frequencies at external flux points separated by at least one flux quantum, which is to be expected in a device with unequal loop areas. The $g \to e$ transition frequency at $\varphi_{\text{ext}} = 3\pi$ was 40 MHz higher than that at $\varphi_{\text{ext}} = \pi$ in device M1.

Any difference in the flux through the two fluxonium loops results in $\frac{1}{2}\overline{\varphi_{\text{dm}}} = \delta_{\mathcal{A}}\varphi_{\text{ext}} \neq 0$ in the Hamiltonian in Eq. 5.2. The two fluxonium atoms then have different potential energies at each flux point. As the applied external flux is increased, this difference in potential landscapes compounds. The potential wells corresponding to currents flowing in opposite directions in the two loops are then no longer nearly degenerate, resulting in the observed larger energy splitting at $\varphi_{\text{ext}} = 3\pi$.

We compare the measured resonant frequencies (open circles in Fig. 5.6) with the theoretical prediction for these transition frequencies (solid lines in Fig. 5.6) obtained from numerical diagonalization of the Hamiltonian in Eq. 5.2 using the techniques in Ch. 4. The only asymmetry we have considered here is the nonzero $\delta_{\mathcal{A}}$ parameter. To fit the data, we constrain the product $E_{\text{J}} \cdot E_{\text{C}}$ based on fabrication parameters and effectively fit the full spectrum using only three fit parameters: $\delta_{\mathcal{A}}$, $E_{\text{J}}/E_{\text{C}}$, and E_{L}. We find excellent agreement between the model and the data over three decades in transition frequencies (from 11.2 GHz at $\varphi_{\text{ext}} = 0$ to 105 MHz at $\varphi_{\text{ext}} = \pi$). This proves the principle of planning the behavior of a complex circuit, such as that in Fig. 5.5a, from a reduced set of engineerable parameters.

We further tested the validity of our approach by measuring multiple devices. The fit parameters for the measured devices are shown in Tab. 5.2. The spectroscopy of device M3, which intentionally had the largest asymmetry between the two fluxonium loops, is shown in Fig. 5.6. For this device, the fit parameter $\delta_{\mathcal{A}}$ is consistent with the asymmetry inferred from optical images. We note again that the agreement between the theoretical fit and the measured data here is excellent. The effects of asymmetry were much more pronounced in this device. The lowest transition frequency $f_{ge} = 197$ MHz no longer occurred at $\varphi_{\text{ext}} = \pi$, but rather at $\varphi_{\text{ext}} = 0.86\pi$. In addition, the transition frequency at $\varphi_{\text{ext}} = 3\pi$ was 354 MHz greater than that at $\varphi_{\text{ext}} = \pi$.

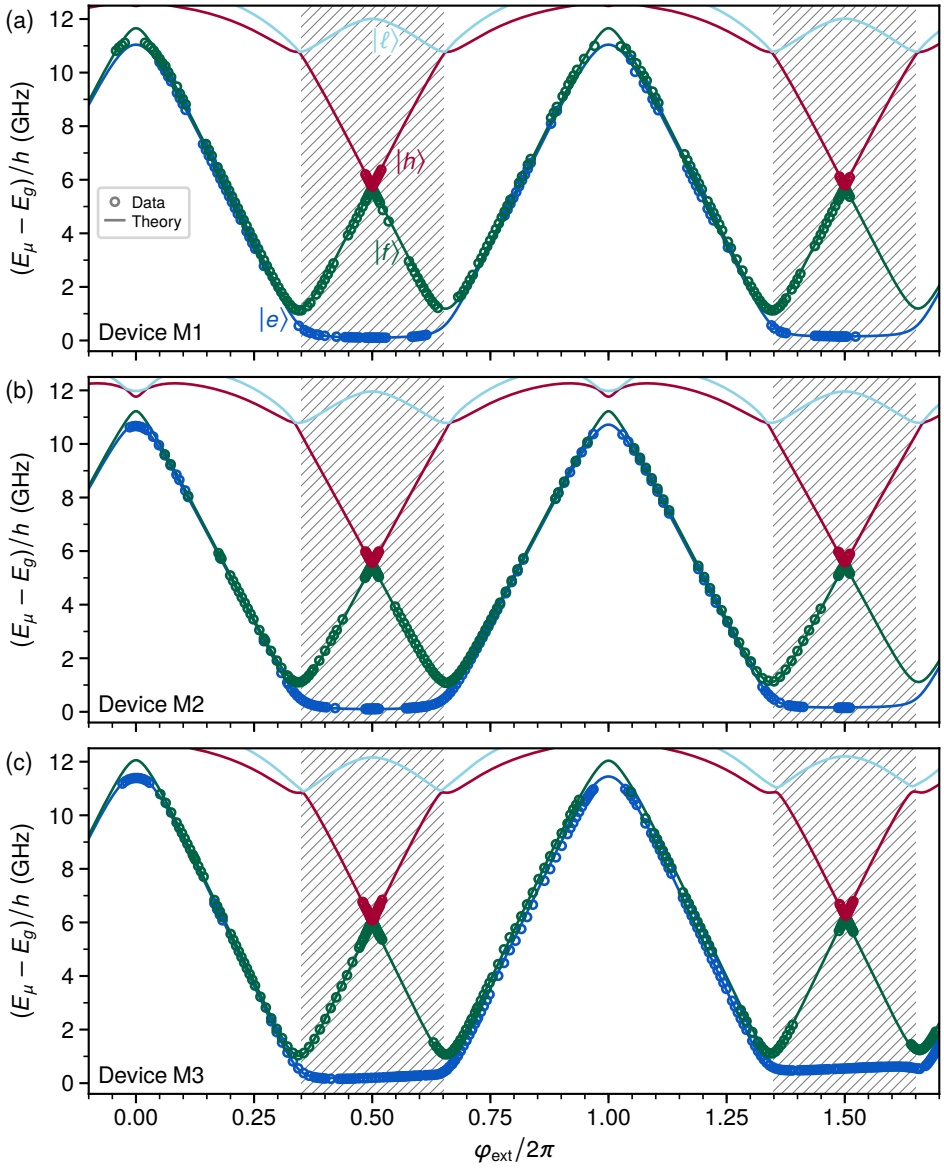

Figure 5.6 Energy spectrum of the double fluxonium molecule: theory vs. experiment as a function of external flux. Circles indicate values measured by two-tone spectroscopy and lines indicate theoretical fits obtained from numerical diagonalization. (a) Results for device M1. (b) Results for device M2. (c) Results for device M3. Devices M1 and M2 have suppressed asymmetry with respect to device M3, as can be seen from the shapes of the $g \to e$ transition frequency at half-integer values of $\varphi_{\text{ext}}/2\pi$.

6

EXPERIMENTAL NOISE CHARACTERIZATION

The theoretical analysis and experimental measurement of the *static properties* of superconducting circuit Hamiltonians were presented in Chs. 2–4 and Ch. 5, respectively, and we now turn our attention to the *dynamic properties*. In particular, we discuss in this chapter the experimental characterization of various noise sources affecting superconducting qubits. Such characterizations are a necessary ingredient both for designing a protected qubit, so that one knows what to protect against, and for demonstrating protection. We structure this chapter by exploring the two underlying channels of decoherence—energy relaxation in Secs. 6.2 and 6.3 and pure dephasing in Secs. 6.4 and 6.5—on conceptual grounds followed by a demonstrative experimental example.

6.1 Relevant noise models for protection

Every Hamiltonian that we have mentioned up to this point, ranging from Eq. 1.1 to Eq. 5.2, has featured two types of mathematical objects in its definition: operator-valued variables like φ and real-valued parameters like φ_{ext}. Dissipation occurs when the system variables couple to fluctuating environmental variables—provided these operators can induce qubit transitions. Dephasing, on the other hand, occurs when these parameters fluctuate in time—provided the qubit energy splitting depends on these parameters.[1]

For dissipation, we recall that a general system operator $\mathcal{O}$ will couple to a noisy operator $\mathcal{E}(t)$ of the bath through an interaction Hamiltonian $H_{\text{int}}(t) = \mathcal{O}\mathcal{E}(t)$. Fluctuations in $\mathcal{E}$ couple to $\mathcal{O}$, and therefore transitions will be induced between certain eigenstates of the system. In the case of the lowest two eigenstates, this is precisely energy relaxation: a nonzero transition rate from the qubit excited state $|e\rangle$ to its ground state $|g\rangle$ enabled by fluctuations of the bath *at the qubit transition frequency*.

On the other hand, an arbitrary system parameter λ will inevitably contribute somewhat to the qubit transition frequency. More precisely, the two-level qubit Hamiltonian can be written as $H = \hbar\omega|e\rangle\langle e|$, where $\omega = \omega(\lambda)$. In this case, fluctuations of λ in time lead to fluctuations of ω, and hence some indeterminacy in the complex phase between $|g\rangle$ and $|e\rangle$ in the general wavefunction, i.e. pure dephasing. As opposed to dissipation, the energy levels fluctuate in a manner that includes contributions from all frequency

1 Of course, the parameters are ultimately quantum degrees of freedom themselves. This depiction tacitly relies on the fact that the low-frequency components of the noise are usually the most significant for dephasing, and at high frequencies near that of the qubit, these quantum operators behave like classical variables.

components of the noise (above a certain low-frequency cutoff) and is usually dominated by the *low-frequency components*.

In designing a protected qubit, we aim to have both of these effects suppressed exponentially in some adjustable property ℓ, as in Eq. 1.2. Though this framework demonstrates the essential concept, it fails to provide means for quantifying the "degree of protection," that is, the actual coherence times we can expect to measure. For this, we need (i) the characterization of the fluctuations in $\mathcal{E}$ and λ combined with (ii) the sensitivities found using Hamiltonian methods [e.g. Burkard et al. 2005, J. Koch et al. 2007]. Experimental measurements in the time domain are necessary for (i), which is the topic of this chapter, and we expand on (ii) in Sec. 7.1.1.

6.2 Relaxation estimates and matrix elements

6.2.1 Fermi's Golden Rule

As above, the interaction between the qubit Hamiltonian $H = \hbar\omega|e\rangle\langle e|$ and the bath is captured by $H_{\text{int}} = \mathcal{O}\mathcal{E}(t)$. Second-order perturbation theory, which is reviewed in App. B, yields time-dependent corrections to the joint qubit-bath eigenstates $|gr\rangle$ and $|e\bar{r}\rangle$, where $|r\rangle$ and $|\bar{r}\rangle$ describe bath eigenstates. If we sum over all bath states, these time-dependent corrections can be converted into an $e \to g$ transition rate

$$\Gamma_{e\to g} = \frac{1}{\hbar^2}|\langle g|\mathcal{O}|e\rangle|^2 S_{\mathcal{E}\mathcal{E}}[\omega_{ge}] \tag{6.1}$$

or vice versa. This is Fermi's Golden Rule and the quantity $S_{\mathcal{E}\mathcal{E}}[\omega_{ge}]$ is the noise spectral density for fluctuations in $\mathcal{E}$ (see App. A) evaluated at the qubit frequency. The two important features of this equation are: the proportionality of the transition rate to the probability of $\mathcal{O}$ mapping $|e\rangle$ to $|g\rangle$ as well as the spectral density. Roughly speaking, qubits protected from relaxation are designed to suppress the matrix element, and the spectral density is taken to be fixed. Research pursuing the inverse, hardware-based approach has been promising in combating relaxation [see, e.g. Martinis et al. 2005, Houck et al. 2008, Barends et al. 2013].

6.2.2 Role of temperature

The above expression for $\Gamma_{e\to g}$ closely corresponds to the relaxation rate $\Gamma_1 = 1/T_1$ when the thermal energy is much lower than the qubit transition energy, $k_B T \ll \hbar\omega$. For experiments mounted on base stages of dilution refrigerators, where $T \sim 20\,\text{mK}$, this correspondence gives the corresponding frequency of 417 MHz. While this is well below the transition frequency of a transmon qubit, for instance, many protected qubits [Dempster et al. 2014, Earnest et al. 2018, Lin et al. 2018], as well as flux-tunable qubits at their sweet spots [Manucharyan et al. 2009, Pop et al. 2014], are based on the principle of nearly-degenerate ground states.[2] Indeed, the parameters in Tab. 2.2 correspond to a transition frequency for the $\cos 2\varphi$ qubit of roughly 0.4 MHz (see Fig. 3.2). At such frequencies, provided that there exists a substantial gap to higher energy levels, the thermal

2 Near-degeneracy can be seen as a desirable feature because it naturally coincides with a nonlocal qubit encoding. This is the case for qubits based on Majorana fermions, for example [Aasen et al. 2016].

occupancy of $|g\rangle$ and $|e\rangle$ are both approximately 50%. Neglecting further complications, the relaxation rate is then

$$\Gamma_1 = \Gamma_{e\to g} + \Gamma_{g\to e} \approx 2\Gamma_{e\to g}$$

since $\Gamma_{g\to e} \approx \Gamma_{e\to g}$, and we refer to Ch. 7 for further details.

6.2.3 Survey of loss mechanisms

Superconducting circuits, including readout resonators in the dispersive regime, are described by Hamiltonians with four types of terms: the capacitive, inductive, and Josephson tunneling terms in Eq. 1.1 as well as those of the readout resonator. At this stage, we regard all forms of loss in the readout to be captured by its linewidth κ. The four common types of relaxation mechanisms [e.g. Pop et al. 2014] in these circuits mirror this structure. They are listed below and quantitatively addressed in Sec. 7.1.1.

Capacitive loss concerns energy leaving the system via the spatially-distributed electric fields generated by the capacitors of the circuit. It is also called dielectric loss. *Inductive loss* describes, for geometric inductances, energy leaving the system via the generated magnetic fields. Kinetic inductances may suffer from energy loss due to resistive electric currents. The superinductances in this thesis, for example, are suspected to be slightly lossy due to quasiparticle tunneling [Pop et al. 2014]. *Quasiparticle loss* describes scattering-based dissipation associated with electron-hole pairs tunneling through Josephson elements [Catelani et al. 2011]. *Purcell loss* encompasses all types of energy leaving the qubit through the readout resonator—either into the weakly coupled external probe or through internal loss in the resonator. It is also called radiative loss.

6.3 Example: Simultaneous monitoring of fluxonium qubits

For the two fluxonium qubits measured in a waveguide, whose experimental setup and dispersive readout scheme was described in Sec. 5.2.2, we performed various time-domain measurements with the aim of understanding whether their coherence properties were correlated. In particular, we measured their quantum jumps simultaneously and analyzed them to estimate the amount of noise jointly affecting the qubit transition rates. In this section, we present the overall coherence times of the qubits in Sec. 6.3.1, the simultaneously measured jump traces in Sec. 6.3.2, and the correlation analysis in Sec. 6.3.3.

6.3.1 Coherence time measurements

Measurements of the relaxation times T_1 and Ramsey decoherence times T_{2R} of the $g \to e$ transition in the two fluxonium qubits are shown in Fig. 6.1. The relaxation time measurement consisted of a Gaussian π-rotation pulse with width $\sim$50 ns on the qubit, followed by a variable-length delay up to $5T_1$ to ensure accurate fitting of the exponential, and then a square pulse of 30 µs on the readout resonator. Data acquisition only occurred for the first 5 µs of this readout pulse; the extra time served to aid reset of the qubit to its steady state. The sequence to measure the Ramsey decoherence time was the same as that for T_1, except that the initial pulse was a $\pi/2$-rotation and, after the delay, a second $\pi/2$-rotation was executed immediately before the readout pulse. These measurements were performed for device S1 and S2, whose parameters are listed in Tab. 4.1., at $\varphi_{\text{ext}} = \pi$. Note

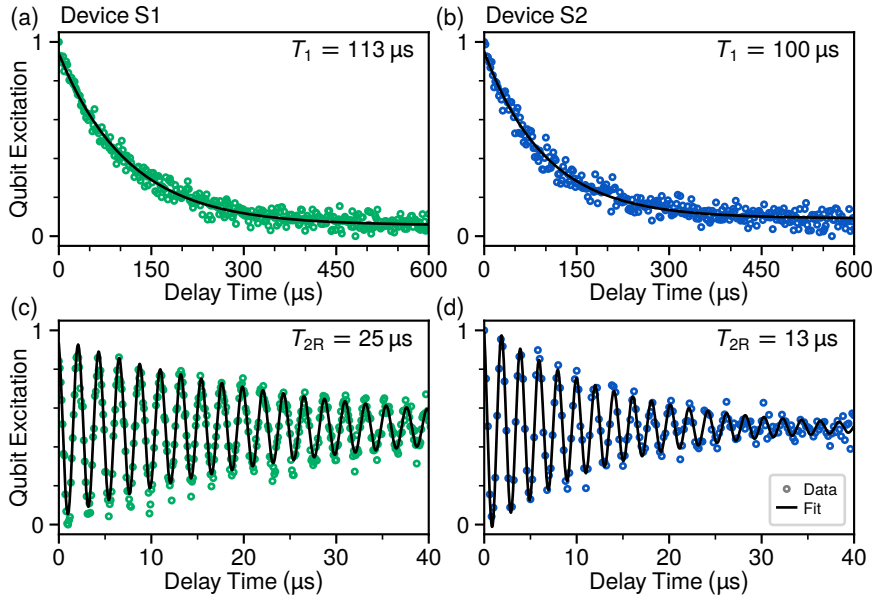

Figure 6.1 Coherence time measurements for two fluxonium artificial atoms at $\varphi_{\text{ext}} = \pi$, where these timescales are expected to be maximized. (a–b) Relaxation times T_1 measured by qubit state readout after a π-pulse and a variable delay time. (c–d) Ramsey coherence times T_{2R} measured by free-induction decay, i.e. qubit state readout after two $\pi/2$-pulses separated by a variable delay time.

that the qubit transition frequencies for devices S1 and S2 were 565 MHz and 579 MHz, respectively. Values for relaxation times exceeded 100 μs for both qubits, as shown in Fig. 6.1, while the respective Ramsey decoherence times were 25 μs and 13 μs. For a spin-echo decoherence measurement, a π-pulse is performed on the qubit at the midpoint of the Ramsey sequence delay, which serves the function of canceling out a portion of low-frequency noise (see App. C). In these samples, this sequence did not yield prolonged coherence times, indicating that the coherences of the two qubits were limited by noise characterized by time scales faster than several microseconds. One possible culprit is photon shot noise (see Sec. 6.4, Ch. 7, and App. C for additional discussion).

6.3.2 Multiplexed quantum jumps in fluxonium artificial atoms

As the results above show, these two fluxonium qubits exhibited very similar coherence properties and Hamiltonians, so it is natural to suspect that their coherence times were limited by the same mechanisms. In an attempt to pinpoint the mechanisms responsible, we probed the time dependence of the noise affecting the qubits using a trajectory approach. Dissipation is an inherently statistical effect—if we subject a qubit to repeated projective measurements of its state, we will observe a roughly telegraphic signal, where the statistics of the trace/trajectory can be translated into excitation and decay rates, or equivalently temperature and T_1. These quantum jumps can be analyzed on different time scales to expose patterns, e.g. correlations between the jump traces of two neighboring qubits.

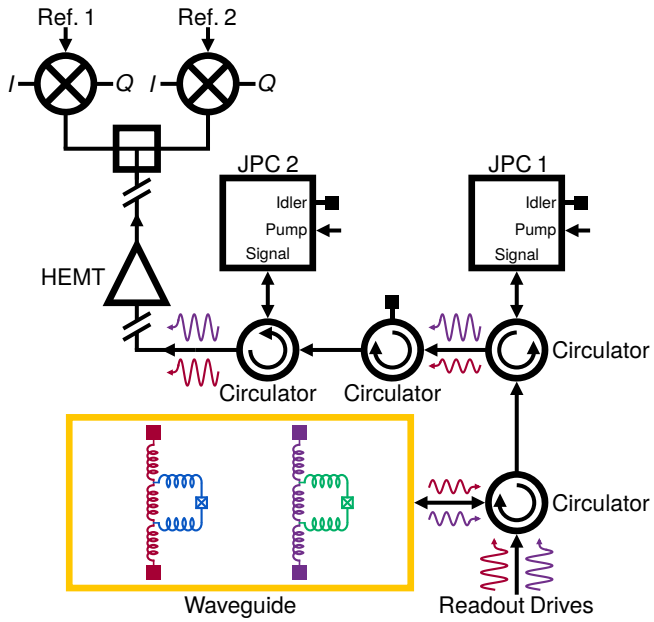

Figure 6.2 Measurement setup for simultaneous single-shot readout of quantum jumps of fluxonium qubits in a waveguide. Readout tones were reflected by the waveguide (see Fig. 5.1) and preamplified in reflection by two Josephson Parametric Converters (JPCs) in series. Each JPC was tuned to provide 20 dB of gain at the frequency of its respective readout antenna. The signals were amplified at 4 K by a High Electron-Mobility Transistor (HEMT), then demodulated and digitized at room temperature using two heterodyne interferometers.

We demonstrated simultaneous monitoring of the fluxonium qubits S1 and S2 with the following measurement setup—see Fig. 6.2. The output of the waveguide was fed into circulators, which then routed the output signals to two cascaded Josephson parametric converter (JPC) quantum-limited amplifiers[3]. The JPCs were tuned to provide a gain of 20 dB with bandwidths of 6 MHz and 5 MHz, respectively. Signals amplified in reflection by the JPCs were fed via circulators into a high electron-mobility transistor amplifier at 4 K. The amplified signals were then split at room temperature and demodulated at 50 MHz for device S1 and 25 MHz for device S2 using two heterodyne interferometer setups.

Fig. 6.3 shows the simultaneously measured in-phase I and out-of-phase Q quadratures of the reflected signals from two fluxonium qubits in equilibrium with their environment at $\varphi_{\text{ext}} \approx \pi$. [4] The optimal measurement fidelity was achieved with a readout power corresponding to $\bar{n} = 1$ photon occupation of the readout resonator. Larger photon numbers resulted in faster measurements but also saturated the output of the JPCs as well as decreased the lifetimes of the two fluxonium qubits. This last effect has also been observed in transmons [Boissonneault et al. 2008, Slichter et al. 2012]. We attained a readout fidelity

3 Alternatively, for a more favorable scaling in qubit number, one might use a large-bandwidth quantum-limited amplifier, such as the traveling-wave parametric amplifier [White et al. 2015, Macklin et al. 2015].

4 Due to slight differences in loop area, Fig. 6.3 corresponds to $\varphi_{\text{ext}} = \pi$ for device S1 and $\varphi_{\text{ext}} = 0.99\pi$ for S2.

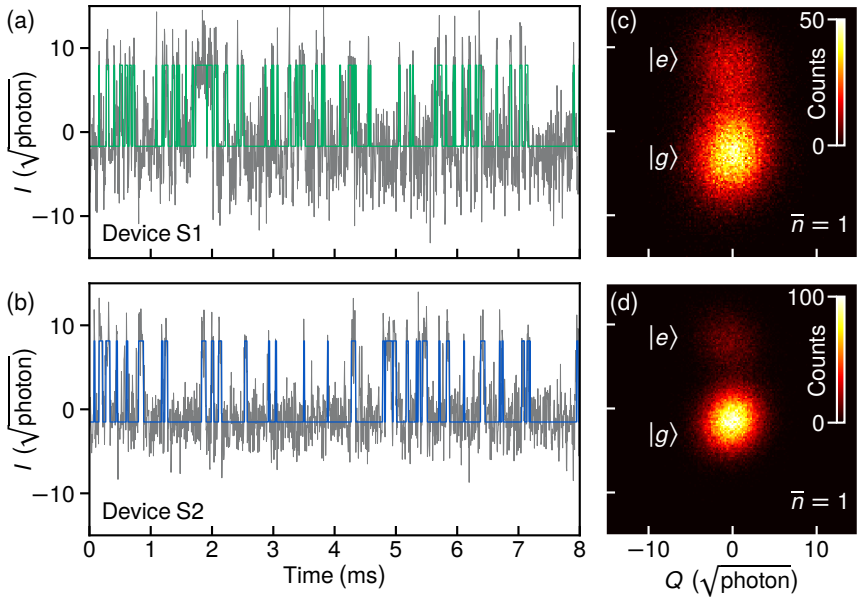

Figure 6.3 Simultaneous measurement of the I and Q quadratures of the output signal of two fluxonium qubits in equilibrium with their environment at $\varphi_{\text{ext}} = \pi$, normalized by the average readout photon number. Each count takes 5 µs of integration time and there are 80 000 counts total. (a–b) Quantum jump traces corresponding to the time evolution of the I quadrature, showing the qubits in their ground state $|g\rangle$ on the bottom level and in their excited state $|e\rangle$ in the top level. Raw data is plotted in grey and filtered data in green/blue. (c–d) Histograms of the I and Q quadratures, indicating effective temperatures of ∼20 mK and ∼25 mK for devices S1 and S2, respectively.

of 95% for each measurement with 5 µs of integration time. The total number of counts in each histogram is 80 000.

We observed the evolution of the I quadratures of the two fluxonium qubits simultaneously, as shown in grey in Fig. 6.3. An estimate of the qubit state was determined using a two-point filter, similar to that used by Vool et al. (2014). The filter declared a change in the qubit state if the quadrature value crossed a threshold set $\sigma/2$ away from the new state, where σ was one standard deviation away from the center of the peak corresponding to the new state obtained from the histogram shown in Fig. 6.3. Otherwise, the qubit was declared to remain in its previous state. The estimated qubit state is shown in green and blue for device S1 and S2 in Fig. 6.3.

6.3.3 Upper bound on quantum jump correlation coefficient

A qubit subject to frequent measurements of its energy stochastically jumps between its energy eigenstates. The characteristic timescale over which a qubit changes its state is T_1. If the relaxation channels become coupled more strongly to the qubit or decrease in quality factor, the qubit will change its state more rapidly (i.e. its T_1 will decrease). Hence, to

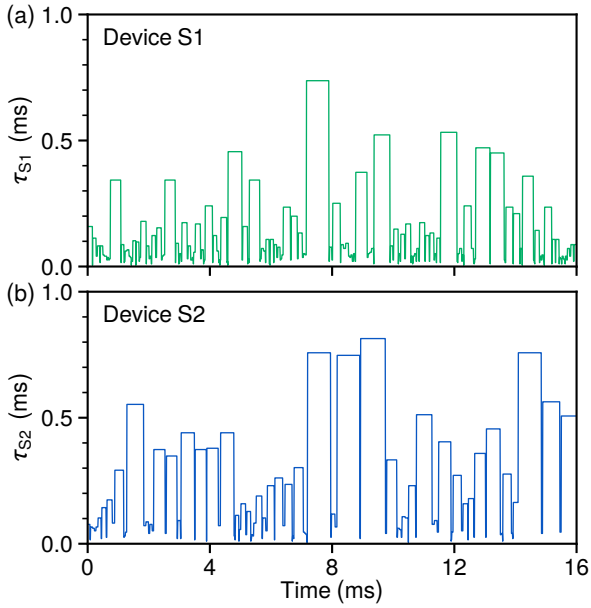

Figure 6.4 Time τ between adjacent quantum jumps, i.e. the time spent in either $|g\rangle$ or $|e\rangle$, as a function of time for two fluxonium qubits monitored simultaneously. (a) Results for device S1. (b) Results for device S2.

look for correlated relaxation channels, one should investigate the correlations between the times that the two qubits spend in either $|g\rangle$ or $|e\rangle$. Using the qubit state evolutions shown in Fig. 6.3, we extracted the total amount of time each qubit spends in a single state before a quantum jump occurs at each time step, which we denote as τ. These processed traces are shown in Fig. 6.4 for a twice larger time span.

The normalized covariance between τ_{S1} and τ_{S2} is

$$\Sigma(t, t+\delta t) = \frac{\overline{\tau_{\mathrm{S1}}(t)\tau_{\mathrm{S2}}(t+\delta t)}}{\overline{\tau_{\mathrm{S1}}}\,\overline{\tau_{\mathrm{S2}}}} - 1,$$

where $\tau_{\mathrm{S1}}(t)$ and $\tau_{\mathrm{S2}}(t)$ are the times that devices S1 and S2 spend in each state at time t, $\overline{\tau_{\mathrm{S1}}}$ and $\overline{\tau_{\mathrm{S2}}}$ are the means of each data set, and δt is the separation in time between the data taken for device S1 and the data taken for device S2. The average for Σ was taken over 2000 data sets of 20.48 ms of continuous monitoring.

For correlated τ between device S1 and device S2 at time $\delta t = 0$, we expect the covariance to decay on a time scale of the order of the mean time that the qubits spend in a state during the correlated times, and the amplitude to depend on the percentage of the total monitoring time that τ_{S1} and τ_{S2} are correlated. The covariance of the measured devices corresponds to devices with correlated τ at $\delta t = 0$ for $<0.5\%$ of the total monitoring time, and the detection threshold of our experimental setup was 0.5%. This was determined by a comparison of the covariance of the data with the covariance of simulated quantum jumps with fixed correlations, in addition to exponential fits (see Fig. 6.5 for the data and the

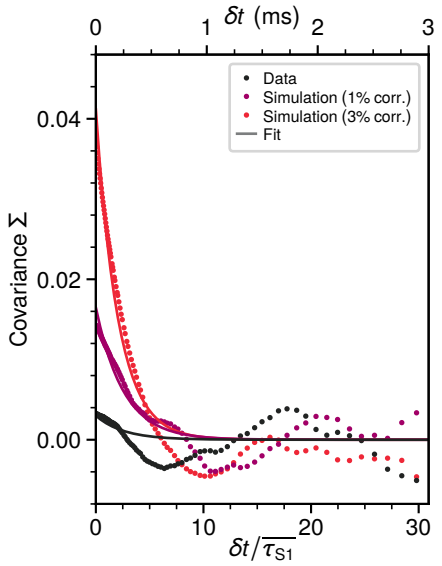

Figure 6.5 Covariance Σ among times $\tau_{S1}(t)$ and $\tau_{S2}(t+\delta t)$ spent between adjacent quantum jumps, as a function of δt. Black circles indicate measured values while purple and red circles indicate simulated values with 1% and 3% correlated τ. Lines indicate exponential fits.

simulated cases of 1% and 3% correlation). We hence conclude that up to the detection efficiency of our experiment, the relaxation of the two devices was not correlated.

6.4 Dephasing estimates and energy levels

6.4.1 Ensemble averages of phase factors

We now return to the qubit Hamiltonian $H = \hbar\omega_{ge}|e\rangle\langle e|$, where $\omega_{ge} = \omega_{ge}(\lambda)$ and $\lambda = \lambda(t)$ is a noisy parameter. Without loss of generality, we can assume that λ has zero mean. Taylor expanding about $\lambda = 0$ yields $\omega_{ge}(\lambda) = \omega_{ge}(0) + \frac{\partial\omega_{ge}}{\partial\lambda}\lambda + \ldots$, where all derivatives are evaluated. The time-evolution operator corresponding to this Hamiltonian is then

$$\mathcal{U}(t) = \exp\left(-i|e\rangle\langle e|\int_0^t \mathrm{d}t'\left[\omega_{ge}(0) + \frac{\partial\omega_{ge}}{\partial\lambda}\lambda(t') + \ldots\right]\right)$$

with respect to the reference time $t = 0$. The first factor in $\mathcal{U}(t)$ corresponds to the deterministic evolution while the second and higher describe a stochastic accumulated phase between $|g\rangle$ and $|e\rangle$. In the simplest case where this phase is Gaussian distributed, the fluctuations of λ are small, and the first-order term in the Taylor expansion does not vanish; the ensemble average of the time-dependent excited state $|e(t)\rangle$ inherits a factor

$$f_{\phi R}(t) = \exp\left(-\frac{1}{2}\left\langle\left[\frac{\partial\omega_{ge}}{\partial\lambda}\int_0^t \mathrm{d}t'\,\lambda(t')\right]^2\right\rangle\right),$$

where we have retained only the leading time-dependent term in the expansion. Under the assumption that the process is stationary, i.e. $\langle\lambda(t)\lambda(t')\rangle = \langle\lambda(t-t')\lambda(0)\rangle$, this becomes

$$f_{\phi\mathrm{R}}(t) = \exp\left[-\frac{1}{2}t^2\left(\frac{\partial\omega_{ge}}{\partial\lambda}\right)^2\int_{-\infty}^{\infty}\frac{\mathrm{d}\omega}{2\pi}S_{\lambda\lambda}[\omega]\,\mathrm{sinc}^2\,\frac{\omega t}{2}\right]. \tag{6.2}$$

Here we have introduced the noise spectral density $S_{\lambda\lambda}[\omega]$ for fluctuations of an arbitrary parameter λ, which obeys the Wiener-Khinchin theorem

$$S_{\lambda\lambda}[\omega] = \int_{-\infty}^{\infty}\mathrm{d}t\,\mathrm{e}^{i\omega t}\langle\lambda(t)\lambda(0)\rangle, \tag{6.3}$$

where ω is the frequency at which the spectral density is taken. Eq. 6.2 is the Ramsey decay envelope, and it is Gaussian in shape when the integral is dominated by the low-frequency component. Here, the two important features are the dependence of the pure dephasing rate $\Gamma_{\phi\mathrm{R}}$ (the factor multiplying t in the exponent) on the derivative of the transition energy with respect to λ and the noise spectral density $S_{\lambda\lambda}$ for fluctuations in λ. For additional derivations of this type, refer to App. C; for the application to the physical noise sources listed below, refer to Sec. 7.1.2. Similar to relaxation, protection from pure dephasing is usually attained by suppressing the dependence of the $g \to e$ frequency on external parameters, instead of the spectral densities themselves. As before, the inverse, hardware-based strategy is also an active and promising area of research [see, e.g. Paik et al. 2011, Rigetti et al. 2012, Kumar et al. 2016].

6.4.2 Survey of dephasing mechanisms

The sketch of an argument above demonstrates the qualitative model of decoherence, but it turns out that certain noise channels require different models, e.g. because some of the assumptions made above do not hold. However, this model and its extensions are adept at dealing with so-called $1/f$ noise, where $S_{\lambda\lambda}$ has a roughly reciprocal dependence on frequency. The four dominant known dephasing channels in superconducting qubits read out dispersively are listed below and discussed further in Sec. 7.1.2.

Charge noise corresponds to fluctuations in the offset charge N_g that are commonly associated with microscopic electrostatic defects and are $1/f$. There are also offset charge jumps, which are low-frequency but large-amplitude [Christensen et al. 2019]. *Flux noise* is the stochastic variation of the external flux φ_ext (see the following section) and a prototypical example of $1/f$ noise. *Critical current noise* corresponds to variations in E_J and it also expected to have a $1/f$ spectrum [van Harlingen et al. 2004, Faoro and Ioffe 2007]. *Shot noise* is a shorthand for fluctuations in the number of photons occupying the readout resonator[see, e.g. Bertet et al. 2005]. These may be coherent photons, in which case the occupation is $\bar{n}$, or incoherent thermal photons, in which case it is n_th. The corresponding decoherence limits differ by a factor of two (see App. C). The spectral density is approximately Lorentzian in shape, i.e. not $1/f$.

6.5 Example: Local and global flux noise in the double fluxonium

In cases where the Hamiltonian depends on multiple instances of the same type of parameter, like two external fluxes, we can introduce the concept of locality in addition

to the frequency spectrum. The central idea here is that spatial correlations in the noise can be estimated, and that they provide valuable information about its physical origin. As a simple example, consider two parameters λ_1 and λ_2 and their transforms $\lambda_\pm = \lambda_1 \pm \lambda_2$. The noise should be considered global when λ_1 and λ_2 have correlated fluctuations, in which case there are no fluctuations in λ_-. Oppositely, it should be considered local when the fluctuations are uncorrelated, and so the fluctuation amplitudes in λ_+ and λ_- are equal.

6.5.1 Mapping coherence times to external flux

In order to demonstrate the insensitivity of the molecule to certain decoherence mechanisms, we measured the Ramsey coherence times of the $g \to e$ transition for devices M1, M2, and M3 in the vicinity of $\varphi_{\text{ext}} = \pi$. Additional measured timescales are listed in Tab. 5.2. Ramsey coherence times for the measured devices were between 0.4–1.25 µs, but spin-echo coherence times were about a factor of 4 larger, indicating the presence of a low-frequency decoherence mechanism, such as $1/f$ flux noise.

The measured Ramsey dephasing rate $\Gamma_{\phi\text{R}}$ is plotted in Fig. 6.6 as a function of φ_{ext}. The dependence of the f_{ge} transition on φ_{ext} allows us to isolate the contributions of common-mode and differential-mode flux noise to dephasing of the molecule as shown by the theoretical curves. Near $\varphi_{\text{ext}} = \pi$, the coherence of the $g \to e$ transition is expected to be limited by differential-mode flux noise while at $\varphi_{\text{ext}} \lesssim 0.6\pi$ it is predominantly expected to be limited by common-mode flux noise.

6.5.2 Evidence for the local origin of flux noise

For common-mode flux noise, the parameter appearing in Eq. 6.3 is $\lambda = \frac{1}{\sqrt{2}}(\Phi_{\text{cm}} - 2\Phi_{\text{ext}})$, while for differential-mode flux noise, it is $\lambda = \frac{1}{\sqrt{2}}(\Phi_{\text{dm}} - 2\delta_{\mathcal{A}}\Phi_{\text{ext}})$. The offsets ensure that the parameters have zero mean and the factors of $\frac{1}{\sqrt{2}}$ permit the comparison to single-loop flux noise measurements. Flux noise is typically assumed to have a $1/f$ spectrum, i.e.

$$S_{\lambda\lambda}[\omega] = \frac{2\pi A_\lambda}{|\omega|},$$

where $\sqrt{A_\lambda}$ is the flux noise amplitude. Note that $S_{\lambda\lambda}$ has units of $[\lambda^2]/\text{Hz}$ while A_λ has units of $[\lambda^2]$. We call the spectral density amplitudes for the common- and differential-modes A_{cm} and A_{dm}, respectively.

The common-mode and differential-mode flux noise amplitudes are given in Tab. 6.1. We found upper bounds for flux noise amplitudes between 4 and 11 $\mu\Phi_0$. The flux noise amplitudes that we measured were somewhat larger but of the same order of magnitude as previous measurements of flux noise in flux qubits [Yoshihara et al. 2006, Bylander et al. 2011, Gustavsson et al. 2011] and coupled flux qubits [Yoshihara et al. 2010].

Global flux noise, from a fluctuating applied magnetic field for example, would induce exclusively common-mode flux noise in the sample, i.e. $A_{\text{dm}}/A_{\text{cm}} = 0$. On the other hand, local flux noise, such as that caused by spins fluctuating at the surface of the superconductor [R. H. Koch et al. 2007] or in defects at the metal/insulator interface [Faoro and Ioffe 2008], induces both common-mode and differential-mode flux noise in the sample. The exact branching ratio depends on the details of the model, but local flux noise will cause both common-mode and differential-mode flux noise on the unshared superinductances and

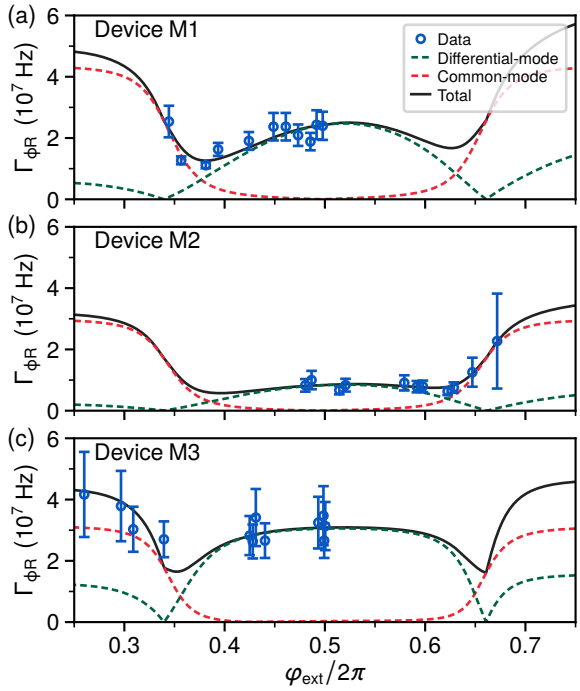

Figure 6.6 Ramsey decoherence rates of the double fluxonium molecule as a function of external flux. Circles indicate measured values with statistical error bars. Dashed lines indicate theoretical predictions using models for differential-mode (green) or common-mode (red) flux noise with fitted noise spectral density amplitudes, while solid lines represent their combination. (a) Results for device M1. (b) Results for device M2. (c) Results for device M3. Note that residual asymmetry in loop areas causes the lack of exact symmetry about $\varphi_{ext} = \pi$ and makes measurement of $\Gamma_{\phi R}$ over the complete flux range intractable.

			A_{dm}/A_{cm}		
Device	A_{cm} ($\mu\Phi_0$)	A_{dm} ($\mu\Phi_0$)	Meas.	Exp. Global	Exp. Local
M1	6 ± 1	10 ± 2	1.7 ± 0.4	0	>1
M2	4 ± 1	4 ± 1	1.0 ± 0.4	0	>1
M3	8 ± 1	11 ± 2	1.4 ± 0.3	0	>1

Table 6.1 Inferred flux noise amplitudes from Ramsey decoherence time T_{2R} measurements for the three double fluxonium devices. The latter three columns display the measured and expected ratios of differential-mode to common-mode flux noise amplitudes for the cases of global and local flux noise.

differential-mode flux noise on the shared superinductance, resulting in a larger differential-mode contribution than common-mode contribution. Hence, for local flux noise, we would expect $A_{\mathrm{dm}}/A_{\mathrm{cm}} > 1$. This is what we observe in all three devices. Near $\varphi_{\mathrm{ext}} = \pi$, the sample is insensitive to common-mode flux noise and is limited by differential-mode flux noise, which can only result from local sources.[5]

To calculate the different flux noise limits on coherence, we rewrite Eq. 5.1 in terms of φ_{ext} and δ_A as

$$H = 4E_{\mathrm{C}}(N_1^2 + N_2^2) + \frac{1}{3}E_{\mathrm{L}}(\varphi_1^2 + \varphi_2^2 + \varphi_1\varphi_2) - E_{\mathrm{J}}\cos\left[\varphi_1 - (1+\delta_A)\varphi_{\mathrm{ext}}\right] - E_{\mathrm{J}}\cos\left[\varphi_2 - (1-\delta_A)\varphi_{\mathrm{ext}}\right],$$

which we numerically diagonalize in a double Fock basis using the methods from Ch. 4. We then take a derivative of f_{ge} as a function of φ_{ext} using finite difference methods. Following the calculation in App. C [Ithier et al. 2005], we fit the Ramsey coherence data using the following equation:

$$\Gamma_{\phi\mathrm{R}} = \sqrt{A_{\mathrm{cm}} \ln \frac{\Gamma_{\phi\mathrm{R}}}{\omega_{\mathrm{ir}}}} \left|\frac{\partial \omega_{ge}}{\partial \Phi_{\mathrm{ext}}}\right|,$$

where A_{cm} is the common-mode flux noise amplitude and ω_{ir} is the low frequency cutoff for the flux noise. We take $\omega_{\mathrm{ir}} = 2\pi \times 1$ Hz, which corresponds to the inverse of our averaging time. This cutoff is consistent with the measured ratio $\Gamma_{\phi\mathrm{R}}/\Gamma_{\phi\mathrm{E}} = \sqrt{\ln[\Gamma_{\phi\mathrm{R}}/\omega_{\mathrm{ir}}]/\ln 2} \sim 4$. From this fit we obtain the common-mode flux noise amplitudes given in Tab. 6.1.

To calculate the differential-mode flux noise limits, we take a derivative of f_{ge} as a function of δ_A again using finite difference methods. We fit the $T_{2\mathrm{R}}$ data using the equation:

$$\Gamma_{\phi\mathrm{R}} = \sqrt{A_{\mathrm{dm}} \ln \frac{\Gamma_{\phi\mathrm{R}}}{\omega_{\mathrm{ir}}}} \frac{1}{\Phi_{\mathrm{ext}}} \left|\frac{\partial \omega_{ge}}{\partial \delta_A}\right|,$$

where A_{dm} is the differential-mode flux noise amplitude and ω_{ir} is the same constant as above. From this fit we obtain the differential-mode flux noise amplitudes given in Tab. 6.1. We remark that a stronger residual asymmetry between the two loops results in lower coherence times of the molecule around $\varphi_{\mathrm{ext}} = \pi$.

6.5.3 Population control using higher levels

As a final remark in this section, we now describe measurements that demonstrate indirect control of the double fluxonium qubit. While these techniques were not used to acquire the data in Fig. 6.6, they constitute an important control experiment and have consequences for the implementation of the $\cos 2\varphi$ qubit, which we will see in Ch. 8. As we remarked in Sec. 5.3, the double fluxonium qubit had a very low transition frequency near 100 MHz for all three devices at certain points in external flux. Since this corresponds to a temperature

5 We note that the residual asymmetry between the two loops in the molecule results in sensitivity to differential-mode flux noise. A locally-applied external flux could be used to compensate this asymmetry, which may improve coherence times. In addition, surface passivation has recently been found to decrease flux noise in SQUIDs [Kumar et al. 2016] and may also increase coherence times.

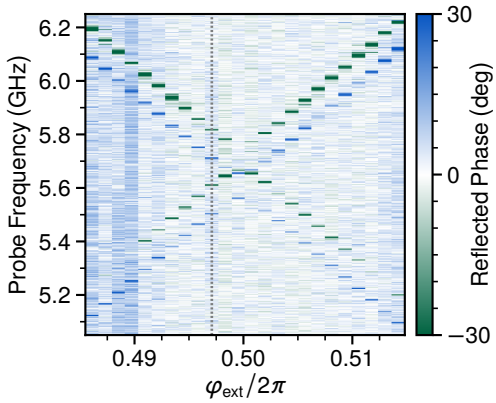

Figure 6.7 Spectroscopy of the second- and third-excited states $|f\rangle$ and $|h\rangle$ from the ground and first-excited states $|g\rangle$ and $|e\rangle$ for the fluxonium artificial molecule. The $g \to \{f, h\}$ and $e \to \{f, h\}$ transitions are seen as increases (green lines) and decreases (blue lines) in the reflected phase, respectively. These latter transitions were made visible by the low $g \to e$ transition frequency and hence the large thermal population of $|e\rangle$.

well below that of the dilution refrigerator, the qubit had a thermal population up to ≈45%. In such systems, which resemble natural atoms [Ludlow et al. 2006] and ions [Langer et al. 2005], higher levels of the system are often used to manipulate low-frequency manifolds. We expect to encounter this situation in the $\cos 2\varphi$ qubit (see Ch. 8), as with many protected qubits. In the double fluxonium, we plot the spectroscopy of transitions from the $\{|g\rangle, |e\rangle\}$ manifold to the next two excited states $|f\rangle$ and $|h\rangle$ in Fig. 6.7. In this figure, the large thermal population makes both the $g \to \{f, h\}$ and $e \to \{f, h\}$ transitions visible.

We demonstrate coherent manipulation of both the population between $|g\rangle$ and $|f\rangle$ in Fig. 6.8a, and the population between $|e\rangle$ and $|f\rangle$ in Fig. 6.8b. In these measurements, we applied a microwave tone with a pulse width of 20 ns at the transition frequencies f_{gf} and f_{ef} with a varying amplitude, and we observed the Rabi oscillations shown. Unfortunately, since the coherence times of the $g \to f$ and $e \to f$ transitions were not significantly shorter than that of the $g \to e$ transition, STImulated Raman Adiabatic Passage (STIRAP) as well as conventional stimulated Raman transitions are not expected to be any more efficient than direct population transfer through $|f\rangle$ [Bergmann et al. 1998, and references therein].

On the other hand, we could significantly increase the readout contrast of the $g \to e$ transition, which was originally limited by the large thermal occupancy, using $|f\rangle$. To this end, we first applied a π-pulse to the $e \to f$ transition to evacuate population from $|e\rangle$. Then, an amplitude Rabi experiment showed a tenfold increase in contrast when compared to the same measurement without the preceding π-pulse from $e \to f$, as shown in Fig. 6.8c.

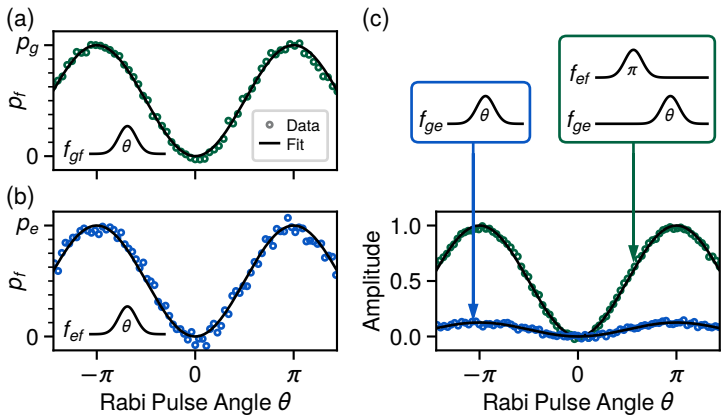

Figure 6.8 Population control in the fluxonium artificial molecule using higher excited states in the vicinity of $\varphi_{\text{ext}} = \pi$ (dashed line in Fig. 6.7). (a–b) Rabi oscillations between $|g\rangle/|e\rangle$ and $|f\rangle$, such that the initial population p_g/p_e of $|g\rangle/|e\rangle$ was transferred to $|f\rangle$. (c) Indirect control of the qubit manifold. The bare Rabi contrast between $|g\rangle$ and $|e\rangle$ was small due to thermal occupation, but increased by an order of magnitude when preceded by a π-pulse that evacuated the population from $|e\rangle$. The signal amplitudes are normalized by that of the latter sequence.

7

DECOHERENCE ESTIMATES FOR PROTECTED QUBITS

In sequence with the last chapter, we proceed with our discussion of the dynamic properties of superconducting circuit Hamiltonians, now focusing on theoretical models of coherence times. At this point, we have completed our discussion of the fluxonium and double fluxonium experiments, which demonstrated our understanding of circuit Hamiltonians, on both a theoretical and experimental level, as well as the common varieties of noise that affect qubits in practice. We are now equipped to continue our analysis of the $\cos 2\varphi$ qubit from Ch. 3, which we argued should be protected in Ch. 1. To this end, we revisit the full Hamiltonian in Eq. 2.15 and apply the results of Chs. 4–6 to predict its coherence properties. Ultimately, we find that the $\cos 2\varphi$ qubit is expected to be insensitive to all typical noise sources.

7.1 Summary for superconducting circuits

7.1.1 Quantitative description of the loss channels

We begin by expanding on Sec. 6.2 by discussing the quantitative features of the four loss mechanisms introduced: capacitive/dielectric, inductive, quasiparticle, and Purcell/radiative. To ease our discussion, we introduce a general expression for the Hamiltonian of one qubit dispersively coupled to its readout resonator in the presence of a bath. This naturally extends Eq. 1.1, along the lines of Eq. 4.3, into

$$\begin{aligned} H = {} & 4E_{\mathrm{C}}(N-N_{\mathrm{g}})^2 + \tfrac{1}{2}E_{\mathrm{L}}(\varphi-\varphi_{\mathrm{ext}})^2 - E_{\mathrm{J}}\cos\varphi + \hbar\omega_0 a^\dagger a + H_{\mathrm{bath}} \\ & - \frac{\phi_0\Phi_{\mathrm{zpf}}}{L_{\mathrm{m}}}(\varphi-\varphi_{\mathrm{ext}})(a+a^\dagger) + i\frac{2eQ_{\mathrm{zpf}}}{C_{\mathrm{m}}}(N-N_{\mathrm{g}})(a^\dagger-a) + \sum_{\mathcal{O}}\mathcal{O}\mathcal{E}(t). \end{aligned} \tag{7.1}$$

In this expression, the first line corresponds to the independent qubit, readout, and bath Hamiltonians. The first two terms on the second line respectively describe inductive and capacitive coupling between the qubit and its readout resonator, which rarely appear together. The coupling strengths are parametrized by a mutual inductance L_{m} and mutual capacitance C_{m}, which tend to infinity as the modes decouple. The parameters Φ_{zpf} and Q_{zpf} represent the amplitude of zero-point fluctuations of the cavity flux and charge, respectively, in accordance with the definitions in Sec. 3.1. The final term on the second line depicts all the couplings between the joint qubit-readout system, with operators $\mathcal{O}$,

and the noisy bath operators $\mathcal{E}(t)$. We recall Fermi's Golden Rule from Eq. 6.1,

$$\Gamma_{i\to f} = \frac{1}{\hbar^2}|\langle f|\mathcal{O}|i\rangle|^2 S_{\mathcal{E}\mathcal{E}}[-\omega_{if}], \tag{7.2}$$

generalized to arbitrary initial and final qubit states $|i\rangle$ and $|f\rangle$, respectively.

Capacitive loss For capacitive loss, where $\mathcal{O} = 2eN$ and $\mathcal{E} = V$, the fluctuation-dissipation theorem [Schoelkopf et al. 2003] gives

$$S_{VV}[\omega] = \hbar\omega \operatorname{Re} Z(\omega)\left(1 + \coth\frac{\hbar\omega}{2k_{\mathrm{B}}T}\right),$$

where $Z(\omega)$ represents the impedance of the relevant component of the bath. In particular, the real part of the impedance associated with a lossy capacitance C is

$$\operatorname{Re} Z_{\mathrm{cap}}(\omega) = \frac{1}{|\omega|CQ_{\mathrm{cap}}(\omega)} \tag{7.3}$$

for large capacitive quality factors Q_{cap}. To reproduce this relation, we simply add a resistor in parallel with the capacitance and recall the definition $Q_{\mathrm{cap}}(\omega) = \operatorname{Im} Y_{\mathrm{cap}}(\omega)/\operatorname{Re} Y_{\mathrm{cap}}(\omega)$ [Masluk 2013]. Note that we have allowed for a frequency-dependent $Q_{\mathrm{cap}}(\omega)$ to account for empirical observations.

For aluminum thin films on sapphire, these quality factors have been measured to be lower-bounded by $Q_{\mathrm{cap}} \approx 1\times10^6$ for a frequency of $\omega = 2\pi\times 6\,\mathrm{GHz}$ [C. Wang et al. 2015]. Their frequency dependence has been empirically observed to be $Q_{\mathrm{cap}} \propto |\omega|^{-0.7}$ [Braginsky et al. 1987]. Hence, we use the expression

$$Q_{\mathrm{cap}}(\omega) = (1\times10^6)\left(\frac{2\pi\times 6\,\mathrm{GHz}}{|\omega|}\right)^{0.7} \tag{7.4}$$

for our calculations. Since this treatment neglects the specific geometry of the capacitance in question, we expect it to be valid only up to geometric factors of order unity.

Inductive loss Inductive loss is the formal dual of capacitive loss. In this case, we have $\mathcal{O} = \phi_0\varphi$ and $\mathcal{E} = I$, so that the fluctuation-dissipation theorem gives

$$S_{II}[\omega] = \hbar\omega \operatorname{Re} Y(\omega)\left(1 + \coth\frac{\hbar\omega}{2k_{\mathrm{B}}T}\right).$$

Here, $Y(\omega)$ depicts the admittance of the relevant component of the bath. The real part of the admittance associated with a lossy inductance L is

$$\operatorname{Re} Y_{\mathrm{ind}}(\omega) = \frac{1}{|\omega|LQ_{\mathrm{ind}}(\omega)} \tag{7.5}$$

for large inductive quality factors $Q_{\mathrm{ind}}(\omega)$. Similar to the case of capacitive loss, we can see this by adding a resistor in series with the inductance and using the definition of the inductive quality factor $Q_{\mathrm{ind}}(\omega) = \operatorname{Im} Z_{\mathrm{ind}}(\omega)/\operatorname{Re} Z_{\mathrm{ind}}(\omega)$ [Masluk 2013].

For inductors made from arrays of Josephson junctions, it has been suggested that inductive loss should occur due to quasiparticle tunneling across the constituent junctions. In these superinductances, the quality factors have been estimated to be lower-bounded by $Q_{\text{ind}} \approx 500 \times 10^6$ at frequency $\omega = 2\pi \times 0.5\,\text{GHz}$ [Pop et al. 2014]. To align with the theoretical model of quasiparticle tunneling (see below), their frequency dependence should be $Q_{\text{ind}} \propto \frac{1}{K_0(x)\sinh x}$ with $x = \frac{\hbar|\omega|}{2k_BT}$, where K_0 is the modified Bessel function of the second kind. In the high-frequency case $\hbar|\omega| \gg k_BT$, this frequency dependence simplifies to $Q_{\text{ind}} \propto \sqrt{|\omega|}$, however this is not a relevant limit for low-frequency qubits such as the $\cos 2\varphi$ qubit. We therefore arrive at the expression

$$Q_{\text{ind}}(\omega) = (500 \times 10^6)\frac{K_0\left(\frac{\hbar\times 0.5\,\text{GHz}}{2k_BT}\right)\sinh\left(\frac{\hbar\times 0.5\,\text{GHz}}{2k_BT}\right)}{K_0\left(\frac{\hbar|\omega|}{2k_BT}\right)\sinh\left(\frac{\hbar|\omega|}{2k_BT}\right)} \tag{7.6}$$

for the inductive quality factor used in our calculations.

Quasiparticle loss For quasiparticle loss, $\mathcal{O} = 2\phi_0 \sin(\varphi/2)$ [Catelani et al. 2011] and the spectral density for quasiparticle tunneling obeys a version of the fluctuation-dissipation theorem

$$S_{\text{qp}}[\omega] = \hbar\omega\,\text{Re}\,Y_{\text{qp}}(\omega)\left(1 + \coth\frac{\hbar\omega}{2k_BT}\right),$$

provided the quasiparticle bath is in thermal equilibrium at a low temperature $k_BT \ll \Delta$, where Δ is the superconducting gap. For arbitrary ω, the dissipative part of the admittance of a Josephson junction with tunneling energy E_J is

$$\text{Re}\,Y_{\text{qp}}(\omega) = \sqrt{\frac{2}{\pi}}\frac{8E_J}{R_K\Delta}\left(\frac{2\Delta}{\hbar\omega}\right)^{3/2} x_{\text{qp}}\sqrt{\frac{\hbar\omega}{2k_BT}}K_0\left(\frac{\hbar|\omega|}{2k_BT}\right)\sinh\frac{\hbar\omega}{2k_BT}, \tag{7.7}$$

where $R_K = h/e^2$ is the normal resistance quantum and x_{qp} is the density of quasiparticles relative to Cooper pairs. Note that the frequency dependence of this admittance, when brought into agreement with Eq. 7.5, justifies Eq. 7.6. This junction admittance, derived by Catelani et al. (2011), has typically been simplified using the limiting behavior of the Bessel function $K_0(x) \sim e^{-x}\sqrt{\pi/2x}$ as $x \to \infty$ [Pop et al. 2014]. Using this expression, Eq. 7.7 takes the form

$$\text{Re}\,Y_{\text{qp}}(\omega) \approx \frac{4E_J}{R_K\Delta}\left(\frac{2\Delta}{\hbar|\omega|}\right)^{3/2} x_{\text{qp}}$$

in the high frequency $\hbar|\omega| \gg k_BT$ case. Although this formula is justified for high-frequency qubits, such as the transmon, it breaks down for low-frequency qubits, such as the $\cos 2\varphi$ qubit. Therefore, we use the full expression. For convenience, we can draw an analogy between Eq. 7.7 and Eq. 7.5 to define a junction quality factor $Q_{\text{qp}}(\omega)$ such that

$$\text{Re}\,Y_{\text{qp}}(\omega) = \frac{1}{|\omega|L_JQ_{\text{qp}}(\omega)}.$$

Moreover, the normalized density of quasiparticles in aluminum superconducting circuits has been measured to be $x_{\rm qp}^{-1} \approx 0.3 \times 10^6$ [Pop et al. 2014].[1] The result is

$$Q_{\rm qp}(\omega) = \left(\tfrac{\pi}{2}\right)^{3/2}(0.3\times 10^6)\frac{\sqrt{k_{\rm B}T/\Delta}}{K_0\left(\frac{\hbar|\omega|}{2k_{\rm B}T}\right)\sinh\left(\frac{\hbar|\omega|}{2k_{\rm B}T}\right)},$$

where the numeric factor in parentheses represents $x_{\rm qp}^{-1}$ as discussed.

Purcell loss One method for treating Purcell loss is to consider it as capacitive or inductive loss in the lumped element model of the readout resonator in Eq. 7.1, depending on the type of qubit-readout coupling. Particularly, capacitive and inductive losses are appropriate for inductive and capacitive coupling between the qubit and readout modes, respectively.[2] Then, we may use $\mathcal{O} = iQ_{\rm zpf}(a^\dagger - a)$ or $\mathcal{O} = \Phi_{\rm zpf}(a + a^\dagger)$ as well as the above expressions for S_{VV} and S_{II}. The only subtlety is that $|i\rangle$ and $|f\rangle$ are no longer simple qubit eigenstates; they also include a readout component $|n\rangle$.[3] Depending on the circumstance, a different estimate for the steady-state $|n\rangle$ should be taken. The most common options are

(i) the vacuum state $|0\rangle$ of the readout mode,
(ii) a coherent state $|\alpha\rangle = \mathrm{e}^{-|\alpha|^2/2}\sum_{n=0}^{\infty}\frac{\alpha^n}{\sqrt{n!}}|n\rangle$ with $|\alpha|^2 = \bar{n}$ photons, or
(iii) a thermal state with $n_{\rm th}$ photons and described by the totally mixed density matrix $\rho = \sum_{n=0}^{\infty}\frac{n_{\rm th}^n}{(1+n_{\rm th})^{1+n}}|n\rangle\langle n|$.

An alternative method for treating Purcell loss is to take $\mathcal{O} = 2eN$ or $\mathcal{O} = \phi_0\varphi$ and then extract $\mathrm{Re}\, Z_{\rm cap}(\omega)$ or $\mathrm{Re}\, Y_{\rm ind}(\omega)$ using an electromagnetic solver like Ansys HFSS [e.g. as used in earlier fluxonium work, see Geerlings 2013, Pop et al. 2014].

Summary As we have seen, the transition rate in Eq. 7.2 corresponding to each type of coupling to the bath, or loss channel, involves a specific instance of the fluctuation-dissipation theorem. We can capture these effects in the unified equation

$$\Gamma_{i\to f} = \frac{1}{\hbar^2}|\langle f|\mathcal{O}|i\rangle|^2 \times \hbar\omega_{if}\,\mathrm{Re}\,\zeta(\omega_{if})\left(-1 + \coth\frac{\hbar\omega_{if}}{2k_{\rm B}T}\right),$$

where $\zeta(\omega)$ is the appropriate complex response. Additionally, we have been able to write $\mathrm{Re}\,\zeta(\omega) = \frac{1}{|\omega|\lambda Q(\omega)}$ for each loss mechanism, where λ is a circuit parameter. We now recall that the qubit relaxation rate Γ_1 is expressed in terms of the $e\to g$ and $g\to e$ transition rates as $\Gamma_1 = \Gamma_{e\to g} + \Gamma_{g\to e}$.[4] Therefore, we are able to write the relaxation rate through an

1 This is a surprisingly low value given that thermal equilibrium predicts $x_{\rm qp}^{-1} \gg 10^{20}$. Indeed, signatures of hot nonequilibrium quasiparticles have recently been detected in superconducting circuits [Serniak et al. 2018].

2 For inductive qubit-readout coupling, the readout mode is eliminated by taking it to be an open circuit, and hence capacitive loss in the readout becomes inductive loss in the coupling inductance. The situation is reversed for capacitive coupling, where the relevant limit is a closed readout circuit. Note that these limits are only valid for circuits with qubit and cavity modes bridged by the coupling element, i.e. Π circuits.

3 These states $|n\rangle$ should not be interpreted as eigenstates of $a^\dagger a$, because then $\langle n|\mathcal{O}|n\rangle = 0$, but rather as eigensubspaces of the full Hamiltonian corresponding to the quantum number n that indexes the number of excitations in the readout mode (see Sec. 4.3.3).

4 To see this, we adhere to the conventional definition of Γ_1 as the decay rate of the qubit polarization $\pi_{ge} = \rho_{gg} - \rho_{ee}$. Then, plugging the loss operators $|g\rangle\langle e|$ and $|e\rangle\langle g|$ with rates $\Gamma_{e\to g}$ and $\Gamma_{g\to e}$ into a Lindblad master equation for the qubit quickly yields $\dot{\pi}_{ge} = -(\Gamma_{e\to g} + \Gamma_{g\to e})\pi_{ge}$.

Channel	Operator $\mathcal{O}$	Parameter λ	Quality factor $\mathcal{Q}$
Capacitive	$2eN$	C	$(1\times10^6)\left(\frac{2\pi\times 6\,\mathrm{GHz}}{\lvert\omega\rvert}\right)^{0.7}$
Inductive	$\phi_0\varphi$	L	$(500\times10^6)\frac{K_0\left(\frac{\hbar\times 0.5\,\mathrm{GHz}}{2k_\mathrm{B}T}\right)\sinh\left(\frac{\hbar\times 0.5\,\mathrm{GHz}}{2k_\mathrm{B}T}\right)}{K_0\left(\frac{\hbar\lvert\omega\rvert}{2k_\mathrm{B}T}\right)\sinh\left(\frac{\hbar\lvert\omega\rvert}{2k_\mathrm{B}T}\right)}$
Quasiparticle	$2\phi_0\sin(\varphi/2)$	L_J	$\left(\frac{\pi}{2}\right)^{3/2}(0.3\times10^6)\frac{\sqrt{k_\mathrm{B}T/\Delta}}{K_0\left(\frac{\hbar\lvert\omega\rvert}{2k_\mathrm{B}T}\right)\sinh\left(\frac{\hbar\lvert\omega\rvert}{2k_\mathrm{B}T}\right)}$
Purcell	$iQ_\mathrm{zpf}(a^\dagger-a)$ $\Phi_\mathrm{zpf}(a+a^\dagger)$	C_r L_r	$\sim10^3$–10^4

Table 7.1 Features and quality factors for different loss channels. Inductive and capacitive quality factors for Purcell loss are order of magnitude estimates based on typical values for readout resonator frequencies $\omega_0/2\pi$ in the gigahertz range and $\kappa\sim 2\pi\times 1\,\mathrm{MHz}$. More accurate estimates require geometric considerations.

arbitrary loss channel as

$$\Gamma_1=\frac{2}{\hbar}|\langle g|\mathcal{O}|e\rangle|^2\frac{1}{\lambda\mathcal{Q}(\omega_{ge})}\coth\frac{\hbar|\omega_{ge}|}{2k_\mathrm{B}T}. \tag{7.8}$$

See Tab. 7.1 for a consolidated account of the different dissipation mechanisms.

7.1.2 Quantitative description of the dephasing channels

Our approach to calculating relaxation times was unified by Eq. 7.8, owing to the strength of the quantum fluctuation-dissipation theorem and Fermi's Golden Rule. The theory of pure dephasing, on the other hand, involves different approaches depending on context. In particular, we must account for both the measurement sequence used, e.g. Ramsey or spin-echo, and the specific frequency dependence of the noise channel in question. This is because relaxation requires the exchange of a fixed energy $\hbar\omega_{ge}$ with the bath, while dephasing describes the integrated drift of the phase between $|g\rangle$ and $|e\rangle$ due to the environment. This drift depends heavily on whether the noise is frequency independent, i.e. white; singular at low frequencies, e.g. $1/f$ noise; or something else, such as Lorentzian in the case of shot noise—in addition to how much noise is canceled using echo pulses.

As a demonstrative example, we return to Eq. 6.2, which describes the dephasing envelope for a Ramsey-type measurement and linear coupling to the noise. For clarity, we repeat it here:

$$f_{\phi\mathrm{R}}(t)=\exp\left[-\frac{1}{2}t^2\left(\frac{\partial\omega_{ge}}{\partial\lambda}\right)^2\int_{-\infty}^{\infty}\frac{\mathrm{d}\omega}{2\pi}S_{\lambda\lambda}[\omega]\,\mathrm{sinc}^2\frac{\omega t}{2}\right],$$

where the evaluation of the derivative at the bias point is implied. If the noise spectral density $S_{\lambda\lambda}[\omega]$ is regular and slow-varying for $|\omega|\lesssim 1/t$, we can use $\lim_{t\to\infty}\frac{\sin\omega t/2}{\omega/2}=$

$2\pi\delta(\omega)$ in the integrand. We then obtain

$$f_{\phi R}(t) = \exp\left[-\frac{1}{2}t\left(\frac{\partial\omega_{ge}}{\partial\lambda}\right)^2 S_{\lambda\lambda}[0]\right], \tag{7.9}$$

which has the exponential form $f_{\phi R}(t) = e^{-\Gamma_{\phi R}t}$ with dephasing rate $\Gamma_{\phi R} = \frac{1}{2}\left(\frac{\partial\omega_{ge}}{\partial\lambda}\right)^2 S_{\lambda\lambda}[0]$. This is perhaps the most transparent description of dephasing, for we see that the rate scales with the squared sensitivity $\frac{\partial\omega_{ge}}{\partial\lambda}$ of the qubit transition frequency to the noisy parameter and the dc component of the noise spectral density $S_{\lambda\lambda}[0]$, i.e. the part corresponding to drift. Unfortunately, this expression is not useful for superconducting qubits that are limited by noise sources either with singular spectral densities at $\omega = 0$ or which are not linearly coupled.

Nonetheless, the affect of each dephasing channel on the qubit can be modeled in terms its phase decay envelope $f_\phi(t)$, which captures the non-oscillatory time dependence of the off-diagonal components ρ_{ge} and ρ_{eg}. Depending on the statistics of the noise, how it couples to the qubit, and the time-scale over which it can be disruptive, functionally different envelopes $f_\phi(t)$ can be obtained. The dephasing time T_ϕ is easily identified for exponential envelopes $f_\phi(t) = e^{-\Gamma_\phi t}$ and Gaussian envelopes $f_\phi(t) = e^{-(\Gamma_\phi t)^2}$, where $T_\phi = 1/\Gamma_\phi$, but slightly ambiguous for other functional forms, such as power laws. We define T_ϕ to be the $1/e$ time, that is, the time at which $f_\phi(t) = f_\phi(0)/e$. We refer to App. C for mathematical details about dephasing theory, with a particular focus on $1/f$ noise in devices with first-order insensitivity.

Charge noise Offset charge noise, which corresponds to fluctuations in N_g, is described by the $1/f$ noise spectral density

$$S_{N_g N_g}[\omega] = \frac{2\pi A_{N_g}}{|\omega|}.$$

The charge noise amplitude has been measured to be $\sqrt{A_{N_g}} \approx 1 \times 10^{-4}$ [Zorin et al. 1996]. Note that a more thorough treatment would include an empirical exponent $p \neq 1$ such that $S_{N_g N_g} \propto |\omega|^{-p}$, but we do not require this level of precision [e.g. Christensen et al. 2019]. Regardless, this model is appropriate only for noise in N_g about a fixed bias value $\overline{N_g}$. Drift in the bias value can be accounted for using the full nonlinear dependence of the qubit frequency on N_g. We defer the details to Sec. C.5 and state the result for the decay envelope,

$$f_{\phi R}(t) = J_0\left(\tfrac{1}{2\hbar}\epsilon t\right), \tag{7.10}$$

where ϵ is the charge dispersion of the qubit transition, i.e. the amplitude of the oscillation of E_{ge} in N_g, and J_0 is the Bessel function of the first kind. In fact, this Bessel function contains an oscillatory component that does not correspond to dephasing, so we use the asymptotic limit $J_0(x) \sim \sqrt{2/\pi x}\cos(x - \frac{\pi}{4})$ for $x \to \infty$ to extract the amplitude envelope

$$f'_{\phi R}(t) = \sqrt{\frac{4\hbar}{\pi\epsilon t}}. \tag{7.11}$$

Our earlier definition of T_ϕ as the $1/e$ time then yields $\Gamma_{\phi R} = \frac{\pi}{(2e)^2}\epsilon/\hbar$. Note that this model effectively describes the worst case scenario of offset charge drift, and does not depend on the charge noise amplitude $\sqrt{A_{N_g}}$.

Flux noise Magnetic flux noise is also a form of $1/f$ noise and it refers to fluctuations in φ_{ext}. The spectral density has the form

$$S_{\varphi_{ext}\varphi_{ext}}[\omega] = \frac{2\pi A_{\varphi_{ext}}}{|\omega|},$$

as in Sec. 6.5. Measured values for the flux noise amplitude $\phi_0\sqrt{A_{\varphi_{ext}}}$ range from $1.3\,\mu\Phi_0$ [Earnest et al. 2018] to $1–5\,\mu\Phi_0$ [Quintana et al. 2017] to $4–11\,\mu\Phi_0$ [Kou et al. 2017]. Hereafter, we use the geometric average of these values, $\phi_0\sqrt{A_{\varphi_{ext}}} = 3\,\mu\Phi_0$. As discussed in App. C.4, the specific decay envelope for $1/f$ noise depends on whether the coupling to φ_{ext} is linear or quadratic, i.e. whether the qubit is biased to its external flux sweet spot. For the purpose of an estimate, we neglect constants of order unity and implementation-dependent details and use the envelopes

$$f_{\phi R}(t) = \exp\left[-A_\lambda\left(\tfrac{\partial\omega_{ge}}{\partial\lambda}\right)^2 t^2\right] \qquad \text{linear coupling} \tag{7.12}$$

$$f_{\phi R}(t) = \exp\left[-A_\lambda\left|\tfrac{\partial^2\omega_{ge}}{\partial\lambda^2}\right| t\right] \qquad \text{quadratic coupling,} \tag{7.13}$$

written for a generic parameter λ, which we take to be φ_{ext} in this case. The evaluation of the derivatives occurs at the biased value of $\varphi_{ext} = \overline{\varphi_{ext}}$.

Critical current noise Noise in the Josephson junction critical current, or equivalently in E_J, is also expected to exhibit a $1/f$ spectrum of the form

$$S_{E_J E_J}[\omega] = \frac{2\pi A_{E_J}}{|\omega|}.$$

This type of noise is not as well understood as charge or flux noise, but its spectral density amplitude has been measured to be $\sqrt{A_{E_J}} \approx 5\times10^{-7}E_J$ [van Harlingen et al. 2004]. As in the case of flux noise, we may use Eqs. 7.12–13 with $\lambda = E_J$.

Shot noise Photons occupying the readout resonator used for dispersive measurement of the qubit will contribute to its dephasing via their discrete absorption and emission, which is also called shot noise. The source of these photons may either be a coherent microwave drive or thermal energy. We refer to the occupancy as $n(t)$ with average $\bar{n}$ and n_{th} in these two cases, respectively. The noise spectral density has the Lorentzian form

$$S_{nn}[\omega] = \begin{cases} 2\bar{n}\eta\frac{\kappa/2}{\omega^2+(\kappa/2)^2} & \text{coherent} \\ 2n_{th}\eta\frac{\kappa}{\omega^2+\kappa^2} & \text{thermal,} \end{cases} \tag{7.14}$$

in the limit of small n_{th} as shown by Gambetta et al. (2006) and Clerk and Utami (2007), and also sketched in App. C.6. As before, κ is the readout resonator linewidth. In these equations, we have introduced the correction factor $\eta = \frac{\kappa^2}{\kappa^2+\chi^2}$ to both $\bar{n}$ and n_{th}, which

includes the dispersive shift χ and accounts for the qubit-readout coupling [Yan et al. 2016]. In this spectral density, the two expressions differ only in their decay rates in the right-hand factors. The coherent case has a rate of $\kappa/2$ while the thermal case has a rate of κ, owing to coherence of the drive in the former [Blais et al. 2004].

The average occupation $\bar{n}$ is generally chosen experimentally to optimize readout fidelity and speed, but n_{th} is governed by the temperature of the bath, which is $T \sim 20\,\text{mK}$. In this situation, the thermal distribution gives $n_{\text{th}} = 1/(e^{\hbar\omega_0/k_B T} - 1)$, where ω_0 is the oscillator frequency. The earlier result Eq. 7.9 is applicable in this situation, and we arrive at the envelopes

$$f_{\phi R}(t) = \begin{cases} \exp\left(-2\bar{n}\kappa t \dfrac{\chi^2}{\chi^2+\kappa^2}\right) & \text{coherent} \\ \exp\left(-n_{\text{th}}\kappa t \dfrac{\chi^2}{\chi^2+\kappa^2}\right) & \text{thermal,} \end{cases} \tag{7.15}$$

where we have recalled that $\frac{\partial\omega_{ge}}{\partial n} = \chi$. Note that these are both of the exponential form $f_{\phi R}(t) = e^{-\Gamma_{\phi R} t}$, with the rate twice as fact for the coherent case.

Summary In Eqs. 7.11–15, we have seen that the phase decay envelopes for the four different noise channels have functional forms including power laws, exponentials, and Gaussians. Despite this, they share the common feature that the decay rate is ultimately a function of the spectral density amplitude and the leading-order sensitivity of the qubit frequency. See Tab. 7.2 for a concise summary. Moreover, all of the channels considered have a roughly $1/f$ spectrum except photon shot noise, which has a Lorentzian spectrum.

7.1.3 State delocalization: An intuition for protection

We conclude this section with a few comments on the difficulty of building a qubit that is simultaneously protected from all of these loss and dephasing channels. As we have argued, protection from relaxation generally requires the suppression of qubit matrix elements, while protection from dephasing essentially corresponds to suppressing the sensitivities of the qubit frequency. Moreover, as demonstrated in Sec. 6.5 for flux noise, each of these eight decoherence channels possesses a degree of "locality," in the sense that they each concern a single dipolar electrical variable or a parameter that is pinned to a single structure, e.g. φ_{ext} enclosed by an inductive loop. We are then led to believe that all protected qubits must ultimately exploit the diffusion of their quantum information onto many local degrees of freedom, in order to benefit from the built-in resilience to these local fluctuations. This idea of *nonlocally encoding* a qubit is the essential ingredient of the $\cos 2\varphi$ qubit, whose predicted coherence is presented in the remainder of this chapter, and which will make this discussion more concrete.

7.2 Decoherence estimates for the $\cos 2\varphi$ qubit

In this section, our goal is to apply the models outlined in Sec. 7.1 to estimate the coherence properties of the $\cos 2\varphi$ qubit, which are discussed in Sec. 7.2.3. The next two subsections, however, explain the remaining characteristics of the static $\cos 2\varphi$ qubit—the

Channel	λ	Spectral density	A_λ	Γ_ϕ	Coupling
Charge	N_g	$\frac{2\pi A_{N_g}}{\lvert\omega\rvert}$	$\left(1\times10^{-4}\right)^2$	$\frac{\pi}{(2e)^2}\epsilon/\hbar$	Sinusoidal
Flux	φ_{ext}	$\frac{2\pi A_{\varphi_{\text{ext}}}}{\lvert\omega\rvert}$	$\left[2\pi(3\times10^{-6})\right]^2$	$\sqrt{A_{\varphi_{\text{ext}}}}\left\lvert\frac{\partial\omega_{ge}}{\partial\varphi_{\text{ext}}}\right\rvert$ $A_{\varphi_{\text{ext}}}\left\lvert\frac{\partial^2\omega_{ge}}{\partial\varphi_{\text{ext}}^2}\right\rvert$	Linear Quadratic
Critical current	E_J	$\frac{2\pi A_{E_J}}{\lvert\omega\rvert}$	$\left(5\times10^{-7}E_J\right)^2$	$\sqrt{A_{E_J}}\left\lvert\frac{\partial\omega_{ge}}{\partial E_J}\right\rvert$ $A_{E_J}\left\lvert\frac{\partial^2\omega_{ge}}{\partial E_J^2}\right\rvert$	Linear Quadratic
Shot	n	$\frac{A_n(\kappa/2)}{\omega^2+(\kappa/2)^2}$ $\frac{A_n\kappa}{\omega^2+\kappa^2}$	$2\bar{n}\frac{\kappa^2}{\kappa^2+\chi^2}$ $2n_{\text{th}}\frac{\kappa^2}{\kappa^2+\chi^2}$	$2\bar{n}\kappa\frac{\chi^2}{\kappa^2+\chi^2}$ $n_{\text{th}}\kappa\frac{\chi^2}{\kappa^2+\chi^2}$	Linear $\bar{n}\lesssim1$ Linear $n_{\text{th}}\lesssim1$

Table 7.2 Features and spectral density amplitudes for different dephasing channels. Refer to App. C for more details. Charge noise, flux noise, and critical current noise are assumed to have $1/f$ spectral densities. Photon shot noise has a Lorentzian noise spectral density.

matrix elements in Sec. 7.2.1 and the effects of disorder in Sec. 7.2.2—which are necessary for the estimate calculations.

7.2.1 Selection rules

In Sec. 2.5, we analyzed the multi-mode Hamiltonian describing the superconducting circuit in Fig. 2.3. Numerical diagonalization of this Hamiltonian showed the emergence of a linear plasmon mode and a nonlinear fluxon mode.[5] In this section and the remainder of this thesis, we consider the properties of the logical qubit formed by $|0+\rangle$ and $|0-\rangle$, the two lowest-energy eigenstates at $\varphi_{\text{ext}}=\pi$. Note that for $\varphi_{\text{ext}}\neq\pi$, we can still define the qubit states as $|0\circ\rangle$ and $|0\bullet\rangle$ as in Sec. 3.3.2.

To better elucidate which types of operators can and cannot induce transitions between the two states of the qubit, we examine the relevant matrix elements corresponding to capacitive and inductive coupling. This discussion is particularly relevant to understanding

5 The number of plasmon and fluxon modes can be seen as classifying a crude superconducting circuit periodic table in a less rigorous, but perhaps more physically transparent, way than the number of islands, inductive loops, and overall degrees of freedom discussed in Sec. 2.3. Note that the transmon is a plasmon mode, the fluxonium is a fluxon mode, and the $\cos 2\varphi$ circuit is two plasmon modes and one fluxon mode. Since one of the plasmon modes has a high frequency and is essentially frozen in its ground state, the $\cos 2\varphi$ qubit can be viewed as a transmon hybridized with a fluxonium [Süsstrunk et al. 2013].

the expected dominant loss mechanisms (see Sec. 7.2.3) and designing a measurement and control apparatus that does not directly couple to the qubit (see Ch. 8).

For capacitive coupling, a generic voltage V couples to the superconducting island of the circuit in Fig. 2.3 via a gate capacitance C_g and will append the term

$$H_{\text{int}} = \frac{C_g}{C_x + C_g}(2eP)V$$

to the Hamiltonian in Eq. 2.15, in addition to dressing the shunt capacitance. We recall that P is the conjugate charge of θ, which is roughly the phase variable for the plasmon mode. This voltage may be a degree of freedom of another mode in the embedding circuit, a noise source, or an ac drive. We therefore see that the susceptibility of undergoing a transition from the ground state, due to capacitive coupling to the qubit island, is directly related to the matrix element $\langle\psi|P|0\circ\rangle$.

For inductive coupling, a generic current I couples to the circuit via an inductance L_s shared with the inductive loop, which adds the term

$$H_{\text{int}} = \frac{L_s}{2L}(\phi_0\phi)I$$

to the Hamiltonian in Eq. 2.15. Here, L is the superinductance in each arm of the qubit (i.e. $E_L = \phi_0^2/L$). Like the voltage source, this current may represent an internal or environmental degree of freedom. We see that the susceptibility of undergoing a transition from the ground state, due to inductive coupling to the inductive loop, is related to the matrix element $\langle\psi|\phi|0+\rangle$.

Limiting the Hilbert space to the six lowest-energy eigenstates $\{|m\pm\rangle : m = 0, 1, 2\}$, we numerically compute the normalized matrix elements

$$|\mathcal{O}_\psi|^2 \equiv \frac{|\langle\psi|\mathcal{O}|0\circ\rangle|^2}{\langle 0\circ|\mathcal{O}^\dagger\mathcal{O}|0\circ\rangle}$$

from the ground state $|0\circ\rangle$ for the operators $\mathcal{O} = P, \phi$. Results are plotted in Fig. 7.1. Note that $\sum_\psi |\mathcal{O}_\psi|^2 = 1$ and $|\mathcal{O}_\psi|^2 > 0$, so we may reasonably consider these as transition probabilities via $\mathcal{O}$.

We see from Fig. 7.1a that transitions mediated by capacitive coupling to the qubit island are only allowed from $|0\circ\rangle$ to $|1\circ\rangle$. These selection rules result from the decoupling of the even and odd Cooper pair number parity manifolds. Most importantly, transitions between qubit states are forbidden, meaning capacitive coupling offers a promising ingredient for qubit measurement and control. Conversely, inductive coupling to the inductive loop of the qubit permits transitions between $|0\circ\rangle$ and $|0\bullet\rangle$ in the vicinity of $\varphi_{\text{ext}} = \pi$, as shown in Fig. 7.1b. This effect arises because the operator ϕ induces transitions between the Cooper pair parity manifolds, as can be seen from the Fourier series for Eq. 3.6. As a consequence, we expect that relaxation of the qubit will be primarily due to inductive loss in the superinductances.

7.2.2 Asymmetry in the arms of the circuit

A highly symmetric superconducting circuit is usually fragile in view of unavoidable fabrication imperfections [Dempster et al. 2014]. The symmetry of our circuit involving

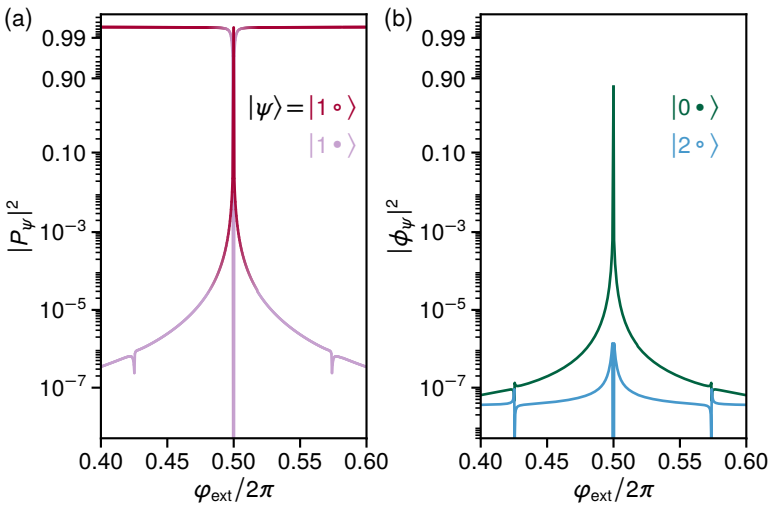

Figure 7.1 Matrix elements of the $\cos 2\varphi$ qubit. (a) Normalized charge matrix elements $|P_\psi|^2$ between the ground state $|0\circ\rangle$ and the excited state $|\psi\rangle$, showing immunity of the qubit manifold to capacitive coupling. The coloring here reflects the assigned quantum numbers, as in Fig. 3.2. (b) Normalized phase matrix elements $|\phi_\psi|^2$ between states $|0\circ\rangle$ and $|\psi\rangle$. This matrix element is near-unity between the two qubit states at $\varphi_{\text{ext}} = \pi$, suggesting that the qubit manifold is primarily susceptible to inductive loss.

the two inductive arms in Fig. 2.3 may be broken in three parameters: the Josephson energies of the junctions, the capacitances of the junctions, or the superinductances. To analyze these effects, we numerically diagonalize Eq. 2.15 and examine the energy splitting ΔE[6] as well as the charge dispersion $\epsilon = \max_{N_g} \Delta E - \min_{N_g} \Delta E$ of the $\{|0+\rangle, |0-\rangle\}$ manifold at $\varphi_{\text{ext}} = \pi$. A dimensionless quantity $\delta \in [0, 1)$ is introduced to parameterize the extent of asymmetry in all three cases, and the δ dependence of the energies ΔE and ϵ is studied.

Disorder in E_J We model disorder in the Josephson energies of the junctions by allowing the values of E_J to deviate. We therefore set the left and right junction tunneling energies to $(1 \pm \delta_J)E_J$, respectively, where δ_J is the aforementioned asymmetry parameter. The Hamiltonian in Eq. 2.15 is perturbed by the term

$$H' = 2E_J\delta_J \sin\varphi \sin\frac{\phi}{2}. \tag{7.16}$$

See Fig. 7.2 for a plot of ΔE and ϵ as a function of δ_J. The important feature in these plots is that the charge dispersion decreases exponentially while the splitting increases exponentially with δ_J.[7] These features arise from the effective Hamiltonian in Eq. 3.7 being

6 The energy splitting ΔE is evaluated at $N_g = 0$.

7 The extrapolation of the charge dispersion as a function of the disorder beyond $\delta = 0.6$ is due to numerical instabilities inherent to low-energy quantities paired with the disappearance of an efficient diagonalization basis

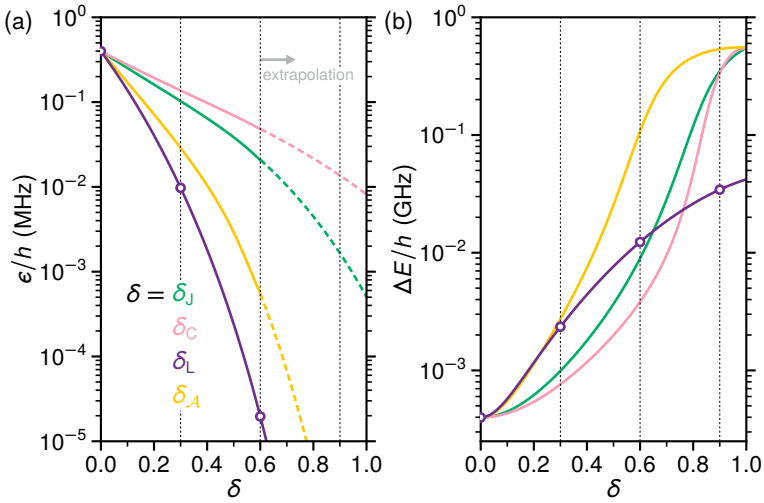

Figure 7.2 Effects of disorder in the $\cos 2\varphi$ qubit. (a) The charge dispersion ϵ of the qubit transition as a function of disorder parameters δ. Here, δ_J, δ_C, and δ_L correspond to disorder in the characteristic energy scales E_J, E_C, and E_L, respectively. Disorder in the Josephson junction area is represented by δ_A. (b) The energy splitting ΔE as a function of δ. Dashed lines and circles indicate the values of δ_L used for inductive disorder in Sec. 7.2.3.

accompanied by 2π-periodic terms in the presence of disorder. In this case of disorder in E_J, the approximations in Sec. 3.3.1 lead to $H' \approx H'_{\text{eff}}$ with

$$\begin{aligned} H'_{\text{eff}} = &-2E_J\delta_J\left\{\tfrac{8}{3\pi} + \tfrac{8}{9\pi}z + \tfrac{1}{27\pi}[56 - 9\pi^2 - 9(\pi-\phi_{\text{ext}})^2]z^2\right\}\sin\varphi \\ &+ \tfrac{1}{2}E_L\delta_J\left(1 - \tfrac{7}{4}z\right)(\pi-\phi_{\text{ext}})\sin 2\varphi \\ &+ 2E_J\delta_J\left\{\tfrac{8}{15\pi} - \tfrac{24}{25\pi}z + \tfrac{1}{3375\pi}[6392 - 225\pi^2 - 225(\pi-\phi_{\text{ext}})^2]z^2\right\}\sin 3\varphi \\ &+ \tfrac{1}{12}E_L\delta_J z(\pi-\phi_{\text{ext}})\sin 4\varphi \end{aligned}$$

up through the fourth harmonic and $O(z^2)$. More aggressive truncation, to leading order, yields

$$H'_{\text{eff}} = -\tfrac{16}{3\pi}E_J\delta_J\left(\sin\varphi - \tfrac{1}{5}\sin 3\varphi\right).$$

This evidently permits the tunneling of single Cooper pairs across the element. The resulting qubit retains characteristics of the symmetric circuit as well as the asymmetric/transmon-like circuit.

Disorder in E_C Analogously, we set the left and right junction charging energies to $E_C/(1 \pm \delta_C)$, respectively. Aside from dressing the charging energy, the Hamiltonian in Eq.

for large disorder. This is particularly obvious in the vicinity of $\delta = 1$, at which point the number of modes of the circuit reduces from three to two.

2.15 inherits the term

$$H' = -8E_{\mathrm{C}}\frac{\delta_{\mathrm{C}}}{1-\delta_{\mathrm{C}}^2}M(N-N_{\mathrm{g}}-P), \tag{7.17}$$

whose affect on the qubit manifold is plotted in Fig. 7.2.

This form for capacitive disorder is assumed due to the fact that, if $\delta_{\mathrm{J}} = \delta_{\mathrm{C}} = \delta_A$, then the product $E_{\mathrm{J}}E_{\mathrm{C}}$ is kept constant for both junctions under the effects of disorder. This corresponds to the physical case where the junction plasma frequencies are fixed by oxidation, but their areas differ due to fabrication imperfections. Here, the junction areas are $(1 \pm \delta_A)\mathcal{A}$ because the area obeys $\mathcal{A} \propto \sqrt{E_{\mathrm{J}}/E_{\mathrm{C}}}$. The consequences of area disorder are also plotted in Fig. 7.2.

Disorder in E_{L} Following the same procedure, we set the left and right superinductive energies to $E_{\mathrm{L}}/(1 \pm \delta_{\mathrm{L}})$, respectively. This form is taken in order to fix the total linear inductance in the loop. Aside from dressing the inductive energy, the Hamiltonian in Eq. 2.15 is perturbed by

$$H' = E_{\mathrm{L}}\frac{\delta_{\mathrm{L}}}{1-\delta_{\mathrm{L}}^2}(\phi-\varphi_{\mathrm{ext}})\theta. \tag{7.18}$$

Note in Fig. 7.2 that the charge dispersion and energy splitting follow the same general trend for inductive disorder as for the other three. The key difference is that the charge dispersion decreases more quickly than for any other form of disorder. Oppositely, the splitting is initially the same as for area disorder, but the slope decreases in δ_{L}. We conclude that disorder allows us to engineer a circuit with a sufficiently non-degenerate ground state manifold whose charge dispersion is largely suppressed.[8] For reasons that will be addressed in the remainder of this chapter, these features are extremely valuable for designing a qubit that is protected from dephasing.

7.2.3 Decoherence in the $\cos 2\varphi$ qubit

Dissipation in the $\cos 2\varphi$ qubit We treat dissipation in the $\cos 2\varphi$ qubit using the models in Sec. 7.1.1, that is, using Fermi's Golden Rule as in Eq. 7.8. The qubit states $|g\rangle$ and $|e\rangle$ are identified as $|0+\rangle$ and $|0-\rangle$, and the frequency ω_{ge} is identified as the splitting $\Delta\omega = \Delta E/\hbar$. The calculation is carried out for various degrees of inductive disorder δ_{L} and using the splitting ΔE and matrix elements obtained by numerical diagonalization of the full Hamiltonian in Eq. 2.15. We consider the effects from all four loss channels discussed in general [see also Pop et al. 2014]. In this circuit in Fig. 2.3, capacitive loss corresponds to the two Josephson junction capacitances, inductive loss to the superinductances in each arm, quasiparticle loss to the two junctions, and Purcell loss to the shunt capacitance. For the $\cos 2\varphi$ qubit, Purcell loss describes dissipation in the qubit due to its coupling to the plasmon mode.

8 The suppression of the charge dispersion in the asymmetric circuit, as compared to the symmetric circuit, can be understood in the following way. The charge dispersion depicts the rate at which single fluxons circulate about the superconducting island, which is one of the shunt capacitor pads. With asymmetry, the shunt capacitance reduces the fluctuations of the phase across one small junction preferentially. Since the fluxons need to traverse both small junctions to completely wind around the island, this effectively severs the path and exponentially suppresses the process.

Loss channel	$\mathcal{O}$	T_1 (ms)			
		$\delta_L = 0.0$	$\delta_L = 0.3$	$\delta_L = 0.6$	$\delta_L = 0.9$
Capacitive	$2eN_i$	780 000	17 000	1 000	18
Inductive	$\phi_0\phi_i$	0.61	0.79	1.1	1.4
Quasiparticle	$2\phi_0 \sin(\varphi_i/2)$	∞	∞	∞	∞
Purcell	$2eP$	∞	2 500	380	470
Dephasing channel	λ	T_ϕ (ms)			
		$\delta_L = 0.0$	$\delta_L = 0.3$	$\delta_L = 0.6$	$\delta_L = 0.9$
Charge	N_g	0.0037	0.15	74	3.3×10^6
Flux	φ_{ext}	0.022	0.13	0.67	1.8
Critical current	E_J	210	40	8.2	2.9
Shot	n_p	4.6	4.8	5.3	8.7

Table 7.3 Expected relaxation times T_1 and pure dephasing times T_ϕ at $\varphi_{ext} = \pi$ through various channels. The operators $\mathcal{O}$ coupling to the bath and the noisy parameters λ are listed. Relaxation and dephasing times are shown for varying cases of inductive disorder: $\delta_L = 0.0, 0.3, 0.6, 0.9$ (see also Fig. 7.2). The operators N_i depict the number of Cooper pairs that have tunneled across the two Josephson junctions, i.e. $N_i = M \pm \frac{1}{2}(N-P)$, and the phases ϕ_i and φ_i are defined in Sec. 2.5. The parameter n_p represents the instantaneous number of photons in the plasmon mode. Entries that read "∞" represent numerical infinity.

The calculated relaxation times and the corresponding components of Eq. 7.8 are shown in Tab. 7.3 for all four loss channels at $\varphi_{ext} = \pi$. We display results for the four values of δ_L shown in Fig. 7.2. For the full range of δ_L, see also Fig. 7.3a. For both capacitive and inductive loss, we note that measurements have not yet been performed using qubits with extremely small energy splittings, and the calculation presented here relies on an extrapolation to such frequencies. A key feature is the complete absence of quasiparticle loss, as in the fluxonium qubit [Pop et al. 2014]. Additionally, we see that the asymmetric qubit is marginally less susceptible to inductive loss than the symmetric qubit. This improvement comes at the cost of the susceptibility to capacitive and Purcell loss. However, we emphasize that the lifetimes shown in Tab. 7.3 are conservative estimates that demonstrate $T_1 \gtrsim 1\,\text{ms}$, which is at least competitive with state-of-the-art qubit implementations [Pop et al. 2014, Bell et al. 2014, Yan et al. 2016, Groszkowski et al. 2018].

Pure dephasing in the $\cos 2\varphi$ qubit We apply the results of Sec. 7.1.2 to the $\cos 2\varphi$ qubit to predict its sensitivity to pure dephasing at $\varphi_{ext} = \pi$, for the same degrees of inductive disorder δ_L used above. In this case, the calculation only requires the energy levels, and not the matrix elements, obtained by numerical diagonalization of Eq. 2.15. The effects of the four noise channels that we described in general are taken into account. In this circuit in Fig. 2.3, charge noise corresponds to fluctuations in N_g, flux noise to φ_{ext}, critical current noise to E_J, and photon shot noise to the plasmon mode occupation n_p. As

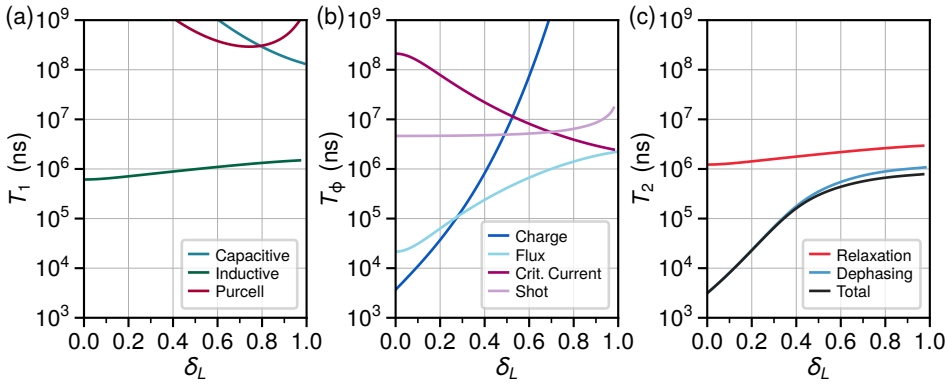

Figure 7.3 Coherence time estimates for the $\cos 2\varphi$ qubit. (a) Calculated relaxation times T_1 for the protected qubit as a function of inductive disorder δ_L (see Tab. 7.3) for four different loss mechanisms. The expected contribution due to quasiparticle loss across the small Josephson junctions is out of the range of this plot. (b) Calculated pure dephasing times T_ϕ for the protected qubit (see Tab. 7.3) for four different noise channels. (c) Combined estimates of the coherence times T_2 inferred using $1/T_2 = 1/2T_1 + 1/T_\phi$.

in the case of Purcell loss, the plasmon mode plays the role of a weakly coupled harmonic oscillator from the point of view of the qubit, and hence its fluctuating population dephases the qubit.

For charge noise, the dephasing rate only depends on the charge dispersion ϵ, which we have already calculated in Fig. 7.2. The $\cos 2\varphi$ couples quadratically to the external flux at the sweet spot $\varphi_\mathrm{ext} = \pi$, so we use the second formula for flux noise in Tab. 7.2. We then recall that ω_{ge} has become $\Delta\omega$, and compute the second derivative using finite difference methods. On the other hand, the $\cos 2\varphi$ qubit couples linearly to the Josephson energy, and therefore we use the first formula for critical current noise in Tab. 7.2. Once more, we compute the derivative using finite difference methods. Finally, we consider the plasmon mode to be thermally occupied with population n_p, which is on average n_th. To compute the resulting shot noise dephasing rate, we identify χ with the dispersive shift of the qubit on the plasmon mode, i.e. $\chi = \left[(E_{1-} - E_{0-}) - (E_{1+} - E_{0+})\right]/\hbar$, and the plasmon frequency ω_p with the energy level difference $(E_{1+} - E_{0+})/\hbar$. Then, we infer κ under the assumption that the plasmon mode will be limited by dielectric loss, in which case $\kappa = \omega_\mathrm{p}/Q_\mathrm{cap}(\omega_\mathrm{p})$ with the quality factor given in Eq. 7.4. For the remaining quantity n_th, we can use the thermal distribution $n_\mathrm{th} = 1/(\mathrm{e}^{\hbar\omega_\mathrm{p}/k_\mathrm{B}T} - 1)$.

The calculated pure dephasing times are shown in Tab. 7.3 for all four noise channels at $\varphi_\mathrm{ext} = \pi$, and for the same four values of δ_L used for the relaxation time calculation. For the results over the complete span of δ_L, in addition to the combined effects of relaxation and dephasing, see Figs. 7.3b–c. Ultimately, we find that both charge noise and flux noise are expected to yield a strict bound on the decoherence time in the case of perfect symmetry, but that this is greatly alleviated in the presence of inductive disorder. On the other hand, both critical current noise and photon shot noise are not expected to limit the coherence time of the qubit.

To understand this effect, we note that in the case of perfect symmetry, the charge

dispersion ϵ is identically mapped to ΔE. As a consequence, resilience to dephasing from offset charge noise demands a high degree of degeneracy, making experimental implementation difficult. On the other hand, the flux noise sensitivity can be expressed[9] as $\partial^2 \Delta E/\partial \varphi_{\text{ext}}^2 \propto 1/\Delta E$ at $\varphi_{\text{ext}} = \pi$ and for arbitrary asymmetry. This shows that resilience to dephasing from to flux noise requires sufficiently weak degeneracy, at odds with the requirement for resilience to charge noise. By introducing inductive disorder into the circuit, we effectively decouple ϵ and ΔE, as shown in Fig. 7.2, thereby allowing the simultaneous suppression of dephasing via charge and flux noise. It is then clear that inductive asymmetry constitutes a necessary ingredient for the protection of this qubit. In light of Eq. 7.18, we attribute this to the resulting hybridization of the ϕ and θ modes, which are not directly coupled in the symmetric case (see Eq. 2.15) [Süsstrunk et al. 2013]. The fluxon transition between the qubit states inherits some character of the plasmon transition, thereby breaking the correspondence between ϵ and ΔE and reducing the flux matrix element $\langle 0-|\phi|0+\rangle$.

7.2.4 Comparison to other circuits

The $\cos 2\varphi$ circuit in Fig. 2.3 bears resemblance to three other protected qubit proposals: the heavy fluxonium [Earnest et al. 2018, Lin et al. 2018], the rhombus [Blatter et al. 2001], and the 0-π qubit [Brooks et al. 2013]. The heavy fluxonium, in which a conventional fluxonium qubit is shunted by a large capacitance, shares many similar features with the $\cos 2\varphi$ qubit. In fact, our circuit roughly reduces to that of the heavy fluxonium in the extremely asymmetric limit of $\delta_{\text{L}} \to 1$, and the eigenstates of both circuits are similarly represented in terms of persistent currents. The two main differences are that our circuit contains an additional small Josephson junction and that the shunt capacitance is placed across the junction along with a subset of the array junctions. An analogy can be drawn between δ_{L} in our circuit and the shunt capacitance in the heavy fluxonium, because they both suppress the qubit transition frequency. Physically, the qubit eigenstates differ when these analogous parameters fall to small values. While the eigenstates collapse to Cooper pair number parity states in our circuit, this is not true for the heavy fluxonium because the variable φ is not compact.

With respect to the rhombus, there are two central differences. First, in the rhombus, the superinductances are replaced by single Josephson junctions, or arrays of a few larger junctions [Douçot and Ioffe 2012, Bell et al. 2014]. This changes the parameter regime of the circuit from $E_{\text{L}} \ll E_{\text{J}}$ to $E_{\text{L}} \sim E_{\text{J}}$, decreasing the amplitude of the $\cos 2\varphi$ term in the Hamiltonian. Second, the shunt capacitance is replaced by a gate capacitance to a voltage source [Bell et al. 2014]. This is akin to substituting an electrostatic gate for a shunt capacitance to obtain the Cooper pair box [Vion et al. 2002] from the transmon [J. Koch et al. 2007]; overall suppression of the charge dispersion is traded for the ability to bias the circuit at its charge sweet spot. Finally, the rhombus by itself is not designed to be a protected qubit. Rather, when multiple rhombi are arranged into a one-dimensional chain (or a two-dimensional fabric), the ground states are eigenstates of a nonlocal operator, which provides topological protection [Ioffe et al. 2002, Douçot and Vidal 2002, Douçot et al. 2003, Douçot and Ioffe 2012]. On one hand, our qubit does not require such scaling

9 For example, this can be done using the double-well Hamiltonian $H = \frac{1}{2}(\Delta E)\sigma_x + \frac{1}{2}\pi E_{\text{L}}(\varphi_{\text{ext}} - \pi)\sigma_z$ for φ_{ext} in the vicinity of π, where the two spin states correspond to $\phi = 0, \pi$. One then has the flux-dependent splitting $\delta E = \sqrt{(\Delta E)^2 + \pi^2 E_{\text{L}}^2(\varphi_{\text{ext}} - \pi)^2}$ and hence $\frac{\partial^2(\delta E)}{\partial \varphi_{\text{ext}}^2} = E_{\text{L}}^2/(\Delta E)$ at $\varphi_{\text{ext}} = \pi$.

to achieve protection. On the other hand, the protection we predict is inherently susceptible to local perturbations (see Ch. 7).

With respect to the 0-π qubit [Brooks et al. 2013], there are three essential distinctions. First, the pairs of superinductances on each arm of the circuit are combined, calling the possibly detrimental effects of stray capacitances to ground into question. Second, there is the addition of a second large capacitance shunting the inductive loop between its two horizontally oriented nodes. When this second capacitance is precisely C_x, this permits the exact decoupling of the θ mode from the φ mode in Eq. 2.15. Third, the 0-π qubit is operated in a parameter regime where $E_L \sim 0.01E_J$, as opposed to our circuit, where $E_L \sim 0.1E_J$ [Dempster et al. 2014]. This additional order of magnitude in the superinductance is currently under development experimentally [Shearrow et al. 2018, Pechenezhskiy et al. 2019]. Notably, the inductive loop in the 0-π qubit is threaded with $\varphi_{ext} \approx 0$ at its working point instead of $\varphi_{ext} = \pi$. This leads to a substantial change in the physics of the ground state manifold; $|0+\rangle$ and $|0-\rangle$ are approximately localized in distinct potential wells [Dempster et al. 2014]. In our case, these states are approximately the symmetric and antisymmetric superpositions of the localized wavefunctions. Only when $\varphi_{ext} = \pi$ are the ground states approximately localized in distinct Cooper pair number parities.

8

EXPERIMENTAL IMPLEMENTATION OF PROTECTED QUBITS

Our discussion up this point has culminated with the coherence estimates in Sec. 7.2.3 for the $\cos 2\varphi$ qubit, which were a synthesis of the results and techniques presented in Chs. 2–6. These estimates exceed $T_2 \sim 1\,\text{ms}$ for the known decoherence channels, which is indeed an order of magnitude higher than typical transmons given the same environmental noise [Z. Wang et al. 2019], and provide support for our claim that the $\cos 2\varphi$ qubit is protected. However, as we argued in Sec. 1.3, the figure of merit for qubit performance is actually T_2/t_{gate}, where t_{gate} is the gate time. Intuitively, this means that higher performing qubits require coherence that is improved faster than their control is inhibited [see, e.g. J. Koch et al. 2007]. In particular, for protected qubits with large T_2 values, the conventional schemes—for example, dispersive measurement as described in Sec. 5.2—begin to break down and it becomes challenging to retain low t_{gate} values.

Therefore, we find it necessary to embark on a discussion of readout and control of the $\cos 2\varphi$ qubit, which is the subject of this final chapter. The general problem of implementing gates and measurement schemes for protected qubits is highly nontrivial, as we outline in Sec. 8.1, and a complete treatment lies outside the scope of this thesis. Nonetheless, we explain the basic proposal for control and readout of the $\cos 2\varphi$ qubit in Sec. 8.2 and a report of the experimental progress in Sec. 8.2.4.

8.1 Control and readout problem in protected qubits

Protected qubits in general face the serious obstacle of realizing state manipulation and measurement while remaining sufficiently isolated from their environments to preserve their coherence. As we commented in Sec. 7.1.3, the essential feature of all protected qubits is their nonlocal encoding of the qubit states. This suppresses their susceptibility to known loss and dephasing channels, which are assumed to be local in the underlying circuit (e.g. the current I across a circuit element and the offset charge N_g on a node). This encoding has the drawback that it makes both *control*, where the $g \to e$ transition is driven, and *readout*, where the qubit state $|g\rangle$ or $|e\rangle$ is measured, difficult because they can no longer rely on local probes. In the transmon, for instance, control is realized using an ac electric field that couples to qubit electric dipole moment and readout is realized by populating a dispersively-coupled ancillary oscillator [J. Koch et al. 2007]. A protected qubit will not have these assets, because they would lead to capacitive loss and shot noise.

To be more specific, the control problem refers to the fact that, by Eq. 1.2, we have $\langle g|\mathcal{O}|e\rangle \sim \mathrm{e}^{-\ell}$ for all operators $\mathcal{O}$ that couple to the fluctuations of the environment, but that manipulation requires a Hamiltonian of the form $H_{\text{int}} = \varepsilon(t)\mathcal{M}$ where $\varepsilon(t)$ depicts a classical control field and $\mathcal{M}$ is an operator endowed with the quality $\langle g|\mathcal{M}|e\rangle = O(1)$. The $\mathcal{O}$ are in general local, as mentioned above, and the solution is for $\mathcal{M}$ to be global in the sense that it contains terms that are the product of many constituent $\mathcal{O}$, i.e. $\mathcal{M}$ is "high weight." These global operations on protected qubits are generally slower than typical operations on unprotected qubits, e.g. $\sim$10 ns for the transmon [Chow et al. 2010], and their interaction Hamiltonian introduces a new loss channel. The strategy is to either switch the interaction on/off [Brooks et al. 2013] or make it sufficiently small and strike a compromise between gate speed and protection.

The (dispersive) readout problem, on the other hand, refers to the inability to perform standard dispersive measurement of a protected qubit, owing to the large degree of insensitivity of its frequency ω_{ge} with respect to the occupation n of an ancillary oscillator, which would otherwise lead to dephasing via shot noise. Equivalently, we may say that there is no dispersive shift χ between the qubit and the oscillator. In this case, the solution is conceptually the inverse of that above: if multiple modes are engineered between the qubit and the oscillator, with substantial pairwise dispersive shifts χ_i, then cascaded dispersive readout becomes possible, where the populations of the constituent modes are inferred sequentially. Of course, the trade-off here is that additional dephasing channels are added as the readout speed increases, and we can choose to incorporate a switch or seek a compromise.

8.2 Experimental status of the $\cos 2\varphi$ qubit

8.2.1 Control and readout problem in the $\cos 2\varphi$ qubit

The $\cos 2\varphi$ qubit, for example, faces both of these problems. From Fig. 7.1 and Sec. 7.2.1, we saw that the direct qubit transition is only accessible at $\varphi_{\text{ext}} = \pi$ via inductive coupling to the qubit loop, and not via capacitive coupling to the qubit superconducting island. Such inductive coupling is unfavorable due to the native sensitivity of the qubit to inductive loss (see Sec. 7.2.3). Therefore, we envision the strategy of using multiple microwave tones, capacitively coupled to the qubit, to indirectly drive the qubit transition. By this, we mean driving $|0+\rangle$ to $|0-\rangle$ using the higher levels of the circuit.[1] We believe that this could be done using direct population transfer, in a similar fashion to the indirect manipulation of the double fluxonium in Sec. 6.5.3, or using Raman transitions, as was recently performed by Vool et al. (2018).[2]

Additionally, the readout problem in the $\cos 2\varphi$ qubit arises because there is no native dispersive shift between the qubit and any external electromagnetic mode. This is because the qubit manifold has neither an electric or magnetic dipole moment; the former can be seen by the vanishing charge matrix element in Fig. 7.1 and the latter can be seen by $\varphi_{\text{ext}} = \pi$ being a flux sweet spot (see also Sec. 5.3 for a similar discussion for the double fluxonium). In this case, we notice that there remains a native dispersive coupling

1 Another possibility is to rapidly change the external flux bias using an on-chip flux bias, so that control could be done away from $\varphi_{\text{ext}} = \pi$.

2 If these higher levels have low lifetimes, STIRAP pulses may prove useful [Bergmann et al. 1998].

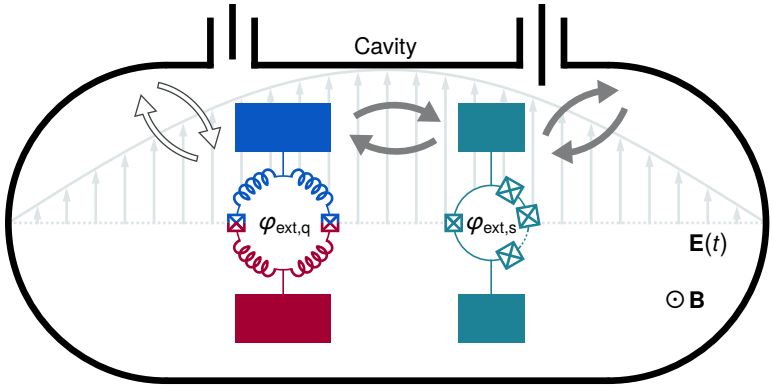

Figure 8.1 Sketch of the experimental setup used for measurement of the $\cos 2\varphi$ qubit. The protected qubit (left) couples capacitively to the ancillary mode (right), and they are together embedded in a microwave cavity. The ancillary mode comprises a Superconducting Nonlinear Asymmetric Inductive eLement (SNAIL) shunted by a capacitance; it both imbues a dispersive shift between the qubit and the cavity and dresses the qubit selection rules. The two inductive loops are threaded by external magnetic fluxes $\varphi_{\text{ext,q}}$ and $\varphi_{\text{ext,s}}$.

of the qubit to the plasmon mode of the circuit of order 20 MHz.[3] This motivates us to imagine a two-tone readout scheme where the plasmon mode serves to mediate an effective dispersive coupling between the qubit and a readout resonator. We expect this to yield a native dispersive shift that is sufficiently small to avoid shot noise dephasing, but which would enable readout via the intermediate mode(s) [see also Zhang et al. 2017].

8.2.2 Ancillary SNAIL mode

There are two remaining subtle challenges faced with this proposal, but they may be resolved by introducing an ancillary anharmonic mode (the teal circuit in Fig. 8.1). This mode is essentially a transmon, with anharmonicity in the 100 MHz range, but with the Josephson junction replaced by a Superconducting Nonlinear Asymmetric Inductive eLement (SNAIL) [Frattini et al. 2017]. This SNAIL circuit element is composed of a small Josephson junction shunted by an small array of 2–10 larger junctions, so that the combined array inductance is comparable to that of the small junction. As opposed to the dc-SQUID, the SNAIL potential energy has odd terms in its Taylor expansion for external fluxes φ_{ext} not divisible by π (i.e. not at sweet spots). This SNAIL mode is capacitively coupled to the $\cos 2\varphi$ mode and they are placed in a rectangular microwave cavity, as shown in Fig. 8.1.

For readout, this SNAIL mode couples dispersively to both the plasmon mode and the cavity mode, and hence there is an inherited dispersive shift between them (see the arrows in Fig. 8.1). Without this mode, the plasmon mode will fail to dispersively couple to the cavity due insufficient anharmonicity of order 10 MHz. This cascaded dispersive

3 Note that the plasmon mode cannot be the readout resonator, although it is very linear, because the resulting large plasmon linewidth would lead to shot noise dephasing and Purcell loss.

readout scheme involves incident microwave tones at the transition frequencies of the SNAIL mode, the plasmon mode, and the qubit.

On the other hand, for manipulation, the odd terms of the SNAIL mode potential have the effect of breaking the strict parity-based selection rules of the $\cos 2\varphi$ circuit—when the SNAIL loop is biased away from a flux sweet spot. Crucially, if we use the higher states $|1+\rangle$ or $|1-\rangle$ as the intermediate state, then one of the two necessary transitions (see Sec. 6.5.3) will have this parity-based selection rule. Hence, with the introduction of the SNAIL mode, both transitions are allowed, and Raman transitions are enabled. Finally, we comment that this proposal may appear highly specialized, but in fact it represents the nearly-ubiquitous strategy of performing manipulation and readout using excursions outside the protected manifold. Indeed, this is also how quantum error correction codes implement control and readout.

8.2.3 Gate speed estimates

Before proceeding to our discussion of the current experimental status of the $\cos 2\varphi$ qubit, we present a brief calculation of the expected gate speeds allowed by the ancillary SNAIL mode. This is done in attempt to address concerns that the $\cos 2\varphi$ qubit is a so-called "neutrino qubit,[4]" which we do not believe that it is. We assume that the $|1+\rangle$ state is used for indirect transitions—the $|1-\rangle$ case is basically identical. At the proper external flux value, the introduction of the SNAIL mode only affects the (natively forbidden) $0- \to 1+$ transition to leading order, due to the special character of the SNAIL nonlinearity [Frattini et al. 2017]. The $0+ \to 1+$ transition remains allowed using a capacitively-coupled drive (see Fig. 7.1a), and the matrix elements between $|0+\rangle$ and $|0-\rangle$ are unaffected. To this end, we simply append the term

$$H' = \hbar y \omega_{\mathrm{p}} \left(|1+\rangle\langle 0-| + |0-\rangle\langle 1+| \right)$$

to the Hamiltonian in Eq. 2.15, where $y \geq 0$ is a dimensionless quantity parameterizing the symmetry breaking and corresponding to the coupling between the SNAIL and $\cos 2\varphi$ modes. Hence we can say that ratio of electric dipole moments between the $0- \to 1+$ transition and the $0+ \to 1+$ transition is y, because $\hbar\omega_{\mathrm{p}} \gg \Delta E$.

For a sequence of two direct transitions between $|0+\rangle$ and $|0-\rangle$ through $|1+\rangle$, the total gate time t_{gate} is the sum of the individual gate times and we find $t_{\mathrm{gate}} = (1 + y^{-1})\tau_{\mathrm{gate}}$, where $\tau_{\mathrm{gate}} \sim 10\,\mathrm{ns}$ is the gate time for the $0+ \to 1+$ plasmon transition. On the other hand, for a stimulated Raman transition through a virtual state detuned from $|1+\rangle$ by $\Delta \sim 100\,\mathrm{MHz}$, the total gate time is $t_{\mathrm{gate}} = 2\Delta y^{-1}\tau_{\mathrm{gate}}^2$ [Steck 2019]. Additionally, for a STIRAP transition, the gate time is limited by the adiabaticity requirement and hence $t_{\mathrm{gate}} \gg (1 + y^2)^{-1/2}\tau_{\mathrm{gate}}$ [Bergmann et al. 1998]. The incorporation of the SNAIL mode is however not fault tolerant in the sense that it enhances the qubit sensitivity to Purcell loss through the plasmon mode. Indeed, the values quoted in Tab. 7.3 for Purcell loss are large in part due to the natively forbidden $0- \to 1+$ transition. With the SNAIL mode, the Purcell-limited relaxation time becomes $T_1 \approx y^{-2} Q_{\mathrm{cap}}(\omega_{\mathrm{p}})$ through the plasmon mode.

From the modified calculation of Purcell loss in the presence of the SNAIL mode, we conclude that we must restrict $y < 1$ in order to preserve the millisecond-range estimated

4 A *neutrino qubit* is a qubit with an enhanced coherence time T_2, but no improvement relative to the gate time t_{gate}, and hence limited practical utility.

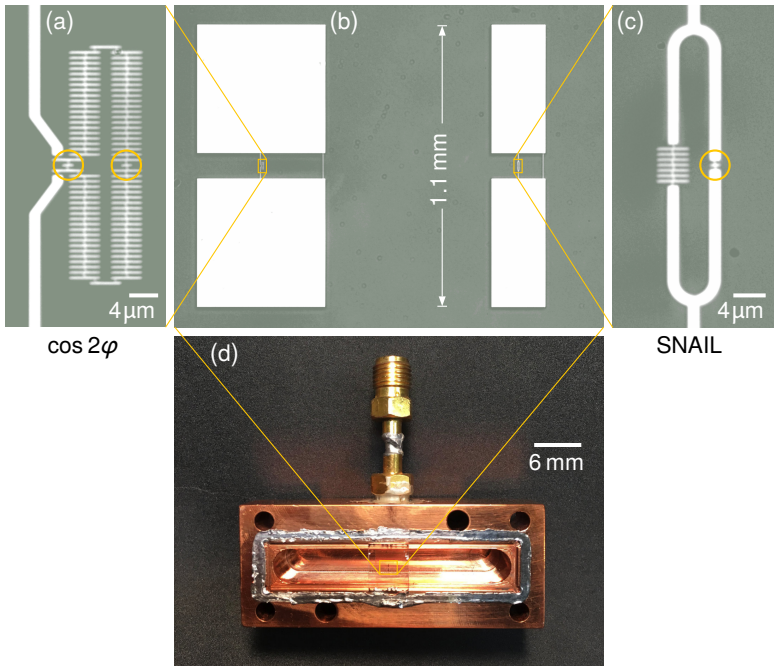

Figure 8.2 Cascaded dispersive measurement of the $\cos 2\varphi$ qubit with an ancillary SNAIL mode in a cavity. (a) Optical image of the $\cos 2\varphi$ qubit. (b) Optical image of the full device. (c) Optical image of the ancillary SNAIL mode. Both magnified panels contain circles identifying the small Josephson junctions. (d) Image of the copper cavity, showing its weakly coupled output coaxial port. The opposite half and the coil of superconducting wire used for magnetic flux biasing are not shown.

coherence of the $\cos 2\varphi$ qubit. In turn, this restricts the total SNAIL-assisted gate time to $20\,\text{ns} < t_{\text{gate}} < 100\,\text{ns}$ provided $y^{-1} < 5$. Therefore, we expect the gate speed in the $\cos 2\varphi$ qubit to be reduced by a fairly benign $O(1)$ factor while the coherence time is improved by an order of magnitude, and hence the figure of merit T_2/t_{gate} has the potential to improve from $\sim 10^4$ to $\sim 10^5$ [Z. Wang et al. 2019].

8.2.4 Spectroscopy of the $\cos 2\varphi$ qubit

In the final section of this chapter, we present the progress made toward physical implementation of the $\cos 2\varphi$ qubit. As described in above, the physical system was composed of two superconducting circuits, fabricated using aluminum on a single sapphire chip as shown in Fig. 8.2b, and mounted in a microwave cavity. In the measured sample, the $\cos 2\varphi$ circuit (see Fig. 8.2a) comprised a loop with two small Josephson junctions and 86 large junctions, connected to two large electrodes. The SNAIL circuit (see Fig. 8.2c) had a loop with one small junction and 7 large junctions, and it was connected to two capacitor pads. The two devices were placed 600 μm apart and mounted in a copper rectangular cavity (see Fig. 8.2d), which was fastened to a superconducting coil used as a magnetic flux bias.

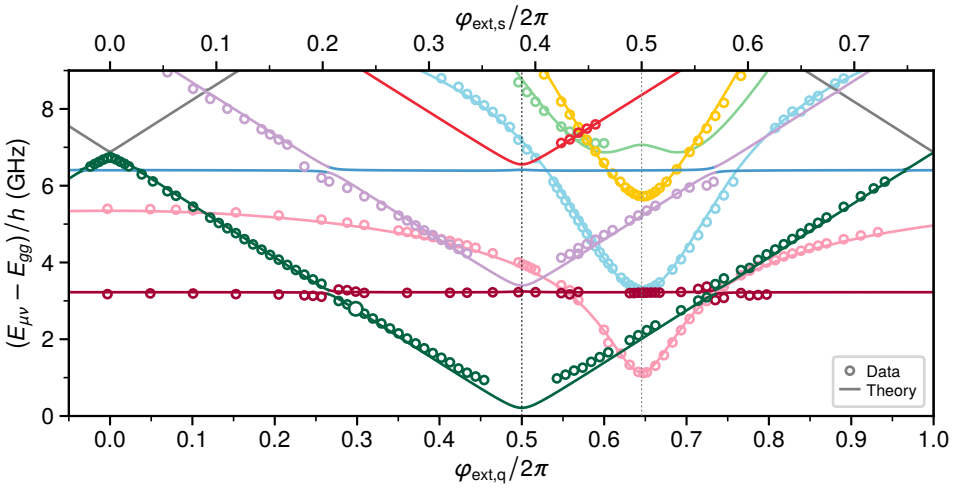

Figure 8.3 Energy spectrum of the $\cos 2\varphi$ qubit and ancillary SNAIL mode: theory vs. experiment as a function of external flux. Circles indicate values measured by two-tone spectroscopy and lines indicate theoretical fits obtained from numerical diagonalization. Curves centered about $\varphi_{\text{ext,q}} = \pi$ (dashed black) correspond to the $\cos 2\varphi$ qubit and those centered about $\varphi_{\text{ext,s}} = \pi$ (dashed grey) correspond to the SNAIL mode. The invisibility of the qubit transition near $\varphi_{\text{ext,q}} = \pi$ is related to its protection.

Moreover, the loop areas of the two devices were designed to differ by approximately 20% to maximize the odd terms in the SNAIL potential when the $\cos 2\varphi$ loop was biased to half flux. The sample was mounted to the base plate of a dilution refrigerator at $\sim$16 mK and measured in a transmission configuration using the techniques described in Ch. 5.

Notably, although the parameters of the $\cos 2\varphi$ qubit used in simulation (see Tab. 2.2) were experimentally feasible, we deliberately chose to use a smaller shunt capacitance as well as a high degree of inductive asymmetry δ_{L}. Together, these differences between the physical and theoretical device enabled us to collect spectroscopy data without facing too severe control and readout problems, as discussed in Sec. 8.2.1.

We performed two-tone spectroscopy of the $\cos 2\varphi$ and SNAIL mode with the cavity as the readout resonator, ultimately observing four transitions from the ground state for both devices, as can be seen in Fig. 8.3. Based on the observed periodicity as well as the size of the avoided crossings in the single-tone cavity spectroscopy, we identify each transition as corresponding to the $\cos 2\varphi$ or the SNAIL. We then fit these data to the results from numerical diagonalization of both individual Hamiltonians, as shown in Fig. 8.3, to obtain the parameters listed in Tab. 8.1. Additionally, at a variety of external flux points we measured the coherence properties of the $|0\circ\rangle$ and $|0\bullet\rangle$ manifold directly. As a representative example, the large white dot near $\varphi_{\text{ext,q}} = 0.6\pi$ corresponds to the measured relaxation time $T_1 = 140\,\mu\text{s}$, Ramsey decoherence time $T_{2\text{R}} = 5\,\mu\text{s}$, and spin-echo decoherence time $T_{2\text{E}} = 20\,\mu\text{s}$. These lifetimes are consistent with those observed in fluxonium and fluxonium-like qubits away from their flux sweet spots—see Ch. 6.

The excellent agreement between the measured values and the energy levels found

	E_C/h (GHz)	E_L/h (GHz)	E_J/h (GHz)	x	δ_L
$\cos 2\varphi$	2.83	0.76	12.03	0.12	0.88
SNAIL	4.56	5.77	7.46	0.06	

Table 8.1 Circuit parameters used for fits of the $\cos 2\varphi$ and SNAIL devices in Fig. 8.3.

from numerical diagonalization, shown in Fig. 8.3, confirms the Hamiltonian in Eq. 2.15.[5] The central result, however, is the complete inability to drive and/or readout the qubit in the vicinity of $\varphi_{ext,q} = \pi$, which we argued in Sec. 8.2 would be a hallmark of the physics of the $\cos 2\varphi$ device. Of course, this is not conclusive proof of protection in the $\cos 2\varphi$ circuit, but rather encouraging evidence. It still remains to demonstrate indirect control and cascaded dispersive readout, and ultimately to measure the coherence times of the $\cos 2\varphi$ qubit.

5 A possible exception is the slight bending of the data points away from the theory curve for the dark green (qubit) transition. Anticrossings like these were also observed to be larger in experiment than in theory for the double fluxonium. We suspect that they are related to phase-slips across Josephson junctions in arrays, which are neglected in our circuit models.

9

CONCLUSION

9.1 Summary of results

This thesis sought to answer the question: with protection defined by Eq. 1.2, how do we design a superconducting circuit that is protected with respect to a given set of operators that couple to the fluctuations of the environment? Over the past seven chapters, we have described the process of evaluating the degree of protection of a given superconducting qubit, from quantizing its circuit to measuring its coherence times. It is difficult to invert this procedure, and thereby answer our original question. This led us to adopt the more pragmatic approach of carrying out this process for multiple candidate circuits, in order to design a protected qubit by trial and error.

Chronologically, we started with the fluxonium qubit, inductively coupled to a readout antenna and measured in a waveguide, where relaxation times in excess of $T_1 = 100\,\mu s$ were measured. Ramsey coherence times, on the other hand, were observed to be $T_{2R} \approx 25\,\mu s$ and likely limited by shot noise (see Fig. 6.1). The double fluxonium circuit was then conceived, in part, due to the extremely weak dependence of the qubit frequency on the common-mode external magnetic flux. This qubit also demonstrated fairly long relaxation times up to $T_1 = 300\,\mu s$, but its Ramsey coherence times were limited to $T_{2R} \lesssim 1\,\mu s$ due to differential-mode flux noise (see Tab. 5.2). Finally, we proposed the $\cos 2\varphi$ circuit in Fig. 2.3, which has a small dispersive shift, and hence insensitivity to shot noise, and a single inductive loop, and hence immunity to differential-mode flux noise. Protection in the $\cos 2\varphi$ qubit is suggested by theoretical estimates of its coherence times, which are in the millisecond range, and understood as a consequence of the conservation of Cooper pair number parity.

9.1.1 Toolkit for designing protected superconducting qubits

In explaining these results, we divided our discussion into seven chapters, each of which introduced a technique useful for the design, implementation, and validation of protected superconducting qubits. In Chs. 2–4, we addressed the theoretical description of the static properties of circuits. This included quantization of lumped element electrical circuits, transformations and approximations for building effective circuit Hamiltonians, as well as numerical diagonalization to obtain energy levels and matrix elements. We turned our attention in Ch. 5 to the experimental measurement of these static properties, using spectroscopic techniques in cQED. Ch. 6 marked a change of focus to dynamic properties of circuits, as we described the experimental characterization of common noise sources.

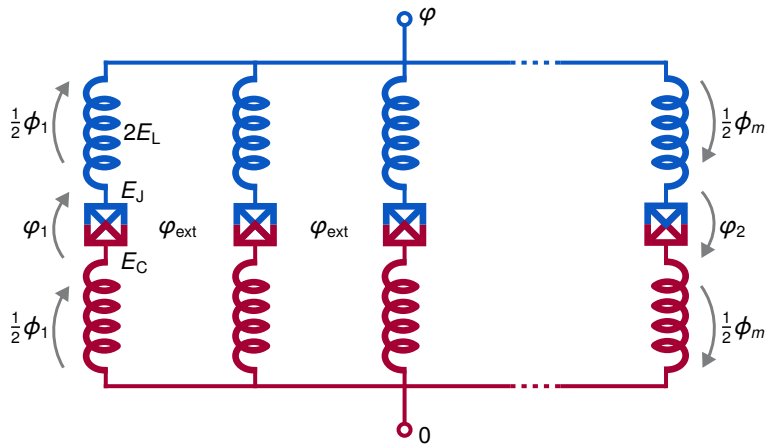

Figure 9.1 Electrical circuit diagram for the generalized $\cos m\varphi$ element. There are m arms in parallel; the i-th arm is composed of two superinductances, each with phase drop $\phi_i/2$, on either side of one small Josephson junction, with phase drop φ_i. Each of the $m-1$ inductive loops is threaded with the same external magnetic flux φ_{ext}, and the total circuit behaves as an effective $\cos m\varphi$ element when $\varphi_{\text{ext}} = 2\pi/m$.

This was followed in Ch. 7 by the associated discussion on a theoretical level: coherence time estimates and noise models. Finally, we presented a brief chapter on the experimental implementation challenges for protected qubits in Ch. 8.

9.1.2 Protection in the $\cos 2\varphi$ and similar qubits

The $\cos 2\varphi$ qubit is a few-body superconducting circuit in which the charge carriers are well-approximated by pairs of Cooper pairs at a particular bias point. The Josephson tunneling element that supports these charge carriers is characterized by a $\cos 2\varphi$ term in the Hamiltonian, whose emergence we have shown analytically. Our numerical simulations supplement these arguments and demonstrate protection against a variety of common relaxation and dephasing sources. We find that this protection is substantially enhanced in the presence of inductive asymmetry, ultimately leading to coherence time estimates of order 1 ms. These coherence times would offer a considerable improvement over the existing qubit varieties.

9.2 Perspectives

9.2.1 Generalized $\cos m\varphi$ circuit element

A natural question that arises from our analysis of the $\cos 2\varphi$ qubit is whether the circuit can be generalized, so that the effective potential energy has the form

$$U = (-1)^m E_{\text{J}} \cos m\varphi. \tag{9.1}$$

Note that the sign prefactor simply ensures that the potential is maximized at the Brillouin zone boundary, i.e. at $\varphi = \pm\pi$. In the $\cos 2\varphi$ qubit, we did not confront this prefactor because the remaining degree of freedom φ was different from the phase across the element by π. We answer this question in the affirmative, and the circuit is shown in Fig. 9.1.

In this circuit, there are m arms in parallel, each of which contains a small Josephson junction in series with two superinductances on either side. The junctions have tunneling energy E_J and charging energy E_C, while the superinductances have inductive energy E_L, and the parameters satisfy $E_\mathrm{L} \ll E_\mathrm{J}$. It is clear that this circuit reduces to the $\cos 2\varphi$ element in Fig. 2.3 when $m = 2$. There are then $m-1$ inductive loops, and the $\cos m\varphi$ term becomes dominant when the bias condition $\varphi_\mathrm{ext} = 2\pi/m$ is met.[1] At this point, Cooper pairs tend to tunnel across the element in multiples of m, and conversely, fluxons traverse the element fractionally in multiples of $1/m$. This can be seen as a single fluxon moving from one loop in the chain to the next. From an experimental point of view, the primary implementation challenge is the ability to incorporate $m-1$ external flux biases. These would be needed to properly bias each loop in the presence of loop area disorder and magnetic field inhomogeneity.

Additionally, we can compare Eq. 9.1 to the potential of a conventional Josephson junction in terms of creation/annihilation operators, $U = -E_\mathrm{J}\cos[\varphi_\mathrm{zpf}(a + a^\dagger)]$ (see Sec. 3.1). This shows that the factor of m in the argument of the cosine may be regarded as

1 Here we sketch the derivation of the effective Lagrangian for the $\cos m\varphi$ circuit in Fig. 9.1. The $m-1$ inductive loops yield the constraints $\varphi_i + \phi_i - (\varphi_{i+1} + \phi_{i+1}) = \varphi_\mathrm{ext}$ for $i = 1, 2, \ldots, m-1$. Note that the φ_i correspond to the small junctions and the ϕ_i to the superinductances. This allows us to eliminate all the ϕ_i except one, which we take to be $\sum_i \phi_i = \phi$. This procedure yields

$$\phi_i = \frac{\phi}{m} + \frac{1}{m}\sum_j \varphi_j - \varphi_i + \left[\tfrac{1}{2}(m+1) - i\right]\varphi_\mathrm{ext}.$$

Now we set $\varphi_\mathrm{ext} = 2\pi/m$ and recall that, in the limit $E_\mathrm{L} \gg E_\mathrm{J}$, the junction phases are approximately $\varphi_i = 2\pi n_i$ for integers n_i. We may then write $\phi_i = \phi/m + 2\pi\delta_i/m$, where the arm-dependent term is

$$\delta_i = \sum_j n_j - mn_i + \tfrac{1}{2}(m+1) - i.$$

Because the superinductances are all equal, they contribute a total energy $\frac{1}{2}E_\mathrm{L}\sum_i \phi_i^2$, where we can write $\sum_i \phi_i^2 = \phi^2/m + (2\pi/m)^2\sum_i \delta_i^2$ since $\sum_i \delta_i = 0$. We then minimize this energy with respect to the n_i to find

$$n_i = \mathrm{round}\left[\frac{1}{2} + \frac{1}{m}\sum_j n_j + \frac{1-2i}{2m}\right],$$

which is a unique solution of the n_i for each $\sum_i n_i$. We see that, as $\sum_i n_i$ is increased, each n_i is incremented by one in turn, corresponding to a helix in φ-space (in two dimensions, the zig-zag in Fig. 3.1). Constraining the system to this path, we obtain the effective Lagrangian

$$\mathcal{L}_\mathrm{eff} = \frac{\hbar^2}{16E_\mathrm{C}}\dot{\varphi}_{\tilde{\imath}}^2 + E_\mathrm{J}\cos\varphi_{\tilde{\imath}}$$

to leading order in $E_\mathrm{J}/E_\mathrm{L}$ and with $\phi \to 0$, where $\tilde{\imath}$ is the index of the junction whose phase is currently being incremented. Up to multiples of 2π, the phase across the whole element is $\varphi = \frac{1}{m}\sum_i \varphi_i + \pi(m+1)/m = \varphi_{\tilde{\imath}}/m + \pi(m+1)/m$ and so the effective Lagrangian is

$$\mathcal{L}_\mathrm{eff} = \frac{\hbar^2}{16E_\mathrm{C}}m^2\dot{\varphi}^2 + (-1)^{m+1}E_\mathrm{J}\cos m\varphi,$$

justifying Eq. 9.1. Note that taking $\phi \to 0$ by energy minimization corresponds in the $\cos 2\varphi$ qubit to $\theta \to 0$ (see Sec. 3.3). Furthermore, the additive constant in φ yields the sign prefactor for $\cos m\varphi$, which ensures that the potential is maximized at the Brillouin zone boundary. Indeed, this is nothing more than a choice of gauge—and in the $\cos 2\varphi$ qubit we avoided the sign altogether—but we present it here for completeness.

dressing the amplitude of zero-point fluctuations of the phase $\varphi_{\text{zpf}} \to m\varphi_{\text{zpf}}$. We also recall that $\varphi_{\text{zpf}} = (2E_{\text{C}}/E_{\text{L}})^{1/4} = \sqrt{Z_0/(2\mathcal{R}_{\text{Q}})}$ for an LC oscillator with charging energy E_{C} and inductive energy E_{L}—or alternatively characteristic impedance $Z_0 = \sqrt{L/C}$. Here, $\mathcal{R}_{\text{Q}} = \hbar/(2e)^2$ is the reduced superconducting resistance quantum, which symmetrically normalizes the phase and charge fluctuations so that $N_{\text{zpf}} = \sqrt{\mathcal{R}_{\text{Q}}/(2Z_0)}$. This shows that the $\cos m\varphi$ element may be viewed as dressing the characteristic impedance $Z_0 \to m^2 Z_0$. This effectively larger oscillator impedance seen by the $\cos m\varphi$ element may prove useful for encoding and manipulating quantum information in long-lived microwave cavities [Reagor et al. 2013] with nonlocal perturbations [Cohen et al. 2017].

9.2.2 Outlook for protected qubits

At various stages of our discussion, we have alluded to the commonalities and shared interests between building protected qubits and implementing quantum error correction [Aharonov and Ben-Or 2008]. The basic idea is that both research goals aim to realize logical qubits, that is, qubits whose T_2/t_{gate} is so large that they can be used for fault-tolerant quantum computation (a commonly-quoted threshold is 10^5 [Aliferis et al. 2006]). The central difference is that quantum error correction is usually seen as a "software" approach, in that energy is injected into the system, while protected qubits are a "hardware" approach, in that no supplemental drives are added.

Work aimed at improving quality factors associated with coupling to different thermal baths [Martinis et al. 2005, Barends et al. 2013, Houck et al. 2008] and noise spectral densities for different Hamiltonian parameters [Paik et al. 2011, Rigetti et al. 2012, Kumar et al. 2016], though similar, does not constitute protection in the Hamiltonian sense that we have been using. For this brand of protection, a popular approach to suppressing qubit relaxation has been to localize wavefunctions in disparate regions of phase space to lessen transition matrix elements [Pop et al. 2014, Bell et al. 2014, Earnest et al. 2018, Lin et al. 2018]. On the other hand, delocalization of the same wavefunctions has been shown to mitigate dephasing effects by reducing qubit sensitivity to Hamiltonian parameters [van der Wal et al. 2000, Vion et al. 2002, J. Koch et al. 2007, Manucharyan et al. 2009, Steffen et al. 2010, Yan et al. 2016]. Superconducting circuits with multiple degrees of freedom whose qubit wavefunctions are both localized and delocalized combine both of these approaches. In these circuits, quantum information is diffused among constituent local degrees of freedom, providing protection from local perturbations. The many-body limit promises topological protection [Ioffe et al. 2002, Douçot and Vidal 2002, Douçot et al. 2003, Kitaev 2006], in which global operators are necessary to manipulate logical qubits, but the few-body case offers an experimentally realistic approximation [Cottet et al. 2002, Gladchenko et al. 2009, Brooks et al. 2013, Bell et al. 2014, Dempster et al. 2014, Groszkowski et al. 2018].

Just as error correction hinges on the assumption that the noise couples to each qubit independently—i.e. the error in each qubit is independent of the errors in all other qubits—protected qubits rely on the system operators that couple to the bath, and the noisy parameters, being local with respect to the encoding basis. Both strategies offer poor protection against correlated errors, for which the error threshold can scale unfavorably, e.g. $T_2/t_{\text{gate}} \gtrsim 10^{10}$ for some two-qubit cases [Aharonov et al. 2006]. In such cases, alternative methods such as dynamical decoupling or decoherence-free subspaces may be beneficial [Lidar et al. 1998, L. Viola et al. 1999, Novais and Baranger 2006]. The most important

peripheral result of this thesis, from Ch. 6, is that our measurements of noise have thus far been entirely uncorrelated. This was shown both for flux noise in the double fluxonium and dissipation in fluxonium artificial atoms.

9.2.3 Final remarks

In closing, we believe that the enterprise of engineering protected qubits has just begun, even if the proposed circuits appear to be quite exotic at this stage. The prospects include circuits tailored specifically for a purpose, such as a high degree of protection from a particularly detrimental effect. Moreover, despite their apparent simplicity, quantum electrical circuits may prove interesting from a topological standpoint. Finally, circuits whose potential energies are dominated by $\cos 2\varphi$ terms open the door to more exotic designs with potentials of the form $\cos m\varphi$ or $\cos(\varphi/m)$, with $m \in \mathbb{N}$. There is, then, the possibility of piecing together the potential of a Hamiltonian using hardware that corresponds to distinct term in the Fourier series. In many ways, these effective circuit elements realize a generalized version of the Josephson effect based on correlated/fractional Cooper pair tunneling.

A

MATHEMATICAL CONVENTIONS

In this brief appendix, we clarify our choice of Fourier transform convention, as used in Chs. 6–7, and other mathematical notation used in the subsequent appendices.

Temporal Fourier transform We employ the one-sided temporal Fourier transform $\mathcal{F}$, defined by[1]

$$f[\omega] = \mathcal{F}[f(t)] = \int_{-\infty}^{\infty} \mathrm{d}t\, \mathrm{e}^{i\omega t} f(t)$$
$$f(t) = \mathcal{F}^{-1}[f[\omega]] = \int_{-\infty}^{\infty} \frac{\mathrm{d}\omega}{2\pi} \mathrm{e}^{-i\omega t} f[\omega].$$

The convolution theorem reads $\mathcal{F}(f \cdot g) = \mathcal{F}(f) * \mathcal{F}(g)$, where our choice of Fourier transform demands that angular frequency convolution be defined by

$$f[\omega] * g[\omega] = \int_{-\infty}^{\infty} \frac{\mathrm{d}\omega'}{2\pi} f[\omega'] g[\omega - \omega'].$$

Spatial Fourier transform A similar convention is used for the spatial Fourier transform $\mathcal{G}$, with two varieties depending on whether we want the transformed variable to be discrete or continuous[1]

$$V_{\mathbf{k}} = \mathcal{G}[V(\mathbf{x})] = \frac{1}{\mathcal{V}} \int \mathrm{d}^3x\, \mathrm{e}^{-i\mathbf{k}\cdot\mathbf{x}} V(\mathbf{x}) \qquad V[\mathbf{k}] = \mathcal{G}[V(\mathbf{x})] = \int \mathrm{d}^3x\, \mathrm{e}^{-i\mathbf{k}\cdot\mathbf{x}} V(\mathbf{x})$$
$$V(\mathbf{x}) = \mathcal{G}^{-1}[V_{\mathbf{k}}] = \sum_{\mathbf{k}} \mathrm{e}^{i\mathbf{k}\cdot\mathbf{x}} V_{\mathbf{k}} \qquad V(\mathbf{x}) = \mathcal{G}^{-1}[V[\mathbf{k}]] = \int \frac{\mathrm{d}^3k}{(2\pi)^3} \mathrm{e}^{i\mathbf{k}\cdot\mathbf{x}} V[\mathbf{k}],$$

where $\mathcal{V}$ is the finite volume of the integration region needed in order for $\mathbf{k}$ to be discrete. The relevant delta function identities (the Dirac delta is the infinite-volume limit of the Kronecker delta) are

$$\int_{-\infty}^{\infty} \mathrm{d}t\, \mathrm{e}^{i\omega t} = 2\pi\delta(\omega) \qquad \int \mathrm{d}^3x\, \mathrm{e}^{i\mathbf{k}\cdot\mathbf{x}} = \mathcal{V}\delta_{\mathbf{k},0} \qquad \int \mathrm{d}^3x\, \mathrm{e}^{i\mathbf{k}\cdot\mathbf{x}} = (2\pi)^3\delta(\mathbf{k}).$$

1 Here we use parentheses and brackets to indicate whether or not the function is the Fourier transform in the continuous case. In the discrete case, the argument of the Fourier transformed function is a subscript.

Distributive notation for integrals We find it convenient, when discussing spin-echo decoherence measurements in App. C, to use the distributive notation for multiple integrals,

$$\left(\int_{I_1} + a \int_{I_2}\right)^2 \mathrm{d}x_1\, \mathrm{d}x_2 = \left(\int_{I_1}\int_{I_1} + a\int_{I_1}\int_{I_2} + a\int_{I_2}\int_{I_1} + a^2 \int_{I_2}\int_{I_2}\right)\mathrm{d}x_1\, \mathrm{d}x_2\,.$$

Note that these integrals do not commute, since their order reflects the relevant integration variable, and that the scalar a has been included for illustration.

Wick's theorem In App. C (in the classical case) and App. D (in the quantum case), we use Wick's theorem. For clarity, we first present it here:

$$\langle \mathcal{O}_1 \mathcal{O}_2 \mathcal{O}_3 \mathcal{O}_4 \rangle = \langle \mathcal{O}_1 \mathcal{O}_2 \rangle \langle \mathcal{O}_3 \mathcal{O}_4 \rangle \pm \langle \mathcal{O}_1 \mathcal{O}_3 \rangle \langle \mathcal{O}_2 \mathcal{O}_4 \rangle + \langle \mathcal{O}_1 \mathcal{O}_4 \rangle \langle \mathcal{O}_2 \mathcal{O}_4 \rangle,$$

where the positive sign is for bosonic operators and the negative sign is for fermionic ones. Note that the result does not change in the presence of daggers and repeated indices.

B

PERTURBATION THEORY FOR ENERGY LEVELS AND TRANSITION RATES

The main purpose of this appendix is to review time-independent perturbation theory insofar as it was used to calculate the parameters of the fluxonium dispersive Hamiltonian in Sec. 4.3, which we compared to those obtained from numerical diagonalization. Additionally, we explain the link between second-order perturbation theory and Fermi's Golden Rule in Eqs. 6.1 and 7.2, for self-consistency.

B.1 Time-independent perturbation theory

B.1.1 Second-order energy corrections

Perturbation theory, in general, describes approximate solutions to the Schrödinger equation for systems whose Hamiltonians can be effectively separated into "large" and "small" components. We recall that the time-independent Schrödinger equation is simply the eigenvalue equation in Eq. 4.1, which takes the form

$$H|n\rangle = \hbar\omega_n|n\rangle \tag{B.1}$$

when the countable eigenvector index μ is replaced by n and the energy levels are $E_n = \hbar\omega_n$. The main assumption is that H has the form $H_0 + H_1$, where H_1 constitutes a perturbation to H_0. An iterative procedure yields a power series solution for the eigenstates and their frequencies,

$$\omega_n = \omega_n^{(0)} + \omega_n^{(1)} + \omega_n^{(2)} + \dots$$
$$|n\rangle = |n^{(0)}\rangle + |n^{(1)}\rangle + |n^{(2)}\rangle + \dots,$$

where the superscript indicates the order of the term. The essential utility lies in the fact that H_1 is small compared to H_0, and so these expansions converge rapidly and may be truncated after the first few terms.

To be more specific, the unperturbed eigenstates $|n^{(0)}\rangle$ and their energies $\hbar\omega_n^{(0)}$ are merely solutions to the Schrödinger equation for H_0, i.e. $H_0|n^{(0)}\rangle = \hbar\omega_n^{(0)}|n^{(0)}\rangle$. The first order correction to the energy levels is

$$\hbar\omega_n^{(1)} = \langle n^{(0)}|H_1|n^{(0)}\rangle, \tag{B.2}$$

while that for the eigenkets is

$$|n^{(1)}\rangle = \frac{1}{\hbar}\sum_{m\neq n}\frac{\langle m^{(0)}|H_1|n^{(0)}\rangle}{\omega_n^{(0)}-\omega_m^{(0)}}|m^{(0)}\rangle. \tag{B.3}$$

The expressions become increasingly complicated to higher orders, and it is often only necessary to go to second order, where the energy level correction is

$$\hbar\omega_n^{(2)} = \frac{1}{\hbar}\sum_{m\neq n}\frac{|\langle m^{(0)}|H_1|n^{(0)}\rangle|^2}{\omega_n^{(0)}-\omega_m^{(0)}}. \tag{B.4}$$

B.1.2 Example: Fluxonium artificial atom

For the perturbative calculation shown in Fig. 4.3, which was our benchmark for the utility of numerical diagonalization, we start with Eq. 4.7 for the Hamiltonian and apply Eqs. B.2 and B.4. Using $|\lambda_3| \ll 1$, we first Taylor expand about $\lambda_3 = 0$ to second order, and find

$$\begin{aligned} H = {} & \frac{1}{2C_\mathrm{R}}Q_\mathrm{R}^2 + \frac{1}{2L_\mathrm{R}}\Phi_\mathrm{R}^2 + \frac{1}{2C_\mathrm{Q}}Q_\mathrm{Q}^2 + \frac{1}{2L_\mathrm{Q}}\Phi_\mathrm{Q}^2 - E_\mathrm{J}\cos(\lambda_4\varphi_\mathrm{Q}-\varphi_\mathrm{ext}) \\ & + E_\mathrm{J}\left[\lambda_3\varphi_\mathrm{R}\sin(\lambda_4\varphi_\mathrm{Q}-\varphi_\mathrm{ext}) + \tfrac{1}{2}(\lambda_3\varphi_\mathrm{R})^2\cos(\lambda_4\varphi_\mathrm{Q}-\varphi_\mathrm{ext})\right]. \end{aligned}$$

Although $|\lambda_3| \ll 1$ justifies both the replacement of Eq. 4.7 by the above and the use of perturbation theory on its last two terms, the majority of error arises from the latter step. We may then consider the first five terms above as the unperturbed Hamiltonian H_0, which coincides with the decoupled Hamiltonian from Sec. 4.3. First- and second-order perturbation theory may then be used on the seventh and sixth terms, respectively. This results in corrections of the form

$$\begin{aligned} E_{n\mu}^{(1)} + E_{n\mu}^{(2)} = {} & E_\mathrm{J}(\lambda_3\varphi_\mathrm{zpf,R})^2\left(n+\tfrac{1}{2}\right)\langle\mu|\cos(\lambda_4\varphi_\mathrm{Q}-\varphi_\mathrm{ext})|\mu\rangle \\ & - E_\mathrm{J}^2(\lambda_3\varphi_\mathrm{zpf,R})^2\sum_{\nu\neq\mu}\frac{(2n+1)E_{\mu\nu}-\hbar\omega_\mathrm{R}}{E_{\mu\nu}^2-(\hbar\omega_\mathrm{R})^2}\left|\langle\nu|\sin(\lambda_4\varphi_\mathrm{Q}-\varphi_\mathrm{ext})|\mu\rangle\right|^2 \end{aligned}$$

for the state with readout index n and qubit index μ. This completes the calculation of the energy levels $E_{n\mu} \approx E_{n\mu}^{(0)} + E_{n\mu}^{(1)} + E_{n\mu}^{(2)}$ for the system via perturbative treatment of the readout-qubit coupling, where we recall that $E_{n\mu}^{(0)} = \hbar\omega_\mathrm{R}(n+\frac{1}{2}) + E_\mu$. Note that the E_μ and $|\mu\rangle$ are computed using numerical diagonalization, and also that $E_{\mu\nu} = E_\nu - E_\mu$.

B.2 Fermi's golden rule

One particularly useful result from perturbation theory is Fermi's Golden Rule, which describes the transition rate between two eigenstates of the unperturbed Hamiltonian, due to the perturbation. We consider the state of the system to be an arbitrary eigenstate $|i\rangle$ of the unperturbed Hamiltonian H_0 at $t = 0$. The system then evolves under the influence of the perturbed Hamiltonian H until time t, at which point there is a nonzero probability of

finding the system to be in another eigenstate $|f\rangle$. Through two applications of Eq. B.3, we find the transition rate

$$\Gamma_{i\to f} = \frac{2}{\hbar^2}|\langle f|H_1|i\rangle|^2 \frac{\sin \omega_{if} t}{\omega_{if}} \approx \frac{2\pi}{\hbar^2}|\langle f|H_1|i\rangle|^2 \delta(\omega_{if}), \tag{B.5}$$

where the transition frequency is $\omega_{if} = \omega_f - \omega_i$. The final approximation holds for $t \gg 1/\omega_{if}$, i.e. after many oscillations of the phase between the states $|i\rangle$ and $|f\rangle$, once we recognize that $\lim_{\epsilon\to 0} \frac{1}{x} \sin \frac{x}{\epsilon} = \pi\delta(x)$—at least in the case where it resides inside an integral.

Eq. B.5 is the most basic form of Fermi's Golden Rule, and the delta function enforces energy conservation over long times. In this thesis, we were mostly interested in transitions that do not conserve the energy of the system, because they involve interactions with the environment. To understand this process, we apply Eq. B.5 to a system with $H_0 = H_S + H_R$ (with H_S and H_R representing the system and reservoir, respectively) and $H_1 = XF$ (with X and F being system and reservoir variables, respectively). We then call $|nr\rangle$ the eigenstates of the unperturbed Hamiltonian with eigenvalues $\hbar(\omega_n + \omega_r)$. Eq. B.5 gives us

$$\Gamma_{ir\to f\bar{r}} = \frac{1}{\hbar^2}|\langle f|X|i\rangle|^2 |\langle \bar{r}|F|r\rangle|^2 \int_{-\infty}^{\infty} \mathrm{d}t\, \mathrm{e}^{-i(\omega_{if}+\omega_{r\bar{r}})t}$$

using the integral representation of the delta function $\int_{-\infty}^{\infty} \mathrm{d}t\, \mathrm{e}^{-i\omega t} = 2\pi\delta(\omega)$. Moving to the interaction picture with respect to H_R yields $F(t) = \mathrm{e}^{iH_R t/\hbar} F(0) \mathrm{e}^{-iH_R t/\hbar}$, and so

$$\Gamma_{ir\to f\bar{r}} = \frac{1}{\hbar^2}|\langle f|X|i\rangle|^2 \int_{-\infty}^{\infty} \mathrm{d}t\, \mathrm{e}^{-i\omega_{if} t} \langle r|F(t)|\bar{r}\rangle\langle \bar{r}|F(0)|r\rangle.$$

We now equate $\Gamma_{i\to f}$ to $\sum_{r,\bar{r}} p_r \Gamma_{ir\to f\bar{r}}$ (with p_r being the population), and employ the definition of the statistical average $\langle F(t)F(0)\rangle = \mathrm{Tr}[\rho F(t)F(0)] = \sum_r p_r \langle r|F(t)F(0)|r\rangle$ (with ρ being the density matrix), to obtain

$$\Gamma_{i\to f} = \frac{1}{\hbar^2}|\langle f|X|i\rangle|^2 \int_{-\infty}^{\infty} \mathrm{d}t\, \mathrm{e}^{-i\omega_{if} t} \langle F(t)F(0)\rangle.$$

We recognize $\langle F(t)F(0)\rangle$ as the autocorrelation function. Its Fourier transform is the noise spectral density $S_{FF}[\omega]$, as promised by the Wiener-Khinchin theorem (so long as F is sufficiently stationary). Mathematically, this amounts to $S_{FF}[\omega] = \int_{-\infty}^{\infty} \mathrm{d}t\, \mathrm{e}^{i\omega t} \langle F(t)F(0)\rangle$, and equivalently $\langle F(t)F(0)\rangle = \int_{-\infty}^{\infty} \frac{\mathrm{d}\omega}{2\pi} \mathrm{e}^{-i\omega t} S_{FF}[\omega]$. We recover the well-known result

$$\Gamma_{i\to f} = \frac{1}{\hbar^2}|\langle f|X|i\rangle|^2 S_{FF}[-\omega_{if}], \tag{B.6}$$

which then yields Eqs. 6.1 and 7.2.

C

DEPHASING THEORY

As we saw in Chs. 6 and 7, modeling the pure dephasing rate of a qubit in general involves detailed assumptions about the character of the noise and the measurement sequence. In this appendix, we supplement the discussion in those chapters by providing a review of certain aspects of dephasing theory. The material here is a synthesis of that in Cottet (2002), Makhlin and Shnirman (2004), and Ithier et al. (2005); with some additional calculations and comparisons for $1/f$ noise in Fig. C.2 and Tab. C.1.

C.1 General framework

Suppose that we have a two-level system whose Hamiltonian is given by

$$H(t) = \hbar\Omega(t)|e\rangle\langle e| = \hbar\left[\Omega_0 + \left.\frac{\partial\Omega}{\partial\lambda}\right|_0 \lambda(t) + \frac{1}{2}\left.\frac{\partial^2\Omega}{\partial\lambda^2}\right|_0 \lambda^2(t) + \dots\right]|e\rangle\langle e|, \tag{C.1}$$

with λ being a noisy external parameter with zero mean. The time-evolution operator $U(t, t_0)$ is easy to construct by plugging $\psi(t) = U(t, t_0)\psi(t_0)$ into the time-dependent Schrödinger equation $i\hbar\frac{\partial}{\partial t}\psi = H\psi$. We obtain

$$U(t, t_0) = \mathcal{T}\exp\left(-\frac{i}{\hbar}\int_{t_0}^{t} \mathrm{d}t'\, H(t')\right)$$

by formal integration. Note that the time-ordering operator $\mathcal{T}$ has been introduced to account for the combinatorial factor in the exponential series expansion. Since λ is a parameter, it commutes with itself at different times and $\mathcal{T}$ may be discarded.

For the Hamiltonian in Eq. C.1, the off-diagonal component of the qubit density matrix ρ evolves according to $\rho_{ge}(t) = \mathrm{e}^{i\Omega_0 t} f_{\phi\mathrm{R}}(t)\rho_{ge}(0)$ under free evolution over time t, where $\rho_{ge} = \langle g|\rho|e\rangle$. The envelope function

$$f_{\phi\mathrm{R}}(t) = \left\langle \mathrm{e}^{i\int_0^t \mathrm{d}t'\,\tilde{\Omega}(t')}\right\rangle,$$

where $\tilde{\Omega}(t) = \Omega(t) - \Omega_0$, describes the decay of phase coherence as measured in a Ramsey-type experiment. On the other hand, for a spin-echo decoherence measurement, we consider

$$f_{\phi\mathrm{E}}(t) = \left\langle \mathrm{e}^{-i\int_{t/2}^t \mathrm{d}t'\,\tilde{\Omega}(t') + i\int_0^{t/2} \mathrm{d}t'\,\tilde{\Omega}(t')}\right\rangle,$$

i.e. free evolution for time t interrupted by a σ_x operation (an echo pulse) at time $t/2$. To simplify some of the expressions, we will consider the general decay envelope

$$f_\phi(t) = \left\langle e^{i\int_{\mathcal{I}} dt' \tilde{\Omega}(t')} \right\rangle,$$

where it should be understood that the integration obeys $\int_{\mathcal{I}} = \int_0^t$ for the Ramsey case and $\int_{\mathcal{I}} = -\int_{t/2}^t + \int_0^{t/2}$ for the echo case (generalizing in the obvious way[1]). In Eq. C.1, the expression for $\tilde{\Omega}(t)$ involves all orders of λ, but we will concentrate on the cases of linear coupling (when $D_1 = \frac{\partial\Omega}{\partial\lambda}\big|_0 \neq 0$) and quadratic coupling (when $D_1 = 0$ and $D_2 = \frac{\partial^2\Omega}{\partial\lambda^2}\big|_0 \neq 0$). The main exception to this will be our discussion of charge noise in App. C.5.

C.2 Linear coupling

For linear coupling, we have $\tilde{\Omega} = D_1\lambda$ and the envelope can be expanded as

$$f_\phi(t) = 1 + iD_1 \int_{\mathcal{I}} dt_1 \langle\lambda(t_1)\rangle + \frac{1}{2}(iD_1)^2 \int_{\mathcal{I}} dt_1 \int_{\mathcal{I}} dt_2 \langle\lambda(t_1)\lambda(t_2)\rangle + \ldots,$$

where all odd terms vanish owing to the assumption that λ has zero mean. To evaluate the remaining terms, we can invoke Wick's theorem[2] to write

$$\langle\lambda(t_1)\lambda(t_2)\cdots\lambda(t_{2n})\rangle = \sum_{\text{pairings}} \prod_{(i,j)} \langle\lambda(t_i)\lambda(t_j)\rangle, \tag{C.2}$$

where the sum and product represent the $(2n-1)!!$ distinct ways of pairing up the $\lambda(t_i)$.

We proceed by assuming stationarity[3] and using the definition of the noise spectral density $S_{\lambda\lambda}[\omega] = \int_{-\infty}^{\infty} dt\, e^{i\omega t}\langle\lambda(t)\lambda(0)\rangle$, or equivalently $\langle\lambda(t)\lambda(0)\rangle = \int_{-\infty}^{\infty} \frac{d\omega}{2\pi} e^{-i\omega t} S_{\lambda\lambda}[\omega]$. This gives

$$\begin{aligned} f_\phi(t) &= \sum_{n=0}^{\infty} \frac{(2n-1)!!}{(2n)!}(-D_1^2)^n \int_{\mathcal{I}} dt_1 \cdots \int_{\mathcal{I}} dt_{2n} \langle\lambda(t_1 - t_2)\lambda(0)\rangle \cdots \langle\lambda(t_{2n-1} - t_{2n})\lambda(0)\rangle \\ &= \exp\left[-\frac{1}{2}D_1^2 \int_{-\infty}^{\infty} \frac{d\omega}{2\pi} S_{\lambda\lambda}[\omega]|P(\omega)|^2\right], \end{aligned} \tag{C.3}$$

since $(2n)! = 2^n n!(2n-1)!!$. Notice that the constituent integrands are off-diagonal in time—in the sense that each factor $\langle\lambda(t_i - t_{i+1})\lambda(0)\rangle$ contributes to two time integrals—but diagonal in frequency. We have introduced the propagation function $P(\omega) = \int_{\mathcal{I}} dt'\, e^{-i\omega t'}$, whose explicit form depends on the measurement sequence.

1 Generalized echo: For the general case with $m-1$ echo pulses, such that $m > 1$ and m is even, we have

$$f_{\phi m}(t) = \left\langle e^{-i\int_{(m-1)t/m}^{t} dt' \tilde{\Omega}(t') + i\int_{(m-2)t/m}^{(m-1)t/m} dt' \tilde{\Omega}(t') - \cdots + \int_0^{t/m} dt' \tilde{\Omega}(t')} \right\rangle.$$

2 Sometimes called Isserlis' theorem in this case, where the operators commute.

3 This also implies that $S_{\lambda\lambda}$ is even in ω in the classical case.

In particular, for the Ramsey and echo sequences, we have the propagation functions

$$P_{\mathrm{R}}(\omega) = \int_0^t \mathrm{d}t'\, \mathrm{e}^{-i\omega t'} = \frac{\sin \omega t/2}{\omega/2} \mathrm{e}^{-i\omega t/2} \tag{C.4}$$

$$P_{\mathrm{E}}(\omega) = -\int_{t/2}^t \mathrm{d}t'\, \mathrm{e}^{-i\omega t'} + \int_0^{t/2} \mathrm{d}t'\, \mathrm{e}^{-i\omega t'} = i\frac{\sin^2 \omega t/4}{\omega/4} \mathrm{e}^{-i\omega t/2}, \tag{C.5}$$

which lead to the envelope functions[4]

$$f_{\phi\mathrm{R}}(t) = \exp\left[-\frac{1}{2}D_1^2 \int_{-\infty}^{\infty} \frac{\mathrm{d}\omega}{2\pi} S_{\lambda\lambda}[\omega] \left(\frac{\sin \omega t/2}{\omega/2}\right)^2\right] \tag{C.8}$$

$$f_{\phi\mathrm{E}}(t) = \exp\left[-\frac{1}{2}D_1^2 \int_{-\infty}^{\infty} \frac{\mathrm{d}\omega}{2\pi} S_{\lambda\lambda}[\omega] \left(\frac{\sin^2 \omega t/4}{\omega/4}\right)^2\right]. \tag{C.9}$$

It is interesting to note that these results coincide exactly with those found using the Gaussian approximation, which is to assume that the random phase $\phi = \int_{\mathcal{I}} \mathrm{d}t'\, \tilde{\Omega}(t')$ obeys Gaussian statistics [Ithier et al. 2005]. In this case, the probability distribution $p(\phi) = \frac{1}{\sqrt{2\pi}\sigma} \mathrm{e}^{-\frac{1}{2}(\phi-\mu)^2/\sigma^2}$ (with $\mu = \langle\phi\rangle$ and $\sigma^2 = \langle\phi^2\rangle - \langle\phi\rangle^2$) gives the average

$$\langle \mathrm{e}^{i\phi} \rangle = \int_{-\infty}^{\infty} \mathrm{d}\phi\, p(\phi) \mathrm{e}^{i\phi} = \frac{1}{\sqrt{2\pi}\sigma} \mathrm{e}^{i\mu - \frac{1}{2}\sigma^2} \int_{-\infty}^{\infty} \mathrm{d}\phi\, \mathrm{e}^{-\frac{1}{2}[(\phi-\mu)/\sigma - i\sigma]^2} = \mathrm{e}^{i\langle\phi\rangle - \frac{1}{2}(\langle\phi^2\rangle - \langle\phi\rangle^2)}. \tag{C.10}$$

For linear coupling, $\langle\phi\rangle = 0$ because λ has zero mean. We immediately find the decay envelope (again using stationarity and the definition of $S_{\lambda\lambda}$) to be

$$\begin{aligned} f_\phi(t) = \mathrm{e}^{-\frac{1}{2}\langle\phi^2\rangle} &= \exp\left[-\frac{1}{2}D_1^2 \int_{\mathcal{I}} \mathrm{d}t' \int_{\mathcal{I}} \mathrm{d}t'' \, \langle\lambda(t'-t'')\lambda(0)\rangle\right] \\ &= \exp\left[-\frac{1}{2}D_1^2 \int_{-\infty}^{\infty} \frac{\mathrm{d}\omega}{2\pi} S_{\lambda\lambda}[\omega] |P(\omega)|^2\right], \end{aligned}$$

in exact agreement with Eq. C.3.

4 Generalized echo: We note that $\int_{jt/m}^{(j+1)t/m} \mathrm{d}t'\, \mathrm{e}^{-i\omega t'} = \frac{2}{\omega} \mathrm{e}^{-i(2j+1)\omega t/2m} \sin \frac{\omega t}{2m}$ and so the geometric series formula gives

$$P_m(\omega) = \frac{2}{\omega} \mathrm{e}^{-i\omega t/2m} \sin \frac{\omega t}{2m} \sum_{j=0}^{m-1} (-\mathrm{e}^{-i\omega t/m})^j = i\frac{\sin \omega t/2}{\omega/2} \tan \frac{\omega t}{2m} \mathrm{e}^{-i\omega t/2} \tag{C.6}$$

for the propagator. In turn, this yields the decay envelope

$$f_{\phi m}(t) = \exp\left[-\frac{1}{2}D_1^2 \int_{-\infty}^{\infty} \frac{\mathrm{d}\omega}{2\pi} S_{\lambda\lambda}[\omega] \left(\frac{\sin \omega t/2}{\omega/2} \tan \frac{\omega t}{2m}\right)^2\right]. \tag{C.7}$$

C.3 Quadratic coupling

For quadratic coupling, we have $\tilde{\Omega} = \frac{1}{2}D_2\lambda^2$ and the envelope can be expanded as

$$\begin{aligned} f_\phi(t) &= 1 + \frac{iD_2}{2}\int_{\mathcal{I}} \mathrm{d}t_1 \,\langle\lambda^2(t_1)\rangle + \frac{1}{2}\left(\frac{iD_2}{2}\right)^2 \int_{\mathcal{I}}\mathrm{d}t_1 \int_{\mathcal{I}}\mathrm{d}t_2\,\langle\lambda^2(t_1)\lambda^2(t_2)\rangle + \dots \\ &= \sum_{n=0}^{\infty}\left(\frac{iD_2}{2}\right)^n X_n(t), \end{aligned}$$

where the odd terms may not vanish (as they did in the case of linear coupling). We follow Makhlin and Shnirman (2004) and have introduced the function

$$X_n = \frac{1}{n!}\int_{\mathcal{I}}\mathrm{d}t_1 \cdots \int_{\mathcal{I}}\mathrm{d}t_n\,\langle\lambda^2(t_1)\cdots\lambda^2(t_n)\rangle,$$

which is still at the mercy of Wick's theorem. We should emphasize that the situation is significantly more complex than for linear coupling due to the fact that each t_i appears twice in the integrand. As such, we have to deal with factors like $\langle\lambda(t_1)\lambda(t_2)\rangle\langle\lambda(t_1)\lambda(t_3)\rangle$ in Eq. C.2, and so on. It is convenient to define the cyclic integrals

$$F_n = \int_{\mathcal{I}}\mathrm{d}t_1 \int_{\mathcal{I}}\mathrm{d}t_2 \cdots \int_{\mathcal{I}}\mathrm{d}t_n\,\langle\lambda(t_1-t_2)\lambda(0)\rangle\langle\lambda(t_2-t_3)\lambda(0)\rangle\cdots\langle\lambda(t_n-t_1)\lambda(0)\rangle,$$

which will inevitably show up after using Wick's theorem and stationarity. In principle, we can write

$$X_n = \frac{1}{n!}\sum_{k\vdash n} g(k)F_1^{k_1}F_2^{k_2}\cdots F_n^{k_n},$$

where $k \vdash n$ means that k is a partition of n and $g(k)$ is a combinatorial factor. We can represent this decomposition diagrammatically by drawing n vertices—one for each time integral in X_n—each connected to exactly two edges (see Fig. C.1).

To find $g(k)$, we imagine choosing k_1 vertices, then $2k_2$ vertices, and so on. This gives

$$g(k) = \prod_{\ell=1}^{n}\binom{n-\sum_{m=1}^{\ell-1}mk_m}{\ell k_\ell} g_\ell(k_\ell) = n!\prod_{\ell=1}^{n}\frac{1}{(\ell k_\ell)!}g_\ell(k_\ell),$$

with $g_\ell(k_\ell)$ being the number of degenerate ways of assembling ℓ-cycles from ℓk_ℓ-many vertices. There are $2(\ell k_\ell - 1)$ options for choosing the first edge, $2(\ell k_\ell - 2)$ options for the second, and so on. There is only one option for choosing the ℓ-th edge, and then the process repeats. Therefore, we have

$$g_\ell(k_\ell) = 2^{(\ell-1)k_\ell}\frac{(\ell k_\ell - 1)!}{(\ell k_\ell - \ell)!_{(\ell)}} = 2^{(\ell-1)k_\ell}\frac{(\ell k_\ell - 1)!}{\ell^{k_\ell-1}(k_\ell-1)!},$$

with $(\cdot)!_{(n)}$ being the multifactorial. In sum, we get

$$g(k) = n!\prod_{\ell=1}^{n}2^{\ell k_\ell}\frac{1}{(2\ell)^{k_\ell}k_\ell!} = 2^n n!\prod_{\ell=1}^{n}\frac{1}{(2\ell)^{k_\ell}k_\ell!}$$

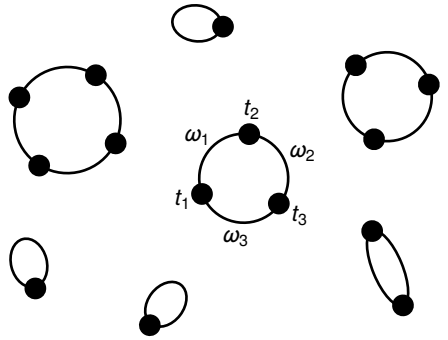

Figure C.1 Example linked-cluster diagram for the partition $(1,1,1,2,3,3,4)$ of 15. Vertices correspond to times and edges to frequencies. The allowed configurations are cycles, which are described by the integrals F_n. For example, the central cycle corresponds to $F_3 = \int_I \mathrm{d}t_1 \int_I \mathrm{d}t_2 \int_I \mathrm{d}t_3 \, \langle\lambda(t_1 - t_2)\lambda(0)\rangle\langle\lambda(t_2 - t_3)\lambda(0)\rangle\langle\lambda(t_3 - t_1)\lambda(0)\rangle$.

since $\sum_{\ell=1}^{n} \ell k_\ell = n$.

This gives use an explicit form for the decomposition

$$X_n = 2^n \sum_{k\vdash n} \prod_{\ell=1}^{n} \frac{1}{k_\ell!}\left(\frac{1}{2\ell}F_\ell\right)^{k_\ell},$$

and hence the decay envelope

$$f_\phi(t) = \sum_{n=0}^{\infty}\sum_{k\vdash n}\prod_{\ell=1}^{n}\frac{1}{k_\ell!}\left[\frac{1}{2\ell}(iD_2)^\ell F_\ell\right]^{k_\ell} = \exp\left[\sum_{n=1}^{\infty}\frac{1}{2n}(iD_2)^n F_n\right], \tag{C.11}$$

using the exponential formula $\sum_{n=0}^{\infty}\sum_{k\vdash n}\prod_{\ell=1}^{n}\frac{1}{k_\ell!}\left(\frac{x_\ell}{\ell}\right)^{k_\ell} = \exp\left(\sum_{n=1}^{\infty}\frac{1}{n}x_n\right)$. Now, it only remains to calculate the cyclic integrals. The expression for F_n is readily recast in the form

$$F_n = \int_{-\infty}^{\infty}\frac{\mathrm{d}\omega_1}{2\pi}\cdots\int_{-\infty}^{\infty}\frac{\mathrm{d}\omega_n}{2\pi}S_{\lambda\lambda}[\omega_1]P(\omega_1-\omega_n)\cdots S_{\lambda\lambda}[\omega_n]P(\omega_n-\omega_{n-1}) \tag{C.12}$$

where $P(\omega) = \int_I \mathrm{d}t' \, \mathrm{e}^{-i\omega t'}$ is the same propagator from App. C.2, which we have evaluated in Eqs. C.4–6. Note that this integrand contains both diagonal and off-diagonal components in frequency, whereas it was purely diagonal for linear coupling. We emphasize that the relevant integrals

$$F_{n\mathrm{R}} = \int_{-\infty}^{\infty}\frac{\mathrm{d}\omega_1}{2\pi}\cdots\int_{-\infty}^{\infty}\frac{\mathrm{d}\omega_n}{2\pi} \times S_{\lambda\lambda}[\omega_1]\frac{\sin[(\omega_1-\omega_n)t/2]}{(\omega_1-\omega_n)/2}\cdots S_{\lambda\lambda}[\omega_n]\frac{\sin[(\omega_n-\omega_{n-1})t/2]}{(\omega_n-\omega_{n-1})/2}$$

$$F_{n\mathrm{E}} = i^n \int_{-\infty}^{\infty} \frac{\mathrm{d}\omega_1}{2\pi} \cdots \int_{-\infty}^{\infty} \frac{\mathrm{d}\omega_n}{2\pi} \times S_{\lambda\lambda}[\omega_1] \frac{\sin^2[(\omega_1-\omega_n)t/4]}{(\omega_1-\omega_n)/4} \cdots S_{\lambda\lambda}[\omega_n] \frac{\sin^2[(\omega_n-\omega_{n-1})t/4]}{(\omega_n-\omega_{n-1})/4}$$

are highly nontrivial. To proceed, we can split the integration region into low-frequency $|\omega_i| \leq 1/t$ and high-frequency $|\omega_i| > 1/t$ components for fixed t. We call these contributions F_n^{lf} and F_n^{hf} [similar definitions hold for $f_\phi^{\mathrm{lf}}(t)$ and $f_\phi^{\mathrm{hf}}(t)$].

In the low-frequency regime, $|\omega_i - \omega_{i-1}| \leq 2/t$ and it is appropriate to use the small-angle approximation for the propagators. In the Ramsey case, this means using $\frac{\sin[(\omega_i-\omega_{i-1})t/2]}{(\omega_i-\omega_{i-1})/2} \approx t$. In the echo case, it means using $\frac{\sin^2[(\omega_i-\omega_{i-1})t/4]}{(\omega_i-\omega_{i-1})/4} \approx \frac{t^2}{4}(\omega_i - \omega_{i-1})$. We obtain

$$F_{n\mathrm{R}}^{\mathrm{lf}} \approx \left[2t \int_0^{1/t} \frac{\mathrm{d}\omega}{2\pi} S_{\lambda\lambda}[\omega]\right]^n$$

$$F_{n\mathrm{E}}^{\mathrm{lf}} \approx 2\left[t^2 \int_0^{1/t} \frac{\mathrm{d}\omega}{2\pi} S_{\lambda\lambda}[\omega] \int_0^{1/t} \frac{\mathrm{d}\omega}{2\pi} \left(\frac{\omega t}{2}\right)^2 S_{\lambda\lambda}[\omega]\right]^{n/2} \delta_{n \bmod 2,0}.$$

For the echo calculation, we used the assumption of stationarity to deduce that $S_{\lambda\lambda}$ will be even, and hence that the symmetric integral would annihilate all but two terms in the product $(\omega_1 - \omega_n)(\omega_2 - \omega_1)\cdots(\omega_n - \omega_{n-1})$, namely $(-\omega_1^2)(-\omega_3^2)\cdots(-\omega_{n-1}^2)$ and $(-\omega_2^2)(-\omega_4^2)\cdots(-\omega_n^2)$. This only works for even n; when n is odd, the integral vanishes altogether. Plugging these into Eq. C.11, we use $-\ln(1-x) = \sum_{n=1}^{\infty} \frac{1}{n} x^n$ to get[5]

$$f_{\phi\mathrm{R}}^{\mathrm{lf}}(t) \approx \left[1 - 2itD_2 \int_0^{1/t} \frac{\mathrm{d}\omega}{2\pi} S_{\lambda\lambda}[\omega]\right]^{-1/2} \tag{C.14}$$

$$f_{\phi\mathrm{E}}^{\mathrm{lf}}(t) \approx \left[1 + t^2 D_2^2 \int_0^{1/t} \frac{\mathrm{d}\omega}{2\pi} S_{\lambda\lambda}[\omega] \int_0^{1/t} \frac{\mathrm{d}\omega}{2\pi} \left(\frac{\omega t}{2}\right)^2 S_{\lambda\lambda}[\omega]\right]^{-1/2}. \tag{C.15}$$

In the high-frequency regime, it is appropriate to examine the limit of the propagators as $t \to \infty$. In the Ramsey case, we can use $\lim_{t\to\infty} \frac{\sin[(\omega_i-\omega_{i-1})t/2]}{(\omega_i-\omega_{i-1})/2} = 2\pi\delta(\omega_i - \omega_{i-1})$. The procedure is slightly more tedious in the echo case, where we find it useful to use the

5 Generalized echo: We have the cyclic integrals

$$F_{nm} = i^n \int_{-\infty}^{\infty} \frac{\mathrm{d}\omega_1}{2\pi} \cdots \int_{-\infty}^{\infty} \frac{\mathrm{d}\omega_n}{2\pi} \times S_{\lambda\lambda}[\omega_1] \frac{\sin[(\omega_1-\omega_n)t/2]}{(\omega_1-\omega_n)/2} \tan\frac{(\omega_1-\omega_n)t}{2m} \cdots S_{\lambda\lambda}[\omega_n] \frac{\sin[(\omega_n-\omega_{n-1})t/2]}{(\omega_n-\omega_{n-1})/2} \tan\frac{(\omega_n-\omega_{n-1})t}{2m}.$$

In this case, the small-angle approximation $\frac{\sin[(\omega_i-\omega_{i-1})t/2]}{(\omega_i-\omega_{i-1})/2} \tan\frac{(\omega_i-\omega_{i-1})t}{2m} \approx \frac{t^2}{2m}(\omega_i - \omega_{i-1})$ is valid for the low-frequency regime. Evidently, the calculation is the same as in the $m = 2$ case, and we find

$$F_{nm}^{\mathrm{lf}} \approx 2\left[t^2 \int_0^{1/t} \frac{\mathrm{d}\omega}{2\pi} S_{\lambda\lambda}[\omega] \int_0^{1/t} \frac{\mathrm{d}\omega}{2\pi} \left(\frac{\omega t}{m}\right)^2 S_{\lambda\lambda}[\omega]\right]^{n/2} \delta_{n \bmod 2,0},$$

which leads to

$$f_{\phi m}^{\mathrm{lf}}(t) \approx \left[1 + t^2 D_2^2 \int_0^{1/t} \frac{\mathrm{d}\omega}{2\pi} S_{\lambda\lambda}[\omega] \int_0^{1/t} \frac{\mathrm{d}\omega}{2\pi} \left(\frac{\omega t}{m}\right)^2 S_{\lambda\lambda}[\omega]\right]^{-1/2}. \tag{C.13}$$

Nyquist-Shannon sampling theorem to first write

$$\lim_{t\to\infty}\frac{\sin^2[(\omega_i-\omega_{i-1})t/4]}{(\omega_i-\omega_{i-1})/4}=\lim_{t\to\infty}\sum_{n\,\text{odd}}\frac{2t}{n\pi}\frac{\sin[(\omega_i-\omega_{i-1})t/2-n\pi]}{(\omega_i-\omega_{i-1})t/2-n\pi}$$
$$=\sum_{n\,\text{odd}}\frac{4}{n}\delta(\omega_i-\omega_{i-1}-2n\pi/t).$$

Multiplying this by the adjacent propagator yields

$$\lim_{t\to\infty}\frac{\sin^2[(\omega_i-\omega_{i-1})t/4]}{(\omega_i-\omega_{i-1})/4}\frac{\sin^2[(\omega_{i+1}-\omega_i)t/4]}{(\omega_{i+1}-\omega_i)/4}$$
$$=\delta(\omega_i-\omega_{i-1})\lim_{t\to\infty}\sum_{n\,\text{odd}}\frac{4}{n}\frac{\cos^2[(\omega_{i+1}-\omega_{i-1})t/4]}{(\omega_{i+1}-\omega_{i-1})/4-n\pi/2t}$$
$$=-2\pi\delta(\omega_i-\omega_{i-1})\lim_{t\to\infty}\frac{\sin[(\omega_{i+1}-\omega_{i-1})t/2]}{(\omega_{i+1}-\omega_{i-1})/2}$$
$$=-(2\pi)^2\delta(\omega_i-\omega_{i-1})\delta(\omega_{i+1}-\omega_{i-1}),$$

using $\sum_{n\,\text{odd}}\frac{1}{n(n-\omega t/2\pi)}=\frac{\pi^2}{\omega t}\tan\omega t/4$ and $\sin x=2\sin\frac{x}{2}\cos\frac{x}{2}$. We obtain

$$F^{\text{hf}}_{n\text{R}}\approx 2t\int_{1/t}^{\infty}\frac{\mathrm{d}\omega}{2\pi}(S_{\lambda\lambda}[\omega])^n$$
$$F^{\text{hf}}_{n\text{E}}\approx 2t\int_{1/t}^{\infty}\frac{\mathrm{d}\omega}{2\pi}(S_{\lambda\lambda}[\omega])^n\delta_{n\bmod 2,0}.$$

Plugging these into Eq. C.11 gives[6]

$$f^{\text{hf}}_{\phi\text{R}}(t)\approx\exp\left[-t\int_{1/t}^{\infty}\frac{\mathrm{d}\omega}{2\pi}\ln\Big(1-iD_2S_{\lambda\lambda}[\omega]\Big)\right] \tag{C.17}$$
$$f^{\text{hf}}_{\phi\text{E}}(t)\approx\exp\left[-\frac{1}{2}t\int_{1/t}^{\infty}\frac{\mathrm{d}\omega}{2\pi}\ln\Big\{1+(D_2S_{\lambda\lambda}[\omega])^2\Big\}\right]. \tag{C.18}$$

It is of moderate interest to also quote the result for quadratic coupling obtained via the Gaussian approximation. Eq. C.10 provides the decay envelope

$$f_\phi(t)=\exp\left[\frac{1}{2}iD_2\int_{\mathcal{I}}\mathrm{d}t'\,\langle\lambda^2(0)\rangle-\frac{1}{8}D_2^2\int_{\mathcal{I}}\mathrm{d}t'\int_{\mathcal{I}}\mathrm{d}t''\left(\langle\lambda^2(t'-t'')\lambda^2(0)\rangle-\langle\lambda^2(0)\rangle^2\right)\right],$$

6 Generalized echo: The high-frequency regime requires us to take the $t\to\infty$ limit of the propagators. Once more, we make use of the Nyquist-Shannon sampling theorem to get

$$\lim_{t\to\infty}\frac{\sin[(\omega_i-\omega_{i-1})t/2]}{(\omega_i-\omega_{i-1})/2}\tan\frac{(\omega_i-\omega_{i-1})t}{2m}=(-1)^{m/2+1}\lim_{t\to\infty}\sum_{n\,\text{odd}}\frac{2t}{n\pi}\frac{\sin[(\omega_i-\omega_{i-1})t/2-nm\pi/2]}{(\omega_i-\omega_{i-1})t/2-nm\pi/2}$$
$$=(-1)^{m/2+1}\sum_{n\,\text{odd}}\frac{4}{n}\delta(\omega_i-\omega_{i-1}-nm\pi/t).$$

using stationarity of λ, which also implies stationarity of λ^2 (e.g. via Wick's theorem). Another application of Wick's theorem gives $\langle\lambda^2(t)\lambda^2(0)\rangle = \langle\lambda^2(0)\rangle^2 + 2\langle\lambda(t)\lambda(0)\rangle^2$ and so

$$f_\phi(t) = \exp\left[\frac{1}{2}iD_2\int_{\mathcal{I}} \mathrm{d}t'\,\langle\lambda^2(0)\rangle - \frac{1}{4}D_2^2\int_{\mathcal{I}}\mathrm{d}t'\int_{\mathcal{I}}\mathrm{d}t''\,\langle\lambda(t'-t'')\lambda(0)\rangle^2\right]. \tag{C.19}$$

Using the definitions of $S_{\lambda\lambda}$ and $P(\omega)$, this expression can be rewritten as

$$f_\phi(t) = \exp\left[\frac{1}{2}iD_2\int_{-\infty}^{\infty}\frac{\mathrm{d}\omega}{2\pi}S_{\lambda\lambda}[\omega]P(0) - \frac{1}{4}D_2^2\int_{-\infty}^{\infty}\frac{\mathrm{d}\omega}{2\pi}\int_{-\infty}^{\infty}\frac{\mathrm{d}\omega'}{2\pi}S_{\lambda\lambda}[\omega]S_{\lambda\lambda}[\omega']|P(\omega+\omega')|^2\right].$$

After the change of variables from ω' to $-\omega'$ (and using the evenness of $S_{\lambda\lambda}$), we find this to coincide with Eq. C.11 without the $n > 2$ terms. As such, we see that the Gaussian approximation neglects all cyclic integrals higher than order two—e.g. the diagram in Fig. C.1 is not considered.

Alternatively, we can change variables from ω to $\omega + \omega'$, in which case the above expression takes the form

$$f_\phi(t) = \exp\left[\frac{1}{2}iD_2\int_{-\infty}^{\infty}\frac{\mathrm{d}\omega}{2\pi}S_{\lambda\lambda}[\omega]P(0) - \frac{1}{4}D_2^2\int_{-\infty}^{\infty}\frac{\mathrm{d}\omega}{2\pi}|P(\omega)|^2\int_{-\infty}^{\infty}\frac{\mathrm{d}\omega'}{2\pi}S_{\lambda\lambda}[\omega']S_{\lambda\lambda}[\omega-\omega']\right].$$

This is also obtained by applying the convolution theorem introduced in App. A to Eq. C.19, since the last integral in the above is merely the convolution $S_{\lambda\lambda} * S_{\lambda\lambda}$. Using the

---

Using the same method, we multiply this by its adjacent propagator to obtain

$$\begin{aligned}
&\lim_{t\to\infty}\frac{\sin[(\omega_i-\omega_{i-1})t/2]}{(\omega_i-\omega_{i-1})/2}\tan\frac{(\omega_i-\omega_{i-1})t}{2m}\frac{\sin[(\omega_{i+1}-\omega_i)t/2]}{(\omega_{i+1}-\omega_i)/2}\tan\frac{(\omega_{i+1}-\omega_i)t}{2m}\\
&\quad=\delta(\omega_i-\omega_{i-1})\lim_{t\to\infty}\sum_{n\,\mathrm{odd}}\frac{4}{n}\frac{\sin[(\omega_{i+1}-\omega_{i-1})t/2]}{(\omega_{i+1}-\omega_{i-1})/2-nm\pi/2t}\cot\frac{(\omega_{i+1}-\omega_{i-1})t}{2m}\\
&\quad=-2\pi\delta(\omega_i-\omega_{i-1})\lim_{t\to\infty}\frac{\sin[(\omega_{i+1}-\omega_{i-1})t/2]}{(\omega_{i+1}-\omega_{i-1})/2}\\
&\quad=-(2\pi)^2\delta(\omega_i-\omega_{i-1})\delta(\omega_{i+1}-\omega_{i-1}),
\end{aligned}$$

which is the same as in the $m = 2$ case. Consequently, we have

$$F_{nm}^{\mathrm{hf}} \approx 2t\int_{1/t}^{\infty}\frac{\mathrm{d}\omega}{2\pi}(S_{\lambda\lambda}[\omega])^n\delta_{n\bmod 2,0},$$

which leads to

$$f_{\phi m}^{\mathrm{hf}}(t) \approx \exp\left[-\frac{1}{2}t\int_{1/t}^{\infty}\frac{\mathrm{d}\omega}{2\pi}\ln\left\{1+(D_2S_{\lambda\lambda}[\omega])^2\right\}\right], \tag{C.16}$$

showing that a greater number of echo pulses does not reduce the sensitivity to high-frequency components of the noise.

propagators in Eqs. C.4–5, and taking the magnitude of the Ramsey envelope, we have[7]

$$|f_{\phi\mathrm{R}}(t)| = \exp\left[-\frac{1}{4}D_2^2\int_{-\infty}^{\infty}\frac{\mathrm{d}\omega}{2\pi}\left(\frac{\sin\omega t/2}{\omega/2}\right)^2(S_{\lambda\lambda}*S_{\lambda\lambda})[\omega]\right] \tag{C.21}$$

$$f_{\phi\mathrm{E}}(t) = \exp\left[-\frac{1}{4}D_2^2\int_{-\infty}^{\infty}\frac{\mathrm{d}\omega}{2\pi}\left(\frac{\sin^2\omega t/4}{\omega/4}\right)^2(S_{\lambda\lambda}*S_{\lambda\lambda})[\omega]\right]. \tag{C.22}$$

C.4 $1/f$ noise

As explained in Sec. 7.1.2, when the noise channel has a regular spectral density at low frequencies $|\omega| \lesssim 1/t$, the expressions found above are approximately only dependent on the value of the dc component of the spectral density $S_{\lambda\lambda}[0]$. This was demonstrated in Eq. 7.9. Unfortunately, in superconducting qubits this regularity is usually only associated with photon shot noise. For other channels, whose origins are microscopic, the spectral densities are observed to diverge at low frequencies [Schriefl et al. 2006, Shnirman et al. 2007]. The simplest empirical model for these types of noise is then to use the spectral density $S_{\lambda\lambda} \propto |\omega|^{-p}$ with $p > 0$, and this is called $1/f$ noise. Measurements have indicated values of $0.5 \lesssim p \lesssim 1.5$, and hereafter we use the value $p = 1$. Specifically, we write

$$S_{\lambda\lambda}[\omega] = \frac{2\pi A_\lambda}{|\omega|} \tag{C.23}$$

for the spectral density in the relevant frequency range.

With any physical measurement, the noise at frequencies below an infrared cutoff ω_{ir} should have no effect. This cutoff roughly corresponds to the inverse total measurement time and its particular value is set by experimental details. Although $\omega_{\mathrm{ir}} > 0$ provides convergence for certain integrals, its origin is physical. We will not take too seriously the form of $S_{\lambda\lambda}$ below ω_{ir} or at very high frequencies. Instead, we will simply replace any integrals that are logarithmically divergent at the origin by their value at ω_{ir}. Of some interest is the convolution

$$\begin{aligned}
(S_{\lambda\lambda}*S_{\lambda\lambda})[\omega] &= \int_{-\infty}^{\infty}\frac{\mathrm{d}\omega'}{2\pi}S_{\lambda\lambda}[\omega']S_{\lambda\lambda}[\omega-\omega'] \\
&= 2\pi A_\lambda^2\left[\int_0^\infty \mathrm{d}\omega'\,\frac{1}{\omega'(\omega'+|\omega|)} + \int_0^{|\omega|}\mathrm{d}\omega'\,\frac{1}{\omega'(|\omega|-\omega')} + \int_{|\omega|}^\infty \mathrm{d}\omega'\,\frac{1}{\omega'(\omega'-|\omega|)}\right] \\
&= \frac{2\pi A_\lambda^2}{|\omega|}\left[\ln\frac{\omega'}{\omega'+|\omega|}\bigg|_0^\infty + \ln\frac{\omega'}{|\omega|-\omega'}\bigg|_0^{|\omega|} - \ln\frac{\omega'}{\omega'-|\omega|}\bigg|_{|\omega|}^\infty\right] \\
&= \frac{2\pi A_\lambda^2}{|\omega|}\left[-\lim_{\epsilon\to0^+}\ln\frac{\epsilon}{|\omega|+\epsilon} + \lim_{\epsilon\to0^+}\ln\frac{|\omega|-\epsilon}{\epsilon} - \lim_{\epsilon\to0^+}\ln\frac{\epsilon}{|\omega|-\epsilon} + \lim_{\epsilon\to0^+}\ln\frac{|\omega|+\epsilon}{\epsilon}\right] \\
&= \frac{8\pi A_\lambda^2}{|\omega|}\lim_{\epsilon\to0^+}\ln\frac{|\omega|}{\epsilon} \to \frac{8\pi A_\lambda^2}{|\omega|}\ln\frac{|\omega|}{\omega_{\mathrm{ir}}},
\end{aligned} \tag{C.24}$$

7 Generalized echo: Eq. C.6 gives

$$f_{\phi m}(t) = \exp\left[-\frac{1}{4}D_2^2\int_{-\infty}^{\infty}\frac{\mathrm{d}\omega}{2\pi}\left(\frac{\sin\omega t/2}{\omega/2}\tan\frac{\omega t}{2m}\right)^2(S_{\lambda\lambda}*S_{\lambda\lambda})[\omega]\right]. \tag{C.20}$$

where in the last line we removed the logarithmic divergence using $\omega_{\rm ir}$. This expression differs slightly from that obtained using a strict infrared cutoff; e.g. $S_{\lambda\lambda} = \frac{2\pi A_\lambda}{|\omega|}\Theta(|\omega| - \omega_{\rm ir})$, which leads to $S_{\lambda\lambda} * S_{\lambda\lambda} = \frac{4\pi A_\lambda^2}{|\omega|}\left[\ln\frac{|\omega|+\omega_{\rm ir}}{\omega_{\rm ir}} + \Theta(|\omega| - 2\omega_{\rm ir})\ln\frac{|\omega|-\omega_{\rm ir}}{\omega_{\rm ir}}\right]$; but only for $|\omega| \sim \omega_{\rm ir}$. Such differences play no role in modeling the dephasing that is measured experimentally, where $\omega_{\rm ir} t \ll 1$ because many averages must be performed. The remainder of this subsection will be evaluating the integrals derived in Secs. C.2–3 for $1/f$ noise.

C.4.1 Linear coupling

For the Ramsey envelope, we can plug Eq. C.23 into Eq. C.8 to get

$$f_{\phi\rm R}(t) = \exp\left[-4D_1^2 A_\lambda \int_0^\infty \frac{{\rm d}\omega}{\omega^3}\sin^2\frac{\omega t}{2}\right],$$

which diverges at zero frequency. As in App. C.3, it proves useful to separate the above integral into its low-frequency $\omega < 1/t$ and high-frequency $\omega > 1/t$ component. For the former, we can safely use the small-angle approximation $\sin\omega t/2 \approx \omega t/2$. For the latter, we can replace the oscillating factor $\sin^2\omega t/2$ by its average value $1/2$. This gives

$$\begin{aligned} f_{\phi\rm R}(t) &\approx \exp\left[-t^2 D_1^2 A_\lambda\left(\int_0^{1/t}\frac{{\rm d}\omega}{\omega} + \frac{2}{t^2}\int_{1/t}^\infty\frac{{\rm d}\omega}{\omega^3}\right)\right] \\ &\to \exp\left[-t^2 D_1^2 A_\lambda\left(\ln\frac{1}{\omega_{\rm ir} t} + 1\right)\right] \end{aligned} \tag{C.25}$$

upon removal of the logarithmic divergence.[8] For the echo envelope, we plug Eq. C.23 into Eq. C.9 and obtain

$$f_{\phi\rm E}(t) = \exp\left[-16D_1^2 A_\lambda\int_0^\infty\frac{{\rm d}\omega}{\omega^3}\sin^4\frac{\omega t}{4}\right] = \exp\left[-t^2 D_1^2 A_\lambda \ln 2\right] \tag{C.26}$$

using $\int_0^\infty {\rm d}x\,\frac{1}{x^3}\sin^4 x = \ln 2$.[9]

8 Instead of using these approximations, we could simply observe that

$$\begin{aligned} \lim_{\epsilon\to 0^+}\int_\epsilon^\infty\frac{{\rm d}\omega}{\omega^3}\sin^2\frac{\omega t}{2} &= \lim_{\epsilon\to 0^+}\frac{1}{4\epsilon^2}\left(1 - \cos\epsilon t + \epsilon t\sin\epsilon t - \epsilon^2 t^2\,{\rm Ci}\,\epsilon t\right) \\ &= \frac{t^2}{4}\lim_{\epsilon\to 0^+}\left(\ln\frac{1}{\epsilon t} + \frac{3}{2} - \gamma\right) \to \frac{t^2}{4}\left(\ln\frac{1}{\omega_{\rm ir} t} + \frac{3}{2} - \gamma\right), \end{aligned}$$

where ${\rm Ci}\,x = -\int_x^\infty {\rm d}t\,\frac{\cos t}{t}$ is the cosine integral, which behaves like ${\rm Ci}\,x \sim \gamma + \ln x$ for $x \to 0^+$, and γ is the Euler-Mascheroni constant. After replacing ϵ with $\omega_{\rm ir}$ in the last expression, we see that it coincides with Eq. C.25 up to small corrections (for $\omega_{\rm ir} t \ll 1$) because $\frac{3}{2} - \gamma \sim 1$.

9 Generalized echo: Eq. C.7 gives

$$f_{\phi m}(t) = \exp\left[-4D_1^2 A_\lambda\int_0^\infty\frac{{\rm d}\omega}{\omega^3}\sin^2\frac{\omega t}{2}\tan^2\frac{\omega t}{2m}\right] = \exp\left[-t^2 D_1^2 A_\lambda B_m\right], \tag{C.27}$$

where $B_m = \int_0^\infty\frac{{\rm d}u}{u^3}\sin^2 u\tan^2\frac{u}{m}$ is numerical factor that scales like $B_m \sim \frac{8}{\pi^2 m}$ for large m. To see this, we recall our earlier use of the Nyquist-Shannon sampling theorem, which gave us

$$\lim_{m\to\infty}\frac{\sin^2 mx}{x} = \lim_{m\to\infty}\sum_{n=-\infty}^\infty\frac{2m}{n\pi}\sin^2(n\pi/2)\frac{\sin(2mx - n\pi)}{2mx - n\pi} = \sum_{n=-\infty}^\infty\frac{1}{n}\sin^2(n\pi/2)\delta(x - n\pi/2m).$$

C.4.2 Quadratic coupling

Plugging Eq. C.23 into Eq. C.14 yields the low-frequency contribution to the Ramsey envelope magnitude

$$|f_{\phi\mathrm{R}}^{\mathrm{lf}}(t)| \approx \left(1+\left[2tD_2A_\lambda\int_0^{1/t}\frac{\mathrm{d}\omega}{\omega}\right]^2\right)^{-1/4} \to \left[1+\left(2tD_2A_\lambda\ln\frac{1}{\omega_{\mathrm{ir}}t}\right)^2\right]^{-1/4}, \tag{C.28}$$

where we have truncated the logarithmic divergence with ω_{ir}. The analogous calculation for the low-frequency contribution to the echo envelope[10] using Eq. C.15 reveals

$$\begin{aligned} f_{\phi\mathrm{E}}^{\mathrm{lf}}(t) &\approx \left[1+\frac{1}{4}t^4D_2^2A_\lambda^2\int_0^{1/t}\frac{\mathrm{d}\omega}{\omega}\int_0^{1/t}\mathrm{d}\omega\,\omega\right]^{-1/2} \\ &\to \left[1+\frac{1}{2}\left(\frac{1}{2}tD_2A_\lambda\right)^2\ln\frac{1}{\omega_{\mathrm{ir}}t}\right]^{-1/2}. \end{aligned} \tag{C.30}$$

For the high-frequency contribution to the Ramsey envelope magnitude, we employ Eq. C.17 and find

$$\begin{aligned} |f_{\phi\mathrm{R}}^{\mathrm{hf}}(t)| &\approx \exp\left[-\frac{1}{4\pi}t\int_{1/t}^{\infty}\mathrm{d}\omega\,\ln\left(1+\frac{4\pi^2D_2^2A_\lambda^2}{\omega^2}\right)\right] \\ &= \exp\left[-\frac{1}{2}t|D_2|A_\lambda\left\{\int_0^{\infty}\mathrm{d}u\,\ln\left(1+\frac{1}{u^2}\right)-g(2\pi t|D_2|A_\lambda)\right\}\right] \\ &= \exp\left[-\frac{1}{2}t|D_2|A_\lambda\left[\pi-g(2\pi t|D_2|A_\lambda)\right]\right], \end{aligned} \tag{C.31}$$

where we have introduced $g(x)=\int_0^{1/x}\mathrm{d}u\,\ln(1+\frac{1}{u^2})=2\arctan\frac{1}{x}+\frac{1}{x}\ln(1+x^2)$ and used $\int_0^{\infty}\mathrm{d}x\,\ln(1+\frac{1}{x^2})=\pi$. We note that $g(x)\sim\frac{2}{x}\ln(1+ex)$ for $x\to\infty$ and so it may be considered a small correction for long times. From Eqs. C.17–18, we see that $|f_{\phi\mathrm{R}}^{\mathrm{hf}}|=f_{\phi\mathrm{E}}^{\mathrm{hf}}$

Changing variables to $x=u/m$, we arrive at

$$\begin{aligned} \lim_{m\to\infty}B_m &= \frac{4}{\pi^2}\sum_{n=1}^{\infty}\frac{1}{n^3}\sin^2(n\pi/2)\tan^2(n\pi/2m) \\ &= \frac{4}{\pi^2}\left[\lim_{n\to m}\frac{1}{n^3}\sin^2(n\pi/2)\tan^2(n\pi/2m)+\sum_{n>0,\,\mathrm{odd}}\frac{1}{n^3}\sin^2(n\pi/2)\tan^2(n\pi/2m)\right] \\ &\approx \frac{4}{\pi^2}\left[\frac{1}{m}+2\sum_{k;j>0,\,\mathrm{odd}}\frac{1}{(km)^3}\left(\frac{2m}{j\pi}\right)^2\right] = \frac{4}{\pi^2m}\left[1+\frac{7}{8}\zeta(3)\right]\approx\frac{8}{\pi^2m} \end{aligned}$$

because the only nonvanishing even term is $n=m$ and the odd terms obey $n=km-j$. There is no problem introducing the second summation index because the resulting sums converge quickly.

10 Generalized echo: The low-frequency contribution using Eq. C.13 is

$$f_{\phi m}^{\mathrm{lf}} \approx \left[1+\frac{1}{m^2}t^4D_2^2A_\lambda^2\int_0^{1/t}\frac{\mathrm{d}\omega}{\omega}\int_0^{1/t}\mathrm{d}\omega\,\omega\right]^{-1/2} \to \left[1+\frac{1}{2}\left(\frac{1}{m}tD_2A_\lambda\right)^2\ln\frac{1}{\omega_{\mathrm{ir}}t}\right]^{-1/2}. \tag{C.29}$$

and hence the high-frequency contribution to the echo envelope[11] is identical. Namely,

$$f_{\phi\mathrm{E}}^{\mathrm{hf}}(t) \approx \exp\left[-\frac{1}{2}t|D_2|A_\lambda\left[\pi - g(2\pi t|D_2|A_\lambda)\right]\right]. \tag{C.33}$$

These equations should be compared to the analogous ones from the Gaussian approximation. Plugging Eq. C.24 into Eq. C.21 yields the Ramsey envelope (magnitude)

$$|f_{\phi\mathrm{R}}(t)| = \exp\left[-8D_2^2A_\lambda^2\int_0^\infty \frac{\mathrm{d}\omega}{\omega^3}\ln\frac{\omega}{\omega_{\mathrm{ir}}}\sin^2\frac{\omega t}{2}\right].$$

Following the same approach as in the linear case (using the small-angle approximation for $\omega < 1/t$ and averaging the oscillatory factor for $\omega > 1/t$), we get

$$\begin{aligned}
|f_{\phi\mathrm{R}}(t)| &\approx \exp\left[-2t^2D_2^2A_\lambda^2\left(\int_0^{1/t}\frac{\mathrm{d}\omega}{\omega}\ln\frac{\omega}{\omega_{\mathrm{ir}}} + \frac{2}{t^2}\int_{1/t}^\infty\frac{\mathrm{d}\omega}{\omega^3}\ln\frac{\omega}{\omega_{\mathrm{ir}}}\right)\right] \\
&= \exp\left[-t^2D_2^2A_\lambda^2\left(\lim_{\epsilon\to0^+}\ln^2\frac{\omega}{\omega_{\mathrm{ir}}}\Big|_\epsilon^{1/t} - \frac{1+2\ln\omega/\omega_{\mathrm{ir}}}{\omega^2t^2}\Big|_{1/t}^\infty\right)\right] \\
&\to \exp\left[-t^2D_2^2A_\lambda^2\left(\ln\frac{1}{\omega_{\mathrm{ir}}t}+1\right)^2\right],
\end{aligned} \tag{C.34}$$

since $\int \mathrm{d}x\,\frac{1}{x^3}\ln x = -\frac{1}{4x^2}(1+2\ln x) + \text{const.}$[12] For the echo envelope,[13] we plug Eq. C.24

11 Generalized echo: Eq. C.16 shows that this is still true,

$$f_{\phi m}^{\mathrm{hf}}(t) \approx \exp\left[-\frac{1}{2}t|D_2|A_\lambda\left[\pi - g(2\pi t|D_2|A_\lambda)\right]\right]. \tag{C.32}$$

12 We could have avoided the approximations and arrived at

$$\begin{aligned}
\lim_{\epsilon\to0^+}\int_\epsilon^\infty\frac{\mathrm{d}\omega}{\omega^3}\ln\frac{\omega}{\omega_{\mathrm{ir}}}\sin^2\frac{\omega t}{2} &= \frac{t^2}{8}\lim_{\epsilon\to0^+}\left[3(1-\gamma)+\frac{1}{2}+\gamma^2-\frac{\pi^2}{12}+(3-2\gamma)\ln\frac{1}{\omega_{\mathrm{ir}}t}+\ln\epsilon t\left(\ln\epsilon t+2\ln\frac{\omega_{\mathrm{ir}}}{\epsilon}\right)\right] \\
&\to \frac{t^2}{8}\left[\left(\ln\frac{1}{\omega_{\mathrm{ir}}t}+\frac{3}{2}-\gamma\right)^2+\frac{15-\pi^2}{12}\right],
\end{aligned}$$

but this agrees with Eq. C.34 up to small corrections (for $\omega_{\mathrm{ir}}t \ll 1$) because $\frac{3}{2}-\gamma \sim 1$ and $\frac{15-\pi^2}{12} \lesssim 1$.

13 Generalized echo: Eq. C.20 gives us

$$f_{\phi m}(t) = \exp\left[-8D_2^2A_\lambda^2\int_0^\infty\frac{\mathrm{d}\omega}{\omega^3}\ln\frac{\omega}{\omega_{\mathrm{ir}}}\sin^2\frac{\omega t}{2}\tan^2\frac{\omega t}{2m}\right] = \exp\left[-2t^2D_2^2A_\lambda^2\left(B_m\ln\frac{2m}{\omega_{\mathrm{ir}}t}+C_m\right)\right], \tag{C.35}$$

where B_m (defined in Eq. C.27) and $C_m = \int_0^\infty\frac{\mathrm{d}u}{u^3}\ln\frac{u}{m}\sin^2u\tan^2\frac{u}{m}$ are numerical factors. In the same vein as $B_m \sim \frac{8}{\pi^2 m}$ was calculated for large m, we find $C_m \sim \frac{8}{\pi^2 m}\ln\frac{\pi}{2}$.

into Eq. C.22 and obtain

$$\begin{aligned} f_{\phi\mathrm{E}}(t) &= \exp\left[-32D_2^2A_\lambda^2\int_0^\infty \frac{\mathrm{d}\omega}{\omega^3}\ln\frac{\omega}{\omega_{\mathrm{ir}}}\sin^4\frac{\omega t}{4}\right] \\ &= \exp\left[-2t^2D_2^2A_\lambda^2\int_0^\infty \frac{\mathrm{d}u}{u^3}\ln\frac{4u}{\omega_{\mathrm{ir}}t}\sin^4 u\right] \\ &\approx \exp\left[-t^2D_2^2A_\lambda^2\ln 4\left(\ln\frac{1}{\omega_{\mathrm{ir}}t}+\ln 4\right)\right] \end{aligned} \tag{C.36}$$

by neglecting the logarithmic term in the integrand[14] and once more making use of $\int_0^\infty \mathrm{d}x\,\frac{1}{x^3}\sin^4 x = \ln 2$.

C.4.3 Summary

It is convenient to define the dimensionless time and (inverse) infrared cutoff

$$x = \Gamma t \qquad\qquad \eta = \frac{\Gamma}{\omega_{\mathrm{ir}}},$$

where $\Gamma = |D_1|\sqrt{A_\lambda}$ for linear coupling and $\Gamma = |D_2|A_\lambda$ for quadratic coupling. For modern superconducting qubit experiments, $\Gamma/2\pi \sim 10\,\mathrm{kHz}$–$1\,\mathrm{MHz}$ (corresponding to pure dephasing times of order 1–100 µs) and $\omega_{\mathrm{ir}}/2\pi \sim 1\,\mathrm{Hz}$ (corresponding to many thousands of averages). Therefore, $\eta \sim 10^4$–10^6 and the bulk of dephasing occurs on the timescale of $1/\Gamma$. With these definitions, the envelopes and their approximate timescales are listed in Tab. C.1 and plotted in Fig. C.2.

C.5 Charge noise

As discussed in Sec. 7.1.2, offset charge noise conventionally refers to the fluctuations of N_{g} about a bias value $\overline{N_{\mathrm{g}}}$, which are approximately as rapid as the individual measurement time—itself on the order of the qubit coherence time. These fluctuations are a form of $1/f$ noise, and the treatment in Sec. C.4 is applicable when the bias value $\overline{N_{\mathrm{g}}}$ is fixed. When this bias value is not fixed, e.g. it drifts over time or exhibits infrequent but large jumps, this treatment breaks down. In this section, we discuss the model in such a situation.

We consider the two-level Hamiltonian

$$H(t) = \hbar\Omega(t)|e\rangle\langle e| = \left[\hbar\Omega_0 + \tfrac{1}{2}\epsilon\cos(2\pi\mu N_{\mathrm{g}})\right]|e\rangle\langle e|,$$

where ϵ is the charge dispersion, N_{g} is the offset charge (in number of Cooper pairs), and $2\pi\mu$ is the period of the Hamiltonian in φ.[15] For a Ramsey-type measurement of the coherence, we have the envelope function

$$f_{\phi\mathrm{R}}(t) = \left\langle \mathrm{e}^{i\frac{\epsilon}{2\hbar}\int_0^t \mathrm{d}t'\,\cos[2\pi\mu N_{\mathrm{g}}(t')]}\right\rangle.$$

14 The neglected term is readily observed to be small, $\int_0^\infty \frac{\mathrm{d}u}{u^3}\ln u\sin^4 u = \frac{1}{2}\ln 2(3-2\gamma-\ln 8) \ll 1$.

15 For the generalized $\cos m\varphi$ circuit element in Sec. 9.2.1, we have $m = 1/\mu$.

	Coupling	Gauss.	Linked	Envelope magnitude $\lvert f_\phi(t)\rvert$	Approx. dephasing rate
Ramsey	Lin.	✓	✓	$\exp\left[-x^2\left(\ln\frac{\eta}{x}+1\right)\right]$	$\sqrt{\ln\eta}\,\Gamma$
	Quad.	✓	–	$\exp\left[-x^2\left(\ln\frac{\eta}{x}+1\right)^2\right]$	$\ln\eta\,\Gamma$
	Quad.	–	✓	$\left(1+4x^2\ln^2\frac{\eta}{x}\right)^{-1/4}\mathrm{e}^{-\frac{1}{2}x[\pi-g(2\pi x)]}$	$\left(\pi+\frac{2}{\mathrm{e}^2}\ln\eta\right)\Gamma$
Echo	Lin.	✓	✓	$\exp\left[-x^2\ln 2\right]$	$\sqrt{\ln 2}\,\Gamma$
	Quad.	✓	–	$\exp\left[-x^2\ln 4\left(\ln\frac{\eta}{x}+\ln 4\right)\right]$	$\sqrt{\ln 4\ln\eta}\,\Gamma$
	Quad.	–	✓	$\left(1+\frac{1}{8}x^2\ln\frac{\eta}{x}\right)^{-1/2}\mathrm{e}^{-\frac{1}{2}x[\pi-g(2\pi x)]}$	$\frac{1}{2}\left(\pi+\frac{1}{\sqrt{2}\mathrm{e}}\sqrt{\ln\eta}\right)\Gamma$
Generalized echo	Lin.	✓	✓	$\exp\left[-x^2 B_m\right]$	$\sqrt{B_m}\,\Gamma$
	Quad.	✓	–	$\exp\left[-2x^2\left(B_m\ln\frac{2m\eta}{x}+C_m\right)\right]$	$\sqrt{2B_m\ln\eta}\,\Gamma$
	Quad.	–	✓	$\left(1+\frac{1}{2m^2}x^2\ln\frac{\eta}{x}\right)^{-1/2}\mathrm{e}^{-\frac{1}{2}x[\pi-g(2\pi x)]}$	$\frac{1}{2}\left(\pi+\frac{1}{m\mathrm{e}}\sqrt{2\ln\eta}\right)\Gamma$

Table C.1 Summary of coherence decay envelopes for linear and quadratic coupling to the noise, assuming a $1/f$ noise spectral density and small fluctuations. Formulas are listed for free induction decay (a Ramsey measurement), a single spin-echo measurement, and a generalized echo-type measurement (with m constituent decay intervals). Note that we use the notation where $B_m = \int_0^\infty \frac{\mathrm{d}u}{u^3}\sin^2 u\tan^2\frac{u}{m}$, $C_m = \int_0^\infty \frac{\mathrm{d}u}{u^3}\ln\frac{u}{m}\sin^2 u\tan^2\frac{u}{m}$, and $g(x) = \int_0^{1/x}\mathrm{d}u\,\ln(1+\frac{1}{u^2})$. The approximate rate at which the decay envelope reaches the value $1/\mathrm{e}$ is also listed as the dephasing rate in the final column.

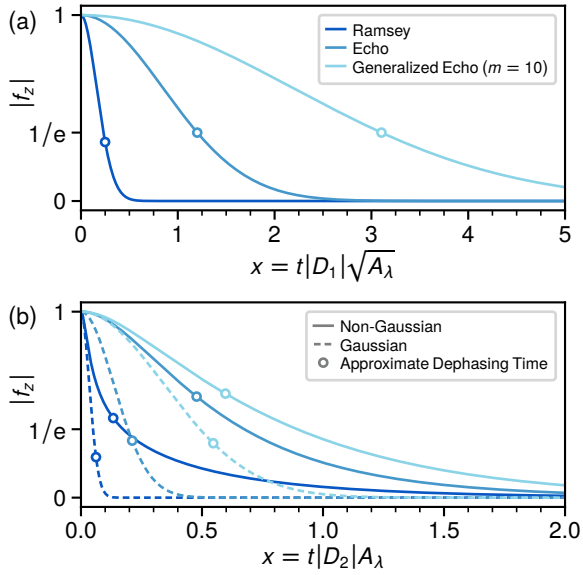

Figure C.2 Dephasing envelopes for $1/f$ noise, as listed in Tab. C.1. Calculations employ $\eta = 10^7$ and $m = 10$ for the generalized echo case. (a) Linear coupling, showing a Gaussian functional form. (b) Quadratic coupling, showing the initial slow power law that reverts to an exponential decay. The Gaussian approximation is plotted in dashed lines and yields similar relative dephasing timescales to those in linear coupling.

When the average value $\overline{N_g}$ is fixed, the integrand may be expanded in powers of $N_g - \overline{N_g}$ and the earlier results may be used. If $\overline{N_g}$ is not fixed, we can model N_g as taking a constant (but randomly distributed) value in $[0, 1]$ for each measurement. Averaging these measurements together, we find

$$f_{\phi R}(t) = \left\langle e^{i\frac{\epsilon t}{2\hbar}\cos(2\pi\mu N_g)} \right\rangle = \int_0^1 dN_g\, e^{i\frac{\epsilon t}{2\hbar}\cos(2\pi\mu N_g)} = J_0\left(\tfrac{1}{2\hbar}\epsilon t\right),$$

for integer-valued μ, justifying Eq. 7.10. Notably, $\mu = 1$ and $\mu = 2$ correspond to the transmon and $\cos 2\varphi$ qubit, respectively [J. Koch et al. 2007].[16] For the echo case, the statistical average must be performed over two offset charge values. We get

$$f_{\phi E}(t) = \left\langle e^{-i\frac{\epsilon t}{4}\cos(2\pi\mu N_g) + i\frac{\epsilon t}{4}\cos(2\pi\mu N_g')} \right\rangle = \left[J_0\left(\tfrac{1}{4\hbar}\epsilon t\right)\right]^2,$$

which readily generalizes to $f_{\phi m}(t) = \left[J_0\left(\frac{1}{2m\hbar}\epsilon t\right)\right]^m$ in the case of $m - 1$ echo pulses.

16 When $\mu = 1/m$ and $m > 2$, as in the case of the $\cos m\varphi$ circuit element, this integral is complex and the calculation is more involved.

C.6 Shot noise

In Eq. 7.15, we stated the results of Gambetta et al. (2006) and Clerk and Utami (2007) for the dephasing envelopes due to fluctuations in the occupancy of a harmonic oscillator dispersively coupled to a two-level system. The two equations correspond to the coherent (e.g. a cavity with an ac drive) and incoherent (e.g. a cavity at nonzero temperature) cases, where the different photon statistics lead to slightly different forms for the phase decay. Indeed, these spectral densities are Lorentzian and a prime example of noise that is not $1/f$. In this final section, we provide a derivation of the result in the driven case in addition to a few comments on the thermal case.

For the coherent case, we consider the Hamiltonian of the system

$$H(t) = \hbar\omega_0 a^\dagger a + \hbar\Omega|e\rangle\langle e| + \hbar\chi a^\dagger a|e\rangle\langle e| + \hbar\epsilon\cos\omega_\mathrm{p} t\,(a + a^\dagger),$$

where ω_0 is the oscillator frequency, ω_p is the drive frequency, χ is the dispersive shift, and ϵ is the drive strength. We apply the unitary $U = \mathrm{e}^{i\omega_\mathrm{p} a^\dagger a t}$, which transforms $a \to a\mathrm{e}^{-i\omega_\mathrm{p} t}$, and the Hamiltonian becomes

$$UHU^\dagger \approx H' = \hbar\Delta a^\dagger a + \hbar\Omega|e\rangle\langle e| + \hbar\chi a^\dagger a|e\rangle\langle e| + \tfrac{1}{2}\hbar\epsilon(a + a^\dagger),$$

where the approximation neglects terms rotating at $\pm 2\omega_\mathrm{p}$, and we have defined $\Delta = \omega_0 - \omega_\mathrm{p}$. The Lindblad equation reads [Haroche and Raimond 2006]

$$\dot\rho = -\frac{i}{\hbar}[H', \rho] + \kappa\Big[a\rho a^\dagger - \tfrac{1}{2}\big(a^\dagger a\rho + \rho a^\dagger a\big)\Big],$$

where κ is the oscillator linewidth and the total density matrix may be written as $\rho = \rho_{gg}|g\rangle\langle g| + \rho_{ge}|g\rangle\langle e| + \rho_{eg}|e\rangle\langle g| + \rho_{ee}|e\rangle\langle e|$. We then seek a solution for the off-diagonal qubit component of the form $\rho_{ge} \propto |\alpha_g\rangle\langle\alpha_e|$, with $|\alpha_g\rangle$ and $|\alpha_e\rangle$ being coherent states. We therefore find the equation

$$\begin{aligned}\dot\rho_{ge} = &\Big(i\Omega - \tfrac{1}{2}i\epsilon\alpha_g + \tfrac{1}{2}i\epsilon\alpha_e^* + \kappa\alpha_g\alpha_e^*\Big)\rho_{ge} \\ &- \Big(i\Delta\alpha_g + \tfrac{1}{2}i\epsilon + \tfrac{1}{2}\kappa\alpha_g\Big)a^\dagger\rho_{ge} + \Big(i\Delta\alpha_e^* + i\chi\alpha_e^* + \tfrac{1}{2}i\epsilon - \tfrac{1}{2}\kappa\alpha_e^*\Big)\rho_{ge}a.\end{aligned}$$

The bottom line can be made to vanish, uncoupling the differential equation, by taking

$$\alpha_g = -\frac{\epsilon}{2\Delta - i\kappa} \qquad \alpha_e^* = -\frac{\epsilon}{2(\Delta + \chi) + i\kappa},$$

which are consistent. The differential equation, using $\delta = \Delta + \chi/2$, then reads

$$\dot\rho_{ge} = i\left[\Omega + \frac{\chi\epsilon^2}{(2\delta)^2 - (\chi + i\kappa)^2}\right]\rho_{ge}.$$

From this, we can read off the Ramsey decay envelope to be

$$|f_{\phi\mathrm{R}}(t)| = \exp\left[-t\,\mathrm{Im}\,\frac{\chi\epsilon^2}{(2\delta)^2 - (\chi + i\kappa)^2}\right] = \exp\left[-(\bar n_g + \bar n_e)\kappa t\frac{\chi^2}{(2\delta)^2 + \chi^2 + \kappa^2}\right]$$

where the average photon occupancies are

$$\bar{n}_g = |\alpha_g|^2 = \frac{\epsilon^2}{(2\delta - \chi)^2 + \kappa^2} \qquad \bar{n}_e = |\alpha_e|^2 = \frac{\epsilon^2}{(2\delta + \chi)^2 + \kappa^2}.$$

For $\delta = 0$, this simplifies to $\bar{n}_g = \bar{n}_e$ (which we can reasonably call $\bar{n}$) and

$$|f_{\phi R}(t)| = \exp\left[-2\bar{n}\kappa t \frac{\chi^2}{\chi^2 + \kappa^2}\right],$$

which justifies the first line of Eq. 7.15. From this, we obtain the dc component of the noise spectral density $S_{nn}[0]$ using Eq. 7.9 and the fact that the total qubit frequency is $\Omega + \chi n$. To reproduce the Lorentzian spectral density in the first line of Eq. 7.14, we then need to consider the decay rate of the photon number autocorrelation function [Blais et al. 2004].

For the incoherent case, the treatment is more involved. We quote the result for the Ramsey decay envelope [Clerk and Utami 2007]

$$|f_{\phi R}(t)| = \exp\left[-\frac{1}{2}\kappa t \,\mathrm{Re}\left\{\sqrt{\left(1 + i\tfrac{\chi}{\kappa}\right)^2 + 4in_{\mathrm{th}}\tfrac{\chi}{\kappa}} - 1\right\}\right],$$

where n_{th} is the thermal occupation. If we now expand this about $n_{\mathrm{th}} = 0$, we arrive at

$$|f_{\phi R}(t)| \approx \left[-n_{\mathrm{th}}\kappa t \frac{\chi^2}{\chi^2 + \kappa^2}\right],$$

justifying the second line of Eq. 7.15.

D

SUPERCONDUCTIVITY

In Sec. 2.2.2, we presented the two Josephson relations and used them to write the Hamiltonian of a Josephson junction $H_\text{J} = 4E_\text{C}(N - N_\text{g})^2 - E_\text{J}\cos\varphi$ in terms of the phase drop φ and the number of tunneled Cooper pairs N (see Eq. 2.2). This Hamiltonian, and in particular the cosine term, was used extensively throughout this thesis without justification. In this appendix, we explain the Josephson effect microscopically by modeling a junction as a weak point contact between two superconductors. The material here draws on the lecture notes on quantum many-body theory by Leonid Glazman in addition to some classic textbooks on condensed matter physics [Schrieffer 1999, de Gennes 1999, Pines 1999, Tinkham 2004, Giuliani and Vignale 2005].

Superconductors are characterized by two length scales. There is the London penetration depth λ_L to which an external magnetic field can enter a superconductor, and there is the coherence length ξ_0 that specifies the spatial extent of a Cooper pair. Type I superconductors have $\xi_0 > \lambda_\text{L}$ while Type II superconductors have $\xi_0 < \lambda_\text{L}$. We concentrate on conventional Type I superconductors, like aluminum, which are well-described by Bardeen-Cooper-Schrieffer (BCS) theory. We describe the basic BCS Hamiltonian starting from second quantization in Secs. D.1–3, some additional technical details in Secs. D.4–5, and finally the Josephson effect in Sec. D.6.

D.1 Second quantization

We start with the first-quantized Hamiltonian for identical particles with pairwise interactions in three dimensions

$$H = \sum_i \left[\frac{\mathbf{p}_i^2}{2m} + \sum_{j>i} V(\mathbf{x}_i, \mathbf{x}_j) \right]. \tag{D.1}$$

Here, i and j index the individual particles and the sum over j is restricted to $j > i$ because we do not consider self-interactions and V is symmetric under particle interchange.

To get a feeling for second quantization, we consider the single-body operator in first quantization,

$$\mathcal{A} = \sum_i A(i),$$

where $A(i) = A(\mathbf{x}_i, \mathbf{p}_i)$ is a shorthand notation. Because of particle indistinguishability, the position eigenstates $|\mathbf{x}_i\rangle$ are complete for any i. We can then multiply the above on both

sides by $\int \mathrm{d}^3x\,|\mathbf{x}\rangle\langle\mathbf{x}| = 1$ and get

$$\mathcal{A} = \sum_i \int \mathrm{d}^3x \int \mathrm{d}^3x'\,|\mathbf{x}\rangle\langle\mathbf{x}|A(i)|\mathbf{x}'\rangle\langle\mathbf{x}'| = \int \mathrm{d}^3x\,|\mathbf{x}\rangle A\langle\mathbf{x}|$$

using $\sum_i \langle\mathbf{x}|A(i)|\mathbf{x}'\rangle = A\langle\mathbf{x}|\mathbf{x}'\rangle$. This can then be expanded in the single-particle states $|\alpha\rangle$,

$$\mathcal{A} = \sum_{\alpha,\alpha'} \int \mathrm{d}^3x\,|\alpha\rangle\langle\alpha|\mathbf{x}\rangle A\langle\mathbf{x}|\alpha'\rangle\langle\alpha'| = \int \mathrm{d}^3x\,\psi^\dagger(\mathbf{x})A\psi(\mathbf{x}),$$

where the last equality employs the representation $|\alpha\rangle\langle\alpha'| = a_\alpha^\dagger a_{\alpha'}$. We have introduced the field operators $\psi(\mathbf{x})$ that annihilate one particle at position $\mathbf{x}$ with any momentum, given by

$$\psi(\mathbf{x}) = \sum_\alpha \psi_\alpha(\mathbf{x})a_\alpha,$$

where $\psi_\alpha(\mathbf{x}) = \langle\mathbf{x}|\alpha\rangle$. The analogous representation for a two-body operator is

$$\begin{aligned}\mathcal{B} = \sum_{i\neq j} B(i,j) &= \int \mathrm{d}^3x \int \mathrm{d}^3x'\,|\mathbf{x}\mathbf{x}'\rangle B\langle\mathbf{x}\mathbf{x}'| \\ &= \int \mathrm{d}^3x \int \mathrm{d}^3x'\,\psi^\dagger(\mathbf{x})\psi^\dagger(\mathbf{x}')B\psi(\mathbf{x}')\psi(\mathbf{x}).\end{aligned}$$

We are now prepared to write Eq. D.1 in second quantization as

$$\begin{aligned}H = &-\frac{\hbar^2}{2m}\int \mathrm{d}^3x\,\psi^\dagger(\mathbf{x})\nabla^2\psi(\mathbf{x}) \\ &+ \frac{1}{2}\int \mathrm{d}^3x \int \mathrm{d}^3x'\,\psi^\dagger(\mathbf{x})\psi^\dagger(\mathbf{x}')V(\mathbf{x},\mathbf{x}')\psi(\mathbf{x}')\psi(\mathbf{x}).\end{aligned} \tag{D.2}$$

D.2 Fermi liquid theory

For fermions, we assign the index α to a wavevector $\mathbf{k}$ and a spin σ. The single-particle wavefunctions are plane waves normalized over a volume $\mathcal{V}$, given by $\psi_\mathbf{k}(\mathbf{x}) = \mathcal{V}^{-1/2}\mathrm{e}^{i\mathbf{k}\cdot\mathbf{x}}$, and the spin-dependent field operators are

$$\psi_\sigma(\mathbf{x}) = \sum_\mathbf{k} \psi_\mathbf{k}(\mathbf{x})c_{\mathbf{k}\sigma} = \frac{1}{\sqrt{\mathcal{V}}}\sum_\mathbf{k} \mathrm{e}^{i\mathbf{k}\cdot\mathbf{x}}c_{\mathbf{k}\sigma}.$$

For the same reason that each $\mathbf{x}$ appears an even number of times in each term in Eq. D.2, so too will each spin index σ. Using $\int \mathrm{d}^3x\,\mathrm{e}^{i\mathbf{k}\cdot\mathbf{x}} = \mathcal{V}\delta_{\mathbf{k},0}$, the kinetic energy becomes

$$\begin{aligned}T &= -\frac{\hbar^2}{2m}\sum_\sigma \int \mathrm{d}^3x\,\psi_\sigma^\dagger(\mathbf{x})\nabla^2\psi_\sigma(\mathbf{x}) = -\frac{\hbar^2}{2m\mathcal{V}}\sum_{\mathbf{k},\mathbf{k}',\sigma} c_{\mathbf{k}\sigma}^\dagger c_{\mathbf{k}'\sigma}\int \mathrm{d}^3x\,\mathrm{e}^{-i\mathbf{k}\cdot\mathbf{x}}\nabla^2\mathrm{e}^{i\mathbf{k}'\cdot\mathbf{x}} \\ &= \frac{\hbar^2}{2m\mathcal{V}}\sum_{\mathbf{k},\mathbf{k}',\sigma} c_{\mathbf{k}\sigma}^\dagger c_{\mathbf{k}'\sigma}|\mathbf{k}'|^2\int \mathrm{d}^3x\,\mathrm{e}^{-i(\mathbf{k}-\mathbf{k}')\cdot\mathbf{x}} = \sum_{\mathbf{k},\sigma}\frac{\hbar^2\mathbf{k}^2}{2m}c_{\mathbf{k}\sigma}^\dagger c_{\mathbf{k}\sigma}.\end{aligned}$$

We must subtract the term $\sum_{\mathbf{k},\sigma} \epsilon_{\mathrm{F}} c^\dagger_{\mathbf{k}\sigma} c_{\mathbf{k}\sigma}$ so that there are a finite number of particles at zero temperature. This constant is the Fermi energy $\epsilon_{\mathrm{F}} = \frac{\hbar^2 k_{\mathrm{F}}^2}{2m}$ and $\epsilon_{\mathbf{k}} = \frac{\hbar^2 \mathbf{k}^2}{2m} - \epsilon_{\mathrm{F}}$ is the single-particle dispersion relation.

For interactions of the form $V(\mathbf{x}, \mathbf{x}') = V(\mathbf{x} - \mathbf{x}')$, the potential energy becomes

$$\begin{aligned} U &= \frac{1}{2} \sum_{\sigma,\sigma'} \int \mathrm{d}^3 x \int \mathrm{d}^3 x' \, \psi^\dagger_\sigma(\mathbf{x}) \psi^\dagger_{\sigma'}(\mathbf{x}') V(\mathbf{x} - \mathbf{x}') \psi_{\sigma'}(\mathbf{x}') \psi_\sigma(\mathbf{x}) \\ &= \frac{1}{2\mathcal{V}^2} \sum_{\mathbf{k},\mathbf{k}',\mathbf{q},\mathbf{q}',\sigma,\sigma'} c^\dagger_{\mathbf{k}\sigma} c^\dagger_{\mathbf{q}\sigma'} c_{\mathbf{q}'\sigma'} c_{\mathbf{k}'\sigma} \int \mathrm{d}^3 x \int \mathrm{d}^3 x' \, V(\mathbf{x} - \mathbf{x}') \mathrm{e}^{-i(\mathbf{k}-\mathbf{k}')\cdot\mathbf{x}} \mathrm{e}^{-i(\mathbf{q}-\mathbf{q}')\cdot\mathbf{x}'} \\ &= \frac{1}{2} \sum_{\mathbf{k},\mathbf{k}',\mathbf{q},\mathbf{q}',\sigma,\sigma'} \left[\frac{1}{\mathcal{V}} \int \mathrm{d}^3 r \, V(\mathbf{r}) \mathrm{e}^{-i(\mathbf{k}-\mathbf{k}')\cdot\mathbf{r}} \right] c^\dagger_{\mathbf{k}\sigma} c^\dagger_{\mathbf{q}\sigma'} c_{\mathbf{q}'\sigma'} c_{\mathbf{k}'\sigma} \delta_{\mathbf{k}-\mathbf{k}',\mathbf{q}'-\mathbf{q}} \\ &= \frac{1}{2} \sum_{\mathbf{k},\mathbf{k}',\mathbf{q},\sigma,\sigma'} V_{\mathbf{k}-\mathbf{k}'} c^\dagger_{\mathbf{k}\sigma} c^\dagger_{\mathbf{q}-\mathbf{k}\sigma'} c_{\mathbf{q}-\mathbf{k}'\sigma'} c_{\mathbf{k}'\sigma}, \end{aligned}$$

where $\mathbf{r} = \mathbf{x} - \mathbf{x}'$ and we have identified the term in brackets as the Fourier transform of the potential $V_{\mathbf{k}-\mathbf{k}'}$. For clarity, we write the result of this calculation

$$H = \sum_{\mathbf{k},\sigma} \epsilon_{\mathbf{k}} c^\dagger_{\mathbf{k}\sigma} c_{\mathbf{k}\sigma} + \frac{1}{2} \sum_{\mathbf{k},\mathbf{k}',\mathbf{q},\sigma,\sigma'} V_{\mathbf{k}-\mathbf{k}'} c^\dagger_{\mathbf{k}\sigma} c^\dagger_{\mathbf{q}-\mathbf{k}\sigma'} c_{\mathbf{q}-\mathbf{k}'\sigma'} c_{\mathbf{k}'\sigma}. \tag{D.3}$$

This form lends itself to BCS theory in that Cooper pairing corresponds to the $\mathbf{q} = 0$ term (which also demands that $\sigma \neq \sigma'$). In other contexts, it is useful to define $\mathbf{p} = \mathbf{k} - \mathbf{k}'$ and $\mathbf{q}' = \mathbf{q} - \mathbf{k}'$ so that Eq. D.3 becomes

$$H = \sum_{\mathbf{k},\sigma} \epsilon_{\mathbf{k}} c^\dagger_{\mathbf{k}\sigma} c_{\mathbf{k}\sigma} + \frac{1}{2} \sum_{\mathbf{k}',\mathbf{q}',\mathbf{p},\sigma,\sigma'} V_{\mathbf{p}} c^\dagger_{\mathbf{k}'+\mathbf{p}\sigma} c^\dagger_{\mathbf{q}'-\mathbf{p}\sigma'} c_{\mathbf{q}'\sigma'} c_{\mathbf{k}'\sigma}. \tag{D.4}$$

D.3 BCS theory

We can model a conventional superconductor using Eq. D.3 if we pick out the $\mathbf{q} = 0$ term corresponding to interacting electron pairs with stationary centers-of-mass. The neglected terms can be important, but that will be handled by Hartree-Fock theory (see Sec. D.4). This gives the pairing Hamiltonian

$$H_{\mathrm{P}} = \sum_{\mathbf{k},\sigma} \epsilon_{\mathbf{k}} c^\dagger_{\mathbf{k}\sigma} c_{\mathbf{k}\sigma} + \sum_{\mathbf{k},\mathbf{k}'} V_{\mathbf{k}-\mathbf{k}'} c^\dagger_{\mathbf{k}\uparrow} c^\dagger_{-\mathbf{k}\downarrow} c_{-\mathbf{k}'\downarrow} c_{\mathbf{k}'\uparrow}, \tag{D.5}$$

since Pauli exclusion prohibits $\sigma = \sigma'$. The factor of $\frac{1}{2}$ is removed because there are two spin configurations for electrons and they are equivalent (and we take $V_{\mathbf{k}-\mathbf{k}'}$ to be real).

The mean-field approximation for an arbitrary coupling term reads

$$XF = (X - \langle X \rangle)(F - \langle F \rangle) + X\langle F \rangle + \langle X \rangle F - \langle X \rangle \langle F \rangle \approx X\langle F \rangle + \langle X \rangle F - \langle X \rangle \langle F \rangle.$$

The notion is that $X - \langle X \rangle$ and $F - \langle F \rangle$ are fluctuation terms, and their product is a quadratic fluctuation term that is negligible for many particles. The pairing Hamiltonian in Eq. D.5

becomes

$$\begin{aligned} H_{\mathrm{BCS}} &= \sum_{\mathbf{k},\sigma} \epsilon_{\mathbf{k}} c^{\dagger}_{\mathbf{k}\sigma} c_{\mathbf{k}\sigma} + \sum_{\mathbf{k},\mathbf{k}'} V_{\mathbf{k}-\mathbf{k}'} \Big[c^{\dagger}_{\mathbf{k}\uparrow} c^{\dagger}_{-\mathbf{k}\downarrow} \langle c_{-\mathbf{k}'\downarrow} c_{\mathbf{k}'\uparrow} \rangle \\ &\qquad + \langle c^{\dagger}_{\mathbf{k}\uparrow} c^{\dagger}_{-\mathbf{k}\downarrow} \rangle c_{-\mathbf{k}'\downarrow} c_{\mathbf{k}'\uparrow} - \langle c^{\dagger}_{\mathbf{k}\uparrow} c^{\dagger}_{-\mathbf{k}\downarrow} \rangle \langle c_{-\mathbf{k}'\downarrow} c_{\mathbf{k}'\uparrow} \rangle \Big] \\ &= \sum_{\mathbf{k},\sigma} \epsilon_{\mathbf{k}} c^{\dagger}_{\mathbf{k}\sigma} c_{\mathbf{k}\sigma} - \sum_{\mathbf{k}} \Big[\Delta_{\mathbf{k}} c^{\dagger}_{\mathbf{k}\uparrow} c^{\dagger}_{-\mathbf{k}\downarrow} + \Delta^{*}_{\mathbf{k}} c_{-\mathbf{k}\downarrow} c_{\mathbf{k}\uparrow} - \Delta^{*}_{\mathbf{k}} \langle c_{-\mathbf{k}\downarrow} c_{\mathbf{k}\uparrow} \rangle \Big], \end{aligned} \tag{D.6}$$

where we have introduced

$$\Delta_{\mathbf{k}} = -\sum_{\mathbf{k}'} V_{\mathbf{k}-\mathbf{k}'} \langle c_{-\mathbf{k}'\downarrow} c_{\mathbf{k}'\uparrow} \rangle.$$

These $\Delta_{\mathbf{k}}$ are the Fourier components of the pair potential. Crucially, the phonon-mediated interaction between electrons in the superconductor can be attractive. In conventional superconductors, this overcomes the repulsive Coulomb interaction for electrons near the Fermi surface and the ground state corresponds to a solution $\Delta_{\mathbf{k}} \neq 0$. This should be contrasted with a normal metal, for which $\Delta_{\mathbf{k}} = 0$ in the ground state.

We now invoke a Bogoliubov transformation, which in general is a linear transformation

$$\begin{aligned} b_{\alpha} &= \sum_{\beta} \left[u_{\alpha\beta} a_{\beta} + v_{\alpha\beta} a^{\dagger}_{\beta} \right] \\ b^{\dagger}_{\alpha} &= \sum_{\beta} \left[u^{*}_{\alpha\beta} a^{\dagger}_{\beta} + v^{*}_{\alpha\beta} a_{\beta} \right] \end{aligned}$$

between creation/annihilation operators together with the requirement that the b_{α} obey the same commutation/anticommutation relations as the a_{α}. This means that

$$uv^{\mathrm{T}} \pm vu^{\mathrm{T}} = 0 \qquad\qquad uu^{\dagger} \pm vv^{\dagger} = 1 \tag{D.7}$$

as matrices, where the positive sign refers to fermions and the negative sign to bosons. For the purpose to diagonalizing Eq. D.6, we take u and v to be block diagonal according to

$$\begin{pmatrix} c_{\mathbf{k}\uparrow} \\ c_{-\mathbf{k}\downarrow} \end{pmatrix} = u^{*}_{\mathbf{k}} \begin{pmatrix} 1 & 0 \\ 0 & 1 \end{pmatrix} \begin{pmatrix} \gamma_{\mathbf{k}\uparrow} \\ \gamma_{-\mathbf{k}\downarrow} \end{pmatrix} + v_{\mathbf{k}} \begin{pmatrix} 0 & 1 \\ -1 & 0 \end{pmatrix} \begin{pmatrix} \gamma^{\dagger}_{\mathbf{k}\uparrow} \\ \gamma^{\dagger}_{-\mathbf{k}\downarrow} \end{pmatrix} \Leftrightarrow \begin{pmatrix} c_{\mathbf{k}\uparrow} \\ c^{\dagger}_{-\mathbf{k}\downarrow} \end{pmatrix} = \begin{pmatrix} u^{*}_{\mathbf{k}} & v_{\mathbf{k}} \\ -v^{*}_{\mathbf{k}} & u_{\mathbf{k}} \end{pmatrix} \begin{pmatrix} \gamma_{\mathbf{k}\uparrow} \\ \gamma^{\dagger}_{-\mathbf{k}\downarrow} \end{pmatrix}. \tag{D.8}$$

This transformation satisfies Eq. D.7 when $|u_{\mathbf{k}}|^2 + |v_{\mathbf{k}}|^2 = 1$, which then means that the $\gamma_{\mathbf{k}\sigma}$ are fermionic creation operators. The inverse transformation is $\gamma_{\mathbf{k}\uparrow} = u_{\mathbf{k}} c_{\mathbf{k}\uparrow} - v_{\mathbf{k}} c^{\dagger}_{-\mathbf{k}\downarrow}$ and $\gamma_{-\mathbf{k}\downarrow} = u_{\mathbf{k}} c_{-\mathbf{k}\downarrow} + v_{\mathbf{k}} c^{\dagger}_{\mathbf{k}\uparrow}$. The operator $\gamma_{\mathbf{k}\uparrow}$ reduces the wavevector by $\mathbf{k}$ and the spin projection by $\hbar/2$, while $\gamma_{-\mathbf{k}\downarrow}$ increases the wavevector by $\mathbf{k}$ and the spin projection by $\hbar/2$.

We can rewrite Eq. D.6 in the form

$$\begin{aligned} H_{\mathrm{BCS}} &= \sum_{\mathbf{k}} \left[\begin{pmatrix} c^{\dagger}_{\mathbf{k}\uparrow} & c_{-\mathbf{k}\downarrow} \end{pmatrix} \begin{pmatrix} \epsilon_{\mathbf{k}} & -\Delta_{\mathbf{k}} \\ -\Delta^{*}_{\mathbf{k}} & -\epsilon_{\mathbf{k}} \end{pmatrix} \begin{pmatrix} c_{\mathbf{k}\uparrow} \\ c^{\dagger}_{-\mathbf{k}\downarrow} \end{pmatrix} + \epsilon_{\mathbf{k}} + \Delta^{*}_{\mathbf{k}} \langle c_{-\mathbf{k}\downarrow} c_{\mathbf{k}\uparrow} \rangle \right] \\ &= \sum_{\mathbf{k}} \left[\begin{pmatrix} \gamma^{\dagger}_{\mathbf{k}\uparrow} & \gamma_{-\mathbf{k}\downarrow} \end{pmatrix} H_{\mathbf{k}} \begin{pmatrix} \gamma_{\mathbf{k}\uparrow} \\ \gamma^{\dagger}_{-\mathbf{k}\downarrow} \end{pmatrix} + \epsilon_{\mathbf{k}} + \Delta^{*}_{\mathbf{k}} \langle c_{-\mathbf{k}\downarrow} c_{\mathbf{k}\uparrow} \rangle \right], \end{aligned}$$

where $H_{\mathbf{k}}$ is the matrix in the first line transformed by Eq. D.8. Explicitly,

$$H_{\mathbf{k}} = \begin{pmatrix} \epsilon_{\mathbf{k}}(|u_{\mathbf{k}}|^2 - |v_{\mathbf{k}}|^2) + \Delta_{\mathbf{k}} u_{\mathbf{k}} v_{\mathbf{k}}^* + \Delta_{\mathbf{k}}^* u_{\mathbf{k}}^* v_{\mathbf{k}} & 2\epsilon_{\mathbf{k}} u_{\mathbf{k}} v_{\mathbf{k}} - \Delta_{\mathbf{k}} u_{\mathbf{k}}^2 + \Delta_{\mathbf{k}}^* v_{\mathbf{k}}^2 \\ 2\epsilon_{\mathbf{k}} u_{\mathbf{k}}^* v_{\mathbf{k}}^* - \Delta_{\mathbf{k}}^* u_{\mathbf{k}}^{*2} + \Delta_{\mathbf{k}} v_{\mathbf{k}}^{*2} & \epsilon_{\mathbf{k}}(|v_{\mathbf{k}}|^2 - |u_{\mathbf{k}}|^2) - \Delta_{\mathbf{k}}^* u_{\mathbf{k}}^* v_{\mathbf{k}} - \Delta_{\mathbf{k}} u_{\mathbf{k}} v_{\mathbf{k}}^* \end{pmatrix}.$$

This can be diagonalized by a proper choice of $u_{\mathbf{k}}$ and $v_{\mathbf{k}}$ (maintaining $|u_{\mathbf{k}}|^2 + |v_{\mathbf{k}}|^2 = 1$). We set the off-diagonal elements to zero and find

$$\Delta_{\mathbf{k}} \frac{u_{\mathbf{k}}}{v_{\mathbf{k}}} = \epsilon_{\mathbf{k}} \pm \sqrt{\epsilon_{\mathbf{k}}^2 + |\Delta_{\mathbf{k}}|^2} = \epsilon_{\mathbf{k}} + \xi_{\mathbf{k}}, \tag{D.9}$$

where $\xi_{\mathbf{k}} = \pm\sqrt{\epsilon_{\mathbf{k}}^2 + |\Delta_{\mathbf{k}}|^2}$. For a canonical transformation, $|u_{\mathbf{k}}|^2 + |v_{\mathbf{k}}|^2 = 1$, and so

$$|u_{\mathbf{k}}|^2 = \frac{(\epsilon_{\mathbf{k}} + \xi_{\mathbf{k}})^2}{(\epsilon_{\mathbf{k}} + \xi_{\mathbf{k}})^2 + |\Delta_{\mathbf{k}}|^2} = \frac{1}{2}\left(1 + \frac{\epsilon_{\mathbf{k}}}{\xi_{\mathbf{k}}}\right) \qquad |v_{\mathbf{k}}|^2 = \frac{1}{2}\left(1 - \frac{\epsilon_{\mathbf{k}}}{\xi_{\mathbf{k}}}\right).$$

The resulting Hamiltonian, separated into operator and constant parts, is

$$H_{\mathrm{BCS}} = \sum_{\mathbf{k},\sigma} \xi_{\mathbf{k}} \gamma_{\mathbf{k}\sigma}^\dagger \gamma_{\mathbf{k}\sigma} + \sum_{\mathbf{k}} \left[\epsilon_{\mathbf{k}} - \xi_{\mathbf{k}} + \Delta_{\mathbf{k}}^* \langle c_{-\mathbf{k}\downarrow} c_{\mathbf{k}\uparrow} \rangle\right]. \tag{D.10}$$

Comments The BCS Hamiltonian in Eq. D.10 and its diagonal form in Eq. D.10 describe accurately the theory of conventional superconductivity and provide the foundation for the Josephson effect. Before moving on, we offer a few comments.

(i) The ground state $|\psi\rangle$ is the vacuum state with respect to the $\gamma_{\mathbf{k}\sigma}$. This means that it is annihilated by all $\gamma_{\mathbf{k}\uparrow}$ and $\gamma_{-\mathbf{k}\downarrow}$. It is not hard to see that $|\psi\rangle = \prod_{\mathbf{k}}(u_{\mathbf{k}} + v_{\mathbf{k}} c_{\mathbf{k}\uparrow}^\dagger c_{-\mathbf{k}\downarrow}^\dagger)|0\rangle$. The overall phase does not matter, so we define $\varphi_{\mathbf{k}}$ to be the phase between $u_{\mathbf{k}}$ and $v_{\mathbf{k}}$ so that $|\psi\rangle = \prod_{\mathbf{k}}(|u_{\mathbf{k}}| + |v_{\mathbf{k}}| e^{i\varphi_{\mathbf{k}}} c_{\mathbf{k}\uparrow}^\dagger c_{-\mathbf{k}\downarrow}^\dagger)|0\rangle$. The ground state energy is the second term in Eq. D.10.

(ii) From the diagonalization condition in Eq. D.9, we have $\Delta_{\mathbf{k}} = |\Delta_{\mathbf{k}}| e^{i\varphi_{\mathbf{k}}}$. The definition of $\Delta_{\mathbf{k}}$ then gives us $|\Delta_{\mathbf{k}}| e^{i\varphi_{\mathbf{k}}} = -\sum_{\mathbf{k}'} V_{\mathbf{k}-\mathbf{k}'} |u_{\mathbf{k}'} v_{\mathbf{k}'}| e^{i\varphi_{\mathbf{k}'}}$, and hence also that $\sum_{\mathbf{k}'} V_{\mathbf{k}-\mathbf{k}'} |u_{\mathbf{k}'} v_{\mathbf{k}'}| \sin(\varphi_{\mathbf{k}'} - \varphi_{\mathbf{k}}) = 0$ since $V_{\mathbf{k}-\mathbf{k}'}$ is real. The kernel of the matrix whose elements are $V_{\mathbf{k}-\mathbf{k}'}$ has dimension zero (by orthogonality of Fourier components), so all $\varphi_{\mathbf{k}}$ must be equal to some φ.

(iii) In operator form, the total number of electrons is $n = \sum_{\mathbf{k},\sigma} c_{\mathbf{k}\sigma}^\dagger c_{\mathbf{k}\sigma}$ and the total number of Cooper pairs is $N = \sum_{\mathbf{k}} c_{\mathbf{k}\uparrow}^\dagger c_{-\mathbf{k}\downarrow}^\dagger c_{-\mathbf{k}\downarrow} c_{\mathbf{k}\uparrow}$.

(iv) The average number of Cooper pairs is $\langle N \rangle = \sum_{\mathbf{k}} |v_{\mathbf{k}}|^2$. This should vanish when $\epsilon_{\mathbf{k}} \to \infty$, so we choose the positive sign for $\xi_{\mathbf{k}}$.

(v) The variance in the Cooper pair number is $N_{\mathrm{zpf}}^2 = \langle N^2 \rangle - \langle N \rangle^2$. Using Wick's theorem, this is evaluated to be $N_{\mathrm{zpf}}^2 = \sum_{\mathbf{k}} |u_{\mathbf{k}} v_{\mathbf{k}}|^2$.

(vi) The Cooper pair number operator applied to the ground state is $N|\psi\rangle = -i\frac{\partial}{\partial\varphi}|\psi\rangle$, and hence N and φ are conjugate variables in the sense that $[\varphi, N] = i$.

(vii) $|\psi\rangle$ depicts the form of the ground state for a precise φ—it is a phase eigenstate. This form is useful provided that the quantum fluctuations of the phase are small—the uncertainty principle then demands that the fluctuations of the Cooper pair number be large. This is a good approximation for large isolated superconductors.

(viii) The nonzero expectation values with respect to the ground state are $\langle c_{-\mathbf{k}\downarrow} c_{\mathbf{k}\uparrow}\rangle = u_{\mathbf{k}}^* v_{\mathbf{k}}$ and $\langle c_{\mathbf{k}\uparrow}^\dagger c_{\mathbf{k}\uparrow}\rangle = |v_{\mathbf{k}}|^2$.

(ix) The normal ground state is $\prod_{|\mathbf{k}|<k_\mathrm{F}} c_{\mathbf{k}\uparrow}^\dagger c_{-\mathbf{k}\downarrow}^\dagger |0\rangle$ and it has an energy of $\sum_{|\mathbf{k}|<k_\mathrm{F}} 2\epsilon_{\mathbf{k}}$.

(x) Excited states are obtained by adding quasiparticles via the action of $\gamma_{\mathbf{k}\sigma}^\dagger$ on $|\psi\rangle$. These operators change the overall electron number by one (impossible in an isolated superconductor), so there should be an even number of quasiparticle excitations, each pair costing an energy at least $2|\Delta_{\mathbf{k}}|$.

(xi) Often times, $\Delta = |\Delta_{\mathbf{k}}|$ is a material property independent of $\mathbf{k}$. For example, $2\Delta \approx h \times 80\,\mathrm{GHz}$ in aluminum.

D.4 Hartree-Fock theory

We now return to the terms neglected in Eq. D.5. The full interaction in Eq. D.3 describes two-electron scattering processes $(\mathbf{k}', \sigma)\ (\mathbf{q} - \mathbf{k}', \sigma') \to (\mathbf{k}, \sigma)\ (\mathbf{q} - \mathbf{k}, \sigma')$. For the lowest-lying states, there are only three options for nonvanishing diagonal matrix elements:

1. $\mathbf{k}' = \mathbf{k}$ (Hartree),
2. $\mathbf{k}' = \mathbf{q} - \mathbf{k}$ and $\sigma' = \sigma$ (Fock), and
3. $\mathbf{q} = 0$ and $\sigma' = -\sigma$ (pairing).

The pairing interaction written in Eq. D.5 includes a Hartree term. Excluding this, we obtain the residual Hartree interaction from Eq. D.4 as

$$\begin{aligned} U_\mathrm{H} &= \frac{1}{2}\sum_{\mathbf{k}',\mathbf{q}',\sigma} V_0 \left[c_{\mathbf{k}'\sigma}^\dagger c_{\mathbf{q}'\sigma}^\dagger c_{\mathbf{q}'\sigma} c_{\mathbf{k}'\sigma} + (1-\delta_{\mathbf{q}',-\mathbf{k}'}) c_{\mathbf{k}'\sigma}^\dagger c_{\mathbf{q}'-\sigma}^\dagger c_{\mathbf{q}'-\sigma} c_{\mathbf{k}'\sigma}\right] \\ &= \frac{1}{2}\sum_{\mathbf{k}',\mathbf{q}',\sigma,\sigma'} V_0 c_{\mathbf{k}'\sigma}^\dagger c_{\mathbf{k}'\sigma} c_{\mathbf{q}'\sigma'}^\dagger c_{\mathbf{q}'\sigma'} - \frac{1}{2}\sum_{\mathbf{k}',\sigma} V_0 c_{\mathbf{k}'\sigma}^\dagger c_{\mathbf{k}'\sigma} - \frac{1}{2}\sum_{\mathbf{k}',\sigma} V_0 c_{\mathbf{k}'\sigma}^\dagger c_{\mathbf{k}'\sigma} c_{-\mathbf{k}'-\sigma}^\dagger c_{-\mathbf{k}'-\sigma}. \end{aligned}$$

The first two terms are the usual Hartree interaction and the last term corresponds to the part already considered in the pairing Hamiltonian. Similarly, the Fock interaction can be written as

$$U_\mathrm{F} = \frac{1}{2}\sum_{\mathbf{k}',\mathbf{q}',\sigma} V_{\mathbf{q}'-\mathbf{k}'} c_{\mathbf{q}'\sigma}^\dagger c_{\mathbf{k}'\sigma}^\dagger c_{\mathbf{q}'\sigma} c_{\mathbf{k}'\sigma} = -\frac{1}{2}\sum_{\mathbf{k}',\mathbf{q}',\sigma} V_{\mathbf{q}'-\mathbf{k}'} c_{\mathbf{q}'\sigma}^\dagger c_{\mathbf{q}'\sigma} c_{\mathbf{k}'\sigma}^\dagger c_{\mathbf{k}'\sigma} + \frac{1}{2}\sum_{\mathbf{k}',\sigma} V_0 c_{\mathbf{k}'\sigma}^\dagger c_{\mathbf{k}'\sigma}.$$

The last term in U_F cancels the second in U_H. Abandoning the primes and interchanging the indices $\mathbf{k}$ and $\mathbf{q}$ in the Fock term, we find that

$$\begin{aligned} U_\mathrm{H} + U_\mathrm{F} = \frac{1}{2}\sum_{\mathbf{k},\mathbf{q},\sigma,\sigma'} & V_0 c_{\mathbf{k}\sigma}^\dagger c_{\mathbf{k}\sigma} c_{\mathbf{q}\sigma'}^\dagger c_{\mathbf{q}\sigma'} \\ & - \frac{1}{2}\sum_{\mathbf{k},\mathbf{q},\sigma} V_{\mathbf{k}-\mathbf{q}} c_{\mathbf{k}\sigma}^\dagger c_{\mathbf{k}\sigma} c_{\mathbf{q}\sigma}^\dagger c_{\mathbf{q}\sigma} - \frac{1}{2}\sum_{\mathbf{k},\sigma} V_0 c_{\mathbf{k}\sigma}^\dagger c_{\mathbf{k}\sigma} c_{-\mathbf{k}-\sigma}^\dagger c_{-\mathbf{k}-\sigma}. \end{aligned}$$

Under the mean-field approximation, this becomes

$$\begin{aligned} U_{\mathrm{mf}} = &\sum_{\mathbf{k},\mathbf{q},\sigma,\sigma'} V_0\left[\langle c^\dagger_{\mathbf{q}\sigma'}c_{\mathbf{q}\sigma'}\rangle c^\dagger_{\mathbf{k}\sigma}c_{\mathbf{k}\sigma} - \tfrac{1}{2}\langle c^\dagger_{\mathbf{k}\sigma}c_{\mathbf{k}\sigma}\rangle\langle c^\dagger_{\mathbf{q}\sigma'}c_{\mathbf{q}\sigma'}\rangle\right] \\ &- \sum_{\mathbf{k},\mathbf{q},\sigma} V_{\mathbf{k}-\mathbf{q}}\left[\langle c^\dagger_{\mathbf{q}\sigma}c_{\mathbf{q}\sigma}\rangle c^\dagger_{\mathbf{k}\sigma}c_{\mathbf{k}\sigma} - \tfrac{1}{2}\langle c^\dagger_{\mathbf{k}\sigma}c_{\mathbf{k}\sigma}\rangle\langle c^\dagger_{\mathbf{q}\sigma}c_{\mathbf{q}\sigma}\rangle\right] \\ &- \sum_{\mathbf{k},\sigma} V_0\left[\langle c^\dagger_{-\mathbf{k}-\sigma}c_{-\mathbf{k}-\sigma}\rangle c^\dagger_{\mathbf{k}\sigma}c_{\mathbf{k}\sigma} - \tfrac{1}{2}\langle c^\dagger_{\mathbf{k}\sigma}c_{\mathbf{k}\sigma}\rangle\langle c^\dagger_{-\mathbf{k}-\sigma}c_{-\mathbf{k}-\sigma}\rangle\right], \end{aligned}$$

where we have combined cross-terms by reindexing and we have taken $V_{\mathbf{k}-\mathbf{q}}$ real as before. Since $\langle c^\dagger_{\mathbf{k}\sigma}c_{\mathbf{k}\sigma}\rangle = \langle c^\dagger_{\mathbf{k}}c_{\mathbf{k}}\rangle$ are independent of spin and the direction of $\mathbf{k}$, we can write

$$\begin{aligned} U_{\mathrm{mf}} &= \sum_{\mathbf{k},\sigma}\left[\sum_{\mathbf{q}}(2V_0 - V_{\mathbf{k}-\mathbf{q}})\langle c^\dagger_{\mathbf{q}}c_{\mathbf{q}}\rangle - V_0\langle c^\dagger_{\mathbf{k}}c_{\mathbf{k}}\rangle\right]\left(c^\dagger_{\mathbf{k}\sigma}c_{\mathbf{k}\sigma} - \tfrac{1}{2}\langle c^\dagger_{\mathbf{k}}c_{\mathbf{k}}\rangle\right) \\ &= \sum_{\mathbf{k},\sigma}\left[\sum_{\mathbf{q}\neq\mathbf{k}}(2V_0 - V_{\mathbf{k}-\mathbf{q}})\langle c^\dagger_{\mathbf{q}}c_{\mathbf{q}}\rangle\right]\left(c^\dagger_{\mathbf{k}\sigma}c_{\mathbf{k}\sigma} - \tfrac{1}{2}\langle c^\dagger_{\mathbf{k}}c_{\mathbf{k}}\rangle\right). \end{aligned}$$

These terms can be added to H_{BCS} as defined in Eq. D.6 so that the form is retained. Specifically, we have

$$H_{\mathrm{BCS}} + U_{\mathrm{mf}} = \sum_{\mathbf{k},\sigma}\varepsilon_{\mathbf{k}}c^\dagger_{\mathbf{k}\sigma}c_{\mathbf{k}\sigma} - \sum_{\mathbf{k}}\left[\Delta_{\mathbf{k}}c^\dagger_{\mathbf{k}\uparrow}c^\dagger_{-\mathbf{k}\downarrow} + \Delta^*_{\mathbf{k}}c_{-\mathbf{k}\downarrow}c_{\mathbf{k}\uparrow} - \Delta^*_{\mathbf{k}}\langle c_{-\mathbf{k}\downarrow}c_{\mathbf{k}\uparrow}\rangle + U_{\mathbf{k}}\langle c^\dagger_{\mathbf{k}}c_{\mathbf{k}}\rangle\right],$$

where we have defined the dispersion relation $\varepsilon_{\mathbf{k}} = \epsilon_{\mathbf{k}} + U_{\mathbf{k}}$, as for Landau quasiparticles in the Fermi liquid. In a similar fashion to $\Delta_{\mathbf{k}}$, we have introduced

$$U_{\mathbf{k}} = \sum_{\mathbf{q}\neq\mathbf{k}}(2V_0 - V_{\mathbf{k}-\mathbf{q}})\langle c^\dagger_{\mathbf{q}}c_{\mathbf{q}}\rangle.$$

D.5 Validity of the mean-field approximation

We have used two varieties of the mean-field approximation. First, we have supposed that the fluctuations of $c_{-\mathbf{k}\downarrow}c_{\mathbf{k}\uparrow}$ are small in getting to Eq. D.6. Using Wick's theorem, we see that the expected value of the neglected term is

$$\begin{aligned} \sum_{\mathbf{k},\mathbf{k}'} V_{\mathbf{k}-\mathbf{k}'}\left[\langle c^\dagger_{\mathbf{k}\uparrow}c^\dagger_{-\mathbf{k}\downarrow}c_{-\mathbf{k}'\downarrow}c_{\mathbf{k}'\uparrow}\rangle - \langle c^\dagger_{\mathbf{k}\uparrow}c^\dagger_{-\mathbf{k}\downarrow}\rangle\langle c_{-\mathbf{k}'\downarrow}c_{\mathbf{k}'\uparrow}\rangle\right] &= \sum_{\mathbf{k}} V_0|v_{\mathbf{k}}|^4 \\ &= V_0(\langle N\rangle - N^2_{\mathrm{zpf}}) \sim V_0\langle N\rangle, \end{aligned}$$

while that of the remaining term is

$$\sum_{\mathbf{k},\mathbf{k}'} V_{\mathbf{k}-\mathbf{k}'}\langle c^\dagger_{\mathbf{k}\uparrow}c^\dagger_{-\mathbf{k}\downarrow}\rangle\langle c_{-\mathbf{k}'\downarrow}c_{\mathbf{k}'\uparrow}\rangle = \sum_{\mathbf{k},\mathbf{k}'} V_{\mathbf{k}-\mathbf{k}'}u_{\mathbf{k}}v^*_{\mathbf{k}}u^*_{\mathbf{k}'}v_{\mathbf{k}'} \sim 4V_0N^4_{\mathrm{zpf}},$$

where we have noticed that the summand is only nonvanishing for $\mathbf{k} \sim \mathbf{k}'$ near the Fermi level (where it can be approximated by $4V_0|u_{\mathbf{k}}v_{\mathbf{k}}u_{\mathbf{k}'}v_{\mathbf{k}'}|^2$).

Our second approximation supposed that the fluctuations of $c^\dagger_{\mathbf{k}\sigma}c_{\mathbf{k}\sigma}$ are small. For the Hartree interaction, this meant neglecting the term whose expectation is

$$\frac{1}{2}\sum_{\mathbf{k},\mathbf{k}',\sigma,\sigma'} V_0\left[\langle c^\dagger_{\mathbf{k}\sigma}c_{\mathbf{k}\sigma}c^\dagger_{\mathbf{k}'\sigma'}c_{\mathbf{k}'\sigma'}\rangle - \langle c^\dagger_{\mathbf{k}\sigma}c_{\mathbf{k}\sigma}\rangle\langle c^\dagger_{\mathbf{k}'\sigma'}c_{\mathbf{k}'\sigma'}\rangle\right] = \sum_{\mathbf{k}} 2V_0|v_{\mathbf{k}}|^2|u_{\mathbf{k}}|^2 = 2V_0N_{\mathrm{zpf}}^2,$$

again using Wick's theorem. The residual term has the expected value

$$\frac{1}{2}\sum_{\mathbf{k},\mathbf{k}',\sigma,\sigma'} V_0\langle c^\dagger_{\mathbf{k}\sigma}c_{\mathbf{k}\sigma}\rangle\langle c^\dagger_{\mathbf{k}'\sigma'}c_{\mathbf{k}'\sigma'}\rangle = \sum_{\mathbf{k},\mathbf{k}'} 2V_0|v_{\mathbf{k}}|^2|v_{\mathbf{k}'}|^2 = 2V_0\langle N\rangle^2.$$

Similarly, the discarded part of the Fock interaction has average

$$-\frac{1}{2}\sum_{\mathbf{k},\mathbf{k}',\sigma} V_{\mathbf{k}-\mathbf{k}'}\left[\langle c^\dagger_{\mathbf{k}\sigma}c_{\mathbf{k}\sigma}c^\dagger_{\mathbf{k}'\sigma}c_{\mathbf{k}'\sigma}\rangle - \langle c^\dagger_{\mathbf{k}\sigma}c_{\mathbf{k}\sigma}\rangle\langle c^\dagger_{\mathbf{k}'\sigma}c_{\mathbf{k}'\sigma}\rangle\right] = -\sum_{\mathbf{k}} V_0|v_{\mathbf{k}}|^2|u_{\mathbf{k}}|^2 = -V_0N_{\mathrm{zpf}}^2$$

and the remaining part has average

$$-\frac{1}{2}\sum_{\mathbf{k},\mathbf{k}',\sigma} V_{\mathbf{k}-\mathbf{k}'}\langle c^\dagger_{\mathbf{k}\sigma}c_{\mathbf{k}\sigma}\rangle\langle c^\dagger_{\mathbf{k}'\sigma}c_{\mathbf{k}'\sigma}\rangle = -\sum_{\mathbf{k},\mathbf{k}'} V_{\mathbf{k}-\mathbf{k}'}|v_{\mathbf{k}}|^2|v_{\mathbf{k}'}|^2 \sim -V_0\langle N\rangle^2.$$

On the grounds that the spatially oscillatory components will average to zero in the final integral, we have taken $V_{\mathbf{k}-\mathbf{k}'} \sim V_0$ in the sum above.[1] Finally, the discarded part of the pairing correction to the Hartree term has expectation

$$-\frac{1}{2}\sum_{\mathbf{k},\sigma} V_0\left[\langle c^\dagger_{\mathbf{k}\sigma}c_{\mathbf{k}\sigma}c^\dagger_{-\mathbf{k}-\sigma}c_{-\mathbf{k}-\sigma}\rangle - \langle c^\dagger_{\mathbf{k}\sigma}c_{\mathbf{k}\sigma}\rangle\langle c^\dagger_{-\mathbf{k}-\sigma}c_{-\mathbf{k}-\sigma}\rangle\right] = -\sum_{\mathbf{k}} V_0|u_{\mathbf{k}}|^2|v_{\mathbf{k}}|^2 = -V_0N_{\mathrm{zpf}}^2$$

while that of the retained term is

$$-\frac{1}{2}\sum_{\mathbf{k},\sigma} V_0\langle c^\dagger_{\mathbf{k}\sigma}c_{\mathbf{k}\sigma}\rangle\langle c^\dagger_{-\mathbf{k}-\sigma}c_{-\mathbf{k}-\sigma}\rangle = -\sum_{\mathbf{k}} V_0|v_{\mathbf{k}}|^4 = -V_0(\langle N\rangle - N_{\mathrm{zpf}}^2) \sim -V_0\langle N\rangle.$$

In many cases, $\langle N\rangle \sim 10^{22}$ while $N_{\mathrm{zpf}} \sim 10^9$. This justifies our use of $\langle N\rangle \gg N_{\mathrm{zpf}}^2$ in the above and validates our mean-field approximations. At this point, we should be convinced that the superconducting Hamiltonian in Eq. D.10 (optionally with Hartree-Fock modifications) is a good approximation at temperatures below $2|\Delta_{\mathbf{k}}|$.

1 To justify this, we notice that $|v_{\mathbf{k}}|^2$ is suppressed for wavevectors beyond the Fermi level. Then, the sum can be estimated as $-\sum_{|\mathbf{k}|,|\mathbf{k}'|\lesssim k_{\mathrm{F}}} V_{\mathbf{k}-\mathbf{k}'} = -\frac{1}{\mathcal{V}}\int \mathrm{d}^3x\, V(\mathbf{x})|\sum_{|\mathbf{k}|\lesssim k_{\mathrm{F}}} \mathrm{e}^{-i\mathbf{k}\cdot\mathbf{x}}|^2$. Replacing the sum by an integral, we get $\frac{\mathcal{V}}{(2\pi)^3}\int_{k<k_{\mathrm{F}}} \mathrm{d}^3k\, \mathrm{e}^{-i\mathbf{k}\cdot\mathbf{x}}$. Choosing the polar axis to be $\mathbf{x}$, the integral is $\frac{\mathcal{V}}{(2\pi)^2}\int_0^{k_{\mathrm{F}}} \mathrm{d}k\, k^2 \int_0^\pi \mathrm{d}\theta\, \sin\theta \mathrm{e}^{-ikx\cos\theta}$. This is evaluated by changing variables to $u = \cos\theta$, and we obtain $\frac{\mathcal{V}}{2\pi^2x^3}(\sin k_{\mathrm{F}}x - k_{\mathrm{F}}x\cos k_{\mathrm{F}}x)$. This becomes $\frac{\mathcal{V}}{2\pi^2}\frac{1}{3}k_{\mathrm{F}}^3$ when $k_{\mathrm{F}}x \ll 1$, which is also the result when $e^{-i\mathbf{k}\cdot\mathbf{x}}$ is discarded altogether.

D.6 Josephson effect

We start with the spinful version of Eq. D.2 in the presence of a single-body potential $J(\mathbf{x})$ and two-body potential $V(\mathbf{x},\mathbf{x}') = V(\mathbf{x}-\mathbf{x}')$,

$$\begin{aligned} H = -\frac{\hbar^2}{2m}\sum_\sigma \int \mathrm{d}^3x\, \psi_\sigma^\dagger(\mathbf{x})\nabla^2\psi_\sigma(\mathbf{x}) \\ + \frac{1}{2}\sum_{\sigma,\sigma'}\int \mathrm{d}^3x \int \mathrm{d}^3x'\, \psi_\sigma^\dagger(\mathbf{x})\psi_{\sigma'}^\dagger(\mathbf{x}')V(\mathbf{x}-\mathbf{x}')\psi_{\sigma'}(\mathbf{x}')\psi_\sigma(\mathbf{x}) \\ + \sum_\sigma \int \mathrm{d}^3x\, \psi_\sigma^\dagger(\mathbf{x})J(\mathbf{x})\psi_\sigma(\mathbf{x}). \end{aligned} \tag{D.11}$$

The integration region spans both superconductors. The coupling is modeled by a single point $\mathbf{x}_0$ of contact between otherwise disjoint regions, such that $J(\mathbf{x}) = J_0\sqrt{\mathcal{V}_\mathrm{L}\mathcal{V}_\mathrm{R}}\delta(\mathbf{x}-\mathbf{x}_0)$ (see Fig. D.1). The single particle states are indexed by a wavevector $\mathbf{k}$ and spin σ for each superconductor. We have

$$\psi_\sigma(\mathbf{x}) = \frac{1}{\sqrt{\mathcal{V}_\mathrm{L}}}\Theta(\mathbf{x}\in\mathrm{L})\sum_\mathbf{k} \mathrm{e}^{i\mathbf{k}\cdot\mathbf{x}}a_{\mathbf{k}\sigma} + \frac{1}{\sqrt{\mathcal{V}_\mathrm{R}}}\Theta(\mathbf{x}\in\mathrm{R})\sum_\mathbf{k}\mathrm{e}^{i\mathbf{k}\cdot\mathbf{x}}c_{\mathbf{k}\sigma},$$

where the left superconductor corresponds to the region L of size $\mathcal{V}_\mathrm{L}$ and annihilation operators $a_{\mathbf{k}\sigma}$ (and similarly for the right superconductor). A crucial subtlety is that different values of $\mathbf{k}$ are allowed depending on the corresponding superconductor.

Plugging this into Eq. D.11, we find that

$$\begin{aligned} H = &\sum_{\mathbf{k},\sigma}\frac{\hbar^2\mathbf{k}^2}{2m}a_{\mathbf{k}\sigma}^\dagger a_{\mathbf{k}\sigma} + \sum_{\mathbf{k},\sigma}\frac{\hbar^2\mathbf{k}^2}{2m}c_{\mathbf{k}\sigma}^\dagger c_{\mathbf{k}\sigma} \\ &+ \frac{1}{2}\sum_{\mathbf{k},\mathbf{k}',\mathbf{q},\sigma,\sigma'} V_{\mathbf{k}-\mathbf{k}'}a_{\mathbf{k}\sigma}^\dagger a_{\mathbf{q}-\mathbf{k}\sigma'}^\dagger a_{\mathbf{q}-\mathbf{k}'\sigma'}a_{\mathbf{k}'\sigma} + \frac{1}{2}\sum_{\mathbf{k},\mathbf{k}',\mathbf{q},\sigma,\sigma'} V_{\mathbf{k}-\mathbf{k}'}c_{\mathbf{k}\sigma}^\dagger c_{\mathbf{q}-\mathbf{k}\sigma'}^\dagger c_{\mathbf{q}-\mathbf{k}'\sigma'}c_{\mathbf{k}'\sigma} \\ &+ \sum_{\mathbf{k},\mathbf{k}',\mathbf{q},\mathbf{q}',\sigma,\sigma'} a_{\mathbf{k}\sigma}^\dagger c_{\mathbf{q}\sigma'}^\dagger c_{\mathbf{q}'\sigma'}a_{\mathbf{k}'\sigma}\frac{1}{\mathcal{V}_\mathrm{L}\mathcal{V}_\mathrm{R}}\int \mathrm{d}^3x_\mathrm{L}\int \mathrm{d}^3x_\mathrm{R}\, V(\mathbf{x}_\mathrm{L}-\mathbf{x}_\mathrm{R})\mathrm{e}^{-i(\mathbf{k}-\mathbf{k}')\cdot\mathbf{x}_\mathrm{L}}\mathrm{e}^{-i(\mathbf{q}-\mathbf{q}')\cdot\mathbf{x}_\mathrm{R}} \\ &+ J_0\sum_{\mathbf{k},\mathbf{k}',\sigma}\left[\mathrm{e}^{-i(\mathbf{k}-\mathbf{k}')\cdot\mathbf{x}_0}a_{\mathbf{k}\sigma}^\dagger c_{\mathbf{k}'\sigma} + \mathrm{e}^{-i(\mathbf{k}'-\mathbf{k})\cdot\mathbf{x}_0}c_{\mathbf{k}'\sigma}^\dagger a_{\mathbf{k}\sigma}\right] \\ &+ J_0\sqrt{\frac{\mathcal{V}_\mathrm{R}}{\mathcal{V}_\mathrm{L}}}\sum_{\mathbf{k},\mathbf{k}',\sigma}\mathrm{e}^{-i(\mathbf{k}-\mathbf{k}')\cdot\mathbf{x}_0}a_{\mathbf{k}\sigma}^\dagger a_{\mathbf{k}'\sigma} + J_0\sqrt{\frac{\mathcal{V}_\mathrm{L}}{\mathcal{V}_\mathrm{R}}}\sum_{\mathbf{k},\mathbf{k}',\sigma}\mathrm{e}^{-i(\mathbf{k}-\mathbf{k}')\cdot\mathbf{x}_0}c_{\mathbf{k}\sigma}^\dagger c_{\mathbf{k}'\sigma}. \end{aligned}$$

The first two lines with their Fermi energies correspond to the independent Fermi liquid Hamiltonians, each of the form in Eq. D.3. The third line corresponds to the bulk interaction between the two superconductors. The fourth line describes tunneling between the superconductors. The fifth describes back-scattering, and its only contributions to first-order in perturbation theory are terms with $\mathbf{k} = \mathbf{k}'$. Therefore, we replace it by

$$J_0\sqrt{\frac{\mathcal{V}_\mathrm{R}}{\mathcal{V}_\mathrm{L}}}\sum_{\mathbf{k},\sigma}a_{\mathbf{k}\sigma}^\dagger a_{\mathbf{k}\sigma} + J_0\sqrt{\frac{\mathcal{V}_\mathrm{L}}{\mathcal{V}_\mathrm{R}}}\sum_{\mathbf{k},\sigma}c_{\mathbf{k}\sigma}^\dagger c_{\mathbf{k}\sigma},$$

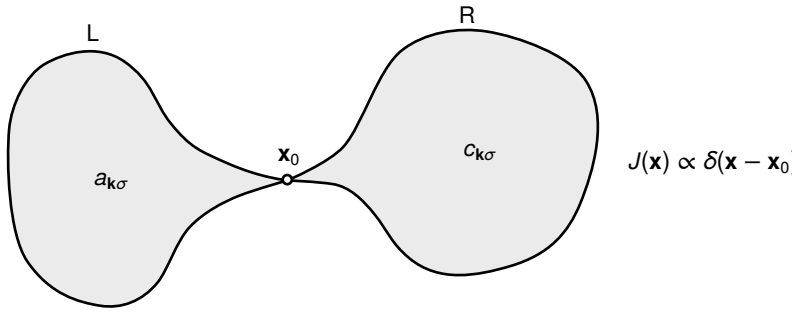

Figure D.1 Josephson effect modeled by a weak interaction $J(\mathbf{x}) = J_0\sqrt{\mathcal{V}_\mathrm{L}\mathcal{V}_\mathrm{R}}\delta(\mathbf{x} - \mathbf{x}_0)$ at the point of contact $\mathbf{x}_0$ between two superconductors. The superconductors in regions L and R have fermionic annihilation operators $a_{\mathbf{k}\sigma}$ and $c_{\mathbf{k}\sigma}$, respectively.

which only serves to renormalize the Fermi energies.[2]

If we include these chemical potentials and use the BCS approximations and transformations from Sec. D.3, we get

$$H \approx \sum_{\mathbf{k},\sigma} \xi_\mathbf{k} \gamma^\dagger_{\mathbf{k}\sigma}\gamma_{\mathbf{k}\sigma} + \sum_{\mathbf{k},\sigma} \zeta_\mathbf{k} h^\dagger_{\mathbf{k}\sigma} h_{\mathbf{k}\sigma} + H_\mathrm{C} + H_\mathrm{T}$$

by neglecting the constant terms. The first two terms describe uncoupled superconductors and are the unperturbed Hamiltonian with ground state $|\psi_\mathrm{L}\psi_\mathrm{R}\rangle$. The remaining Coulomb and tunneling terms are perturbations. To first order in perturbation theory, only terms with $\mathbf{k} = \mathbf{k}'$ and $\mathbf{q} = \mathbf{q}'$ in the Coulomb term contribute, and we get

$$H_\mathrm{C} \approx \sum_{\mathbf{k},\mathbf{k}',\sigma,\sigma'} \left[\frac{1}{\mathcal{V}_\mathrm{L}\mathcal{V}_\mathrm{R}} \int \mathrm{d}^3 x_\mathrm{L} \int \mathrm{d}^3 x_\mathrm{R}\, V(\mathbf{x}_\mathrm{L} - \mathbf{x}_\mathrm{R}) \right] a^\dagger_{\mathbf{k}\sigma} a_{\mathbf{k}\sigma} c^\dagger_{\mathbf{k}'\sigma'} c_{\mathbf{k}'\sigma'}.$$

The interaction $V(\mathbf{x})$ should mostly comprise electrostatic effects, and the term in brackets becomes a geometrical constant $\mathcal{G}$.

The tunneling term contributes no first-order corrections. To proceed with second-order perturbation theory, we recall

$$\begin{aligned}
a^\dagger_{\mathbf{k}\uparrow} c_{\mathbf{k}'\uparrow} |\psi_\mathrm{L}\psi_\mathrm{R}\rangle &= +u_\mathbf{k} \tilde{v}_{\mathbf{k}'} \gamma^\dagger_{\mathbf{k}\uparrow} h^\dagger_{-\mathbf{k}'\downarrow} |\psi_\mathrm{L}\psi_\mathrm{R}\rangle \\
c^\dagger_{\mathbf{k}'\uparrow} a_{\mathbf{k}\uparrow} |\psi_\mathrm{L}\psi_\mathrm{R}\rangle &= -v_\mathbf{k} \tilde{u}_{\mathbf{k}'} \gamma^\dagger_{-\mathbf{k}\downarrow} h^\dagger_{\mathbf{k}'\uparrow} |\psi_\mathrm{L}\psi_\mathrm{R}\rangle \\
a^\dagger_{-\mathbf{k}\downarrow} c_{-\mathbf{k}'\downarrow} |\psi_\mathrm{L}\psi_\mathrm{R}\rangle &= -u_\mathbf{k} \tilde{v}_{\mathbf{k}'} \gamma^\dagger_{-\mathbf{k}\downarrow} h^\dagger_{\mathbf{k}'\uparrow} |\psi_\mathrm{L}\psi_\mathrm{R}\rangle \\
c^\dagger_{-\mathbf{k}'\downarrow} a_{-\mathbf{k}\downarrow} |\psi_\mathrm{L}\psi_\mathrm{R}\rangle &= +v_\mathbf{k} \tilde{u}_{\mathbf{k}'} \gamma^\dagger_{\mathbf{k}\uparrow} h^\dagger_{-\mathbf{k}'\downarrow} |\psi_\mathrm{L}\psi_\mathrm{R}\rangle,
\end{aligned}$$

and so the matrix element between the ground state and an excited state is nonzero only when both superconductors are excited. The second-order perturbative correction to the

2 Note that at zero voltage difference, the two superconductors have the same Fermi energy.

ground state energy (see App. B) is

$$E_{\mathrm{T}}^{(2)} = -\langle\psi_{\mathrm{L}}\psi_{\mathrm{R}}|H_{\mathrm{T}}\left[\sum_{m\neq 0}\frac{|m\rangle\langle m|}{E_m}\right]H_{\mathrm{T}}|\psi_{\mathrm{L}}\psi_{\mathrm{R}}\rangle,$$

where $H_{\mathrm{T}} = \sum_{\mathbf{k},\mathbf{k}',\sigma}(J_{\mathbf{k}-\mathbf{k}'}a^\dagger_{\mathbf{k}\sigma}c_{\mathbf{k}'\sigma} + J^*_{\mathbf{k}-\mathbf{k}'}c^\dagger_{\mathbf{k}'\sigma}a_{\mathbf{k}\sigma})$ and $J_{\mathbf{k}-\mathbf{k}'} = J_0\mathrm{e}^{-i(\mathbf{k}-\mathbf{k}')\cdot\mathbf{x}_0}$. The intermediate states $|m\rangle$ run over joint excited states. When applied to the ground state, H_{T} assumes the simple form

$$\begin{aligned}H_{\mathrm{T}}|\psi_{\mathrm{L}}\psi_{\mathrm{R}}\rangle &= \sum_{\mathbf{k},\mathbf{k}'}\left[J_{\mathbf{k}-\mathbf{k}'}a^\dagger_{\mathbf{k}\uparrow}c_{\mathbf{k}'\uparrow} + J^*_{\mathbf{k}-\mathbf{k}'}a^\dagger_{-\mathbf{k}\downarrow}c_{-\mathbf{k}'\downarrow} + J^*_{\mathbf{k}-\mathbf{k}'}c^\dagger_{\mathbf{k}'\uparrow}a_{\mathbf{k}\uparrow} + J_{\mathbf{k}-\mathbf{k}'}c^\dagger_{-\mathbf{k}'\downarrow}a_{-\mathbf{k}\downarrow}\right]|\psi_{\mathrm{L}}\psi_{\mathrm{R}}\rangle\\ &= \sum_{\mathbf{k},\mathbf{k}'}(u_{\mathbf{k}}\tilde{v}_{\mathbf{k}'} + v_{\mathbf{k}}\tilde{u}_{\mathbf{k}'})\left[J_{\mathbf{k}-\mathbf{k}'}\gamma^\dagger_{\mathbf{k}\uparrow}h^\dagger_{-\mathbf{k}'\downarrow} - J^*_{\mathbf{k}-\mathbf{k}'}\gamma^\dagger_{-\mathbf{k}\downarrow}h^\dagger_{\mathbf{k}'\uparrow}\right]|\psi_{\mathrm{L}}\psi_{\mathrm{R}}\rangle.\end{aligned}$$

Both of the terms in the summand have energy $\xi_{\mathbf{k}} + \zeta_{\mathbf{k}'}$. Hence, we can write the effective Hamiltonian as

$$\begin{aligned}H_{\mathrm{T}} &\approx -\sum_{\mathbf{k},\mathbf{k}'}\frac{J_0^2}{\xi_{\mathbf{k}}+\zeta_{\mathbf{k}'}}|u_{\mathbf{k}}\tilde{v}_{\mathbf{k}'} + v_{\mathbf{k}}\tilde{u}_{\mathbf{k}'}|^2\left(h_{-\mathbf{k}'\downarrow}\gamma_{\mathbf{k}\uparrow}\gamma^\dagger_{\mathbf{k}\uparrow}h^\dagger_{-\mathbf{k}'\downarrow} + h_{\mathbf{k}'\uparrow}\gamma_{-\mathbf{k}\downarrow}\gamma^\dagger_{-\mathbf{k}\downarrow}h^\dagger_{\mathbf{k}'\uparrow}\right)\\ &\to \sum_{\mathbf{k},\mathbf{k}',\sigma,\sigma'}\frac{J_0^2}{\xi_{\mathbf{k}}+\zeta_{\mathbf{k}'}}a^\dagger_{\mathbf{k}\sigma}a_{\mathbf{k}\sigma}c^\dagger_{\mathbf{k}'\sigma'}c_{\mathbf{k}'\sigma'} - 2\sum_{\mathbf{k},\mathbf{k}'}\frac{J_0^2}{\xi_{\mathbf{k}}+\zeta_{\mathbf{k}'}}\left(a^\dagger_{\mathbf{k}\uparrow}a^\dagger_{-\mathbf{k}\downarrow}c_{-\mathbf{k}'\downarrow}c_{\mathbf{k}'\uparrow} + c^\dagger_{\mathbf{k}'\uparrow}c^\dagger_{-\mathbf{k}'\downarrow}a_{-\mathbf{k}\downarrow}a_{\mathbf{k}\uparrow}\right),\end{aligned}$$

where the final line was obtained by again analyzing the effect on the ground state.

The total perturbing Hamiltonian is then

$$\begin{aligned}H_{\mathrm{C}} + H_{\mathrm{T}} \approx \sum_{\mathbf{k},\mathbf{k}',\sigma,\sigma'}&\left[\mathcal{G} + \frac{J_0^2}{\xi_{\mathbf{k}}+\zeta_{\mathbf{k}'}}\right]a^\dagger_{\mathbf{k}\sigma}a_{\mathbf{k}\sigma}c^\dagger_{\mathbf{k}'\sigma'}c_{\mathbf{k}'\sigma'}\\ &- 2\sum_{\mathbf{k},\mathbf{k}'}\frac{J_0^2}{\xi_{\mathbf{k}}+\zeta_{\mathbf{k}'}}\left(a^\dagger_{\mathbf{k}\uparrow}a^\dagger_{-\mathbf{k}\downarrow}c_{-\mathbf{k}'\downarrow}c_{\mathbf{k}'\uparrow} + c^\dagger_{\mathbf{k}'\uparrow}c^\dagger_{-\mathbf{k}'\downarrow}a_{-\mathbf{k}\downarrow}a_{\mathbf{k}\uparrow}\right).\end{aligned}$$

Since the ground state only involves Cooper pairs, we can replace $a^\dagger_{\mathbf{k}\sigma}a_{\mathbf{k}\sigma}$ by $a^\dagger_{\mathbf{k}\uparrow}a^\dagger_{-\mathbf{k}\downarrow}a_{-\mathbf{k}\downarrow}a_{\mathbf{k}\uparrow}$ (and similarly for $c^\dagger_{\mathbf{k}'\sigma'}c_{\mathbf{k}'\sigma'}$) in the first term. The energy denominators are minimized in the vicinity of the Fermi surface, where they become $\xi_{\mathbf{k}} + \zeta_{\mathbf{k}'} \approx |\Delta_{\mathbf{k}}| + |\Delta_{\mathbf{k}'}| \sim 2\Delta$ for $\Delta_{\mathbf{k}} = \Delta_0\mathrm{e}^{i\varphi_{\mathrm{L}}}$ and $\Delta_{\mathbf{k}'} = \Delta\mathrm{e}^{i\varphi_{\mathrm{R}}}$. We can then discard the second term in brackets, and we get

$$\begin{aligned}H_{\mathrm{C}} + H_{\mathrm{T}} \approx 4\mathcal{G}&\sum_{\mathbf{k},\mathbf{k}'}a^\dagger_{\mathbf{k}\uparrow}a^\dagger_{-\mathbf{k}\downarrow}a_{-\mathbf{k}\downarrow}a_{\mathbf{k}\uparrow}c^\dagger_{\mathbf{k}'\uparrow}c^\dagger_{-\mathbf{k}'\downarrow}c_{-\mathbf{k}'\downarrow}c_{\mathbf{k}'\uparrow}\\ &- \frac{J_0^2}{\Delta}\sum_{\mathbf{k},\mathbf{k}'\sim k_{\mathrm{F}}}\left(a^\dagger_{\mathbf{k}\uparrow}a^\dagger_{-\mathbf{k}\downarrow}c_{-\mathbf{k}'\downarrow}c_{\mathbf{k}'\uparrow} + c^\dagger_{\mathbf{k}'\uparrow}c^\dagger_{-\mathbf{k}'\downarrow}a_{-\mathbf{k}\downarrow}a_{\mathbf{k}\uparrow}\right).\end{aligned}$$

The second term tunnels a Cooper pair from one superconductor to the other (both near the Fermi surface). This process changes the number N of tunneled Cooper pairs by one and the energy of the first term. We conclude that

$$H_{\mathrm{C}} + H_{\mathrm{T}} \approx 4\mathcal{G}N^2 - \frac{J_0^2}{\Delta}\sum_N\left(|N\rangle\langle N+1| + |N+1\rangle\langle N|\right).$$

Recalling the conjugacy relation $[\varphi, N] = i$ (where $\varphi = \varphi_\mathrm{L} - \varphi_\mathrm{R}$), we can apply Eq. 2.5. This gives us the perturbative Hamiltonian

$$H_\mathrm{C} + H_\mathrm{T} \approx 4\mathcal{G}N^2 - 2\frac{J_0^2}{\Delta}\cos\varphi,$$

which may well have excitation frequencies far below the gap Δ. These correspond to excited states where the individual superconductors are frozen in their ground states and Cooper pairs tunnel between them. Since the BCS ground state is not a number eigenstate, this is not contradictory.

We identify

$$E_\mathrm{C} = \mathcal{G} = \frac{e^2}{4\pi\epsilon_0}\frac{1}{\mathcal{V}_\mathrm{L}\mathcal{V}_\mathrm{L}}\int \mathrm{d}^3x_\mathrm{L}\int \mathrm{d}^3x_\mathrm{R}\,\frac{1}{|\mathbf{x}_\mathrm{L} - \mathbf{x}_\mathrm{R}|} \qquad E_\mathrm{J} = 2\frac{J_0^2}{\Delta}.$$

Notably, E_C is readily observed to be the electrostatic energy if the left superconductor has uniform charge $+e$ and the right has uniform charge $-e$. This justifies Eq. 2.2. The absolutely essential feature is the existence of excitations with energy on the order of $\sqrt{8E_\mathrm{J}E_\mathrm{J}}$, which can be much smaller than the quasiparticle excitation energy 2Δ. They can have any relation to the thermal energy $k_\mathrm{B}T$.

We can identify the perturbative Hamiltonian $H_\mathrm{C} + H_\mathrm{T}$, which we rewrite as

$$H_\mathrm{J} = 4E_\mathrm{C}(N - \langle N\rangle)^2 - E_\mathrm{J}\cos\varphi,$$

as that for a Josephson junction in Figs. 2.1 and 2.2. Note that we have included the equilibrium number of excess Cooper pairs $\langle N\rangle$, which is usually associated with the offset charge N_g. The classical equation of motion corresponds to the constitutive relation of the element, $\hbar\dot{N} = -E_\mathrm{J}\sin\varphi$ and $\hbar\dot{\varphi} = 8E_\mathrm{C}(N - \langle N\rangle)$. Since the charge is $Q = 2e(N - \langle N\rangle)$ and the current is $I = -\dot{Q}$, these become $\phi_0 I = E_\mathrm{J}\sin\varphi$ and $\phi_0\dot{\varphi} = Q/C$. These are the usual Josephson relations

$$I = I_0\sin\varphi \qquad\qquad V = \phi_0\dot{\varphi}$$

since $Q = CV$ is the constitutive relation for a capacitance.

E

RECTANGULAR WAVEGUIDE SAMPLE HOLDER

This final appendix addresses the design of the three-dimensional waveguide sample holder used in the fluxonium and double fluxonium experiments discussed in Chs. 4–6. These waveguides, as opposed to their microwave cavity counterparts, allow for cryogenic measurement without the additional resonant mode (this is also possibly with planar geometries, but we do not consider those here).

Generally, waveguides are tube-like conductive structures that channel propagating electromagnetic waves using constructive interference. The basic principle can be understood using the two-dimensional model of two half-infinite conductive sheets separated by a gap of width d and an ac source in the center. The conductivity and retardation effects can be captured by an infinite number of image sources above and below the source, each separated by d. Propagation will only occur if the fields produced by all the sources constructively interfere, which selects out the radiative component with $d \sin\theta = \lambda/2$ for a wavelength λ and with θ measured relative to the direction of the gap. Below the vacuum cutoff frequency $c/2d$, propagation of this type cannot occur—it must instead be evanescent and hence exponentially attenuated. Generalizing to three dimensions, we must include a second transverse dimension d' such that $d' \leq d$ without loss of generality. For frequencies above $c/2d'$, at least two modes of propagation exist with different field profiles, leading to certain practical challenges.[1] Of course, other modes will arise, like the second harmonic at c/d. This defines the passband of the waveguide as frequencies from $c/2d$ to the next mode frequency. The bandwidth is maximized for $c/2d' = c/d$, i.e. for $d' = d/2$, which is why commercial rectangular waveguides have transverse inner dimensions in a 2:1 ratio.

We used the WR-102 standard, which corresponds to dimensions $d = 1.020\,\text{in.}$ and $d' = 0.510\,\text{in.}$ and a passband of 5.786–11.57 GHz (see Fig. E.1a). Our waveguides were machined using electrical discharge techniques from Oxygen-Free High-Conductivity (OFHC) copper. The crucial design feature was the OFHC copper 50Ω impedance-matched coupler, which radiated a coaxially propagating signal into the waveguide. This was done by extending the inner pin of the coaxial cable into the interior of the waveguide, where it was soldered to an OFHC copper barrel. The full coupler assembly, consisting of the coaxial cable, the barrel (Fig. E.1c), and the mounting flange (Fig. E.1b), were screwed to the outside of the waveguide (Fig. E.1a) with an indium seal for electrical continuity.

1 In particular, these two modes are orthogonal transverse electric modes for the rectangular waveguide, and only the lower-frequency one directly couples to the dipole antennas.

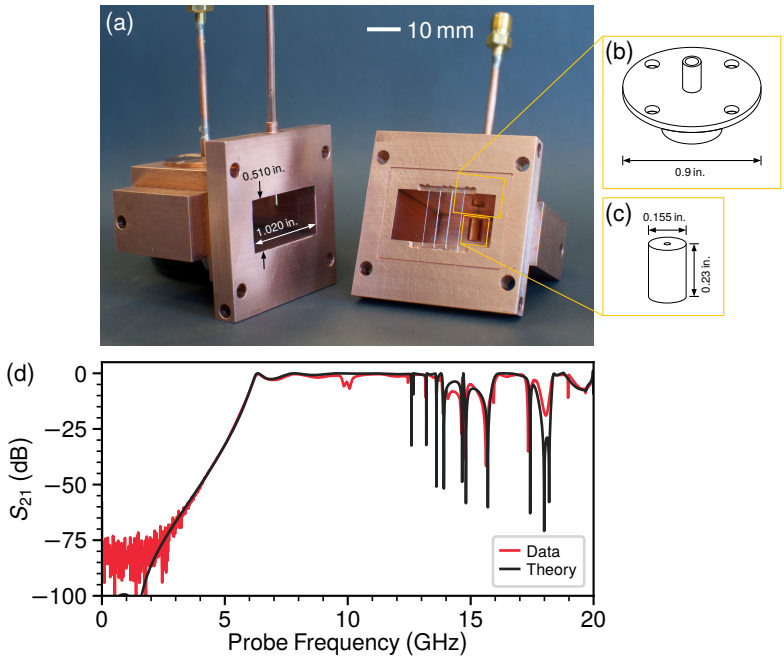

Figure E.1 Rectangular waveguide sample holder operated in a transmission configuration. (a) Image of the copper waveguide, showing two impedance-matched transmission terminations. (b) Schematic of the impedance-matched coupler housing for a 50Ω coaxial cable. (c) Schematic of the barrel for the coupler. (d) Transmission through the waveguide, with data plotted in red and theory (using a finite-element electromagnetic solver) in black.

In addition to the passband, an important specification of any waveguide is its insertion loss, or the minimum fraction of electromagnetic amplitude that successfully passes through the waveguide for frequencies within the band. In our design, we threaded two nonmagnetic aluminum screws into the bottom of the waveguide to adjust the unavoidable trade-off between the bandwidth and insertion loss. We ultimately narrowed the passband to 6–8 GHz, plus or minus 0.5 GHz for different particular waveguides, to consistently achieve an insertion loss of −0.3 dB (see Fig. E.1d). This corresponds to a transmission coefficient of $S_{21} = 93\%$, which may suitably be considered low-loss.

Additional features of our waveguide design include a through-hole for an auxiliary coaxial line with plunging inner pin approximately 3 mm away from the samples, used for below-cutoff ac input drives, and a large recessed outer groove for winding a superconducting dc wire, used as a solenoid for generating a static magnetic field. Finally, we note that waveguides were screwed to copper brackets, which were mounted to the mixing chamber of the dilution refrigerator, and that all components of the waveguide assembly were made out of nonmagnetic materials.

The experiments in this thesis made use of waveguides in two configurations: transmission and reflection. The transmission arrangement uses two waveguide-to-SMA adapters (see Fig. E.1a) bolted to each other, while the reflection arrangement uses one waveguide-

to-SMA adapter and one quarter-wavelength waveguide termination (see Fig. 5.1a), so that the samples are placed at an electric field antinode. Device set A was measured using the transmission setup and device sets S and M were measured using the reflection setup.

REFERENCES

List of publications

Journal articles corresponding to the original work presented in this dissertation

Cohen, J., W. C. Smith, M. H. Devoret, and M. Mirrahimi, "Degeneracy-preserving quantum nondemolition measurement of parity-type observables for cat qubits," Phys. Rev. Lett. **119**, 060503 (2017). Cited on p. 94.

Kou, A., W. C. Smith, U. Vool, R. T. Brierley, H. Meier, L. Frunzio, S. M. Girvin, L. I. Glazman, and M. H. Devoret, "Fluxonium-based artificial molecule with a tunable magnetic moment," Phys. Rev. X **7**, 031037 (2017). Cited on pp. 46, 73.

Kou, A., W. C. Smith, U. Vool, I. M. Pop, K. M. Sliwa, M. Hatridge, L. Frunzio, and M. H. Devoret, "Simultaneous monitoring of fluxonium qubits in a waveguide," Phys. Rev. Appl. **9**, 064022 (2018). Cited on p. 44.

Smith, W. C., A. Kou, U. Vool, I. M. Pop, L. Frunzio, R. J. Schoelkopf, and M. H. Devoret, "Quantization of inductively shunted superconducting circuits," Phys. Rev. B **94**, 144507 (2016). Cited on pp. 26, 34.

Smith, W. C., A. Kou, X. Xiao, U. Vool, and M. H. Devoret, "Superconducting circuit protected by two-cooper-pair tunneling," arXiv:1905.01206 (2019). Cited on pp. 5, 26, 28.

Vool, U., A. Kou, W. C. Smith, N. E. Frattini, K. Serniak, P. Reinhold, I. M. Pop, S. Shankar, L. Frunzio, S. M. Girvin, et al., "Driving forbidden transitions in the fluxonium artificial atom," Phys. Rev. Appl. **9**, 054046 (2018). Cited on p. 85.

Core bibliography

Selected references of particular relevance

Bell, M. T., J. Paramanandam, L. B. Ioffe, and M. E. Gershenson, "Protected Josephson rhombus chains," Phys. Rev. Lett. **112**, 167001 (2014). Cited on pp. 28, 47, 80, 82, 94.

Blais, A., R.-S. Huang, A. Wallraff, S. M. Girvin, and R. J. Schoelkopf, "Cavity quantum electrodynamics for superconducting electrical circuits: An architecture for quantum computation," Phys. Rev. A **69**, 062320 (2004). Cited on pp. 43, 74, 117.

Blatter, G., V. B. Geshkenbein, and L. B. Ioffe, "Design aspects of superconducting-phase quantum bits," Phys. Rev. B **63**, 174511 (2001). Cited on p. 82.

Brooks, P., A. Kitaev, and J. Preskill, "Protected gates for superconducting qubits," Phys. Rev. A **87**, 052306 (2013). Cited on pp. 18, 82–83, 85, 94.

Cottet, A., "Implementation of a quantum bit in a superconducting circuit," Ph.D. thesis (Université Paris VI, 2002). Cited on p. 101.

Devoret, M. H., "Quantum fluctuations in electrical circuits," in *Quantum Fluctuations (Les Houches Session LXIII)*, edited by S. Reynaud, E. Giacobino, and J. Zinn-Justin (North-Holland, Amsterdam, 1997), pp. 351–386. Cited on pp. 12, 29.

Douçot, B. and L. B. Ioffe, "Physical implementation of protected qubits," Rep. Prog. Phys. **75**, 072001 (2012). Cited on pp. 4, 82.

Gambetta, J., A. Blais, D. I. Schuster, A. Wallraff, L. Frunzio, J. Majer, M. H. Devoret, S. M. Girvin, and R. J. Schoelkopf, "Qubit-photon interactions in a cavity: Measurement-induced dephasing and number splitting," Phys. Rev. A **74**, 042318 (2006). Cited on pp. 73, 116.

Girvin, S. M., "Circuit QED: Superconducting qubits coupled to microwave photons," in *Quantum Machines: Measurement and Control of Engineered Quantum Systems (Les Houches Session XCVI)*, edited by M. Devoret, B. Huard, R. Schoelkopf, and L. F. Cugliandolo (Oxford University Press, New York, 2014), pp. 113–256. Cited on p. 13.

Gladchenko, S., D. Olaya, E. Dupont-Ferrier, B. Doucot, L. B. Ioffe, and M. E. Gershenson, "Superconducting nanocircuits for topologically protected qubits," Nat. Phys. **5**, 48–53 (2009). Cited on pp. 5–6, 94.

Ioffe, L. B. and M. V. Feigel'man, "Possible realization of an ideal quantum computer in Josephson junction array," Phys. Rev. B **66**, 224503 (2002). Cited on pp. 5–6.

Ithier, G., E. Collin, P. Joyez, P. J. Meeson, D. Vion, D. Esteve, F. Chiarello, A. Shnirman, Y. Makhlin, J. Schriefl, et al., "Decoherence in a superconducting quantum bit circuit," Phys. Rev. B **72**, 134519 (2005). Cited on pp. 64, 101, 103.

Kitaev, A., "Protected qubit based on a superconducting current mirror," arXiv:cond-mat/0609441 (2006). Cited on pp. 18, 94.

Koch, J., T. M. Yu, J. Gambetta, A. A. Houck, D. I. Schuster, J. Majer, A. Blais, M. H. Devoret, S. M. Girvin, and R. J. Schoelkopf, "Charge-insensitive qubit design derived from the Cooper pair box," Phys. Rev. A **76**, 042319 (2007). Cited on pp. 2, 6, 21, 54, 82, 84, 94, 115.

Makhlin, Y. and A. Shnirman, "Dephasing of solid-state qubits at optimal points," Phys. Rev. Lett. **92**, 178301 (2004). Cited on pp. 101, 104.

Manucharyan, V. E., "Superinductance," Ph.D. thesis (Yale University, 2012). Cited on p. 34.

Manucharyan, V. E., J. Koch, L. I. Glazman, and M. H. Devoret, "Fluxonium: Single

Cooper-pair circuit free of charge offsets," Science **326**, 113–116 (2009). Cited on pp. 3, 18, 20, 29, 34, 51, 54, 94.

Masluk, N. A., I. M. Pop, A. Kamal, Z. K. Minev, and M. H. Devoret, "Microwave characterization of Josephson junction arrays: Implementing a low loss superinductance," Phys. Rev. Lett. **109**, 137002 (2012). Cited on pp. 18, 23, 34–35, 41.

Matveev, K. A., A. I. Larkin, and L. I. Glazman, "Persistent current in superconducting nanorings," Phys. Rev. Lett. **89**, 096802 (2002). Cited on pp. 24–25, 49.

Nigg, S. E., H. Paik, B. Vlastakis, G. Kirchmair, S. Shankar, L. Frunzio, M. H. Devoret, R. J. Schoelkopf, and S. M. Girvin, "Black-box superconducting circuit quantization," Phys. Rev. Lett. **108**, 240502 (2012). Cited on pp. 15, 22, 36–37.

Pop, I. M., K. Geerlings, G. Catelani, R. J. Schoelkopf, L. I. Glazman, and M. H. Devoret, "Coherent suppression of electromagnetic dissipation due to superconducting quasiparticles," Nature **508**, 369–372 (2014). Cited on pp. 35, 54–55, 69–70, 79–80, 94.

Schoelkopf, R. J., A. A. Clerk, S. M. Girvin, K. W. Lehnert, and M. H. Devoret, "Qubits as spectrometers of quantum noise," in *Quantum Noise in Mesoscopic Physics*, edited by Y. V. Nazarov (Springer, Dordrecht, 2003), pp. 175–203. Cited on p. 68.

Yan, F., S. Gustavsson, A. Kamal, J. Birenbaum, A. P. Sears, D. Hover, T. J. Gudmundsen, D. Rosenberg, G. Samach, S. Weber, et al., "The flux qubit revisited to enhance coherence and reproducibility," Nat. Commun. **7**, 12964 (2016). Cited on pp. 3, 74, 80, 94.

Extended bibliography

Additional referenced material

Aasen, D., M. Hell, R. V. Mishmash, A. Higginbotham, J. Danon, M. Leijnse, T. S. Jespersen, J. A. Folk, C. M. Marcus, K. Flensberg, et al., "Milestones toward Majorana-based quantum computing," Phys. Rev. X **6**, 031016 (2016). Cited on pp. 27, 54.

Aharonov, D. and M. Ben-Or, "Fault-tolerant quantum computation with constant error rate," SIAM J. Comput. **38**, 1207–1282 (2008). Cited on p. 94.

Aharonov, D., A. Kitaev, and J. Preskill, "Fault-tolerant quantum computation with long-range correlated noise," Phys. Rev. Lett. **96**, 050504 (2006). Cited on p. 94.

Albert, V. V., L. I. Glazman, and L. Jiang, "Topological properties of linear circuit lattices," Phys. Rev. Lett. **114**, 173902 (2015). Cited on p. 14.

Aliferis, P., D. Gottesman, and J. Preskill, "Quantum accuracy threshold for concatenated distance-3 codes," Quantum Inf. Comput. **6**, 97–165 (2006). Cited on p. 94.

Barends, R., J. Kelly, A. Megrant, D. Sank, E. Jeffrey, Y. Chen, Y. Yin, B. Chiaro, J. Mutus, C. Neill, et al., "Coherent Josephson qubit suitable for scalable quantum integrated circuits," Phys. Rev. Lett. **111**, 080502 (2013). Cited on pp. 4, 54, 94.

Bell, M. T., I. A. Sadovskyy, L. B. Ioffe, A. Y. Kitaev, and M. E. Gershenson, "Quantum superinductor with tunable nonlinearity," Phys. Rev. Lett. **109**, 137003 (2012). Cited on p. 34.

Bergmann, K., H. Theuer, and B. W. Shore, "Coherent population transfer among quantum states of atoms and molecules," Rev. Mod. Phys. **70**, 1003 (1998). Cited on pp. 65, 85, 87.

Bertet, P., I. Chiorescu, G. Burkard, K. Semba, C. J. P. M. Harmans, D. P. DiVincenzo, and J. E. Mooij, "Dephasing of a superconducting qubit induced by photon noise," Phys. Rev. Lett. **95**, 257002 (2005). Cited on p. 61.

Boissonneault, M., J. M. Gambetta, and A. Blais, "Nonlinear dispersive regime of cavity QED: The dressed dephasing model," Phys. Rev. A **77**, 060305(R) (2008). Cited on p. 57.

Bouchiat, V., D. Vion, P. Joyez, D. Esteve, and M. H. Devoret, "Quantum coherence with a single Cooper pair," Phys. Scr. **T76**, 165 (1998). Cited on p. 1.

Braginsky, V. B., V. S. Ilchenko, and K. S. Bagdassarov, "Experimental observation of fundamental microwave absorption in high-quality dielectric crystals," Phys. Lett. A **120**, 300–305 (1987). Cited on p. 68.

Burkard, G., D. P. DiVincenzo, P. Bertet, I. Chiorescu, and J. E. Mooij, "Asymmetry and decoherence in a double-layer persistent-current qubit," Phys. Rev. B **71**, 134504 (2005). Cited on p. 54.

Burkard, G., R. H. Koch, and D. P. DiVincenzo, "Multilevel quantum description of decoherence in superconducting qubits," Phys. Rev. B **69**, 064503 (2004). Cited on p. 15.

Bylander, J., S. Gustavsson, F. Yan, F. Yoshihara, K. Harrabi, G. Fitch, D. G. Cory, Y. Nakamura, J.-S. Tsai, and W. D. Oliver, "Noise spectroscopy through dynamical decoupling with a superconducting flux qubit," Nat. Phys. **7**, 565–570 (2011). Cited on p. 62.

Caldeira, A. O. and A. J. Leggett, "Quantum tunnelling in a dissipative system," Ann. Phys. (N.Y.) **149**, 374–456 (1983). Cited on p. 1.

Catelani, G., R. J. Schoelkopf, M. H. Devoret, and L. I. Glazman, "Relaxation and frequency shifts induced by quasiparticles in superconducting qubits," Phys. Rev. B **84**, 064517 (2011). Cited on pp. 55, 69.

Chen, Y., C. Neill, P. Roushan, N. Leung, M. Fang, R. Barends, J. Kelly, B. Campbell, Z. Chen, B. Chiaro, et al., "Qubit architecture with high coherence and fast tunable coupling," Phys. Rev. Lett. **113**, 220502 (2014). Cited on p. 46.

Chen, Y., D. Sank, P. OMalley, T. White, R. Barends, B. Chiaro, J. Kelly, E. Lucero, M. Mariantoni, A. Megrant, et al., "Multiplexed dispersive readout of superconducting phase qubits," Appl. Phys. Lett. **101**, 182601 (2012). Cited on p. 44.

Chiorescu, I., P. Bertet, K. Semba, Y. Nakamura, C. J. P. M. Harmans, and J. E. Mooij, "Coherent dynamics of a flux qubit coupled to a harmonic oscillator," Nature **431**, 159–162 (2004). Cited on p. 34.

Chiorescu, I., Y. Nakamura, C. J. P. M. Harmans, and J. E. Mooij, "Coherent quantum dynamics of a superconducting flux qubit," Science **299**, 1869–1871 (2003). Cited on p. 34.

Chow, J. M., L. DiCarlo, J. M. Gambetta, F. Motzoi, L. Frunzio, S. M. Girvin, and R. J. Schoelkopf, "Optimized driving of superconducting artificial atoms for improved single-qubit gates," Phys. Rev. A **82**, 040305 (2010). Cited on pp. 4, 85.

Christensen, B. G., C. D. Wilen, A. Opremcak, J. Nelson, F. Schlenker, C. H. Zimonick, L. Faoro, L. B. Ioffe, Y. J. Rosen, J. L. DuBois, et al., "Anomalous charge noise in superconducting qubits," arXiv:1905.13712 (2019). Cited on pp. 61, 72.

Chu, Y., P. Kharel, W. H. Renninger, L. D. Burkhart, L. Frunzio, P. T. Rakich, and R. J. Schoelkopf, "Quantum acoustics with superconducting qubits," Science **358**, 199–202 (2017). Cited on p. 1.

Cirac, J. I. and P. Zoller, "Quantum computations with cold trapped ions," Phys. Rev. Lett. **74**, 4091 (1995). Cited on p. 1.

Clarke, J. and A. I. Braginski, eds., *The SQUID Handbook*, Vol. I (Wiley-VCH, Weinheim, 2004). Cited on p. 20.

Clerk, A. A. and D. W. Utami, "Using a qubit to measure photon-number statistics of a driven thermal oscillator," Phys. Rev. A **75**, 042302 (2007). Cited on pp. 73, 116–117.

Cottet, A., D. Vion, A. Aassime, P. Joyez, D. Esteve, and M. H. Devoret, "Implementation of a combined charge-phase quantum bit in a superconducting circuit," Physica C **367**, 197–203 (2002). Cited on p. 94.

Dempster, J. M., B. Fu, D. G. Ferguson, D. I. Schuster, and J. Koch, "Understanding degenerate ground states of a protected quantum circuit in the presence of disorder," Phys. Rev. B **90**, 094518 (2014). Cited on pp. 29, 54, 76, 83, 94.

Devoret, M. H. and R. J. Schoelkopf, "Superconducting circuits for quantum information: An outlook," Science **339**, 1169–1174 (2013). Cited on p. 1.

Devoret, M. H. and J. M. Martinis, "Implementing qubits with superconducting integrated circuits," Quantum Inf. Process. **3**, 163–203 (2004). Cited on p. 10.

Douçot, B., M. V. Feigel'man, and L. B. Ioffe, "Topological order in the insulating Josephson junction array," Phys. Rev. Lett. **90**, 107003 (2003). Cited on pp. 82, 94.

Douçot, B., M. V. Feigel'man, L. B. Ioffe, and A. S. Ioselevich, "Protected qubits and Chern-Simons theories in Josephson junction arrays," Phys. Rev. B **71**, 024505 (2005). Cited on p. 6.

Douçot, B., L. B. Ioffe, and J. Vidal, "Discrete non-Abelian gauge theories in Josephson-junction arrays and quantum computation," Phys. Rev. B **69**, 214501 (2004). Cited on p. 6.

Douçot, B. and J. Vidal, "Pairing of Cooper pairs in a fully frustrated Josephson-junction chain," Phys. Rev. Lett. **88**, 227005 (2002). Cited on pp. 5, 82, 94.

Earnest, N., S. Chakram, Y. Lu, N. Irons, R. K. Naik, N. Leung, L. Ocola, D. A. Czaplewski, B. Baker, J. Lawrence, et al., "Realization of a Λ system with metastable states of a capacitively shunted fluxonium," Phys. Rev. Lett. **120**, 150504 (2018). Cited on pp. 3, 20, 54, 73, 82, 94.

Faoro, L. and L. B. Ioffe, "Microscopic origin of critical current fluctuations in large, small, and ultra-small area Josephson junctions," Phys. Rev. B **75**, 227005 (2007). Cited on p. 61.

Faoro, L. and L. B. Ioffe, "Microscopic origin of low-frequency flux noise in Josephson circuits," Phys. Rev. Lett. **100**, 132505 (2008). Cited on p. 62.

Ferguson, D. G., A. A. Houck, and J. Koch, "Symmetries and collective excitations in large superconducting circuits," Phys. Rev. X **3**, 011003 (2013). Cited on pp. 35, 41.

Feynman, R. P., "Simulating physics with computers," Int. J. Theor. Phys. **21**, 467–488 (1982). Cited on p. 1.

Frattini, N. E., U. Vool, S. Shankar, A. Narla, K. M. Sliwa, and M. H. Devoret, "3-wave mixing Josephson dipole element," Appl. Phys. Lett. **110**, 222603 (2017). Cited on pp. 86–87.

Freedman, M., A. Kitaev, M. Larsen, and Z. Wang, "Topological quantum computation," Bull. Am. Math. Soc. **40**, 31–38 (2003). Cited on p. 1.

Friedman, J. R., V. Patel, W. Chen, S. K. Tolpygo, and J. E. Lukens, "Quantum superposition of distinct macroscopic states," Nature **406**, 43–46 (2000). Cited on p. 3.

Gao, Y. Y., B. J. Lester, K. S. Chou, L. Frunzio, M. H. Devoret, L. Jiang, S. M. Girvin, and R. J. Schoelkopf, "Entanglement of bosonic modes through an engineered exchange interaction," Nature **566**, 509–512 (2019). Cited on p. 4.

Geerlings, K. L., "Improving coherence of superconducting qubits and resonators," Ph.D. thesis (Yale University, 2013). Cited on pp. 44, 70.

de Gennes, P. G., *Superconductivity of Metals and Alloys* (CRC Press, Boca Raton, 1999). Cited on p. 118.

Giuliani, G. F. and G. Vignale, *Quantum Theory of the Electron Liquid* (Cambridge University Press, New York, 2005). Cited on p. 118.

Gottesman, D., "Stabilizer codes and quantum error correction," Ph.D. thesis (California Institute of Technology, 1997). Cited on p. 4.

Gottesman, D., A. Kitaev, and J. Preskill, "Encoding a qubit in an oscillator," Phys. Rev. A **64**, 012310 (2001). Cited on pp. 6, 28, 32.

Gradshteyn, I. S. and I. M. Ryzhik, *Table of Integrals, Series, and Products*, edited by A. Jeffrey and D. Zwillinger, 7th ed. (Academic Press, San Diego, 2007). Cited on p. 38.

Groszkowski, P., A. D. Paolo, A. L. Grimsmo, A. Blais, D. I. Schuster, A. A. Houck, and J. Koch, "Coherence properties of the 0-π qubit," New J. Phys. **20**, 043053 (2018). Cited on pp. 80, 94.

Gustavsson, S., J. Bylander, F. Yan, W. D. Oliver, F. Yoshihara, and Y. Nakamura, "Noise correlations in a flux qubit with tunable tunnel coupling," Phys. Rev. B **84**, 014525 (2011). Cited on pp. 47, 62.

Guth, A. H., K. Huang, and R. L. Jaffe, eds., *Asymptotic Realms of Physics: Essays in Honor of Francis E. Low* (The MIT Press, Cambridge, 1983). Cited on p. 30.

van Harlingen, D. J., T. L. Robertson, B. L. T. Plourde, P. A. Reichardt, T. A. Crane, and J. Clarke, "Decoherence in Josephson-junction qubits due to critical-current

fluctuations," Phys. Rev. B **70**, 064517 (2004). Cited on pp. 61, 73.
Haroche, S. and J.-M. Raimond, *Exploring the Quantum: Atoms, Cavities, and Photons* (Oxford University Press, Oxford, 2006). Cited on p. 116.
Hatridge, M., S. Shankar, M. Mirrahimi, F. Schackert, K. Geerlings, T. Brecht, K. M. Sliwa, B. Abdo, L. Frunzio, S. M. Girvin, et al., "Quantum back-action of an individual variable-strength measurement," Science **339**, 178–181 (2013). Cited on p. 43.
Hays, M., G. de Lange, K. Serniak, D. J. van Woerkom, D. Bouman, P. Krogstrup, J. Nygård, A. Geresdi, and M. H. Devoret, "Direct microwave measurement of Andreev-bound-state dynamics in a semiconductor-nanowire Josephson junction," Phys. Rev. Lett. **121**, 047001 (2018). Cited on p. 9.
Houck, A. A., J. A. Schreier, B. R. Johnson, J. M. Chow, J. Koch, J. M. Gambetta, D. I. Schuster, L. Frunzio, M. H. Devoret, S. M. Girvin, et al., "Controlling the spontaneous emission of a superconducting transmon qubit," Phys. Rev. Lett. **101**, 080502 (2008). Cited on pp. 4, 54, 94.
Hu, L., Y. Ma, W. Cai, X. Mu, Y. Xu, W. Wang, Y. Wu, H. Wang, Y. P. Song, C.-L. Zou, et al., "Quantum error correction and universal gate set operation on a binomial bosonic logical qubit," Nat. Phys. **15**, 503–508 (2019). Cited on p. 4.
Ioffe, L. B., M. V. Feigelman, A. Ioselevich, D. Ivanov, M. Troyer, and G. Blatter, "Topologically protected quantum bits using Josephson junction arrays," Nature **415**, 503–506 (2002). Cited on pp. 82, 94.
Izmalkov, A., M. Grajcar, E. Il'ichev, T. Wagner, H.-G. Meyer, A. Y. Smirnov, M. H. S. Amin, A. M. van den Brink, and A. M. Zagoskin, "Evidence for entangled states of two coupled flux qubits," Phys. Rev. Lett. **93**, 037003 (2004). Cited on p. 46.
Jelezko, F., T. Gaebel, I. Popa, A. Gruber, and J. Wrachtrup, "Observation of coherent oscillations in a single electron spin," Phys. Rev. Lett. **92**, 076401 (2004). Cited on p. 1.
Jones, E., T. E. Oliphant, P. Peterson, et al., "SciPy: Open source scientific tools for Python," `scipy.org` (2001). Cited on p. 31.
Josephson, B. D., "Possible new effects in superconductive tunnelling," Phys. Lett. **1**, 251–253 (1962). Cited on pp. 1, 10.
Kelly, J., R. Barends, A. G. Fowler, A. Megrant, E. Jeffrey, T. C. White, D. Sank, J. Y. Mutus, B. Campbell, Y. Chen, et al., "State preservation by repetitive error detection in a superconducting quantum circuit," Nature **519**, 66–69 (2015). Cited on p. 4.
Koch, J., V. Manucharyan, M. H. Devoret, and L. I. Glazman, "Charging effects in the inductively shunted Josephson junction," Phys. Rev. Lett. **103**, 217004 (2009). Cited on pp. 3, 34.
Koch, R. H., D. P. DiVincenzo, and J. Clarke, "Model for $1/f$ flux noise in SQUIDs and qubits," Phys. Rev. Lett. **98**, 267003 (2007). Cited on p. 62.
Kubo, R., "Statistical-mechanical theory of irreversible processes. I. General theory and simple applications to magnetic and conduction problems," J. Phys. Soc. Jpn. **12**, 570–586 (1957). Cited on p. 31.
Kumar, P., S. Sendelbach, M. A. Beck, J. W. Freeland, Z. Wang, H. Wang, C. C. Yu, R. Q. Wu, D. P. Pappas, and R. McDermott, "Origin and reduction of $1/f$ magnetic flux noise in superconducting devices," Phys. Rev. Appl. **6**, 041001 (2016). Cited on pp. 4, 61, 64, 94.
Langer, C., R. Ozeri, J. Jost, J. Chiaverini, B. DeMarco, A. Ben-Kish, R. Blakestad,

J. Britton, D. Hume, W. Itano, et al., "Long-lived qubit memory using atomic ions," Phys. Rev. Lett. **95**, 060502 (2005). Cited on p. 65.

Lecocq, F., I. M. Pop, Z. Peng, I. Matei, T. Crozes, T. Fournier, C. Naud, W. Guichard, and O. Buisson, "Junction fabrication by shadow evaporation without a suspended bridge," Nanotechnology **22**, 315302 (2011). Cited on p. 44.

Leghtas, Z., S. Touzard, I. M. Pop, A. Kou, B. Vlastakis, A. Petrenko, K. M. Sliwa, A. Narla, S. Shankar, M. J. Hatridge, et al., "Confining the state of light to a quantum manifold by engineered two-photon loss," Science **347**, 853–857 (2015). Cited on pp. 4, 22.

Leroux, C., L. C. G. Govia, and A. A. Clerk, "Enhancing cavity quantum electrodynamics via antisqueezing: Synthetic ultrastrong coupling," Phys. Rev. Lett. **120**, 093602 (2018). Cited on p. 23.

Lidar, D. A., I. L. Chuang, and K. B. Whaley, "Decoherence-free subspaces for quantum computation," Phys. Rev. Lett. **81**, 2594 (1998). Cited on p. 94.

Lin, Y.-H., L. B. Nguyen, N. Grabon, J. S. Miguel, N. Pankratova, and V. E. Manucharyan, "Demonstration of protection of a superconducting qubit from energy decay," Phys. Rev. Lett. **120**, 150503 (2018). Cited on pp. 54, 82, 94.

van Loo, A. F., A. Fedorov, K. Lalumière, B. C. Sanders, A. Blais, and A. Wallraff, "Photon-mediated interactions between distant artificial atoms," Science **342**, 1494–1496 (2013). Cited on p. 44.

Ludlow, A. D., M. M. Boyd, T. Zelevinsky, S. M. Foreman, S. Blatt, M. Notcutt, T. Ido, and J. Ye, "Systematic study of the ^{87}Sr clock transition in an optical lattice," Phys. Rev. Lett. **96**, 033003 (2006). Cited on p. 65.

Macklin, C., K. OBrien, D. Hover, M. E. Schwartz, V. Bolkhovsky, X. Zhang, W. D. Oliver, and I. Siddiqi, "A near-quantum-limited Josephson traveling-wave parametric amplifier," Science **350**, 307–310 (2015). Cited on p. 57.

Majer, J. B., J. M. Chow, J. M. Gambetta, J. Koch, B. R. Johnson, J. A. Schreier, L. Frunzio, D. I. Schuster, A. A. Houck, A. Wallraff, et al., "Coupling superconducting qubits via a cavity bus," Nature **449**, 443–447 (2007). Cited on p. 46.

Majer, J. B., F. G. Paauw, A. C. J. ter Haar, C. J. P. M. Harmans, and J. E. Mooij, "Spectroscopy on two coupled superconducting flux qubits," Phys. Rev. Lett. **94**, 090501 (2005). Cited on p. 46.

Manucharyan, V. E., N. A. Masluk, A. Kamal, J. Koch, L. I. Glazman, and M. H. Devoret, "Evidence for coherent quantum phase slips across a Josephson junction array," Phys. Rev. B **85**, 024521 (2012). Cited on p. 18.

Martinis, J. M., K. B. Cooper, R. McDermott, M. Steffen, M. Ansmann, K. D. Osborn, K. Cicak, S. Oh, D. P. Pappas, R. W. Simmonds, et al., "Decoherence in Josephson qubits from dielectric loss," Phys. Rev. Lett. **95**, 210503 (2005). Cited on pp. 4, 54, 94.

Masluk, N. A., "Reducing the losses of the fluxonium artificial atom," Ph.D. thesis (Yale University, 2013). Cited on p. 68.

McDermott, R., R. W. Simmonds, M. Steffen, K. B. Cooper, K. Cicak, K. D. Osborn, S. Oh, D. P. Pappas, and J. M. Martinis, "Simultaneous state measurement of coupled Josephson phase qubits," Science **307**, 1299–1302 (2005). Cited on p. 44.

Meier, H., R. T. Brierley, A. Kou, S. M. Girvin, and L. I. Glazman, "Signatures of quantum phase transitions in the dynamic response of fluxonium qubit chains," Phys. Rev. B **92**, 064516 (2015). Cited on p. 49.

Meixner, J., F. W. Schäfke, and G. Wolf, *Mathieu Functions and Spheroidal Functions and their Mathematical Foundations* (Springer-Verlag, Berlin, 1980).

Cited on pp. 6, 21.
Mirrahimi, M., Z. Leghtas, V. V. Albert, S. Touzard, R. J. Schoelkopf, L. Jiang, and M. H. Devoret, "Dynamically protected cat-qubits: A new paradigm for universal quantum computation," New J. Phys. **16**, 045014 (2014). Cited on p. 4.
Mooij, J. E. and Y. V. Nazarov, "Superconducting nanowires as quantum phase-slip junctions," Nature Physics **2**, 169–172 (2006). Cited on p. 32.
Mooij, J. E., T. P. Orlando, L. Levitov, L. Tian, C. H. van der Wal, and S. Lloyd, "Josephson persistent-current qubit," Science **285**, 1036–1039 (1999). Cited on p. 34.
Murch, K. W., U. Vool, D. Zhou, S. J. Weber, S. M. Girvin, and I. Siddiqi, "Cavity-assisted quantum bath engineering," Phys. Rev. Lett. **109**, 183602 (2012). Cited on p. 4.
Nakamura, Y., Y. A. Pashkin, and J. S. Tsai, "Coherent control of macroscopic quantum states in a single-Cooper-pair box," Nature **398**, 786–788 (1999). Cited on pp. 2–3.
Novais, E. and H. U. Baranger, "Decoherence by correlated noise and quantum error correction," Phys. Rev. Lett. **97**, 040501 (2006). Cited on p. 94.
Ofek, N., A. Petrenko, R. Heeres, P. Reinhold, Z. Leghtas, B. Vlastakis, Y. Liu, L. Frunzio, S. M. Girvin, L. Jiang, et al., "Extending the lifetime of a quantum bit with error correction in superconducting circuits," Nature **536**, 441–445 (2016). Cited on p. 4.
Orlando, T. P., J. E. Mooij, L. Tian, C. H. van der Wal, L. S. Levitov, S. Lloyd, and J. J. Mazo, "Superconducting persistent-current qubit," Phys. Rev. B **60**, 15398 (1999). Cited on p. 34.
Paik, H., D. I. Schuster, L. S. Bishop, G. Kirchmair, G. Catelani, A. P. Sears, B. R. Johnson, M. J. Reagor, L. Frunzio, L. I. Glazman, et al., "Observation of high coherence in Josephson junction qubits measured in a three-dimensional circuit QED architecture," Phys. Rev. Lett. **107**, 240501 (2011). Cited on pp. 4, 61, 94.
Pechenezhskiy, I. V., R. A. Mencia, L. B. Nguyen, Y.-H. Lin, and V. E. Manucharyan, "Quantum dynamics of quasicharge in an ultrahigh-impedance superconducting circuit," arXiv:1907.02937 (2019). Cited on pp. 34, 83.
Petta, J. R., A. C. Johnson, J. M. Taylor, E. A. Laird, A. Yacoby, M. D. Lukin, C. M. Marcus, M. P. Hanson, and A. C. Gossard, "Coherent manipulation of coupled electron spins in semiconductor quantum dots," Science **309**, 2180–2184 (2005). Cited on p. 1.
Pines, D., *Elementary Excitations in Solids: Lectures on Protons, Electrons, and Plasmons* (CRC Press, Boca Raton, 1999). Cited on p. 118.
Pino, M., A. Tsvelik, and L. Ioffe, "Unpaired Majorana modes in Josephson-junction arrays with gapless bulk excitations," Phys. Rev. Lett. **115**, 197001 (2015). Cited on p. 14.
Pozar, D. M., *Microwave Engineering*, 4th ed. (Wiley, Hoboken, 2012). Cited on p. 23.
Puri, S., S. Boutin, and A. Blais, "Engineering the quantum states of light in a Kerr-nonlinear resonator by two-photon driving," npj Quantum Inf. **3**, 18 (2017). Cited on pp. 4, 22.
Quintana, C. M., Y. Chen, D. Sank, A. G. Petukhov, T. C. White, D. Kafri, B. Chiaro, A. Megrant, R. Barends, B. Campbell, et al., "Observation of classical-quantum crossover of $1/f$ flux noise and its paramagnetic temperature dependence," Phys. Rev. Lett. **118**, 057702 (2017). Cited on p. 73.
Reagor, M., H. Paik, G. Catelani, L. Sun, C. Axline, E. Holland, I. M. Pop, N. A. Masluk, T. Brecht, L. Frunzio, et al., "Reaching 10 ms single photon lifetimes for superconducting aluminum cavities," Appl. Phys. Lett. **102**, 192604 (2013). Cited on p. 94.

Rigetti, C., J. M. Gambetta, S. Poletto, B. L. T. Plourde, J. M. Chow, A. D. Córcoles, J. A. Smolin, S. T. Merkel, J. R. Rozen, G. A. Keefe, et al., "Superconducting qubit in a waveguide cavity with a coherence time approaching 0.1 ms," Phys. Rev. B **86**, 100506 (2012). Cited on pp. 4, 44, 61, 94.

Ristè, D., S. Poletto, M.-Z. Huang, A. Bruno, V. Vesterinen, O.-P. Saira, and L. DiCarlo, "Detecting bit-flip errors in a logical qubit using stabilizer measurements," Nat. Commun. **6**, 6983 (2015). Cited on p. 4.

Riwar, R.-P., M. Houzet, J. S. Meyer, and Y. V. Nazarov, "Multi-terminal Josephson junctions as topological matter," Nat. Commun. **7**, 11167 (2016). Cited on p. 9.

Schmitt, V., X. Zhou, K. Juliusson, B. Royer, A. Blais, P. Bertet, D. Vion, and D. Esteve, "Multiplexed readout of transmon qubits with Josephson bifurcation amplifiers," Phys. Rev. A **90**, 062333 (2014). Cited on p. 44.

Schreier, J. A., A. A. Houck, J. Koch, D. I. Schuster, B. R. Johnson, J. M. Chow, J. M. Gambetta, J. Majer, L. Frunzio, M. H. Devoret, et al., "Suppressing charge noise decoherence in superconducting charge qubits," Phys. Rev. B **77**, 180502 (2008). Cited on p. 3.

Schrieffer, J. R., *Theory of Superconductivity* (CRC Press, Boca Raton, 1999). Cited on p. 118.

Schriefl, J., Y. Makhlin, A. Shnirman, and G. Schön, "Decoherence from ensembles of two-level fluctuators," New J. Phys. **8**, 1 (2006). Cited on p. 109.

Serniak, K., M. Hays, G. de Lange, S. Diamond, S. Shankar, L. D. Burkhart, L. Frunzio, M. Houzet, and M. H. Devoret, "Hot nonequilibrium quasiparticles in transmon qubits," Phys. Rev. Lett. **121**, 157701 (2018). Cited on p. 70.

Shankar, S., M. Hatridge, Z. Leghtas, K. M. Sliwa, A. Narla, U. Vool, S. M. Girvin, L. Frunzio, M. Mirrahimi, and M. H. Devoret, "Autonomously stabilized entanglement between two superconducting quantum bits," Nature **504**, 419–422 (2013). Cited on p. 4.

Shearrow, A., G. Koolstra, S. J. Whiteley, N. Earnest, P. S. Barry, F. J. Heremans, D. D. Awschalom, E. Shirokoff, and D. I. Schuster, "Atomic layer deposition of titanium nitride for quantum circuits," Appl. Phys. Lett. **113**, 212601 (2018). Cited on pp. 34, 83.

Shnirman, A., G. Schön, I. Martin, and Y. Makhlin, "$1/f$ noise and two-level systems in Josephson qubits," in *Electron Correlation in New Materials and Nanosystems*, edited by K. Scharnberg and S. Kruchinin (Springer, Dordrecht, 2007), pp. 343–356. Cited on p. 109.

Slichter, D. H., R. Vijay, S. J. Weber, S. Boutin, M. Boissonneault, J. M. Gambetta, A. Blais, and I. Siddiqi, "Measurement-induced qubit state mixing in circuit QED from up-converted dephasing noise," Phys. Rev. Lett. **109**, 153601 (2012). Cited on p. 57.

Solgun, F., D. W. Abraham, and D. P. DiVincenzo, "Blackbox quantization of superconducting circuits using exact impedance synthesis," Phys. Rev. B **90**, 134504 (2014). Cited on pp. 15, 36.

Steck, D. A., "Quantum and Atom Optics," `steck.us/teaching` **0.12.6** (2019). Cited on p. 87.

Steffen, M., M. Ansmann, R. McDermott, N. Katz, R. C. Bialczak, E. Lucero, M. Neeley, E. M. Weig, A. N. Cleland, and J. M. Martinis, "State tomography of capacitively shunted phase qubits with high fidelity," Phys. Rev. Lett. **97**, 050502 (2006). Cited on p. 3.

Steffen, M., S. Kumar, D. P. DiVincenzo, J. R. Rozen, G. A. Keefe, M. B. Rothwell, and

M. B. Ketchen, "High-coherence hybrid superconducting qubit," Phys. Rev. Lett. **105**, 100502 (2010). Cited on p. 94.

Süsstrunk, R., I. Garate, and L. I. Glazman, "Aharonov-Casher effect for plasmons in a ring of Josephson junctions," Phys. Rev. B **88**, 060506 (2013). Cited on pp. 26, 75, 82.

Tabuchi, Y., S. Ishino, A. Noguchi, T. Ishikawa, R. Yamazaki, K. Usami, and Y. Nakamura, "Coherent coupling between a ferromagnetic magnon and a superconducting qubit," Science **349**, 405–408 (2015). Cited on p. 1.

Tinkham, M., *Introduction to Superconductivity* (Dover, Mineola, 2004). Cited on p. 118.

Viola, G. and G. Catelani, "Collective modes in the fluxonium qubit," Phys. Rev. B **92**, 224511 (2015). Cited on p. 41.

Viola, L., E. Knill, and S. Lloyd, "Dynamical decoupling of open quantum systems," Phys. Rev. Lett. **82**, 2417 (1999). Cited on p. 94.

Vion, D., A. Aassime, A. Cottet, P. Joyez, H. Pothier, C. Urbina, D. Esteve, and M. H. Devoret, "Manipulating the quantum state of an electrical circuit," Science **296**, 886–889 (2002). Cited on pp. 2–3, 82, 94.

Vool, U., I. M. Pop, K. Sliwa, B. Abdo, C. Wang, T. Brecht, Y. Y. Gao, S. Shankar, M. Hatridge, G. Catelani, et al., "Non-Poissonian quantum jumps of a fluxonium qubit due to quasiparticle excitations," Phys. Rev. Lett. **113**, 247001 (2014). Cited on pp. 35, 58.

van der Wal, C. H., A. C. J. ter Haar, F. K. Wilhelm, R. N. Schouten, C. J. P. M. Harmans, T. P. Orlando, S. Lloyd, and J. E. Mooij, "Quantum superposition of macroscopic persistent-current states," Science **290**, 773–777 (2000). Cited on pp. 3, 51, 94.

Wallraff, A., D. I. Schuster, A. Blais, L. Frunzio, R.-S. Huang, J. Majer, S. Kumar, S. M. Girvin, and R. J. Schoelkopf, "Strong coupling of a single photon to a superconducting qubit using circuit quantum electrodynamics," Nature **431**, 162–167 (2004). Cited on p. 43.

Wang, C., C. Axline, Y. Y. Gao, T. Brecht, Y. Chu, L. Frunzio, M. H. Devoret, and R. J. Schoelkopf, "Surface participation and dielectric loss in superconducting qubits," Appl. Phys. Lett. **107**, 162601 (2015). Cited on p. 68.

Wang, Z., S. Shankar, Z. Minev, P. Campagne-Ibarcq, A. Narla, and M. Devoret, "Cavity attenuators for superconducting qubits," Phys. Rev. Appl. **11**, 014031 (2019). Cited on pp. 1, 4, 43, 84, 88.

White, T. C., J. Y. Mutus, I.-C. Hoi, R. Barends, B. Campbell, Y. Chen, Z. Chen, B. Chiaro, A. Dunsworth, E. Jeffrey, et al., "Traveling wave parametric amplifier with Josephson junctions using minimal resonator phase matching," Appl. Phys. Lett. **106**, 242601 (2015). Cited on p. 57.

Yoshihara, F., K. Harrabi, A. O. Niskanen, Y. Nakamura, and J. S. Tsai, "Decoherence of flux qubits due to $1/f$ flux noise," Phys. Rev. Lett. **97**, 167001 (2006). Cited on p. 62.

Yoshihara, F., Y. Nakamura, and J. S. Tsai, "Correlated flux noise and decoherence in two inductively coupled flux qubits," Phys. Rev. B **81**, 132502 (2010). Cited on pp. 46–47, 62.

Yurke, B. and J. S. Denker, "Quantum network theory," Phys. Rev. A **29**, 1419–1437 (1984). Cited on p. 9.

Zhang, G., Y. Liu, J. J. Raftery, and A. A. Houck, "Suppression of photon shot noise dephasing in a tunable coupling superconducting qubit," npj Quantum Inf. **3**, 1 (2017). Cited on p. 86.

Zhu, G., D. G. Ferguson, V. E. Manucharyan, and J. Koch, "Circuit QED with fluxonium qubits: Theory of the dispersive regime," Phys. Rev. B **87**, 024510 (2013).

Cited on p. 41.
Zorin, A. B., F.-J. Ahlers, J. Niemeyer, T. Weimann, H. Wolf, V. A. Krupenin, and S. V. Lotkhov, "Background charge noise in metallic single-electron tunneling devices," Phys. Rev. B **53**, 13682 (1996). Cited on p. 72.